Theory of solar oscillations in the inertial frequency range

Dissertation
zur Erlangung des mathematisch-naturwissenschaftlichen Doktorgrades

"Doctor rerum naturalium"

der Georg-August-Universität Göttingen

im Promotionsstudiengang Physik
der Georg-August University School of Science (GAUSS)

vorgelegt von

Yuto Bekki

aus Fukushima, Japan

Göttingen, 2022

Betreuungsausschuss

Prof. Dr. Laurent Gizon
Max-Planck-Institut für Sonnensystemforschung, Göttingen, Germany
Institut für Astrophysik, Georg-August-Universität Göttingen, Germany

Dr. Robert Cameron
Max-Planck-Institut für Sonnensystemforschung, Göttingen, Germany

Prof. Dr. Andreas Tilgner
Institut für Geophysik, Georg-August-Universität Göttingen, Germany

Mitglieder der Prüfungskommision

Referent: **Prof. Dr. Laurent Gizon**
Max-Planck-Institut für Sonnensystemforschung, Göttingen, Germany
Institut für Astrophysik, Georg-August-Universität Göttingen, Germany

Korreferent: **Prof. Dr. Andreas Tilgner**
Institut für Geophysik, Georg-August-Universität Göttingen, Germany

Weitere Mitglieder der Prüfungskommission:

P.D. Dr. Olga Shishkina
Max-Planck-Institut für Dynamik und Selbstorganisation, Göttingen, Germany

Prof. Dr. Stefan Dreizler
Institut für Astrophysik, Georg-August-Universität Göttingen, Germany

Prof. Dr. Wolfram Kollatschny
Institut für Astrophysik, Georg-August-Universität Göttingen, Germany

Prof. Dr. Ramin Yahyapour
Gesellschaft für wissenschaftliche Datenverarbeitung mbH Göttingen
Institut für Informatik, Georg-August-Universität Göttingen, Germany

Tag der mündlichen Prüfung: 25.03.2022

Printed in Germany

Cover figure:
Three-dimensional visualization of the $m = 1$ high-latitude inertial mode (*red / blue*) and the $m = 8$ columnar convective mode (*yellow / cyan*) of the Sun computed by my linear eigenmode solver. The longitudinal velocity eigenfunctions are shown. *Background:* A snapshot of vertical velocity from my numerical simulation of the near-surface convection of the Sun.

Contents

Abstract

Recent observations have revealed that we lack a fundamental understanding of the large scale (with spherical harmonic degrees $l \lesssim 60$) flows in the Sun. Flows at these large scales are strongly influenced by rotation. In this thesis, we report both observational detection and identification of a number of different types of inertial modes where the restoring force is the Coriolis force. We then use numerical techniques to investigate the modes, first in the linear regime where we investigate the effect of viscosity, superadiabaticity and latitudinal entropy gradients on the modes. We further proceed by identifying some of modes in fully non-linear 3D stratified convection simulations, and in mean-field simulations. The knowledge obtained in this thesis will help us to establish a novel method of using the inertial modes to probe the interior of the Sun, i.e., inertial mode helioseismology.

In particular, in Chapter 2, we report a comprehensive observational detection of the inertial modes on the Sun. With the help of linear-eigenmode calculations (described in Chapter 3), we successfully identify three classes of solar inertial modes: the equatorial Rossby modes, critical-latitude modes, and high-latitude modes. Since these modes are sensitive to properties of the deep convection zone, they give us a new diagnostic potential to learn about the deep interior of the Sun.

In Chapter 3, we develop a 2.5D numerical code to study the linear eigenmodes of rotating compressible fluid with the solar-like stratification. We take into account the effects of turbulent diffusion, entropy gradients, and helioseismically-constrained differential rotation in the Sun. We focus on the vorticity modes of oscillation in the inertial frequency range at low azimuthal orders, and show that the equatorial Rossby modes with one radial node ($n = 1$) are essentially mixed with the north-south anti-symmetric columnar convective modes. We also find that when the we include turbulent viscosity at a level of about 10^{12} cm^2 s^{-1} the radial eigenfunction of the $n = 0$ Rossby modes very different from the theoretically-expected r^m dependence and become confined near the base of the convection zone.

In Chapter 4, we carry out a numerical simulation of rotating turbulent convection in a stratified spherical shell to examine if the linear modes persist in this highly nonlinear regime. The code has been newly developed for this purpose and uses the reduced-speed of sound technique and a Yin-Yang grid. Various types of vorticity modes are extracted from the simulation data by performing a singular-value decomposition. The simulated power spectra and the extracted eigenfunctions are compared with the results of the linear analysis. We successfully identify both columnar convective modes and the equatorial Rossby modes in our simulation. North-south symmetric columnar convective modes contain the dominant velocity power and contribute substantially to the convective energy and angular momentum transport. Furthermore, we confirm the existence of the "mixed"

modes between the $n = 1$ Rossby modes and the north-south anti-symmetric columnar convective modes near the surface where convection is most vigorous. These results are in a qualitative agreement with our linear calculations.

In Chapter 5, we give a physical explanation for the high amplitudes of the observed high-latitude inertial modes on the Sun. We propose that they are driven by a baroclinic instability due to the latitudinal entropy gradient in the solar convection zone.

Chapter 6 is finally devoted to a development of the first three-dimensional magnetohydrodynamic(MHD) Babcock-Leighton-type solar dynamo code. In this framework, large-scale mean flows are maintained by the parameterized convective angular momentum transport (Λ-effect) without explicitly solving the thermal convection. We include a time-dependent random contribution in the Λ-effect which mimics the stochastic turbulent convective motions and can excite large-scale inertial modes. We successfully demonstrate that several inertial modes discussed above exist in this type of simulation. Therefore, our model can be potentially used to further study the effect of torsional oscillations, subsurface magnetic fields, and active region inflows on the Rossby and baroclinic modes.

1 Introduction

The Sun is a dynamic star. The thermal energy generated by nuclear fusion at the core of the Sun is continuously transported upward by radiation in the inner 70% (radiation zone) and by convection in the outer 30% of the interior (convection zone) (§1.1). Without a doubt, convection is what exactly makes the solar physics challenging and interesting. When convection occurs, many dynamical processes are caused by convection: It does not only transport the thermal energy in the Sun. Influenced by solar rotation, convection also transports the angular momentum and drives the large-scale mean flows such as differential rotation and meridional circulation (§1.3). These large-scale mean flows are believed to play critical roles in generating strong magnetic fields in the Sun and maintaining its magnetic activity with 11-yr periodicity (§1.4).

However, it has been widely recognized that our understanding on large-scale convection in the Sun is far from complete, as commonly known as "convective conundrum" (§1.6). Recently, equatorial Rossby waves have been unambiguously observed on the Sun. Interestingly, it is found that the Rossby waves contribute a significant fraction of the large-scale velocity power and thus can have a substantial impact on the convection zone dynamics. In this thesis, we study the theoretical aspects of the Rossby waves in the Sun in the linear and nonlinear regimes (with and without magnetic fields), and discuss their implications in the context of the convective conundrum. In the following, we briefly review the relevant topics from both observational and theoretical perspectives.

1.1 Internal structure of the Sun

Standard solar model S

The internal structure of the Sun is described by the "solar standard model" (Model S) (Christensen-Dalsgaard et al. 1996a), which is obtained by solving the equations of mass conservation, hydrostatic equilibrium, and thermal equilibrium (energy balance) under the boundary conditions at the core and at the surface of the Sun. It will be instructive to give readers some important observational solar parameters such as the solar radius $R_\odot = 6.96 \times 10^{10}$ cm,mass $M_\odot = 1.99 \times 10^{33}$ g, and luminosity $L_\odot = 3.84 \times 10^{33}$ erg s^{-1}. In order to close the equations, the energy flux in the Sun needs to be determined. In general, energy is transported by radiation when the background temperature gradient is moderate compared to the adiabatic gradient and by convection when the temperature gradient is sufficiently steep. Since the deep interior of the Sun is optically-thick, the radiative energy flux can be easily estimated using the diffusion approximation. On the

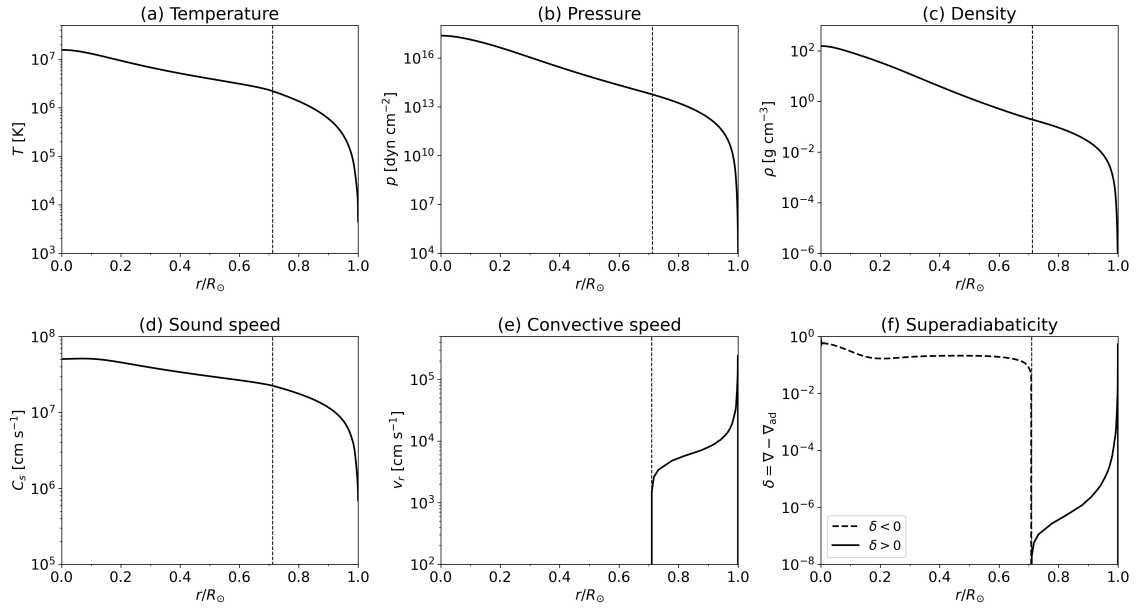

Figure 1.1: Profiles of (a) temperature, (b) pressure, (c) density, (d) sound speed, (e) convective speed, and (f) superadiabaticity as function of radius obtained by the solar standard model (Model S) (Christensen-Dalsgaard et al. 1996a). The typical convective speed v_r is estimated by local-mixing length model. The figure is reproduced using the data provided at https://users-phys.au.dk/jcd/solar_models/ and by Stix (2002).

other hand, the convective energy transport is much more difficult to model owing to the turbulent nature of the solar convection.

Convective energy transport (local mixing-length model)

Practically, this can be done using the mixing length theory (Vitense 1953, Böhm-Vitense 1958), which is based on the assumption that a convective fluid parcel will dissolve into its surroundings after moving a typical mixing-length distance $l_{\rm MLT}$ and deposit its energy there. The mixing length $l_{\rm MLT}$ is conventionally assumed to be comparable to the pressure scale height $H_p = -(d\ln p/dz)^{-1}$ as $l_{\rm MLT} = \alpha_{\rm MLT} H_p$, where $\alpha_{\rm MLT}$ is a mixing-length parameter. Then, the enthalpy flux $F_{\rm e}$ can be estimated as

$$F_{\rm e} = \langle \rho c_p v_r \Delta T \rangle = \frac{\alpha_{\rm MLT}}{2} \rho c_p v_r T \delta, \tag{1.1}$$

where $\delta = \nabla - \nabla_{\rm ad}$ is the superadiabaticity and $\nabla = d\ln T/d\ln p$ is the double-logarithmic temperature gradient. Positive (negative) δ represents the convectively unstable (stable) background for Schwarzschild criterion. Considering the buoyancy acceleration, the typical convective speed (radial component) v_r can be estimated as

$$v_r \approx l_{\rm MLT} \sqrt{\frac{g\delta}{8H_p}\left(\frac{\partial \ln \rho}{\partial \ln T}\right)_p}. \tag{1.2}$$

The coefficient $(\partial \ln \rho/\partial \ln T)_p$ can be obtained from the equation of state. Thus, the only remaining free parameter in the equations describing the solar internal structure is the

mixing-length parameter $\alpha_{\rm MLT}$. In practice, $\alpha_{\rm MLT}$ is adjusted so as to make the solutions fit with the observations. The typical value of $\alpha_{\rm MLT}$ is $\approx$ 1.8, which leads to the depth of the convection zone $r_{\rm base} = 0.71$. Figure 1.1 shows the internal stratification obtained by the standard model (Model S) of Christensen-Dalsgaard et al. (1996a). The validity of this solar standard model is well confirmed by global helioseismology.

A typical value of the superadiabaticity within the solar convection zone is very small $O(10^{-6})$. Therefore, the stratification within the solar convection zone is often approximated as adiabatic. The convective velocity obtained in the solar standard model is typically about $50 - 100$ m s^{-1} inside the convection zone, but increases significantly towards the photosphere up to $1000 - 2000$ m s^{-1}, which is just one order of magnitude smaller than the local sound speed.

As we will discuss in §1.6, the validity of the local mixing-length model recently comes into question. We note here that the effects of rotation (§1.3) and magnetic fields (§1.4) are not considered in this model.

1.2 High-frequency oscillations in the Sun

Power spectrum

The Sun is oscillating at various spatial and temporal scales. The greatest manifestation is the so-called 5 minutes oscillations of the Sun which has been observed in the fluctuations of the Doppler velocity at the solar surface (Leighton et al. 1962). This 5 minutes oscillations are later interpreted as standing acoustic waves that are trapped in a resonant cavity in the Sun (Ulrich 1970, Leibacher and Stein 1971, Deubner 1975, Rhodes et al. 1977). Ridges in the power spectrum, corresponding to the *global* eigenmodes of acoustic waves traveling through the entire Sun, were identified by Claverie et al. (1979), Grec et al. (1980) and Duvall and Harvey (1983). Their studies opened up a new branch of solar physics research, i.e., *helioseismology*, in which the solar eigenmodes of oscillation are used to probe properties of the Sun's interior. For more details, see Christensen-Dalsgaard (2002) and Basu (2016).

Figure 1.2a shows the observed power spectrum of the Sun obtained from SOHO/MDI, where a brighter part represents high wave power originating from the superposition of acoustic oscillations in the Sun. Each ridge represents the acoustic modes (p-modes) with different radial order n (e.g., Chou et al. 1995, Rhodes et al. 1997). The lowest-frequency ridge with faint power is the so-called f-modes (surface gravity waves) where $n = 0$. Internal gravity waves (g-modes) are expected to exist on frequencies below 0.5 mHz. When integrated over the solar disk (*Sun-as-a-star* observation), the power peaks at around $\nu_{\rm max} \approx 3$ mHz, corresponding to a period of 5 minutes, as shown in Fig. 1.2b (e.g., Elsworth et al. 1995). In the integrated light, signals associated with the modes for $l \leq 3$ are strongly cancelled, and therefore, the spectrum is dominated by modes of $l = 0, 1, 2$, and 3. The inset of Fig. 1.2b provides an expanded view around the frequency range of 3 mHz, where the four prominent peaks can be labelled by their spherical harmonic degree l. The associated so-called *Echelle* diagram (Grec et al. 1983) of the Sun is presented in Fig. 1.2c, where almost vertical power ridges can be identified for $l = 0, 2$ on

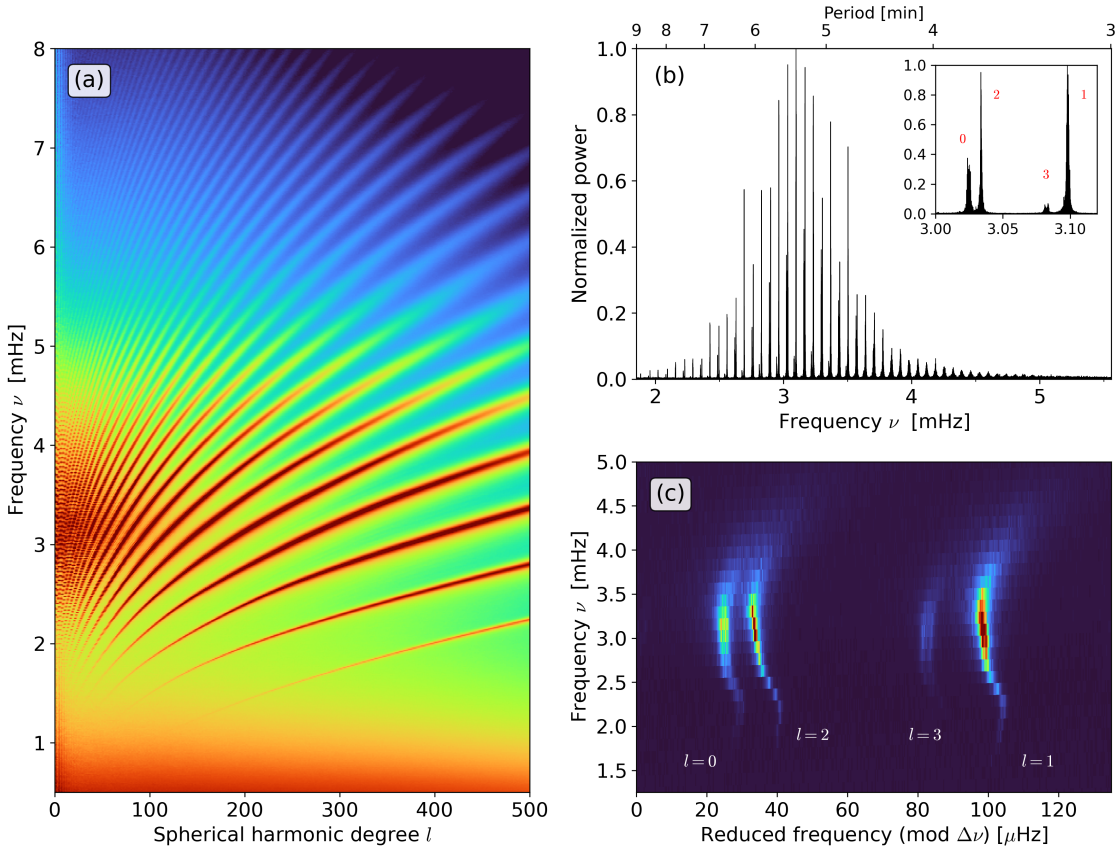

Figure 1.2: (a) Power spectrum of the oscillations on the Sun, obtained by SOHO/MDI over a time span of 10 days (1-10, December 2019). Shown is the power of Doppler velocity as a function of spherical harmonic degree l and frequency ν, averaged over all azimuthal orders m. Red regions indicate areas of high wave power formed by acoustic modes. (b) Spectrum of solar oscillations integrated over the full solar disk (*sun-as-a-star* observation), obtained from SOHO/GOLF instrument over a time span of 22 years (Appourchaux et al. 2018). The power is normalized. The inset shows a zoom-in focusing on the frequency range of about 3 mHz. (c) Echelle diagram of the Sun; the same power spectrum as panel (b) but plotted against the frequency modulo with the large separation of $\Delta\nu = 135.3$ μHz. The four vertical stripes of high power correspond to $l = 0, 2$, and $l = 1, 3$ from left to right. The power spectra data was provided by courtesy of Zhi-Chao Liang.

the left and for $l = 1, 3$ on the right with the large separation of $\Delta\nu = 135$ μHz. The small separation between $l = 0$ and $l = 2$ modes can be estimated as $\delta\nu = 9$ μHz for the Sun (Christensen-Dalsgaard 2002). In fact, stellar radius, mass, and evolutionary stage can be asteroseismocally-determined by measuring the peak frequency $\nu_{\max}$, large separation $\Delta\nu$, and small separation $\delta\nu$ obtained from the stellar (point-source) observations (e.g., Aerts et al. 2010).

Propagation diagram

Let us consider the linear non-radial oscillations in the Sun under the following approximations:

- A fluid motion is adiabatic, i.e., when a fluid parcel is perturbed (displacement is small), there is no heat exchange between the surroundings and the timescale of this displacement is slow compared to the thermal diffusive timescale.
- Rotational effects are ignored. Therefore, low-frequency inertial modes are omitted.
- Stratification is spherically symmetric.
- The change in a gravitational potential due to the density perturbation is neglected. This is called *Cowling* approximation (Cowling 1941).
- The perturbations can be expressed by spherical harmonics Y_l^m (where l is the spherical degree and m is the azimuthal order) and have the time dependence in a form of $\exp(-i\omega t)$ (where ω is the angular frequency).

The (locally-defined) radial wavenumber k_r of the perturbation must satisfy

$$k_r^2 = \frac{\omega^2}{Cs^2}\left(\frac{N^2}{\omega^2} - 1\right)\left(\frac{S_l^2}{\omega^2} - 1\right), \tag{1.3}$$

where the the Brunt-Väisälä frequency N and the Lamb frequency S_l are defined by

$$N^2 = g\left[\frac{1}{\gamma}\frac{d\ln p_0}{dr} - \frac{d\ln\rho_0}{dr}\right], \tag{1.4}$$

$$S_l^2 = l(l+1)\frac{Cs^2}{r^2}. \tag{1.5}$$

Figure 1.3 shows the radial profiles of N and S_l computed for the standard solar model S, which is often called as a propagation diagram. For a wave to propagate (oscillatory solution), $k_r^2 > 0$ is demanded, leading to the following two conditions.

$$\text{(I)} \quad \omega^2 > N^2 \quad \text{and} \quad \omega^2 > S_l^2 \tag{1.6}$$

$$\text{(II)} \quad \omega^2 < N^2 \quad \text{and} \quad \omega^2 < S_l^2 \tag{1.7}$$

The modes are thought to be damped in the evanescent region where, for example, $S_{l=1}^2 < \omega^2 < N^2$ in the middle convection zone.

p-modes (acoustic waves)

The first condition (I) corresponds to p-modes (acoustic modes) whose main restoring force is the pressure gradient force. In fact, in the limit of $\omega \to \infty$, Equation (1.5) can be reduced to the dispersion relation of sound waves $\omega^2 = C_s^2(k_r^2 + k_h^2)$ where $k_h^2 = l(l+1)/r^2$. p-modes can propagate as oscillatory waves in the outer layer of the Sun denoted by orange-shades in Figure 1.3. The depth that a p-mode with frequency ν can propagate into the Sun depends on l: The turning point (depth) can be roughly given by r that satisfies $C_s^2(r)/r^2 = \omega^2/l(l+1)$, i.e., the depth where the horizontal phase speed equals

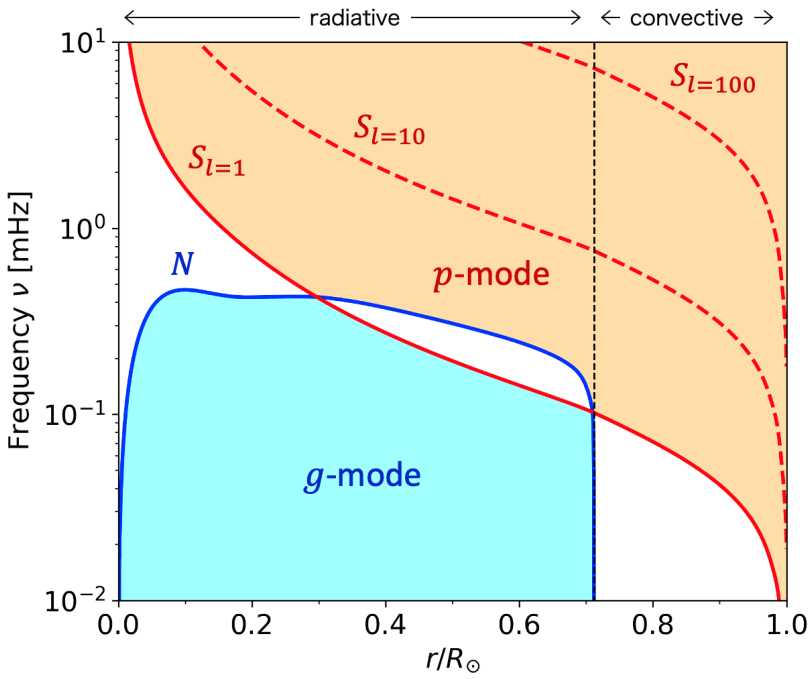

Figure 1.3: The propagation diagram for a standard solar model S (Christensen-Dalsgaard et al. 1996b). The blue and red lines show the Brunt-Väisälä frequency N and the Lamb frequency S_l (for $l = 1, 10, 100$), respectively. The cyan- and orange-sheded regions denote the regions where g-modes and p-modes can propagate.

to the local sound speed. Therefore, the modes are more and more localized near the surface as l increases. A more detail analysis using the ray theory can be found in Gough (1984). For p-modes with frequencies of about 3 mHz (corresponding to the period of 5 minutes oscillation), the turning depths of the modes $l = 1, 40$, and 100 are calculated as $r/R_\odot = 0.05, 0.71$, and 0.9. Therefore, for $l \geq 40$, the modes are trapped in the convection zone.

Excitation and damping mechanism of the p-modes are still controversial. Particularly, it is still difficult to identify the exact places and timings of the excitation sources. A widely accepted idea is that they are stochastically excited by turbulent convection near the surface such as granulation (e.g., Goldreich and Keeley 1977). Whenever the pressure is perturbed due to the random turbulent motions, p-modes arise. Since convection can produce noises with a wide range of frequencies, some of them become resonant with the eigenmodes of acoustic oscillations.

g-modes (internal gravity waves)

The second condition (II) in Eq. (1.7) corresponds to g-modes (gravity modes or internal gravity waves) whose main restoring force is the buoyancy (gravity) force in a stably-stratified medium. g-modes can propagate as oscillatory waves in the inner part of the Sun denoted by cyan-shades in Figure 1.3. The lower and upper turning depths of the g-modes are given by $\omega = N$. Here, it is instructive to note that the Brunt-Väisälä fre-

quency N^2 is proportional to the radial gradient of the background specific entropy ds_0/dr and to the superadiabaticity δ,

$$N^2 = \frac{g}{c_p}\frac{ds}{dr} = -\frac{g}{H_p}\delta = -\frac{1}{\gamma}\frac{C_s^2}{H_p^2}\delta. \tag{1.8}$$

The upper limit of g-mode frequency is determined by the maximum Brunt-Väisälä frequency $N_{\max}$. From Eq. (1.5), it also follows that the g-modes with lower frequency (small ω) have more radial nodes (large k_r).

Similarly to the p-modes, the solar g-modes are considered to be excited by turbulent convection some of which penetrates into a stably-stratified radiation zone (overshoot layer) at the base of the convection zone. However, in contrast to the p-modes, the solar g-modes are extremely difficult to detect at the solar surface because the modes become evanescent owing to $N^2 < 0$ (very close to adiabatic) in the convection zone (e.g., Appourchaux et al. 2010).

1.3 Large-scale mean flows

Since the Coriolis force introduces a proffered direction $\mathbf{\Omega}_0$, rotationally-constrained turbulent convection in the Sun becomes anisotropic, transports the (angular) momentum inside the convection zone, and drives the mean flows such as differential rotation and meridional circulation.

1.3.1 Helioseismic observations

Helioseismology uses the solar oscillations (p-modes in most cases) to probe the solar interior. It has revealed the structure of the mean flows in the Sun, imposing observational constraints on the theories of rotating turbulent convection and the dynamo models.

Differential rotation

The internal angular velocity distribution of the Sun $\Omega(r,\theta) = \langle v_\phi \rangle / r\sin\theta$ is obtained by global helioseismology (Duvall et al. 1984, Thompson et al. 1996, Schou et al. 1998). The Sun is filled with acoustic waves excited by stochastic turbulent convection. The interferences or resonances of these acoustic waves lead to the global standing modes, whose eigenfrequencies can be used to probe the internal structure in global helioseismology: If the Sun rotates rigidly, the frequencies of the resonant oscillations should depend only on the spherical harmonic degree l, the radial order n, and the sound speed. However, helioseismic measurements show small frequency splittings (rotational splittings) depending on the azimuthal order m owing to the waves traveling in different directions (eastward or westward). Linear inversions are used to infer the internal rotation profile from the frequency splittings.

Figure 1.4 shows the observationally-inferred profile of the solar differential rotation (Larson and Schou 2018). It is clearly seen that the equator rotates faster than the poles, requiring that angular momentum is transported equatorward by convection in the Sun. There are other interesting features of the solar differential rotation. For example, a strong

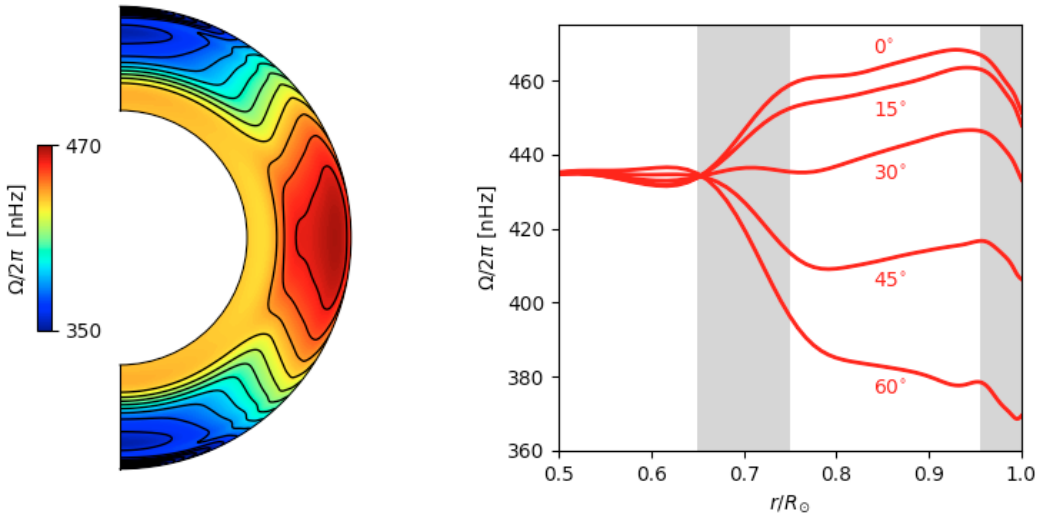

Figure 1.4: Observed differential rotation in the Sun. Left: contours of the rotation rate in a meridional plane. Right: Radial structure of the solar differential rotation at different latitudes. Shaded areas indicate the locations of strong radial shears near the base and top of the convection zone. The figure is reproduced using the data obtained by 2D regularized least-squares global helioseismology inversions from MDI and HMI (Larson and Schou 2018, Goddard et al. 2020). Courtesy of Chris. R. Goddard.

angular velocity shear is concentrated on a very thin layer at the base of the convection zone, located around $r = 0.71R_\odot$. This strong shear layer is called the tachocline and was thought to be the main place where the generation of the toroidal magnetic field by Ω-effect occurs (§1.4). The angular velocity also changes strongly in radius near the surface, consisting another shear layer called the near surface shear layer. Lastly, the contour lines of the angular velocity are not cylindrical as was expected before helioseismology, but are conical having an inclination of about 25° with respect to the rotational axis. This means that the solar convection does not follow the Taylor-Proudman's theorem, implying that the thermal wind plays a critical role inside the solar convection zone.

Meridional circulation

The axisymmetric flow in a meridional plane, $\langle v_r \rangle$ and $\langle v_\theta \rangle$, is known as the meridional circulation. The meridional circulation is much weaker than the rotation (about 100 times smaller in amplitude) and therefore extremely difficult to measure. Many attempts have been conducted using a variety of techniques including direct Doppler measurements (e.g., Duvall 1979, Hathaway 1996, Ulrich 2010), magnetic feature tracking (e.g., Hathaway and Rightmire 2010, Hathaway and Upton 2014), and local helioseismology (e.g., Braun and Fan 1998, Basu and Antia 2010). At the solar photosphere, a poleward flow of about $10-20$ m s^{-1} that peaks at latitudes of about 40° have been robustly detected (Giles et al. 1997).

Although it is believed that the equatorward return flow exists inside the convection

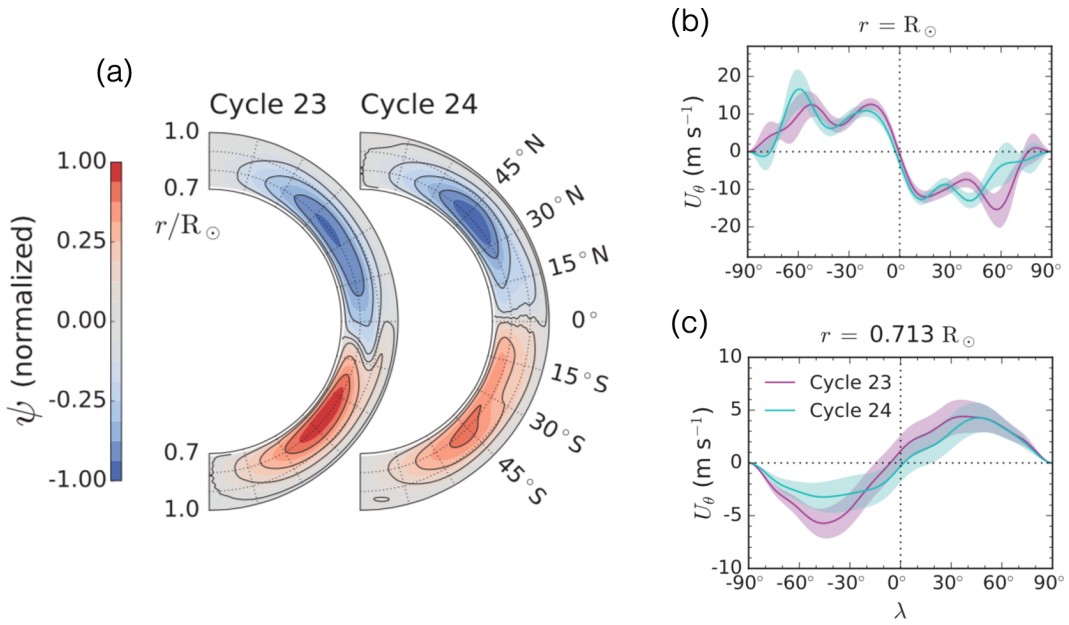

Figure 1.5: Observationally-inferred meridional circulation in the Sun for the last two solar cycles. (a) Streamfunction Ψ for the cycle 23 and 24, defined by $\rho\boldsymbol{v} = \nabla\times(\Psi\boldsymbol{e}_\phi/r\sin\theta)$. Red and blue represents clockwise and counter-clockwise circulation, respectively. (b) The latitudinal dependence of the latitudinal flow at the surface. (c) The same as panel (b) but at the base of the convection zone. The figure is taken from Gizon et al. (2020a) with small modifications, reprinted with permission ©AAAS.

zone to meet the mass conservation, the exact structure of the deeper meridional flow is still controversial because of the lack of inversion accuracy in the local helioseismology (e.g., Duvall et al. 1993, Gizon and Birch 2005). One of the most striking results was reported by Zhao et al. (2013) who analyzed the HMI data and detected the equatorward flow in the middle convection zone between $0.82R_\odot - 0.91R_\odot$, and poleward flow again below $0.82R_\odot$. Their results suggest a double-cell structure of the solar meridional circulation with the counter-clockwise circulation cell in the upper convection zone (poleward near the surface) and the clockwise circulation cell in the lower layer (poleward near the base). Kholikov and Hill (2014) used the other helioseismic measurements and also detected evidence that the latitudinal flow changes its direction at several depths of the convection zone, supporting the findings of Zhao et al. (2013). More recently, Jackiewicz et al. (2015) and Böning et al. (2017) further argued that the shallow equatorward return flow at around $0.9R_\odot$ can be confirmed on GONG ground-based data which is in good agreement with HMI analysis of Zhao et al. (2013), although some discrepancies exist in the deeper convection zone. On the other hand, Rajaguru and Antia (2015) and Mandal et al. (2018) recently found the equatorward return flow beneath the depth of $0.77 - 0.78R_\odot$, clearly suggesting the single-cell meridional circulation per each hemisphere. Most recently, using the two data sets covering the last two solar cycles, Gizon et al. (2020a) have unambiguously shown that the meridional circulation structure in the convection zone is single-cell in each hemisphere, as shown in Fig.1.5. It should be noted

that their result is consistent with the flux transport dynamo model that attributes the equatorward migration of sunspot groups to the equatorward advection of deep-seated toroidal fields by the meridional flow near the base of the convection zone. For a comprehensive review on the observational and theoretical aspects of the solar meridional circulation, see Choudhuri (2021).

Recently, Stejko et al. (2021) have computed the travel-time differences using the deep-focusing method for the model convection zone with single- and double-cell meridional flow patterns. They found that the computed travel time differences fall within a standard deviation error of both single-cell and double-cell cases, implying the current local-helioseismology techniques can hardly distinguish the meridional flow profiles in the deep interior.

1.3.2 Theories and numerical simulations

Turbulent angular momentum transport

To see how this happens theoretically, let us examine the mean equation of motion. In the following discussion, the bracket $\langle\ \rangle$ is regarded as zonal averaging (not necessarily in general) that satisfies the Reynolds' averaging rules. By decomposing the velocity is decomposed into the mean and fluctuation parts, $\boldsymbol{v} = \langle \boldsymbol{v} \rangle + \boldsymbol{v}$, and substituting it into the equation of motion, we have

$$\rho_0 \frac{\partial \langle v_i \rangle}{\partial t} = -\nabla \cdot (\rho_0 \langle v_i \rangle \langle v_j \rangle) - \nabla \cdot (\rho_0 \langle v_i' v_j' \rangle) + [\ \ldots\ ]. \tag{1.9}$$

It is seen that the correlation of (small-scale) turbulence $\langle v_i' v_j' \rangle$ acts as an effective stress tensor for the mean velocity. Now, we define the Reynolds stress as $R_{ik} = \rho_0 \langle v_i' v_k' \rangle$. If $\boldsymbol{v}'$ is isotropic, the Reynolds stress mostly acts as an enhanced turbulent diffusion, which can be approximated as $R \propto \nabla \langle \boldsymbol{v} \rangle$. Only the non-diffusive part acts as additional forcing term and transports the mean momentum to drive the large-scale mean flows. Conventionally, the non-diffusive part assumed to be proportional to the rotation rate Ω_0, i.e., as the rotational influence increases, turbulence becomes more anisotropic and the associated Reynolds stresses have more non-diffusive contribution. This is called the Λ-effect (e.g., Rüdiger 1989, Kitchatinov and Rüdiger 1993).

In the following, we focus on the angular momentum transport by non-diffusive components of the Reynolds stress. For simplicity, we assume that the azimuthal (ϕ) component of the equation of motion has no external forcing terms, such as Lorentz force and viscous force. The conservation of the angular momentum density can be expressed as

$$\frac{\partial}{\partial t}(\rho_0 r^2 \sin^2\theta \Omega) = -\nabla \cdot \left[\rho_0 r^2 \sin^2\theta \langle \boldsymbol{v}_m \rangle \Omega + \rho_0 r \sin\theta \langle \boldsymbol{v}_m' v_\phi' \rangle \right], \tag{1.10}$$

where $\boldsymbol{v}_m = (v_r, v_\theta)$ is the meridional velocity and $\langle v_\phi \rangle = r \sin\theta \Omega$ is used. Here, the first term on the right hand side describes the advection of the angular momentum by the meridional circulation and the second term describes the sum of angular momentum diffusion and transport via the Reynolds stresses. We can readily see that if $\langle v_r' v_\phi' \rangle$ is positive (negative), anisotropic convection transports the angular momentum radially outward

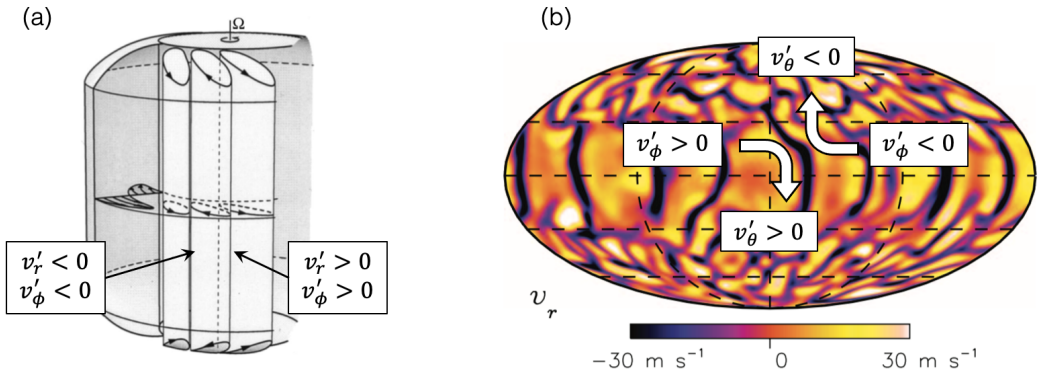

Figure 1.6: (a) Schematic illustration of the radially-inclined convective columns, taken from Busse (2002) with small modifications. The image reproduced with permission of AIP publishing. (b) Snapshot of the radial velocity v_r in a rotating convection simulation. The figure is taken from Miesch et al. (2006) with small modifications, ©AAS. Reproduced with permission.

(inward). Similarly, if $\langle v_\theta' v_\phi' \rangle$ is positive (negative), the angular momentum transport is transported equatorward (poleward).

Since the equatorial region rotates faster in our Sun as discussed in §1.3.1, it is generally believed that $\langle v_r' v_\phi' \rangle$ is positive near the equator and $\langle v_\theta' v_\phi' \rangle$ is positive (negative) in the northern (southern) hemisphere in the Sun. Possible mechanisms to generate these velocity correlations are explained as follows (e.g., Miesch 2005). First, the positive $\langle v_r' v_\phi' \rangle$ can be explained by convective columns outside the tangential cylinder that are inclined in a prograde direction towards the surface, as shown in Fig. 1.6a. These columnar structures of convection are often called as "Busse columns" or "Taylor columns" in the geophysical context, and as "Banana cells" in the solar and stellar context (Miesch et al. 2000). As we will unambiguously show in §3.3.2, both of these convective structures are interpreted in terms of the "thermal Rossby waves", originating from the conservation law of potential vorticity (Miesch et al. 2008). Next, the positive $\langle v_\theta' v_\phi' \rangle$ in the northern hemisphere can also be attributed to the existence of the banana cells. Banana cells can be observed as a coherent north-south alignment of downflow lanes at low latitudes. Coherent azimuthal inflows into these downflow lanes provide a dominant source for the velocity correlation $\langle v_\theta' v_\phi' \rangle$ as illustrated in Fig.1.6b: In the northern hemisphere, the positive (negative) v_ϕ' is bent by the Coriolis force equatorward (poleward) so that positive (negative) latitudinal velocity v_ϕ' is produced. Therefore, the correlation $\langle v_\theta' v_\phi' \rangle$ becomes positive at low latitudes. The same argument can be applied to the southern hemisphere to produce a negative $\langle v_\theta' v_\phi' \rangle$.

Gyroscopic Pumping

Meridional circulation is mainly driven by the Coriolis forces acting on the differential rotation, rather than driven directly by the meridional turbulent momentum transport associated with $\langle v_r' v_\theta' \rangle$. Now, let us consider the angular momentum balance in a statistically stationary state to see how the structure of the meridional circulation is determined

in the Sun. Using an anelastic approximation $\nabla \cdot (\rho_0 \langle \boldsymbol{v}_m \rangle) = 0$, the Eq.(1.10) reduces to the so-called the equation of "gyroscopic pumping"

$$\rho_0 \langle \boldsymbol{v}_m \rangle \cdot \nabla \langle \mathcal{L} \rangle = -\nabla \cdot (r \sin\theta \rho_0 \langle \boldsymbol{v}'_m v'_\phi \rangle), \tag{1.11}$$

where $\langle \mathcal{L} \rangle \equiv r^2 \sin^2\theta \Omega$ denotes the mean angular momentum density per unit mass. The left and right hand sides of the equation represent the advection of the angular momentum by meridional circulation and the turbulent angular momentum transport by the Reynolds stresses, respectively. The profile of the meridional circulation is determined so as to balance with the Reynolds stresses. This equation can be used to impose constraints on the turbulent Reynolds stress for given large-scale mean flows $\langle \boldsymbol{v}_m \rangle$ and $\langle \mathcal{L} \rangle$. Refer Miesch and Hindman (2011), Miesch et al. (2012), Bekki and Yokoyama (2017) for example.

Thermal Wind Balance

As pointed out in §1.3.1, the solar differential rotation deviates from the Taylor-Proudman's theorem. This is explained by the thermal wind balance in the solar convection zone (Kitchatinov and Ruediger 1995, Durney 1999, Brun and Toomre 2002, Thompson et al. 2003, Rempel 2005, Miesch et al. 2006).

By taking a curl of this meridional motion equation, we have a ϕ component of the vorticity equation in the following form;

$$\frac{\partial \omega_\phi}{\partial t} = [\ldots] + r\sin\theta \frac{\partial \Omega^2}{\partial z} - \frac{g}{c_p r}\frac{\partial s_1}{\partial \theta}, \tag{1.12}$$

where s_1 is the entropy perturbation and z denotes the coordinate parallel to the rotational axis. In the case where the baroclinic term can be ignored ($\partial s_1/\partial\theta = 0$), we have $\partial\Omega^2/\partial z = 0$ in the stationary state, which is what exactly results from the Taylor-Proudman's theorem. Since $\partial\Omega^2/\partial z$ is negative in the northern hemisphere in the solar convection zone, a negative latitudinal entropy gradient is required, i.e., $\partial s_1/\partial\theta < 0$ in the northern hemisphere. In other words, the polar regions should be warmer than the equatorial region from the theoretical point of view. Several studies indicate that the temperature difference of 10 K is necessary to break the Taylor-Proudman's constraint and obtain the observed conical profile of the differential rotation (e.g., Kitchatinov and Ruediger 1995, Rempel 2005, Miesch et al. 2006). The observational detection of this temperature (or entropy) perturbation is a very challenging task because the temperature fluctuation of 10 K is almost negligible compared with the high background temperature of $\approx 10^6$ K.

It still remains controversial how this latitudinal entropy gradient is maintained in the Sun. Kitchatinov and Ruediger (1995) suggested that the anisotropic turbulent convection also transports the thermal energy poleward sufficiently enough to break the Taylor-Proudman's constraint. On the other hand, Rempel (2005) argued that the the latitudinal entropy gradient can be produced via the interaction of the radial meridional flow penetrating into the weakly subadiabatic tachocline, which spreads into the convection zone due to the turbulent thermal diffusion. It is shown that, if $\delta \approx -2 \times 10^{-5}$ near the base of the convection zone, the solar-like differential rotation can be reproduced. It should be pointed out that the lower half of the convection zone can be weakly subadiabatic if the convective energy transport is highly nonlocal (e.g., Skaley and Stix 1991, Brandenburg 2016). Furthermore, Masada (2011) proposed the turbulent heating originating from

the magneto-rotational instability in the tachocline as a possible source for the latitudinal entropy gradient.

In three-dimensional rotating convection simulations of the Sun, a fixed-entropy boundary condition is sometimes used to artificially force the thermal wind balance and to achieve the solar-like rotational profile (Miesch et al. 2006, 2008, Fan and Fang 2014). On the other hand, Brun et al. (2011) have carried out a simulation that covers both the subadiuabatic radiative interior and the superadiabatic convection zone, and have shown that the differential rotation becomes conical owing to the dynamical coupling with the radiative zone. More recently, Hotta (2018), Hotta and Kusano (2021) has discussed a possibility that an efficient small-scale dynamo action can substantially enhance the anisotropic convective heat transport via the small-scale Lorentz force feedback and produce a negative entropy gradient.

1.4 Magnetic activity of the Sun

The Sun has self-excited magnetic fields as clearly manifested by sunspots at the surface. The magnetic fields of the Sun can drive energetic eruption events like flares and coronal mass ejection that can affect our lives.

Observational constraints

It is well known that the solar magnetic activity exhibits a11-year periodicity, as shown in Fig. 1.7. There are several other striking features in the solar magnetic fields, such as periodic reversals of the polar fields, the emergence of sunspots in the middle latitudes, and the equatorward propagation of the sunspot emergence latitude in each cycle (see, Charbonneau 2020, for a comprehensive review). These features can be seen in the time-latitude plot of the longitudinally-averaged radial field at the photosphere, i.e., so-called *magnetic butterfly diagram*, as shown in Fig. 1.8. There are also well-known observational facts called Hale's polarity law on the hemispheric regularities and Joy's law on the tilts between the leading and following sunspots (Hale et al. 1919).

Dynamo theory

The magnetic fields in the Sun is generally believed to be generated via the so-called dynamo processes, by which kinetic energy of the plasma flow is converted to magnetic energy (e.g., Parker 1955, 1975). However, how exactly the dynamo operates inside the convection zone is still largely uncertain. The evolution of magnetic fields in the MHD system (as in the Sun) is described by the induction equation

$$\begin{aligned} \frac{\partial \boldsymbol{B}}{\partial t} &= \nabla \times (\boldsymbol{v} \times \boldsymbol{B}) \\ &= (\boldsymbol{B} \cdot \nabla)\boldsymbol{v} - \boldsymbol{B}(\nabla \cdot \boldsymbol{v}) - (\boldsymbol{v} \cdot \nabla)\boldsymbol{B}, \end{aligned} \tag{1.13}$$

where the ohmic diffusion term is omitted because the molecular diffusivity ($\approx 10^3$ cm^2 s^{-1}) is so small in the Sun that the corresponding magnetic Reynolds number is estimated as Rm $\approx 10^8 - 10^{10}$ (Ossendrijver 2003). Three terms of the right-hand side represent the effects of shearing, compression, and advection of magnetic fields, respectively.

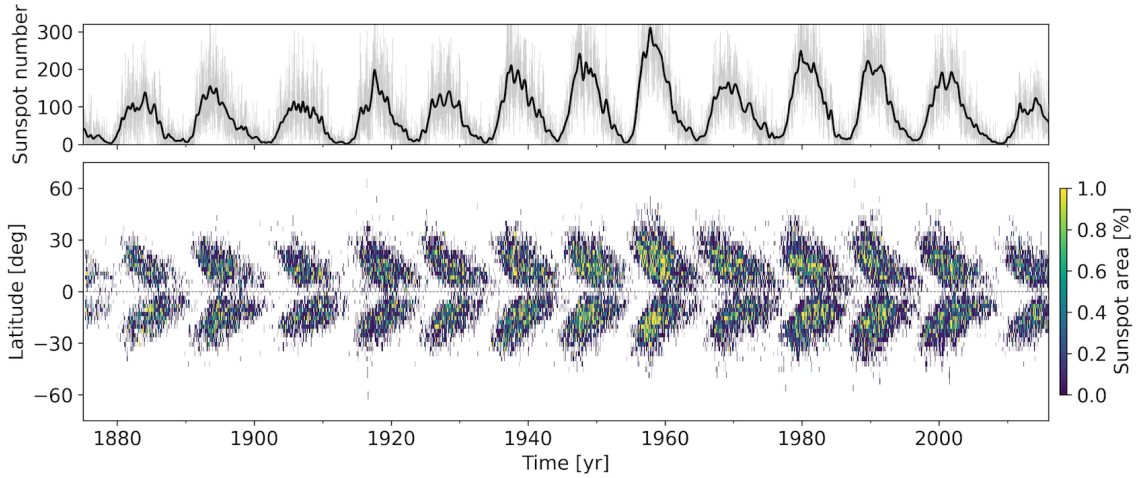

Figure 1.7: Sunspot cycles observed on the Sun. (Top) Sunspot number as a function of time, covering the cycles 12-24. Grey and black lines show the daily and monthly-averaged sunspot numbers, respectively. (Bottom) Sunspot area averaged over individual solar rotation as a function of time and latitude. This figure is produced using the data provided at http://solarcyclescience.com/activeregions.html.

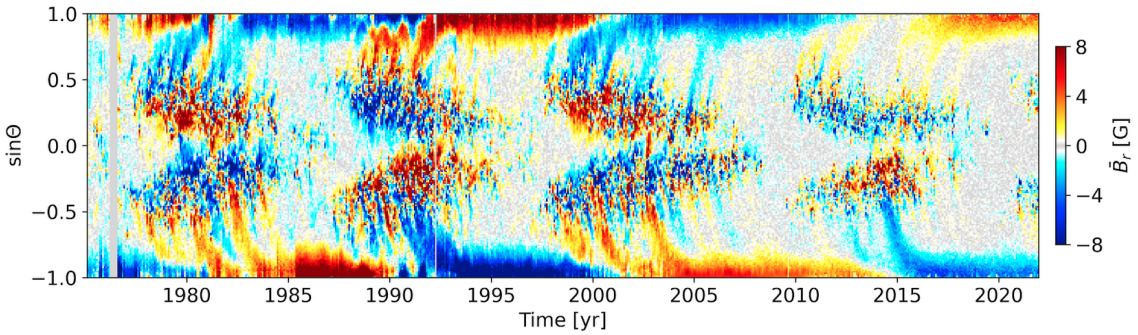

Figure 1.8: Magnetic butterfly diagram observed on the Sun showing the longitudinally-averaged radial field at the photosphere as a function of time and sine of latitude. The synoptic magnetogram data is obtained from NSO/KPVT, SOHO/MDI, and SDO/HMI.

Although the surface observations show a variety of complicated magnetic structures, we are primarily interested in the large-scale spatio-temporal evolution. Thus, let us decompose $\boldsymbol{B}$ and $\boldsymbol{v}$ into the mean components ($\langle \boldsymbol{B} \rangle$ and $\langle \boldsymbol{v} \rangle$) and the small-scale fluctuations ($\boldsymbol{b}'$ and $\boldsymbol{v}'$) to see how the mean fields equations are described. For simplicity, let us assume the mean as an azimuthal average. Using the Reynolds averaging rules, the mean induction equation can be written as

$$\frac{\partial \langle \boldsymbol{B} \rangle}{\partial t} = \nabla \times (\langle \boldsymbol{v} \rangle \times \langle \boldsymbol{B} \rangle + \boldsymbol{\mathcal{E}}), \tag{1.14}$$

$$\boldsymbol{\mathcal{E}} = \langle \boldsymbol{v}' \times \boldsymbol{b}' \rangle, \tag{1.15}$$

where $\boldsymbol{\mathcal{E}}$ is the turbulent electro-motive-force that serves as an additional source for the

mean magnetic field generation. The importance of $\boldsymbol{\mathcal{E}}$ can be recognized when the mean induction equation is decomposed into the toroidal and poloidal components: Although the toroidal fields can be generated by shearing of the poloidal fields (Ω-effect), there is no term associated with the poloidal field generation from the toroidal fields if $\boldsymbol{\mathcal{E}} = 0$. Hence, in order to be a self-excited dynamo (in which mutual generation between toroidal and poloidal fields is required), the non-axisymmetric contribution from the electro-motive-force $\mathcal{E}$ is necessary (Cowing's anti-dynamo theorem) (Cowling 1933). In order to close the mean-field equations, $\boldsymbol{\mathcal{E}}$ needs to be described in terms of $\langle \boldsymbol{B} \rangle$. Under the assumption that the fluctuating fields $\boldsymbol{b}'$ is primarily generated by turbulent flows $\boldsymbol{v}'$ acting on the mean magnetic fields $\langle \boldsymbol{B} \rangle$, i.e.,

$$\frac{\partial \boldsymbol{b}'}{\partial t} = \nabla \times (\boldsymbol{v}' \times \langle \boldsymbol{B} \rangle) + [\,\ldots\,], \tag{1.16}$$

a useful formula of $\boldsymbol{\mathcal{E}}$ is conventionally obtained as

$$\boldsymbol{\mathcal{E}} \;=\; \alpha \langle \boldsymbol{B} \rangle + \boldsymbol{\gamma} \times \langle \boldsymbol{B} \rangle - \beta \nabla \times \langle \boldsymbol{B} \rangle. \tag{1.17}$$

Here, the coefficients α, β, and $\boldsymbol{\gamma}$ are given as

$$\alpha \;=\; -\frac{\tau_c}{3} \langle \boldsymbol{v}' \cdot \nabla \times \boldsymbol{v}' \rangle, \tag{1.18}$$

$$\beta \;=\; \frac{\tau_c}{3} \langle \boldsymbol{v}'^2 \rangle, \tag{1.19}$$

$$\boldsymbol{\gamma} \;=\; -\frac{\tau_c}{3} \nabla \langle \boldsymbol{v}'^2 \rangle, \tag{1.20}$$

where τ_c is the correlation time which is assumed to be smaller than the eddy turnover time scale of the turbulence. The first term in the Eq.(1.17) is called the "turbulent" α-effect and represents the dynamo action by helical turbulence. The pseudoflow $\boldsymbol{\gamma}$ is known as turbulent pumping and acts as an additional transporter of magnetic fluxes. The last term represents the turbulent diffusion, which is much more dominant than the molecular diffusion in the Sun.

In the turbulent dynamo where the α-effect and Ω-effect work simultaneously, dynamo waves propagate in a direction given by $\alpha \nabla \Omega \times \boldsymbol{e}_\phi$ (Parker 1955, Yoshimura 1975, Stix 1976). In the Sun, since α tends to be positive (negative) in the bulk of the northern (southern) hemisphere and $\nabla \Omega \approx d\Omega/dr > 0$, the dynamo waves are expected to propagate poleward, which disagrees with the observed equatorward sunspot migration.

Babcock-Leighton flux transport model

A Babcock-Leighton flux-transport dynamo model is a widely-accepted dynamo model at present in which the meridional circulation and the sunspot tilts play critical roles. In this model, the equatorward migration of the activity belts is attributed to an eqautorward transport of toroidal fields generated by the Ω-effect near the base of the convection zone (e.g., Wang et al. 1991, Choudhuri et al. 1995). Moreover, the main source of the surface poloidal fields is the east-west tilts of the sunspots (Joy's law): The dipolar field can be produced by the combined effects of the diffusive cancellation of the leading sunspots across the equator and by the poleward advection of the following sunspots. This process

are commonly called the Babcock-Leighton mechanism or the Babcock-Leighton α-effect (Babcock 1961, Leighton 1964). The east-west tilt of sunspot pairs is thought to be originating from the effects of Coriolis force acting on the plasma flows inside a spot-forming flux tube during its rise though the convection zone (e.g., Fan et al. 1993, D'Silva and Choudhuri 1993, Caligari et al. 1995).

Numerical studies on the Babcock-Leighton flux-transport dynamo model have been carried out mostly in two-dimensional (2D) kinematic models where the large-scale mean flows are given by hand (Dikpati and Charbonneau 1999, Chatterjee et al. 2004, Hazra et al. 2014, Karak and Cameron 2016), although several studies have been made in the MHD regime (Rempel 2006, Ichimura and Yokoyama 2017, Inceoglu et al. 2017). Although these studies generally reproduce many observed features of the solar dynamo such as the 11-yr periodicity and the equatorward migration of activity belts, it should be noted that, in these 2D models, the Babcock-Leighton α-effect is crudely given as a source term for the poloidal potential. Recently, there are several studies that aim to realize the three dimensionality of the Babcock-Leighton process in the full-spherical simulations. A first model in this line has been presented in Yeates and Muñoz-Jaramillo (2013) in which the upward velocity perturbation associated with the magnetic buoyant flux tubes is explicitly prescribed in the kinematic regime so as to produce the tilted sunspot pairs at the surface. The same method has also been employed in Kumar et al. (2019) and Whitbread et al. (2019). On the other hand, Miesch and Dikpati (2014), Miesch and Teweldebirhan (2016) have developed a model of the Babcock-Leighton dynamo in which the sunspots are instantaneously placed at the surface in response to the toroidal field at the base under the constraint of Joy's law. This model has been used to study the long-term cycle variability (Karak and Miesch 2017). However, both of these models are kinematic. Therefore, the future models of the Babcock-Leighton flux-transport dynamo are expected to operate in both three-dimensional and MHD regimes.

Reduced 1D model of Babcock-Leighton dynamo

Leighton (1969) presented a 1D model of the Babcock-Leighton type solar dynamo which takes into account the Babcock (1961)'s original idea that the emergence of dipolar magnetic regions is the source of the surface radial field. The model consists of two partial differential equations (of time and latitude) for the azimuthally averaged radial field at the surface and the toroidal field in the subsurface layer. Such a simplifying treatment to reduce the complicated model into a 1D model has often been made: Cameron and Schüssler (2015) has applied Stokes'theorem to derive a 1D equation that describes the evolution of the net toroidal flux in the solar convection zone as a function only of the observables at the solar surface (e.g., radial field and differential rotation). They have demonstrated that the net toroidal flux in each hemisphere generated by the latitudinal differential rotation is determined by the emerged poloidal flux at the surface, strongly supporting the validity of the Babcock-Leighton scenario in the solar dynamo. Cameron and Schüssler (2017) have further extended the Leighton (1969)'s 1D model by considering the evolution of the radially integrated toroidal field in the convection zone. Updates have also been made by incorporating the effects of the turbulent diffusion, turbulent pumping, meridional flow, and the near surface shear layer to show that the model can capture many essential features of the solar dynamo behavior. Careful validation regarding the assump-

tions used in this 1D model using self-consistent convective dynamo simulations will be required in the future.

1.5 Measuring solar flows

Granulation tracking

Solar granulation has a typical size of $\approx 0.5 - 2$ Mm, lifetime of $\approx 5 - 10$ min, and flow velocity $\approx 0.5 - 1.5$ km s^{-1} (Nordlund et al. 2009, Rieutord and Rincon 2010). Granulation tracking is a technique that uses the solar granules at the photosphere as tracers to measure the horizontal component of the underlying larger-scale flows (e.g., November and Simon 1988, Roudier et al. 2012, Löptien et al. 2017). The essential idea is that the granules are advected passively by the larger scale flows over time lags of $\approx$ 1 min. The validity of this technique has been confirmed in realistic numerical simulations of solar surface convection (Matloch et al. 2010).

Supergranulation tracking

Solar supergranulation has a typical size of $\approx$ 30 Mm, lifetime of $\approx 1 - 2$ days, and horizontal velocity $\approx$ 300 m s^{-1} (Rieutord and Rincon 2010). Similarly to granulation tracking, the motions of supergranules seen in the surface Doppler-velocity measurements have been be tracked to infer the underlying larger-scale flow motions (Hathaway et al. 2013). The issue here is that supergranulation does not behave like a passive scalar as in the case of granulation over time lags scale of a few hours (see, Figure. 63 in Gizon and Birch 2005): In fact, supergranulation has wave-like properties with periods of $\approx$ 6 days (Gizon et al. 2003).

Time-distance method (local helioseismology)

In time-distance helioseismology (Duvall et al. 1993), the cross-covariance of the signal (e.g. Doppler velocity) at two locations on the solar surface (A and B) is computed. This cross-covariance is filtered in Fourier space, e.g. with a phase speed filter. The filtered cross-covariance is then fitted by a reference model with a few degrees of freedom (a Gabor wavelet) or with a single degree of freedom, phase travel time (Gizon and Birch 2002). The phase travel times contain information about the subsurface flows of the Sun, and the difference between the travel time from A to B and B to A contains information about the background flows (Duvall et al. 1997, Gizon and Birch 2005). To make a 3D map of the flows, many different sets of points (A and B) need to be considered and an inversion is required (e.g., Švanda 2012).

Ring-diagram analysis (local helioseismology)

Ring diagram analysis considers the 3D power spectra of solar oscillations over local areas (called patches or tiles) at the surface (Hill 1988), and thus, can be regarded as a local application of the global helioseismology techniques. The local power spectrum contains

the information of acoustic waves traveling through the subsurface layer of each patch, and the power ridges of these waves form rings when seen at fixed frequency (Gizon et al. 2010, Kosovichev 2012). The distortions of these ring shapes are caused by the Doppler frequency shifts due to the background subsurface flows (otherwise the rings become concentric circles). Therefore, by fitting the distortions in the power spectrum, we can obtain the subsurface flow velocity for each patch (Basu et al. 1999, Haber et al. 2000, Bogart et al. 2011a,b). For a more comprehensive review on local helioseismology, see Gizon and Birch (2005).

1.6 Convective conundrum

As discussed so far, it is crucial to understand the complicated interactions among turbulent convection, rotation, and magnetism. This is essentially nonlinear problem and thus numerical simulations are regarded as the most powerful tool to study the convection zone dynamics (e.g., Glatzmaier 1984, Miesch et al. 2000, Brun et al. 2004). However, it has been recently recognized that numerical simulations of solar rotating convection and dynamo produce the wrong results on large scales ($l \lesssim 120$) in the deep convection zone (typically beneath 20 Mm from the photosphere) for some unknown reason. This is a common issue shared by all the existing numerical codes and does not seem to largely depend on the details of the numerical schemes. This problem is often termed as the "convective conundrum" (e.g., Hanasoge et al. 2012, Gizon and Birch 2012, O'Mara et al. 2016, Brandenburg 2016, Bekki et al. 2017, Karak et al. 2018, Nelson et al. 2018). In the following, we will show four evidence which all suggest the inherent problem in the global simulations.

1.6.1 Inconsistent horizontal velocity spectra

Local helioseismology

Using the deep-focusing time-distance helioseismology, Hanasoge et al. (2012) analyzed HMI observational data and measured the east-west travel times to infer the upper limit of longitudinal subsurface velocity amplitudes at $r = 0.92R_\odot, 0.96R_\odot$, as shown in Fig. 1.9. On large scales with the spherical harmonic degree $l < 60$, the observational upper limit was found to be orders of magnitudes smaller than what is typically predicted in global simulations (Miesch et al. 2008) and by local mixing-length model (Stix 2002). Although the results have been recently revised and the corrected power spectrum of the longitudinal velocity rises up at higher spherical orders (Birch et al. 2022., in prep), there is still a huge discrepancy from the global simulations to be resolved.

Greer et al. (2015) have carried out a three-dimensional ring-diagram inversion and found that subsurface flow amplitudes at $r = 0.96R_\odot$. The result broadly agrees with the results of global simulations of Miesch et al. (2008), which means that there is a drastic difference in the inferred flow amplitudes between the two different local-helioseismology techniques (time-distance and ring-diagram methods). Nagashima et al. (2020) have recently revised Greer et al. (2015)'s analysis and reported that the corrected results become

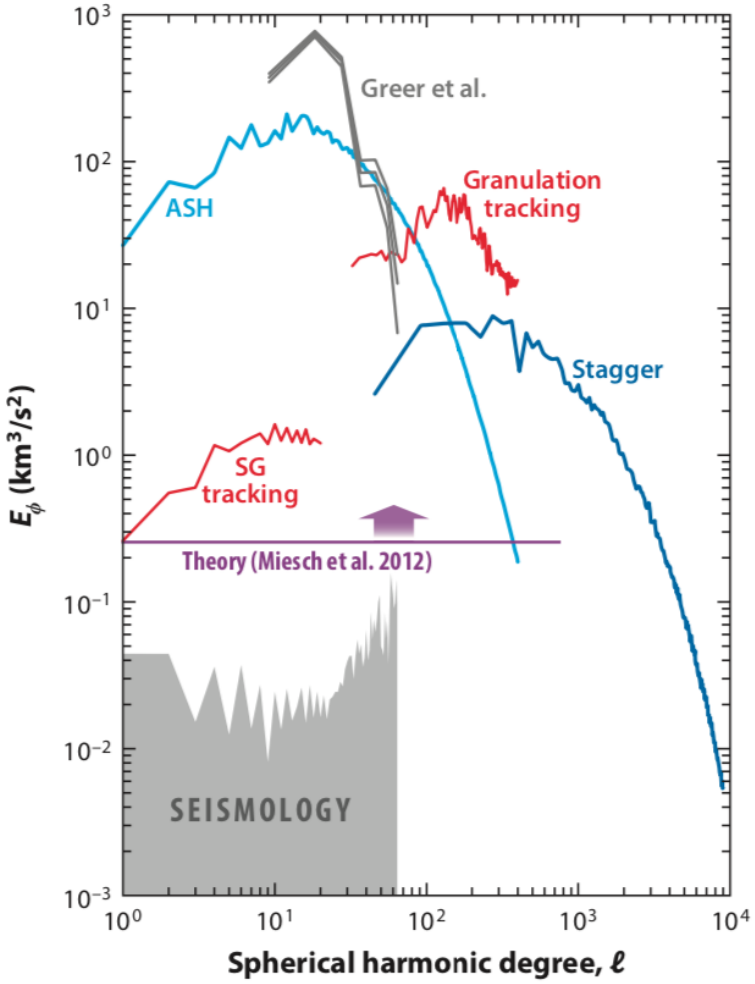

Figure 1.9: Comparison of the horizontal velocity power spectra near the solar surface. (Cyan): A global simulation of rotating convection using ASH code Miesch et al. (2008) at $r = 0.98R_\odot$. (Darkblue): A local box simulation of the stagger code (Stein and Nordlund 2006) at $r = 0.98R_\odot$. (Grey dashed area): An upper limit inferred by time-distance helioseismic measurements at $r = 0.96R_\odot$ (Hanasoge et al. 2012). (Grey lines): Ring-diagram analysis by Greer et al. (2015) at $r = 0.96R_\odot$. (Red): Local-correlation-tracking (LCT) and supergranulation tracking at the surface (Hathaway et al. 2013). (Purple): A theoretical lower limit based on the angular momentum balance in the Sun (Miesch et al. 2012). The figure is taken from Hanasoge et al. (2016). The image reproduced with permission of Annual Reviews, Inc.; permission conveyed through Copyright Clearance Center, Inc.

slightly reduced (less than one order of magnitude). Nonetheless, this modification was not sufficient enough to explain the difference from the time-distance results.

Global simulations and theoretical models

In global convection simulation of Miesch et al. (2008), the large-scale velocity amplitudes are about 2 orders of magnitudes larger than the observational upper limit obtained by Hanasoge et al. (2012). In fact, the overstimation of convective speed is a general trend seen in other simulations. A high-resolution simulation of Hotta et al. (2014a), which solves the fully-compressible convection unlike the anelastic models, also show a very similar power spectrum at large scales, although the inertial range of turbulent extends further down to $l \approx 1000$ and smoothly connects to the spectrum of local box near-surface convection simulation of Stein and Nordlund (2006) in their calculation (see, Figure 6.1. in Lord 2014).

The theoretical lower limits of the convective speed in the Sun was estimated by Miesch et al. (2012): They calculated the amplitudes of the Reynolds stresses required to maintain the observed differential rotation by examining the equation of "gyroscopic pumping". The estimated lower limits are 8 m s^{-1} in the deeper convection zone ($r \approx 0.75R_\odot$) and 30 m s^{-1} near the surface ($r \approx 0.95R_\odot$). These values are roughly located in between the global simulation and the revised time-distance results as shown in Fig. 1.9.

In short, except for the ring-diagram analysis of Greer et al. (2015), the observations are inconsistent with numerical and theoretical models, casting doubt on our conventional understanding of solar convection (Gizon and Birch 2012, Hanasoge et al. 2016). Particularly, it is strongly implied that, in the Sun, thermal energy is likely transported non-locally by enhanced thermal plumes that penetrate deeper into the convection zone (Rieutord and Zahn 1995, Brandenburg 2016, Bekki et al. 2017, Anders et al. 2019).

1.6.2 Rossby numbers in global convection simulations

Numerical simulations have an inherent problem so that even heliosesimic constraints are need to conclude that the simulations are incorrect. Global simulations with the solar parameters such as the rotation rate $\Omega_\odot$ and the luminosity $L_\odot$ tend to produce the so-called anti-solar differential rotation with faster equator and slower poles (e.g., Gastine et al. 2013, Käpylä et al. 2014, Fan and Fang 2014, Hotta et al. 2015c, Karak et al. 2015). As we decrease the viscous diffusivity ν, differential rotation changes from solar-like to to the anti-solar profile (Nelson et al. 2016). In short, the simulation results tend to deviate from the solar observations as we aim to a more realistic turbulent regime of the Sun.

The transition from solar to anti-solar rotational regime is owing to the change in the (convective) Rossby number $\mathrm{Ro} = v_{\mathrm{rms}}/\Omega_0 l$, which is an inverse measure of the rotational effect with respect to convection. Figure.1.10a shows the equatorial rotation rate as a function of Ro, which clearly shows that the transition occurs at $\mathrm{Ro} \approx 1$. Since simulations tend to overpower the convective speed, Ro is over-estimated as well, leading to an anti-solar differential rotation (Featherstone and Miesch 2015).

It should be noted that, in most of the "solar-like" rotating convection simulations, several "tricks" are employed to artificially reduce the effective Ro and to circumvent this problem. In Brown et al. (2008, 2010), Nelson et al. (2013), Augustson et al. (2015), Käpylä et al. (2017), the rotation rate is increased typically by a factor of $3-5$. Another way is to use stronger viscous or thermal diffusivities to simply damp the convective motions or to relax the constraint of thermal energy transport of convection (Miesch et al. 2000, Fan and Fang 2014, Hotta et al. 2016). Moreover, it is also possible to lower the Rossby number by decreasing the luminosity by a factor of $10-20$ to artificially suppress

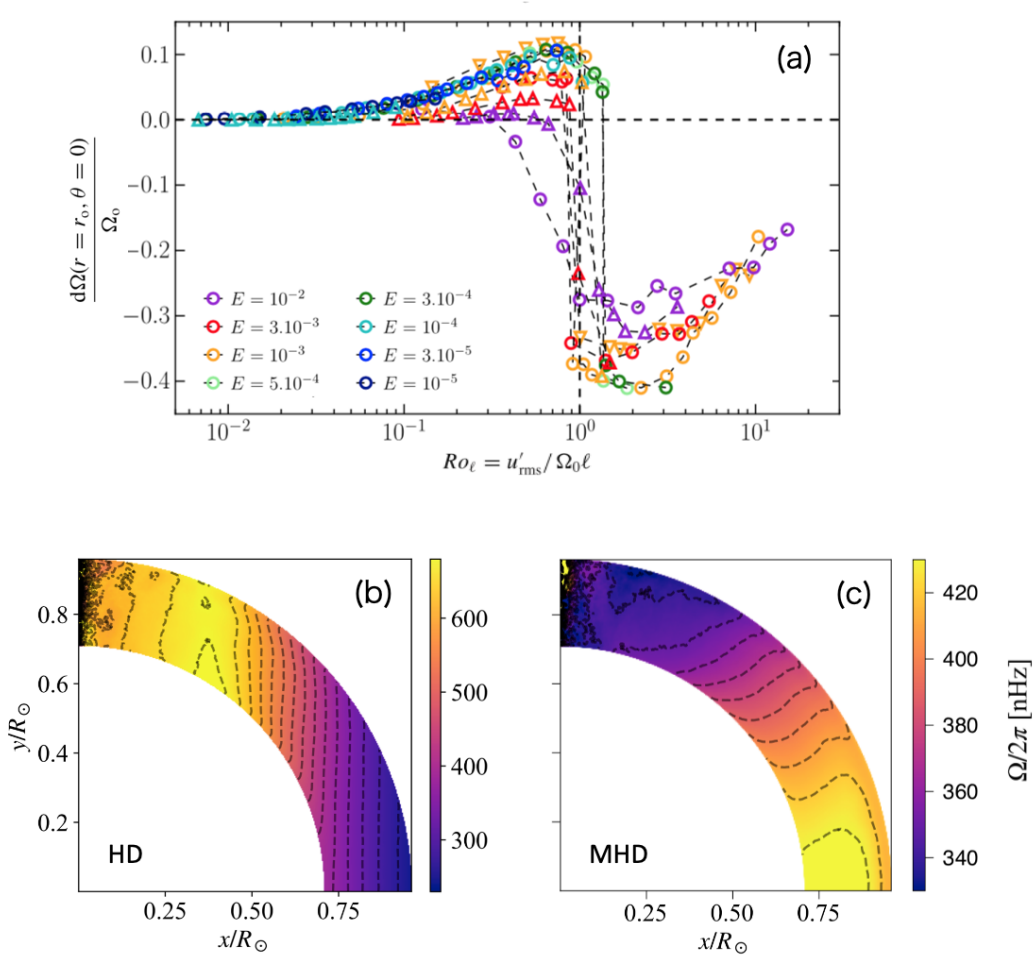

Figure 1.10: Top: (a) Differential rotation regime in terms of the equatorial rotation rate at the surface $d\Omega(r_o, 0)/\Omega_0$ as a function of the local Rossby number $u'_{\rm rms}/\Omega_0 l$ where $u'_{\rm rms}$ and l are the typical velocity and length scale of convection. Different colors represent the results for different Ekman number E. The figure is taken from Gastine et al. (2014) with small modifications. The image reproduced with permission of Oxford University Press, conveyed through Copyright Clearance Center, Inc. Bottom: Differential rotation profiles of the recent high-resolution simulations using the solar rotation rate $\Omega_\odot$ and luminosity $L_\odot$. Panels (b) and (c) are the results from hydrodynamic (non-magnetic) and magnetohydrodynamic calculations with the same grid resolution, respectively. The figure is taken from Hotta and Kusano (2021) with small modifications, ©Springer Nature. Reprinted with permission.

the convective driving (Guerrero et al. 2013, Käpylä et al. 2014, Fan and Fang 2014, Hotta et al. 2015c).

It has been proposed that the problem is likely due to the lack of spatial resolution in the simulation. The Reynolds number achieved even in the highest-resolution simulation at present ($\approx 10^3$) is still far too small compared to the solar value ($\approx 10^{13}$). Hotta et al. (2015b) have suggested that, in a more turbulent regime, small-scale dynamo becomes increasingly efficient. As a consequence, there exists a strong small-scale Lorentz-

force feedback to the turbulent convection that acts just like an effective viscosity, which leads to a reduction in the convective speed and thus the effective Rossby number in the simulation. In fact, Hotta and Kusano (2021) have recently demonstrated that that the solar-like differential rotation can be reproduced with the solar parameters ($\Omega_\odot$, $L_\odot$) in a high-resolution simulation only when the magnetic field is taken into account as shown in Fig.1.10b and c. They also implied that the solar-like differential rotation can be achieved even in the high-Ro regime as long as small-scale dynamo is efficiently excited and the resulting Maxwell stress transports the angular momentum radially upward near the equator.

1.6.3 Search for equatorial giant cell convection

As explained in §1.3.2, the equatorward angular momentum transport in the Sun is attributed to an existence of the columnar convective modes (thermal Rossby waves) (e.g., Busse 2002) or banana cells (e.g., Miesch et al. 2008). They originate from the effect of density stratification (compressional β-effect) (Ingersoll and Pollard 1982, Evonuk 2008, Glatzmaier et al. 2009, Evonuk and Samuel 2012, Verhoeven and Stellmach 2014) and propagate in a prograde direction. These prograde-propagating convective modes have been first seen in linear models of rotating convection of Boussinesq (Gilman 1975) and compressible fluids (Gilman and Glatzmaier 1981). In numerical simulations of convection in a strongly rotationally-constrained regime, equatorial columnar modes are found as the most dominant convective modes (Miesch et al. 2008, Bessolaz and Brun 2011, Matilsky et al. 2020). Near the surface, they appear as a north-south alignment of downflow lanes with azimuthal converging flows across the equator (Miesch et al. 2000, Miesch 2005). Therefore, it is expected that these large-scale convective modes can be readily seen in the surface power spectra of the north-south symmetric component of radial velocity, longitudinal velocity, or horizontal divergence.

However, they have never been successfully detected on and near the solar surface for some yet-unknown reason. It still remains open whether this is because of the near-surface convection concealing the signal or because the signal is absent. If the latter is the case, the theory of solar convection and angular momentum transport need to be reconsidered. As reported in Chapter 2, the columnar convective modes remain illusive in surface observations of solar flows.

1.6.4 Theories on the origin of supergranulation

The physical origin of supergranulation remains one of the open questions in the solar physics (e.g., Rieutord and Rincon 2010) and could be related to the convective conundrum. The question to be answered is whether the supergranulation is convective in nature or the outcome of strong rotational influence. It has been repeatedly proposed that the solar convection is driven essentially by surface cooling rather than internal heating from below (e.g., Stein and Nordlund 1989, Spruit 1997). In this picture, low-entropy fluid parcels generated by the photospheric radiation can sustain a substantial amount of thermal contents during their descent into deeper convection zone, significantly contributing to the non-local heat transport in the Sun. Based on this picture, Cossette and Rast (2016) have demonstrated using the non-rotating convection model that the supergranulation-like

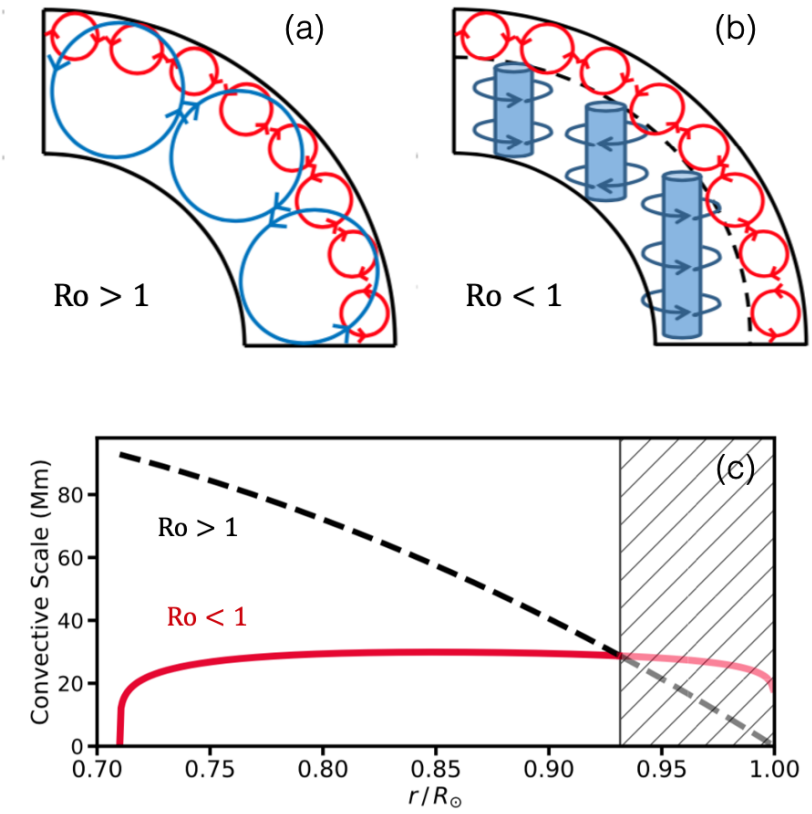

Figure 1.11: Top: Schematic of expected convective structures in (a) high-Ro regime and (b) low-Ro regime. The figure is taken from Featherstone and Hindman (2016b) with small modifications, with permission ©AAS. Bottom (c): Estimates of the convective length-scale as a function of radii based on the geostrophycal balance of the convective vortices. The solid red and black dashed lines denote for the results from the high-Ro case and the low-Ro case, respectively. The figure is taken from Vasil et al. (2021) with small modifications.

peak can be obtained if the stratification is very close to adiabatic (or slightly subadiabatic) below 20 – 30 Mm in depth. It is therefore implied that, if such small-scale low-entropy downdrafts are not properly captured in numerical simulations due to the lack of spatial resolution, this might be compensated by a strong excitation of large-scale convection. Brandenburg (2016) proposed that the effects of these non-local energy transport can be incorporated into the mixing-length model as an additional contribution called "Deardorff term" (Deardorff 1972), owing to which the enthalpy can be transported upward even in a weakly subadiabatic background. This has been confirmed in several numerical experiments (Käpylä et al. 2017, Bekki et al. 2017, Karak et al. 2018, Nelson et al. 2018, Käpylä et al. 2019)

In fact, Lord et al. (2014) have extended the numerical domain of near-surface non-rotating convection simulation of MURaM code, which can successfully reproduce the observed properties of granules, both horizontally and vertically sufficiently enough to capture the supergranules. However, they found that the simulations tend to overesti-

mate the low wavenumber power on scales larger than supergranulation, and thus failed to reproduce the supergranulation peak at $l \approx 120$. This is because the deep convection drives the large-scale flows on scales comparable to the four local density scale heights, which imprints the surface horizontal velocity spectrum. Lord et al. (2014) have shown that, the observed photospheric power spectrum can be reproduced if the convective flow amplitude is selectively suppressed below a depth of 10 Mm by a factor of 2.5. Therefore, it is also suggested by the surface convection simulation as well as global ones that simulations cannot properly solve the deep convection on the Sun.

The work of Lord et al. (2014) implies that the supergranulation peak is a consequence of the suppression of power on large scales, and not that they are thermally-driven convection on that spatial scale. One possible cause of a reduction in the large-scale power is due to strong rotation. Featherstone and Hindman (2016b) have carried out a set of rotating convection simulations and argued that the power peak shifts to higher wavenumber as the deep convection is more and more rotationally-constrained. The associated transition of convective pattern from high-Ro to low-Ro is schematically illustrated in Figure 1.11 (a) and (b). Indeed, a theoretical model of rotationally-constrained convection predicts a dynamical scale of convection at 30 Mm (which corresponds to the scale of supergranulation) throughout below the near-surface layer of the Sun (Vasil et al. 2021), as shown in Figure 1.11 (c).

1.7 Low-frequency oscillations in the Sun

In addition to the high-frequency modes of oscillation such as p-modes and g-modes, inertial modes are expected to exist at much lower frequency range. They are restored by Coriolis force and hence have periods comparable to the solar rotation period of 28 days. Long-term continuous observations over 10 years by SDO/MDI have enabled us to detect the inertial modes in the large-scale power spectrum of the Sun (see Chapter 2). In the following sections we adopt the language and classification of inertial modes discussed by Rieutord and Valdettaro (1997). In this section, we first review inertial modes and then focus on the special class of inertial modes, Rossby modes.

1.7.1 Inertial oscillations

Poincaré equation

Inertial waves are defined as travelling waves in a rotating fluid whose restoring force is the Coriolis force (e.g., Greenspan et al. 1968). To review some of their fundamental properties, let us consider the Navier-Stokes equation of incompressible, inviscid fluid in a rigidly-rotating system (with angular velocity $\boldsymbol{\Omega}_0 = \Omega_0 \boldsymbol{e}_z$). For simplicity, the effects of gravity and magnetic fields are omitted. Using the equation of continuity to eliminate the velocity, we have the equation for pressure perturbation,

$$\frac{\partial^2}{\partial t^2} \nabla^2 p_1 + (2\boldsymbol{\Omega}_0 \cdot \nabla)^2 p_1 = 0. \tag{1.21}$$

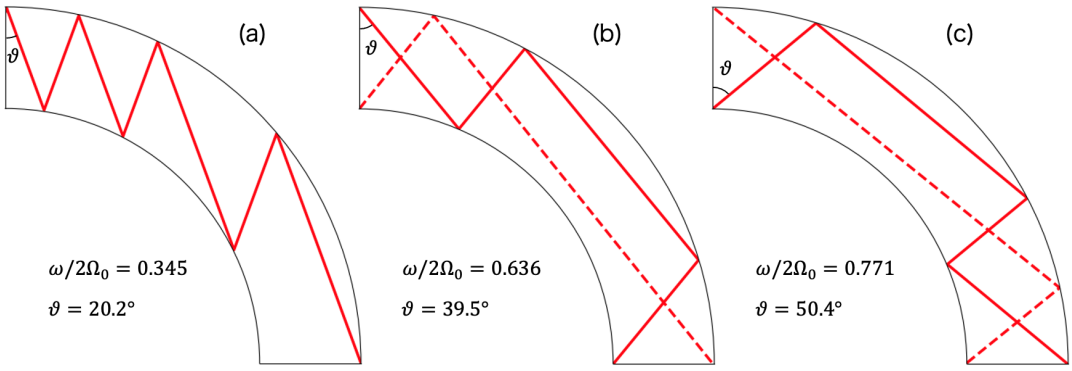

Figure 1.12: Example ray attractors of the inertial modes in a spherical shell with $r_{\rm min}/r_{\rm max} = 0.715$ (solar convection zone). Panels (a), (b), and (c) show the attractors for different frequencies $\omega/2\Omega_0 = 0.345,\ 0.636$ (0.626 for the second attractor denoted by dashed line) and , 0.771 (0.778 for the second attractor denoted by dashed line). The corresponding angles from the rotational axis $\vartheta = \sin^{-1}(\omega/2\Omega_0)$ are also shown.

This equation is known as the *Poincaré equation* after Cartan (1922). Assuming that the perturbations are proportional to $\exp[i(\boldsymbol{k}\cdot\boldsymbol{x} - \omega t)]$, the dispersion relation of inertial waves is given by

$$\omega = \pm 2\boldsymbol{\Omega}_0 \cdot \frac{\boldsymbol{k}}{|\boldsymbol{k}|} \tag{1.22}$$

from which we see that the frequencies of inertial waves are limited to a range of $-2\Omega_0 \le \omega \le 2\Omega_0$, depending on the angle between the rotational axis and the wavenumber vector: The frequency becomes maximum ($|\omega| = 2\Omega_0$) when the wavenumber is parallel to the rotational axis ($\boldsymbol{k} \parallel \boldsymbol{\Omega}_0$), and vanishes (non-oscillating, $|\omega| = 0$) when it is perpendicular to the rotational axis ($\boldsymbol{k} \perp \boldsymbol{\Omega}_0$). Note that the associated fluid motions are always perpendicular to their wavenumber vectors, i.e., the inertial waves *transverse*. Also note that the group velocity is perpendicular to the phase propagation direction.

Inertial modes in a spherical shell

Inertial waves trapped in a spherical shell (like the stellar convection zones) have been extensively studied by, e.g., Rieutord and Valdettaro (1997), Rieutord et al. (2001). Since the propagation direction of inertial waves is fixed by their frequencies, they undergo reflections such that the angle between $\boldsymbol{\Omega}_0$ and $\boldsymbol{k}$ remains constant. Consequently, the waves can no longer have a continuous spectrum of frequencies and the resonant modes (standing waves) are setup as global modes of oscillation. They are known as *inertial modes* (Thomson 1880, Greenspan et al. 1968). In fact, this reflects the fact that the Poincaré equation is hyperbolic and thus is ill-posed when the boundary condition is taken into account (e.g., Stewartson and Rickard 1969).

Due to the ill-poseness of the problem, one would expect singularities in solutions. When viscosity is included, these singularities can be regularized and converted to the so-called internal shear layers in eigenfunctions (e.g., Bondi and Lyttleton 1953, Rieu-

tord et al. 2001, Tilgner 1999). Nonetheless, the singularities still have a dominant effect in determining the shape (concentration of power) of inertial modes in a rotating spherical shell especially at small viscosity limit. Therefore, it is convenient to consider the characteristics of the Poincaré equation along which the wave energy propagates. The characteristic surfaces (or cones) are characterized by the angle with respect to the rotational axis $\vartheta = \sin^{-1}(\omega/2\Omega_0)$. Note that ϑ is also the critical latitude where the characteristic surfaces are tangent to the inner and upper spherical shells. It is known that the characteristics tend to converge towards the so-called *attractor* which is, in most cases, a closed periodic orbit or a wedge made by spherical boundaries in a meridional plane (Maas and Lam 1995, Rieutord and Valdettaro 1997, Rieutord et al. 2001, Rieutord and Valdettaro 2018, Sibgatullin and Ermanyuk 2019). Figure 1.12 shows example attractors in the spherical shell (resemble to the solar convection zone) for selected frequencies. Laboratory experiments as well as numerical studies have repeatedly confirmed that the some inertial modes are strongly localized onto the attractors that are determined by topography of the spherical shell and the mode frequencies (e.g., Manders and Maas 2003, Grisouard et al. 2008).

Models of inertial modes in the Sun and stars

In the Sun and stars, inertial waves can propagate in the convection zones where the stratification is close to adiabatic and therefore the main restoring force is the Coriolis force. In rapidly-rotating high or intermediate-mass stars, inertial modes propagating in the convective cores can have a dense frequency spectrum (due to the absence of the inner spherical boundary) (Bryan 1889), and thus can resonantly couple with the rotationally-influenced (sub-inertial) g-modes in the radiative envelopes (e.g., Lee and Saio 1987, Saio and Lee 1991, Ogilvie and Lin 2004). In fact, such resonances have been recently detected in γ Doradus stars (Ouazzani et al. 2020). In low-mass stars with radiative cores and convective envelopes, such a resonance can hardly occur due to the sparsely-spaced frequencies of the inertial modes trapped inside a spherical shell. In these stars, the main focus has long been the tidal excitation of inertial modes in two celestial bodies (such as binary stars or extrasolar planetary systems), since their dissipation can have a substantial impact on their long-term orbital evolution by redistributing the energy and angular momentum of the system (e.g., Ogilvie 2014).

From the theoretical perspectives, Baruteau and Rieutord (2013) and Guenel et al. (2016) have studied the effects of differential rotation and found that properties of inertial modes are significantly affected by differential rotation which introduces the critical layers and limits the size of their resonant cavity. However, simplifying assumptions were made in their studies such as the fluid being incompressible fluid and the background homogeneous. A background density variation was considered in some literature (Dintrans and Ouyed 2001, Wu 2005) but there only uniform rotation was considered. As far as the author recognize, there is no study that takes into account both the realistic (helioseismocally-determined) differential rotation and the solar internal stratification (model S).

1.7.2 Equatorial Rossby modes

Rossby waves (Rossby 1939, 1940) are a type of inertial wave. They are global-scale radial vorticity waves arising from the conservation law of potential vorticity (e.g., Ertel 1942, Platzman 1968, Müller 1995). They are the class of inertial waves for which the wave motions are quasi-toroidal, i.e., the radial flows are very small compared to horizontal flows (e.g., Rieutord et al. 2001). The readers may refer to Zaqarashvili et al. (2021) for a comprehensive review on Rossby waves.

The classical Rossby waves originate from the radial component of the absolute vorticity conservation with the so-called "planetary" β-effect representing the latitudinal variation of the Coriolis forces as a source (e.g., Vallis 2006). In the solar and stellar context, they are also known as r modes (e.g., Papaloizou and Pringle 1978, Smeyers et al. 1981, Saio 1982, Wolff and Blizard 1986).

To better understand the nature of the Rossby modes, let us consider a simplified form of the absolute vorticity conservation,

$$\frac{D}{Dt}\left(\zeta_r + 2\Omega_0\right) = 0, \tag{1.23}$$

where ζ_r denotes the radial vorticity and Ω_0 is the rotation rate of the star. Assuming that the motion is toroidal, i.e., the radial velocity is substantially weak, the above equation can be reduced to

$$\frac{\partial \zeta_r}{\partial t} - \frac{2\Omega_0}{r}\sin\theta \approx 0. \tag{1.24}$$

Using the constraint of the equation of continuity ($\nabla\cdot\boldsymbol{v} = 0$) and assuming that the velocity is proportional to $\exp\left[i(m\phi - \omega t)\right]$ dependence, we have

$$\frac{\partial}{\partial\theta}\left\{\sin\theta\frac{\partial}{\partial\theta}\left(\sin\theta v_\theta\right)\right\} - m^2 v_\theta - \frac{2m\Omega_0}{\omega}\sin^2\theta v_\theta = 0. \tag{1.25}$$

The non-trivial solution of the Eq.(1.25) is given by

$$v_\theta \propto P_l^m(\cos\theta)\sin^{-1}\theta, \tag{1.26}$$

when the frequency ω satisfies

$$\omega = -\frac{2m\Omega_0}{l(l+1)}. \tag{1.27}$$

Here, $P_l^m(\cos\theta)$ represents the associated Legendre function with azimuthal order m and spherical degree l. Therefore, it is shown that, under the assumption of toroidal motion, the eigenfunction of the r modes is given by the spherical harmonics and their dispersion relation is given by the Eq.(1.27). The minus sign manifests that they propagate in a retrograde (opposite to rotation) direction. It can also be shown that the r modes have a radial dependence of $v_\theta \propto r^m$ due to the radial force balance between the Coriolis force and the pressure gradient force.

Although the existence of r modes in the Sun and other stars has been predicted since 1970s (e.g., Papaloizou and Pringle 1978), it was only recently that they have been unambiguously detected on the solar surface. Figure 1.13a shows the observed power spectrum of radial vorticity at the photosphere (Löptien et al. 2018). It is clearly shown that

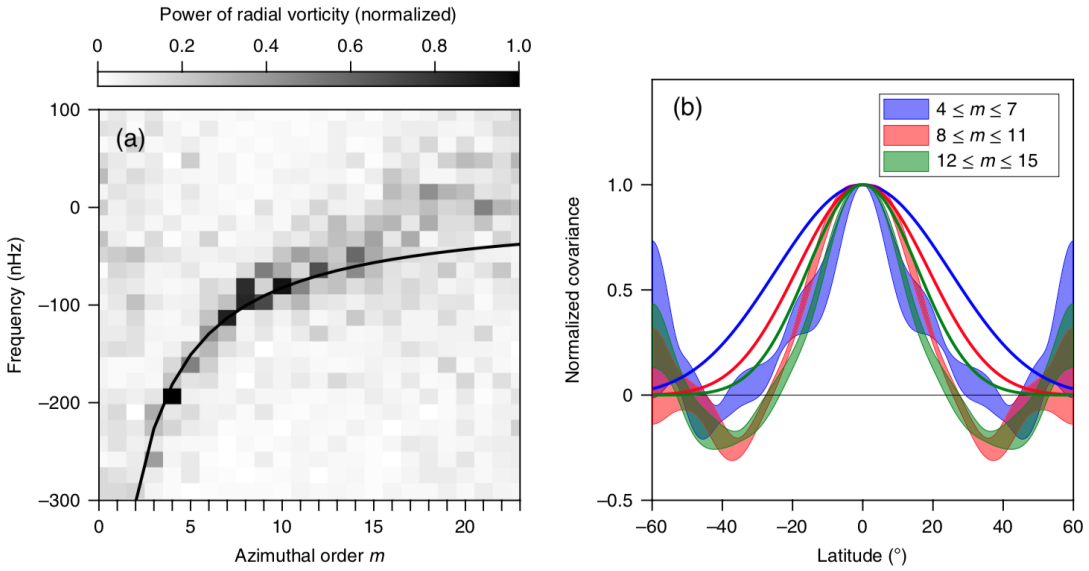

Figure 1.13: Observations of the equatorial Rossby modes on the Sun. (a) Power spectrum of radial vorticity calculated from local granulation tracking at the photosphere. Overplotted in the black solid line denotes the sectoral Rossby mode dispersion relation. (b) Measured latitudinal eigenfunctions at different azimuthal orders m. Solid lines denote the spherical harmonics with $l = m$. The figure is taken from Löptien et al. (2018) with slight modifications, ©Springer Nature. Reprinted with permission.

the vorticity power dominantly lies along the dispersion relation of the sectoral ($l = m$) Rossby modes, $\omega = -2\Omega/(m+1)$ with $\Omega/2\pi = 453.1$ nHz for a range of azimuthal order $3 \leq m \leq 15$. Figure 1.13b shows the measured latitudinal eigenfunctions of the r-modes at different azimuthal orders. Although the dispersion relation of the solar Rossby modes is clearly characterized by that of the sectoral component, the eigenfunctions turn out to be substantially deviating from the expected spherical harmonics. These results have then been robustly confirmed using different measurements and helioseismic methods (Liang et al. 2019, Hanasoge and Mandal 2019, Proxauf et al. 2020, Mandal and Hanasoge 2020, Hanson et al. 2020, Gizon et al. 2021).

Even though the velocity amplitudes of the solar Rossby modes are small ($\approx 1-3$ m s^{-1}), it is still striking that, on large scales, modes are by far dominant over convection in the Sun at low latitudes. It is sometimes speculated that turbulent convection might be confined on scales smaller than the rhines scale (Rhines 1975)

$$l_r \approx \sqrt{\frac{R_\odot v_{\rm rms}}{\Omega_\odot}} \approx 40 \text{ Mm}, \tag{1.28}$$

where $v_{\rm rms}$ is the root-mean-square turbulent convective speed. On scales larger than l_r, Rossby modes dominate over turbulence. So far, there has been no such a study to evaluate the impact of turbulent convection on the Rossby modes in a realistic solar convection zone setup.

Another interesting question about the solar Rossby modes is whether they contribute a driving mechanism to the differential rotation in the Sun. Although Rossby modes are

considered to play a critical role in driving the atmospheric zonal jets on gas planets (e.g., Liu and Schneider 2010, Liu and Schneider 01 Nov. 2011, Read and Lebonnois 2018) and in exoplanets (e.g., Showman and Polvani 2011), the impact of the solar Rossby modes on the differential rotation is elusive. Using a one-dimensional β-plane model, Gizon et al. (2020b) recently argued that, under latitudinal differential rotation, the eigenfunctions of the Rossby waves are modified and the resulting amplitudes of the Reynolds stress $\langle v'_\theta v'_\phi \rangle$ can be substantial in the vicinity of the viscous critical layers where the phase speed of the Rossby modes become equal to the local differential rotation speed. It is necessary to extend their study to a more realistic three-dimensional regime to assess the transport properties of the Rossby modes in the Sun.

Observational and theoretical studies of the inertial modes including Rossby modes in the Sun can have a profound implications not only to internal dynamics in the Sun but also to the mode physics in general because they can potentially be used to probe the interior as a possible application. For instance, there is a recent study that aims to account for the temporal variations in the Rossby mode frequencies during the solar magnetic cycles (Goddard et al. 2020).

1.8 High-latitude flows

Hathaway et al. (2013) used supergranulation tracking to estimate horizontal flows on scales larger than the supergranulation, and found that the high-latitude flows are characterized by strong longitudinal flows at $m = 1$ that are largely north-south anti-symmetric. These flows exist at latitudes above $\pm 45^\circ$ with velocity amplitudes up to 30 m s^{-1} and display a spiral structure, as shown in Fig.1.14. A similar high-latitude flow pattern has also been observed in the ring-diagram measurements (Bogart et al. 2015).

Hathaway et al. (2013) claim that the flows are due to giant cell convection and are associated with a Reynolds stress $\langle v_\theta v_\phi \rangle$ at high latitudes which is positive (negative) in the northern (southern) hemisphere, implying equatorward angular momentum transport.

In the paper Gizon et al. (2021) and in this thesis, we propose that these high-latitude flow features are not giant cell convection in nature but are instead global modes of inertial oscillation. This is based on an analysis of SDO/HMI observations. This invalidates the interpretation by Hathaway and Upton (2021) that the spiral feature is the result of advection by the meridional flow at the base of the convection zone. We also give a theoretical interpretation for the origin of the high-latitude mode in terms of the baroclinic instability and compute the Reynolds stresses associated with mode (Chapter 5).

1.9 Overview of the thesis

1.9.1 Motivation

As discussed in §1.6, recent observations disagree with the theoretical models in many aspect, which calls our current understanding on large-scale convection in the Sun into question. Recent observations suggest that the large-scale velocity power on the Sun is dominated by low-frequency modes of oscillation such as Rossby modes. Therefore,

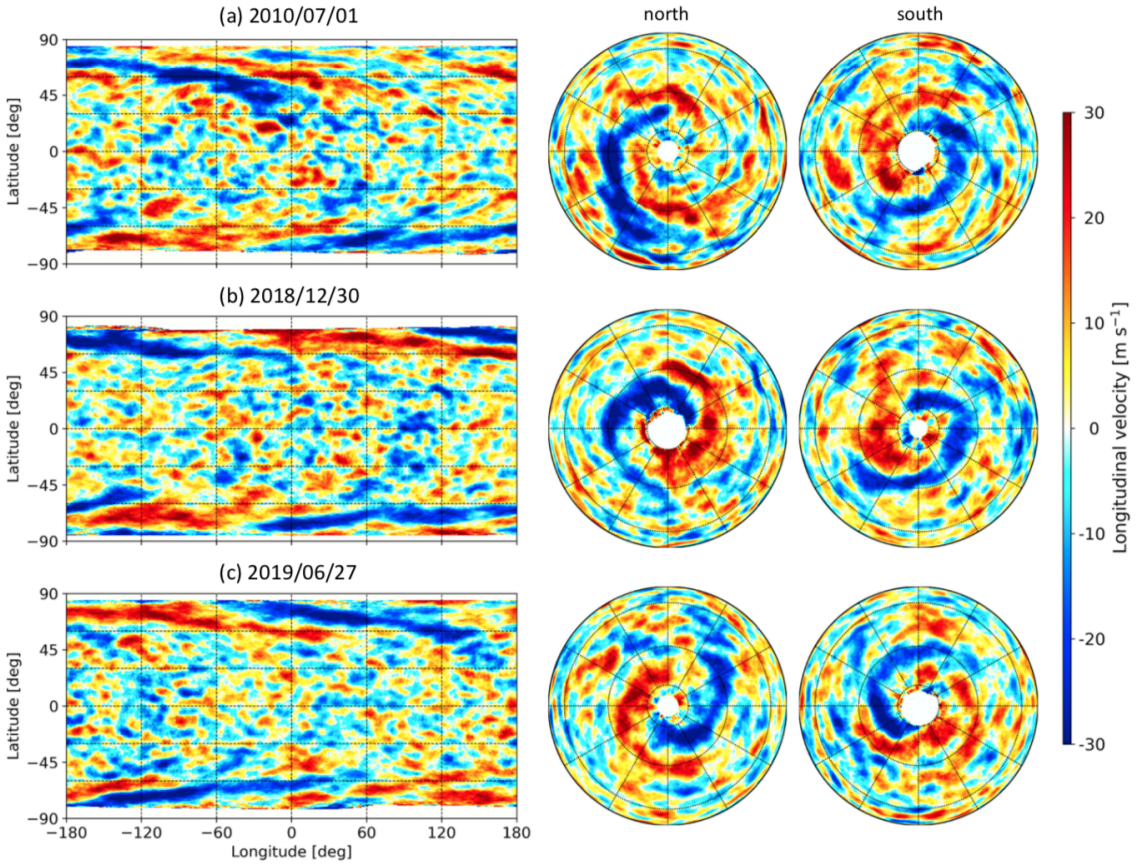

Figure 1.14: Snapshots of the non-axisymmetric component of longitudinal velocity at the solar surface obtained by supergranulation tracking (Hathaway and Upton 2021). Top, middle, and bottom panels show the flows at (a) 2010 July 1, (b) 2018 December 30, and (c) 2019 June 27, respectively, all at 00:00:00 UT. Left panels show the surface longitudinal flow in a Mercator projection. Center and right panels show the same flow but seen from north and south poles, respectively. This figure is produced using the data provided at http://solarcyclescience.com/giantcells.html, with permission.

as a first step to crack the solar convective conundrum, we will make use of them as fundamental observational clues.

The convective conundrum can in fact be reinterpreted in terms of the low-frequency global modes of oscillation as follows: Numerical models typically attribute the origin of solar equatorial acceleration to strong columnar convective modes (thermal Rossby waves) that have never been successfully detected on the Sun. On the other hand, what we robustly observe on the Sun are the equatorial Rossby modes (r modes) that are essentially incompressible and non-convective modes. Now, solar surface observational data from SDO/HMI for more than 10 years enables us to search for other kinds of inertial modes propagating in the convection zone. These observations might potentially be used to infer important unknown parameters in Sun's interior such as superadiabaticity, turbulent diffusivities, and convective velocity amplitudes. To this end, in this thesis, we study various types of low-frequency modes of oscillation in the Sun including equatorial

Rossby modes, columnar convective modes, and high-latitude modes in both linear and nonlinear regimes.

1.9.2 Structure

The remaining parts of the thesis are organized as follows. In Chapter 2, we first report observational detection of the solar inertial modes. In Chapter 3, we aim to systematically characterize the observed global-scale low-frequency vorticity modes inside the solar convection zone in the linear regime. The dispersion relations and the eigenfunctions are derived for each modes and compared with the observations. We also investigate how the (non-convective) equatorial Rossby modes interact with the convective modes. In order to further evaluate how much these linear modes persist in the turbulent convection zone or to see which modes acquire the velocity amplitudes sufficient enough to have an impact on the angular momentum transport, nonlinear simulations are indeed required. Here, we present two distinct ways to do this.

In Chapter 4, we work on fully nonlinear simulations of rotating compressible convection in the solar convection zone. The rotationally-influenced convection transports the angular momentum so that the large-scale mean flows are self-consistently driven. In this framework, we compute the velocity power spectra, extract the Rossby and convective modes from the nonlinear simulation, and characterize their mode properties in detail. Amplitudes of the extracted modes are compared with the solar observations. Note that this approach is regarded as the most fundamental because we try to keep the number of assumptions as less as possible. As a consequence, however, the outcome is almost uncontrollable and the simulation cannot exactly reproduce the Sun (mostly from a viewpoint of differential rotation and meridional circulation).

In Chapter 5, we present another type of nonlinear simulations: mean-field simulations of the large-scale flows in the Sun with parameterized Λ-effect in a sphere. In this framework, small-scale turbulent convection is not explicitly solved but the convective Reynolds stress (Λ-effect) is parameterized so that the solar-like differential rotation and meridional circulation can readily be obtained. We then study the nonlinear behaviour of the inertial modes in the solar convection zone, particularly the modes at high latitudes. We find that the various observational properties of the high-latitude flow features (polar spiral) can be explained in terms of the baroclinically-unstable modes.

In Chapter 6, we extend a mean-field model discussed in 5 into magnetohydrodynamic (MHD) regime, in which the solar-like magnetic cycles are simulated. This enables us to study not only the cycle dependence of the solar inertial modes but also the torsional oscillations and the active region flows.

In Chapter 7, we summarize our findings and discuss the implications of our study.

2 Solar inertial modes: Observations, identification, and diagnostic promise

Abstract

The oscillations of a slowly rotating star have long been classified into spheroidal and toroidal modes. The spheroidal modes include the well-known 5-min acoustic modes used in helioseismology. Here we report observations of the Sun's toroidal modes, for which the restoring force is the Coriolis force and whose periods are on the order of the solar rotation period. By comparing the observations with the normal modes of a differentially rotating spherical shell, we are able to identify many of the observed modes. These are the high-latitude inertial modes, the critical-latitude inertial modes, and the equatorial Rossby modes. In the model, the high-latitude and critical-latitude modes have maximum kinetic energy density at the base of the convection zone, and the high-latitude modes are baroclinically unstable due to the latitudinal entropy gradient. As a first application of inertial-mode helioseismology, we constrain the superadiabaticity and the turbulent viscosity in the deep convection zone.

2.1 Introduction

The free oscillations of a nonrotating spherical star have zero radial vorticity and are called spheroidal modes: they are the pressure (p), surface-gravity (f), and gravity (g) modes. The p and f modes, discovered on the Sun by Leighton et al. (1962), are used to infer the structure and dynamics of the solar interior (Christensen-Dalsgaard 2002). The solar g modes would also have important diagnostic potential regarding the radiative interior of the Sun; however, they evanesce in the convection zone and their amplitudes at the surface are exceedingly small (García et al. 2007, Alvan et al. 2015).

When slow uniform rotation is included in the model, additional modes of oscillation become possible. In particular, quasi-toroidal modes that resemble classical Rossby

This chapter reproduces the article *Solar inertial modes: Observations, identification, and diagnostic promise* by L. Gizon, R.H. Cameron, Y. Bekki, A.C. Birch, R.S. Bogart, A.S. Brun, C. Damiani, D. Fournier, L. Hyest, K. Jain, B. Lekshmi, Z.-C. Liang, and B. Proxauf, published in Astronomy and Astrophysics 652, L6 (2021). DOI: https://doi.org/10.1051/0004-6361/202141462. Contribution: Y. Bekki solved the 2D eigenvalue problem. All authors contributed to the final manuscript.

modes, known as r modes, are predicted (Papaloizou and Pringle 1978). They owe their existence to the Coriolis force, have frequencies on the order of the rotation frequency, and propagate in the retrograde direction. Adding the Sun's differential rotation introduces critical latitudes where the phase speed of a mode is equal to the local rotation velocity. In the inviscid case, the eigenvalue problem is singular at the critical latitudes (Watson 1981, Charbonneau et al. 1999). Adding viscosity changes the eigenvalue problem from second order to fourth order (e.g., Baruteau and Rieutord 2013). The singularity disappears and new quasi-toroidal modes appear, which are analogous to those of the plane Poiseuille viscous flow in classical hydrodynamics (Gizon et al. 2020b, and references therein). In the following, we loosely refer to the modes with frequencies on the order of the rotational frequency as inertial modes.

Inertial modes were detected on some rapidly rotating stars (see the review by Aerts 2021). The search for the Sun's inertial modes requires observations over many times the 27-day solar rotation period due to their low frequencies and amplitudes. Equatorial Rossby modes modified by the solar differential rotation have already been reported (Löptien et al. 2018). Here we report observations of a rich spectrum of inertial modes of the Sun over a wide range of latitudes, and we show they can be used to directly probe the superadiabaticity and turbulent viscosity in the deep convection zone. The degree to which the lower half of the convection zone is superadiabatic (or subadiabatic) is important in the context of storing the toroidal magnetic field so that it can build up over the course of the 11-year solar cycle (Hotta 2017). The turbulent viscosity is one of the important turbulent transport processes that acts in combination with the observed meridional flow (Gizon et al. 2020a) to explain the equatorward drift of the latitudes at which sunspots emerge (Cameron and Schüssler 2016).

By definition, a normal mode is separable in time and space; it is characterized by a single eigenfrequency that is independent of position and by a displacement eigenfunction that is independent of time. Working in the frequency–latitude domain is key to the observational discovery and the identification of the quasi-toroidal normal modes of the Sun.

2.2 Observations

We use helioseismic maps of horizontal flows near the solar surface provided by the Stanford ring-diagram pipeline (Bogart et al. 2011a,b) applied to continuous high-resolution observations from the Helioseismic and Magnetic Imager (HMI) onboard the Solar Dynamics Observatory (SDO) for the period from 1 May 2010 to 6 September 2020. The two horizontal flow components are standard data products: $u_\theta(\theta, \phi, t)$ in the colatitudinal direction and $u_\phi(\theta, \phi, t)$ in the longitudinal direction (θ and ϕ increase southward and prograde, respectively; see Proxauf et al. 2020). The flows are measured either with a cadence of $dt = 27.28$ hr and an effective spatial resolution of 15° in both coordinates, or with a more rapid cadence of $dt/3$ and a finer spatial resolution of 5°; the spatial sampling is half the resolution such that there is a 50% overlap between neighboring measurements. The highest latitude is 67.5° for the low-resolution maps and 80.0° for the high-resolution maps. The longitude, ϕ, is defined in the Carrington frame of reference, which rotates at the frequency $\Omega_{\rm Carr}/2\pi = 456.0$ nHz with respect to an inertial frame (close to the equato-

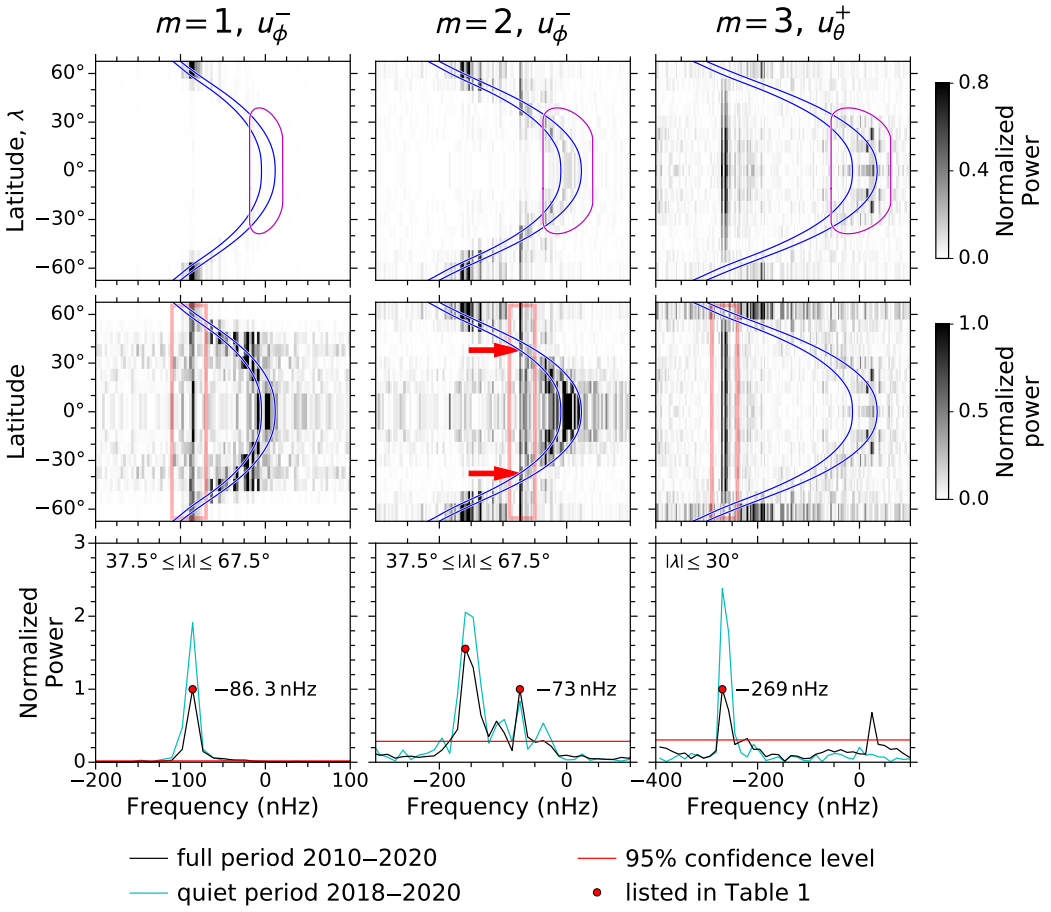

Figure 2.1: Power spectra showing selected modes of oscillation in the Carrington frame. Each column corresponds to a particular m and velocity component, as indicated at the top. Each row shows a different representation of the power spectrum. In the top row, the power spectral density is plotted as a function of frequency and latitude. The two blue curves show $m(\Omega - \Omega_{\rm Carr})/2\pi$ at the surface and at $r = 0.95R_\odot$, where $\Omega(r, \theta)$ is the solar angular velocity in the inertial frame. The purple contour delineates the region in frequency–latitude space affected by inflows into active regions, $m(\Omega_{\rm AR} - \Omega_{\rm Carr})/2\pi$ (see Fig. 2.9). In the second row, the power at each latitude is normalized by its average value over the frequency range between the red bars; this shows that each mode has excess power over a large range of latitudes. The red arrows point to the critical latitudes of $\pm 38^\circ$ at the surface for the mode with frequency -73 nHz. In the third row, the power is averaged over the selected latitude bands specified on the plots, and the frequency resolution is reduced to 12.24 nHz. The red dots point to modes that are not activity-related (see text) and they are listed in Table 2.1.

rial rotation rate at the surface). The zero and yearly frequencies were removed from the data.

The structure of the Sun and its differential rotation is nearly symmetric with respect to the solar equator. Consequently, modes with a toroidal component can be called either symmetric or antisymmetric depending on the north–south symmetry of the surface ra-

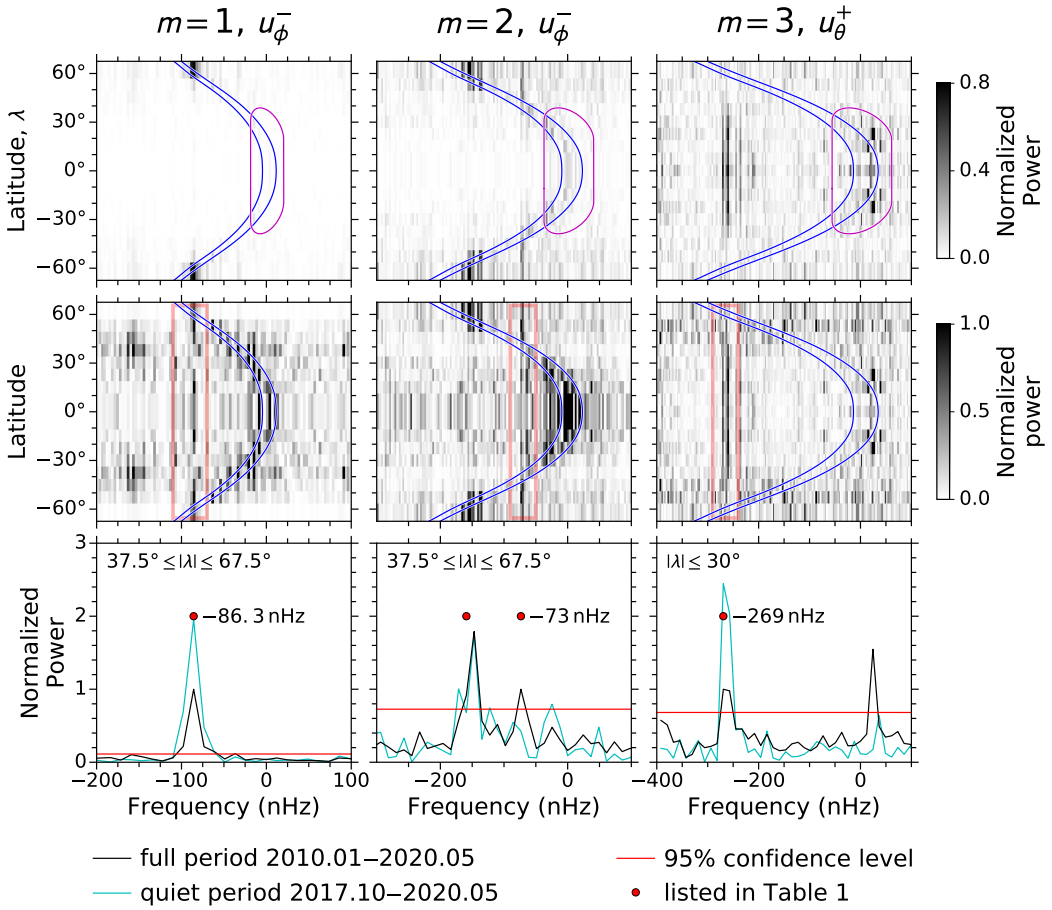

Figure 2.2: Same as Fig. 2.1, but using GONG data. The red dots mark the HMI frequencies for comparison.

dial vorticity. This terminology has been used before in the literature (Charbonneau et al. 1999). A symmetric mode has a symmetric u_θ and antisymmetric u_ϕ, while an antisymmetric mode has an antisymmetric u_θ and symmetric u_ϕ. After symmetrizing (superscript "+") or anti-symmetrizing ("−") the data with respect to the equator, we computed the Fourier transform of the two velocity components in longitude and in time,

$$\hat{u}_j^{\pm}(\theta, m, \omega) = \sum_{\phi,t} u_j^{\pm}(\theta, \phi, t)\, \mathrm{e}^{-i(m\phi-\omega t)}, \tag{2.1}$$

where j is either θ or ϕ, ω is the angular frequency, m is the integer longitudinal wavenumber, and the sums were taken over all longitudes and all times. We considered frequencies in the range $|\omega/2\pi| \leq 400$ nHz and m in the range from 1 to 10 to focus on the large-scale motions. For each choice of velocity component j, symmetry s, and wavenumber m, the power spectral density $PSD = |\hat{u}_j^s(\theta, m, \omega)|^2$ is a function of colatitude and frequency.

For illustration purposes, we show the detection of three global modes of oscillation in the inertial frequency range in Fig. 2.1 (15° resolution). For each mode, there is clear excess power at the same frequency over a range of latitudes. Several types of modes can be seen. The symmetric $m = 1$ mode at a frequency near −86 nHz is visible at all latitudes in the power spectrum; it has most of its power at latitudes of 50° and above

Table 2.1: Solar inertial modes detected in HMI ring-diagram flow maps for 2010–2020. Frequencies are defined in the Carrington frame.

m	(j, s)	mode frequency [a] [nHz]	significance [b]	critical latitude [c] at $r = R_\odot$	latitude at max(u_j^s) [multiples of 7.5°]	max(u_θ) [m s^{-1}]	max(u_ϕ) [m s^{-1}]	linewidth [nHz]	excess power range (not activity related)
Equatorial Rossby modes:									
3	$(\theta, +)$	−269 [d]	$> 8\,\sigma_L$	59°	0°	1.5	1.2	< 24	[−280, −200] nHz
4	$(\theta, +)$	−208 [d]	$7.5\,\sigma_L$	45°	0°	1.6	1.1	< 37	[−250, −190] nHz
5	$(\theta, +)$	−171 [d]	$> 8\,\sigma_L$	37°	0°	1.0	—	< 12	[−210, −150] nHz
6	$(\theta, +)$	−147 [d]	$5.7\,\sigma_L$	31°	0°	1.3	—	< 24	[−170, −125] nHz
7	$(\theta, +)$	−130.7 ± 2.8 [d,e]	$> 8\,\sigma_L$	25°	7.5°	1.5	—	9.9 ± 2.4	[−175, −110] nHz
8	$(\theta, +)$	−110.9 ± 2.4 [d,e]	$> 8\,\sigma_L$	22°	0°	2.0	—	10.6 ± 1.0	[−135, −65] nHz
9	$(\theta, +)$	−122 [d]	$> 8\,\sigma_L$	22°	0°	1.1	—	< 12	[−135, −55] nHz
10	$(\theta, +)$	−110 [d]	$> 8\,\sigma_L$	19°	0°	1.4	—	< 24	[−145, −70] nHz
High-latitude inertial modes:									
1	$(\phi, +)$	−86	$> 8\,\sigma_H$	58°	≥ 67.5°	—	2.5	< 12	[−110, −50] nHz
1	$(\phi, -)$	−86.3 ± 1.6 [e,f]	$> 8\,\sigma_H$	58°	≥ 67.5°	3.0	9.8	7.8 ± 0.2	[−150, −10] nHz
2	$(\phi, +)$	−171 [f]	$> 8\,\sigma_H$	58°	60°	—	2.3	< 12	[−195, −100] nHz
2	$(\phi, -)$	−151.1 ± 4.3 [e,f]	$> 8\,\sigma_H$	56°	≥ 67.5°	2.5	3.4	30.6 ± 3.3	[−185, −90] nHz
3	$(\phi, +)$	−224.7 ± 2.5 [e,f]	$> 8\,\sigma_H$	53°	60°	1.6	1.8	9.7 ± 1.7	[−265, −180] nHz
4	$(\theta, +)$	−294	$3.9\,\sigma_H$	53°	≥ 67.5°	1.0	0.8	< 12	[−310, −240] nHz
4	$(\theta, +)$	−245	$5.3\,\sigma_H$	49°	60°	1.1	1.1	< 24	
5	$(\theta, -)$	−343	$5.3\,\sigma_H$	52°	60°	0.7	—	< 12	[−355, −275] nHz
5	$(\phi, +)$	−282	$2.6\,\sigma_H$	47°	52.5°	0.8	0.8	< 24	
Critical-latitude inertial modes:									
1	$(\phi, +)$	−37	$> 8\,\sigma_M$	38°	37.5°	—	1.3	< 24 [g]	
1	$(\phi, -)$	−37	$7.1\,\sigma_M$	38°	37.5°	0.5	0.9	< 12 [g]	
1	$(\phi, -)$	−12	$> 8\,\sigma_L$	20°	30°	—	1.2	< 24	
2	$(\phi, +)$	−61	$6.8\,\sigma_M$	34°	52.5°	—	1.1	< 24	[−65, 0] nHz
2	$(\phi, +)$	−12	$> 8\,\sigma_L$	10°	22.5°	0.9	1.1	< 12	
2	$(\phi, -)$	−73	$> 8\,\sigma_H$	38°	45°	0.8	1.3	< 12	
2	$(\phi, -)$	−24	$> 8\,\sigma_M$	20°	22.5°	0.9	1.4	< 24	[−90, 30] nHz
2	$(\phi, -)$	0	$7.2\,\sigma_L$	n/a	7.5°	—	1.0	< 12 [g]	
3	$(\phi, +)$	−147	$4.0\,\sigma_H$	44°	45°	—	0.9	< 12	
3	$(\theta, -)$	−61	$3.6\,\sigma_M$	28°	37.5°	0.7	0.8	< 24	
3	$(\phi, +)$	−24	$> 8\,\sigma_M$	15°	15°	—	1.0	< 12	[−50, 10] nHz
3	$(\phi, -)$	−73 [h]	$3.0\,\sigma_M$	31°	30°	—	0.7	< 12	
3	$(\phi, -)$	−37	$6.6\,\sigma_L$	20°	22.5°	—	1.0	< 24	[−50, 30] nHz
3	$(\phi, -)$	0	$6.6\,\sigma_L$	n/a	15°	—	1.0	< 24 [g]	
4	$(\phi, +)$	−220	$4.3\,\sigma_H$	46°	45°	—	0.5	< 12	
4	$(\phi, +)$	−110	$4.4\,\sigma_M$	33°	37.5°	—	0.6	< 12	
4	$(\phi, +)$	−12	$4.3\,\sigma_L$	n/a	15°	0.6	1.0	< 12 [g]	[−120, 35] nHz
4	$(\phi, +)$	24	$5.5\,\sigma_L$	n/a	0°	—	1.4	< 24	
4	$(\phi, -)$	−171	$3.4\,\sigma_H$	41°	45°	—	0.6	< 12	
4	$(\phi, -)$	−24	$> 8\,\sigma_L$	10°	22.5°	—	1.0	< 24	[−50, 30] nHz
4	$(\phi, -)$	24	$5.9\,\sigma_L$	n/a	7.5°	—	1.0	< 24	
5	$(\phi, +)$	−135 [h]	$3.7\,\sigma_M$	32°	37.5°	—	0.8	< 24	
5	$(\phi, +)$	−24	$3.5\,\sigma_L$	5°	15°	—	1.0	< 24 [g]	
5	$(\theta, -)$	37	$4.3\,\sigma_L$	n/a	15°	0.7	—	< 24	
5	$(\theta, +)$	−330	$2.3\,\sigma_H$	51°	60°	0.7	—	< 24	[−330, −190] nHz
5	$(\phi, -)$	−294	$2.1\,\sigma_H$	48°	52.5°	—	0.7	< 24	
5	$(\phi, -)$	−245	$5.7\,\sigma_H$	44°	45°	—	0.8	< 12	
5	$(\theta, +)$	−86	$4.0\,\sigma_M$	25°	37.5°	0.7	—	< 12	
6	$(\theta, -)$	−343 [h]	$2.1\,\sigma_H$	47°	60°	0.5	—	< 12	
6	$(\phi, +)$	−306	$3.3\,\sigma_H$	45°	60°	—	0.4	< 12	
6	$(\theta, -)$	−61	$2.0\,\sigma_M$	18°	30°	0.6	—	< 12	
6	$(\phi, +)$	−24	$4.5\,\sigma_M$	n/a	15°	—	1.1	< 12	
6	$(\phi, -)$	−245 [h]	$2.7\,\sigma_H$	40°	45°	—	0.5	< 12	
6	$(\phi, -)$	37	$2.5\,\sigma_L$	n/a	7.5°	—	0.7	< 12 [g]	
7	$(\theta, -)$	−196	$2.4\,\sigma_H$	33°	45°	0.7	—	< 24 [g]	
7	$(\phi, +)$	−86	$3.6\,\sigma_L$	20°	22.5°	—	0.6	< 12	
7	$(\theta, +)$	−73	$3.0\,\sigma_M$	18°	0°	0.5	—	< 12	
7	$(\phi, -)$	0	$3.6\,\sigma_L$	n/a	22.5°	—	0.7	< 24	
9	$(\phi, +)$	0	$5.3\,\sigma_L$	n/a	15°	0.7	0.6	< 12	
9	$(\theta, +)$	−269	$2.5\,\sigma_H$	34°	45°	0.5	—	< 12	
10	$(\theta, -)$	−49	$3.3\,\sigma_M$	6°	22.5°	0.5	—	< 12	
10	$(\theta, +)$	−282	$2.9\,\sigma_H$	33°	45°	0.3	—	< 12	

[a] The search range was limited to $1 \le m \le 10$ and $|\omega/2\pi| \le 400$ nHz.

[b] The statistical significance of each peak is given in terms of the standard deviation computed for the most significant of the latitudinal averages shown in Figs. 2.10–2.19 (σ_L for low latitudes, σ_M for mid latitudes, and σ_H for high latitudes).

[c] "n/a" means not applicable (no critical latitude at the surface, only deeper).

[d] Mode reported by Löptien et al. (2018).

[e] Mode parameters measured with a Lorentzian fit.

[f] Frequency near that reported by Hathaway and Upton (2021).

[g] Measured during the quiet Sun period 2018–2020.

[h] Outside the activity frequency range, however not significant during the quiet Sun period 2018–2020.

(the 5° observations show that the power keeps increasing with latitude up to at least 80°). It corresponds to the high-latitude velocity features previously reported (Hathaway et al. 2013, Bogart et al. 2015, Hathaway and Upton 2021), although it was not recognized as a normal mode of the whole convection zone. The second example is the symmetric $m = 2$ mode of oscillation at −73 nHz. This mode is also seen over the entire latitude range of the observations, but it has most of its power concentrated near the critical latitude of 38° (see Fig. 2.1). The power is strong above the critical latitude, but decreases toward the poles. The third example is the $m = 3$ equatorial Rossby modes (Löptien et al. 2018) at a frequency of −269 nHz, for which the power is mostly confined to lie between the critical latitudes (±59° for this mode's frequency) where the mode is trapped (Gizon et al. 2020b).

We have detected many tens of normal modes of oscillation at low frequencies, as shown in Figs. 2.10 – 2.19 and reported in Table 2.1. These modes are associated with significant (above 95% confidence level) excess power in at least one of three latitude bands (low latitudes below 30°, mid latitudes from 15° to 45°, and high latitudes from 37.5° to 67.5°). While the most striking features in the power spectra are narrow peaks, a closer inspection reveals ranges in frequency and latitude of additional excess power. For example, the $m = 8$ power spectrum for u_θ^+ (Fig. 2.20) has excess power at low latitudes at frequencies between −135 nHz and −65 nHz, which can be attributed to the presence of a dense spectrum of modes adjacent to the equatorial Rossby mode.

To avoid misidentifying active-region inflows (Gizon et al. 2001) as modes of oscillation in the power spectra, we defined a region in frequency–latitude space based on the active-region rotation rates and latitudes (Kutsenko 2021), as shown in Fig. 2.9. A peak in the power spectrum for the entire observation period is not reported in Table 2.1 if it is in the activity area and does not have significant power during the quiet-Sun period (February 2018 to September 2020), see Figs. 2.10 – 2.19. We also checked that the reported modes were not misidentified due to leakage from the window function (Liang et al. 2019), and that they are also seen in the Global Oscillation Network Group (GONG) data (Fig. 2.2).

For each mode, we extracted the two velocity components of a mode eigenfunction in a narrow frequency range around the mode frequency within one linewidth (Proxauf et al. 2020). Examples of the surface eigenfunctions are shown in the left column of Fig. 2.3.

2.3 Eigenmodes of the differentially rotating Sun

2.3.1 2D linear model

To identify the observed modes of oscillation, we computed the eigenmodes of a spherical shell with $0.710 \leq r/R_\odot \leq 0.985$ that rotates like the Sun. In the Carrington frame, the linearized equations for the conservation of momentum, mass, and energy, together with

the equation of state, are as follows:

$$\rho D_t \boldsymbol{u}' = -\boldsymbol{\nabla} p' + \rho' \boldsymbol{g} - 2\rho \boldsymbol{\Omega} \times \boldsymbol{u}' - \rho r \sin\theta \, (\boldsymbol{u}' \cdot \boldsymbol{\nabla}) \boldsymbol{\Omega} + \boldsymbol{\nabla} \cdot \boldsymbol{\mathcal{D}}, \tag{2.2}$$

$$D_t \rho' = -\boldsymbol{\nabla} \cdot (\rho \boldsymbol{u}'), \tag{2.3}$$

$$D_t s' = \frac{c_p \, \delta}{H_p} u_r' - \frac{u_\theta'}{r} \frac{\partial s}{\partial \theta} + \frac{1}{\rho T} \boldsymbol{\nabla} \cdot (\kappa \rho T \boldsymbol{\nabla} s'), \tag{2.4}$$

$$\frac{p'}{p} = \frac{\gamma \rho'}{\rho} + \frac{s'}{c_v}, \tag{2.5}$$

where

$$D_t = \partial/\partial t + (\Omega - \Omega_{\mathrm{Carr}}) \partial/\partial \phi \tag{2.6}$$

is the material derivative and $\Omega(r, \theta)$ is a differential rotation model close to the helioseismic measurements averaged over 2010 – 2020 (Larson and Schou 2018). Linear perturbations are denoted with primes. The background model is based on a standard solar model (Christensen-Dalsgaard et al. 1996a), except for the superadiabaticity $\delta = \nabla - \nabla_{\mathrm{ad}}$, which is a constant parameter in the convection zone (the radiative zone is very stable below with $\delta \approx -0.1$). In the above equation, H_p is the pressure scale height, and c_v and c_p are the heat capacities per unit mass at constant volume and constant pressure. The viscous stress tensor $\mathcal{D}_{ij} = \rho \nu_{\mathrm{t}} [\partial_i u_j' + \partial_j u_i' - \frac{2}{3} (\partial_k u_k') \delta_{ij}]$ accounts for wave attenuation, where δ_{ij} is the Kronecker delta. The energy equation includes advection and thermal diffusion. In our model, the viscous and thermal diffusivities are those resulting from the turbulence and, therefore, were considered to be equal. For the sake of simplicity, we chose the model to have very few free parameters: a constant fluid viscosity ν_{t} and a constant superadiabaticity δ, which gives the degree of convective instability.

The latitudinal entropy gradient is obtained by assuming that the differential rotation is the result of a thermal wind balance (Miesch et al. 2006):

$$\frac{g}{c_p} \frac{\partial s}{\partial \theta} = r^2 \sin\theta \frac{\partial (\Omega^2)}{\partial z}, \tag{2.7}$$

where $z = r \cos\theta$ is the coordinate along the rotation axis.

Boundary conditions need to be applied at $\theta = 0$ and π. Since we only considered modes with $m \neq 0$, we imposed $\boldsymbol{u}' = 0$ and $\rho' = p' = s' = 0$. The numerical domain is bounded above by the photosphere and below by the radiative interior, both of which are strongly stably stratified and where radial flows are difficult to drive because of the strong, restoring buoyancy force. Therefore, we used an impenetrable and stress-free boundary condition at both radial boundaries.

We looked for solutions to the above problem where each physical quantity is proportional to $\exp(im\phi - i\sigma t)$, where σ is the complex mode angular frequency and m is the integer longitudinal wavenumber. We discretized the spatial derivatives with second-order central differences with 16 radial and 72 latitudinal grid points. The above equations were combined in matrix form into a complex eigenvalue problem, which was solved using the LAPACK routine. We focused on the low-frequency solutions. We refer to the modes of oscillation obtained in this problem as the "modes of the 2D model".

2.3.2 1D linear model

In order to highlight the main physics, we also considered fluid motions that are purely toroidal (horizontal), restricted to a spherical surface of radius $r = R_\odot$. Keeping the density constant, the linearized momentum equations in a frame rotating at $\Omega_{\rm carr}$ are as follows:

$$D_t u'_\theta = -\frac{1}{r}\frac{\partial}{\partial\theta}\left(\frac{p'}{\rho}\right) + 2\Omega\cos\theta\, u'_\phi + \nu_{\rm t}\,\Delta u'_\theta, \tag{2.8}$$

$$D_t u'_\phi = -\frac{1}{r\sin\theta}\frac{\partial}{\partial\phi}\left(\frac{p'}{\rho}\right) - 2\Omega\cos\theta\, u'_\theta - \sin\theta\, u'_\theta\frac{\partial\Omega}{\partial\theta} + \nu_{\rm t}\,\Delta u'_\phi, \tag{2.9}$$

where the material derivative D_t is given above by Eq. (2.6), and Δ is the horizontal part of the Laplacian. For purely toroidal modes, we introduced the stream function $\Psi(\theta,\phi,t)$ such that

$$\boldsymbol{u}' = \boldsymbol{\nabla}\times\left[\Psi(\theta,\phi,t)\,\hat{\boldsymbol{r}}\right] = \frac{1}{r\sin\theta}\frac{\partial\Psi}{\partial\phi}\,\hat{\boldsymbol{\theta}} - \frac{1}{r}\frac{\partial\Psi}{\partial\theta}\,\hat{\boldsymbol{\phi}}. \tag{2.10}$$

The two above equations can be combined to obtain

$$D_t\Delta\Psi - \frac{1}{r^2\sin\theta}\frac{\partial}{\partial\theta}\left(\frac{1}{\sin\theta}\frac{\partial}{\partial\theta}(\Omega\sin^2\theta)\right)\frac{\partial\Psi}{\partial\phi} = \nu_{\rm t}\,\Delta^2\Psi. \tag{2.11}$$

We looked for solutions of the form

$$\Psi(\theta,\phi,t) = {\rm Re}\left[\psi(\theta)\exp(im\phi - i\sigma t)\right], \tag{2.12}$$

where m is the longitudinal wavenumber and σ is the (complex) angular frequency. The equation for ψ is of fourth-order and requires four boundary conditions. The condition that the flow vanishes at the poles implies

$$\psi = \frac{{\rm d}\psi}{{\rm d}\theta} = 0 \quad \text{at } \theta = 0 \text{ and } \pi. \tag{2.13}$$

In order to discretize the problem, we projected ψ onto a basis of associated Legendre polynomials. For the numerical value of the eddy viscosity at the surface, we used the value $\nu_{\rm t} = 500$ km^2 s^{-1} (Gizon et al. 2020b), unless otherwise specified. The resulting eigenvalue problem was solved for each m using the eigenvalue solver `scipy.linalg.eig`. We refer to the modes of oscillation obtained in this problem as the "modes of the 1D model".

2.4 Mode identification

We then sought a match with the observed modes. We did not tune the parameters of the 2D model to match the observations exactly; we performed a sensitivity study using $\delta = -10^{-6}$, -2×10^{-7}, 0, 2×10^{-7}, 10^{-6} (Fig. 2.7) and $\nu_{\rm t} = 50$, 100, 250, 500 km^2 s^{-1} (Fig. 2.8). We found that $\delta = 0$ and $\nu_{\rm t} = 100$ km^2 s^{-1} provide a good match (Fig. 2.3) for the surface eigenfunctions and eigenfrequencies of the three modes of Fig. 2.1. As part of the identification, we sought modes of the models that have long lifetimes or are growing

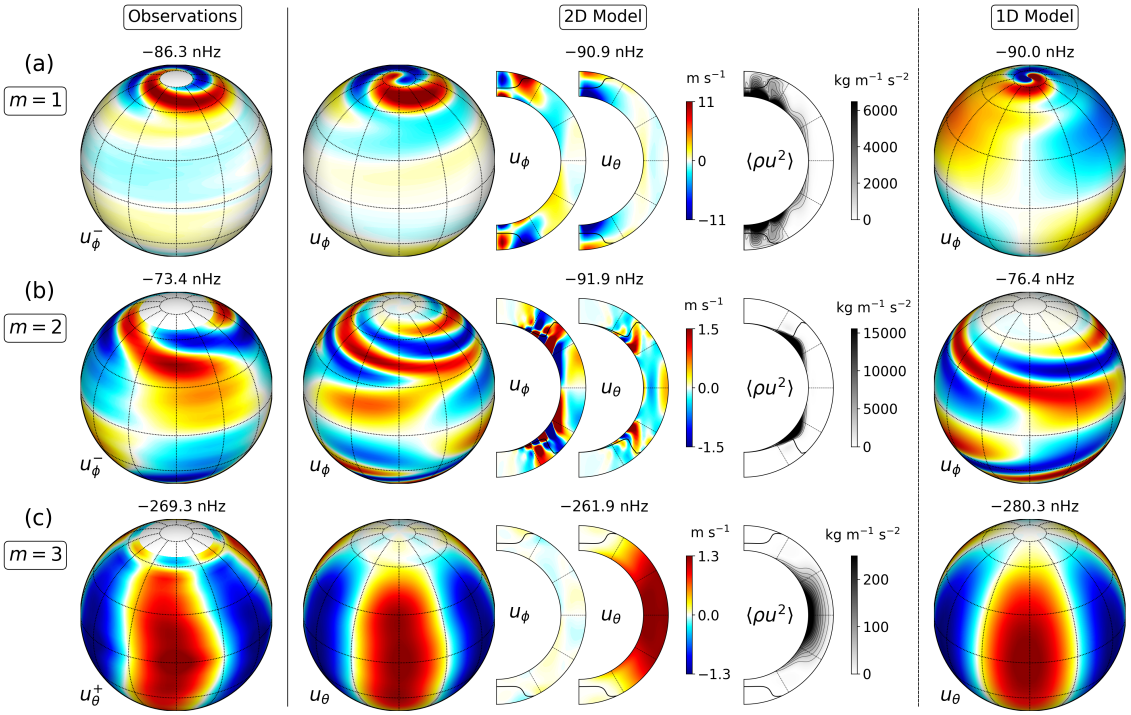

Figure 2.3: Observed and model eigenfunctions for the modes shown in Fig. 2.1. The left column shows the observed velocity (u_ϕ^- for the $m = 1$ and $m = 2$ modes, u_θ^+ for the $m = 3$ mode). The middle columns show the corresponding eigenfunctions of the 2D model for $\nu_t = 100$ km^2 s^{-1} and $\delta = 0$, at the surface and through the central meridian, together with the kinetic energy density. The thick black curves show the critical latitudes. The rightmost column shows the eigenfunctions of the 1D model at the surface. The other velocity components are shown in Fig. 2.4 and the radial vorticity is shown in Fig. 2.5.

(Fig. 2.21). The identified modes are representatives of three main families of modes: the high-latitude inertial modes (Fig. 2.3a), the critical-latitude inertial modes (Fig. 2.3b), and the equatorial Rossby modes (Fig. 2.3c). This classification is supported by the dispersion relations at small m (Fig. 2.6).

2.4.1 High-latitude inertial modes

The high-latitude inertial modes are analogous to the "wall modes" in plane Poiseuille flows (Gizon et al. 2020b). They are seen in both the 1D and 2D eigenvalue problems for $m \leq 5$. In the 2D model, the eigenfunctions are dominantly toroidal and extend to the bottom of the convection zone, with their highest kinetic energy density near the base of the convection zone (Fig. 2.3a). This is unlike the kinetic energy density of the p modes, which always peaks near the surface. The correct tilt of the spiral structure is only obtained in the 2D model (Fig. 2.3a). In this model, the high-latitude modes become baroclinically unstable (Fig. 2.21) due to the latitudinal entropy gradient resulting from the thermal wind balance (Knobloch and Spruit 1982; Bekki et al., in prep.). [1] In the 1D

[1] The formation of a spiral at high latitudes by baroclinic instability has also been discussed in the context of Venus' atmosphere (Kashimura et al. 2019).

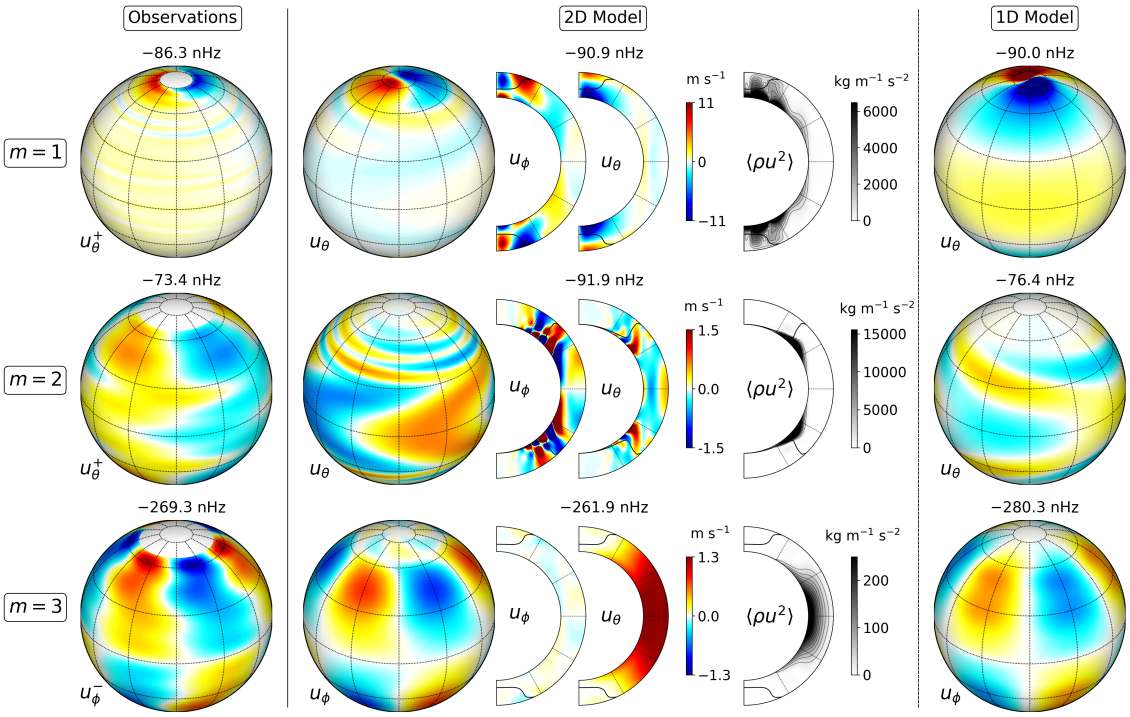

Figure 2.4: Same as Fig. 2.3, but for the complementary velocity components.

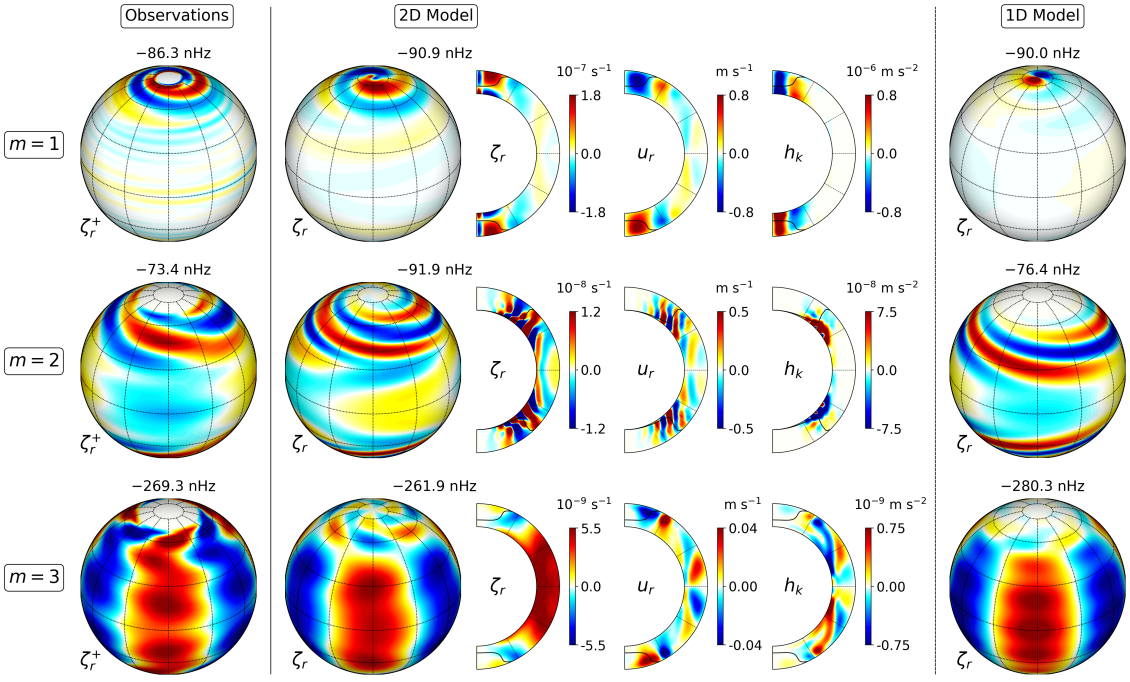

Figure 2.5: Observed and model radial vorticity for the selected modes of Fig. 2.3. The first, second, and rightmost columns show the radial vorticity $\zeta_r = (\boldsymbol{\nabla} \times \boldsymbol{u})_r$ for the observations, the 2D model, and the 1D model, respectively. The remaining columns in the middle show meridional cuts of ζ_r, radial velocity u_r, and the kinetic helicity $h_\mathrm{k} = \langle \boldsymbol{u} \cdot \boldsymbol{\zeta} \rangle$ for the 2D model.

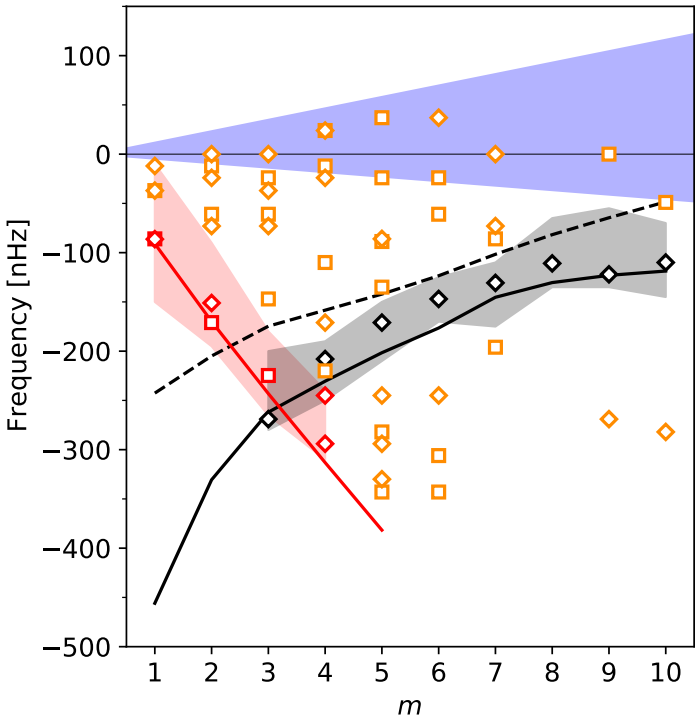

Figure 2.6: Mode frequencies in the Carrington frame for the observations and the 2D model (Re σ). The symbols show the observed modes (diamonds for symmetric modes and squares for antisymmetric modes). The red symbols show the high-latitude modes, the orange symbols the critical-latitude modes, and the black symbols the equatorial Rossby modes. The rose- and gray-shaded areas show the observed frequency ranges of excess power (last column of Table 2.1). For reference, the blue-shaded area gives the range of rotation rates at the equator between the surface and $0.95R_\odot$. The curves give the dispersion relations for the modes of the 2D model with $\nu_t = 100$ km^2 s^{-1} and $\delta = 0$. The red curve is the dispersion relation for the high-latitude modes. The solid and dashed-black curves are for the fundamental ($n = 0$) and first overtone ($n = 1$) equatorial Rossby modes.

model, only the $m = 1$ high-latitude modes are self-excited (Fig. 2.21) as a result of a shear instability at high latitudes; however, the tilt of the spiral is not consistent with the observations.

2.4.2 Critical-latitude modes

Critical-latitude inertial modes are found for both the 1D and 2D models. Their amplitudes are maximum near their critical latitudes; they are known as "center modes" in 1D hydrodynamics (Gizon et al. 2020b). The kinetic energy density of the $m = 2$ mode of the 2D model at −92 nHz (−73 nHz observed) is concentrated near the base of the convection zone near 45° latitude (Fig. 2.3b). This is a very important place in the Sun, as it is where the toroidal magnetic field generation should be strongest (Spruit 2011).

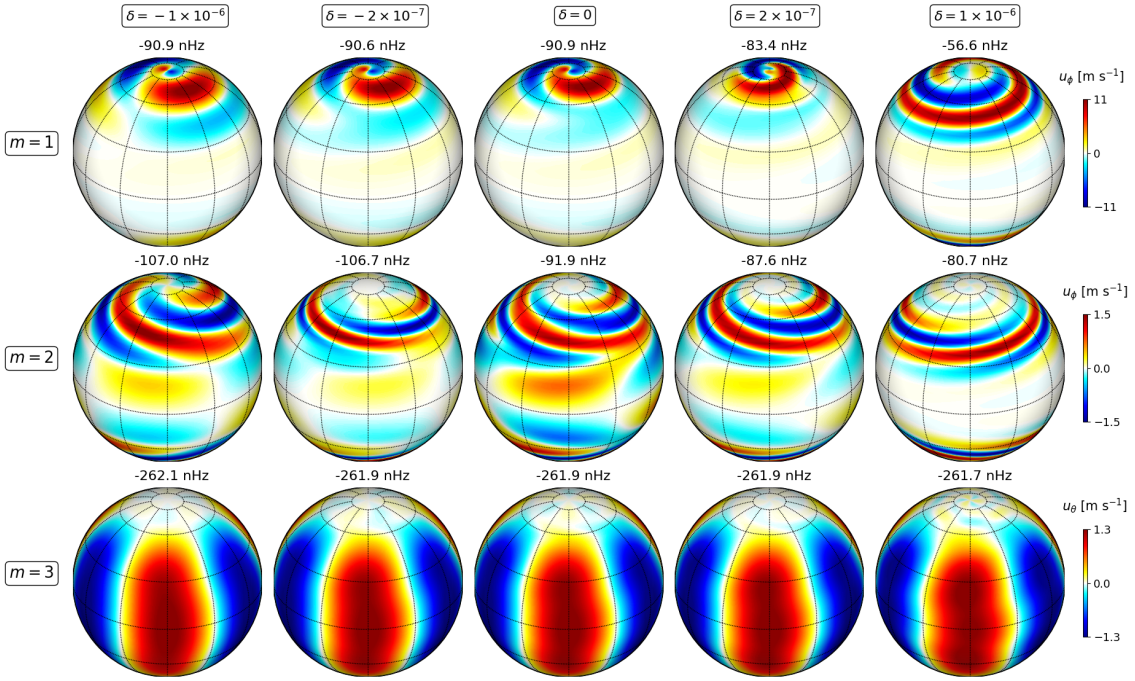

Figure 2.7: Parameter study (2D model) for different values of the superadiabaticity δ, at fixed $\nu_t = 100$ km^2 s^{-1}. The modes are those shown in Fig. 2.1. The spiral patterns in u_ϕ of the $m = 1$ high-latitude and $m = 2$ critical-latitude modes are sensitive to a small change in δ. To obtain a pattern consistent with the observations, $\delta < 2 \times 10^{-7}$ is implied. The case $\delta = 10^{-6}$ is excluded by both the eigenfunctions and the eigenfrequencies. The $m = 3$ equatorial Rossby mode is almost independent of δ because it is nearly purely horizontal (quasi-toroidal).

2.4.3 Equatorial Rossby modes

Equatorial Rossby modes are the easiest to identify: their frequencies are close to the classical dispersion relation for uniform rotation, $\sigma = -2\Omega/(m + 1)$. The 2D model supports modes with a different number of nodes in the radial direction, n. The frequencies of the observed equatorial Rossby modes span the range between the $n = 0$ and the $n = 1$ branches of the dispersion relation (Fig. 2.6). For example, the $m = 3$ mode is identified as a fundamental mode ($n = 0$).

2.5 Discussion and conclusion

We observed and identified three families of global-scale inertial modes in the solar convection zone, within the search range $|\omega/2\pi| \leq 400$ nHz and $1 \leq m \leq 10$. Some of these modes are self-excited in the models. We also found extended regions in frequency space where closely packed modes exist. The modes we have identified are sensitive to the physical conditions deep in the convection zone (see plots of the kinetic energy density in Fig. 2.3). The eigenfrequencies and surface eigenfunctions of the high- and critical-latitude inertial modes have diagnostic potential for the latitudinal entropy gradient, the superadiabaticity (Fig. 2.7), and the turbulent viscosity (Fig. 2.8), which are

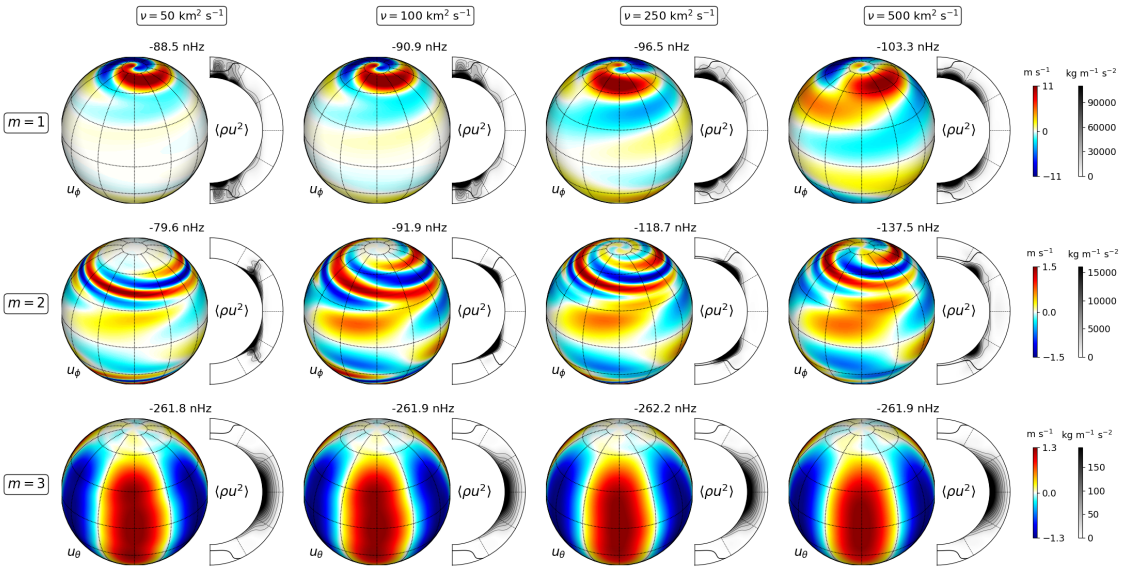

Figure 2.8: Parameter study (2D model) for different values of the turbulent viscosity ν_t, for a convection zone that is adiabatically stratified ($\delta = 0$). The modes are those shown in Fig. 2.1. The frequencies of the $m = 1$ high-latitude mode and the $m = 2$ critical-latitude modes are sensitive to the choice of ν_t. The smaller values of ν_t (≤ 100 km^2 s^{-1}) give a better agreement with the observed frequencies (respectively -86.3 nHz and -73.4 nHz). The $m = 3$ equatorial Rossby modes is essentially insensitive to ν_t.

largely unconstrained by traditional p-mode helioseismology. We find that the observed inertial modes are compatible with $\delta < 2 \times 10^{-7}$ and $\nu_t \leq 100$ km^2 s^{-1} at the bottom of the convection zone. These observational upper limits are substantially below the expectation from mixing length theory — by approximately one order of magnitude each (Christensen-Dalsgaard et al. 1996a, Muñoz-Jaramillo et al. 2011) — and they imply that the convective motions in the lower half of the convection zone are weak. This might correspond to the slightly subadiabatic conditions seen below 0.8 $R_\odot$ in recent numerical simulations of solar convection (see e.g. Hotta 2017, Käpylä et al. 2017, Bekki et al. 2017). While our upper limit on the turbulent velocities ($\approx \sqrt{3\nu_t/\tau} \leq 11$ m s^{-1} for a correlation time $\tau = 1$ month) is well below the mixing length value, it is just above the lower limit required to drive solar differential rotation (8 m s^{-1} according to (Miesch et al. 2012)). A lower convection zone that is only marginally unstable (or even stable) would allow a flux transport dynamo to wind up and transport the magnetic field in this region. We expect that the characteristics of the observed inertial modes, including amplitudes and lifetimes, will allow us to infer $\delta(r)$ and $\nu_t(r)$ and understand in which regime of rotating convection the Sun operates (Hindman et al. 2020).

Acknowledgements

Author contributions: This project was initiated and supervised by LG and RHC. The helioseismic ring parameter fits were provided by RSB for HMI and KJ for GONG. BP and Z-CL measured the mode parameters. YB solved the 2D eigenvalue problem. DF and LH

solved the 1D eigenvalue problem. LG, RHC and ACB wrote the draft paper. All authors contributed to the final manuscript. We are very grateful to John Leibacher for useful comments. LG thanks the Max Planck Institute for Astrophysics for the opportunity to present a preliminary account of these results at the 2020 Biermann Lectures. The HMI data are courtesy of NASA/SDO and the HMI Science Team. This work utilizes GONG data from the National Solar Observatory (NSO), which is operated by AURA under a cooperative agreement with NSF and with additional financial support from NOAA, NASA, and USAF. This work was supported in part by NASA contract NAS5-02139 to Stanford University. YB is a member of the International Max Planck Research School for Solar System Science at the University of Göttingen, and acknowledges partial support from the Japan Student Services Organization (JASSO). We acknowledge support from ERC Synergy Grant WHOLE SUN 810218. LG acknowledges support from NYUAD Institute Grant G1502. LG, DF and BP acknowledge funding by Deutsche Forschungsgemeinschaft (DFG, German Research Foundation) through SFB 1456/432680300 Mathematics of Experiment, project C04. The computational resources were provided by the German Data Center for SDO through German Aerospace Center (DLR) grant 50OL1701. LG, ACB, and CD acknowledge support from DLR under PLATO Data Center grant 50OO1501.

2.6 Appendix

2.6.1 Supplementary figures

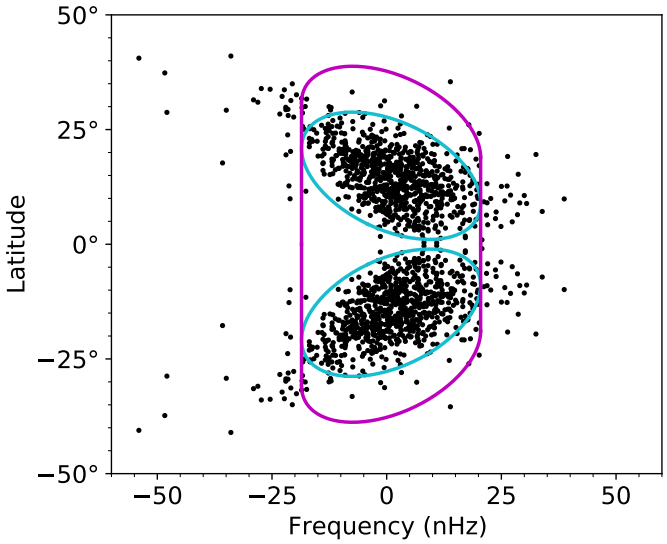

Figure 2.9: Rotational frequencies of solar active regions versus latitude, measured in the Carrington frame (from May 2010 to December 2016, Kutsenko 2021). The data (black dots) have been symmetrized in latitude. The cyan ellipses contain 90% of the active regions. The ellipses are extended to higher latitudes by 10° and down to the equator to include flows around active regions. The resulting region in frequency–latitude space is given by the purple contour, which we denote via the equation $\omega = \Omega_{\mathrm{AR}}(\theta) - \Omega_{\mathrm{Carr}}$. We note that the HMI data used in the main text cover a longer observation period (from May 2010 to September 2020); however, the purple contour is not significantly affected by the very few active regions from the nearly quiet period 2017–2020 (about 5% of all cycle 24 active regions).

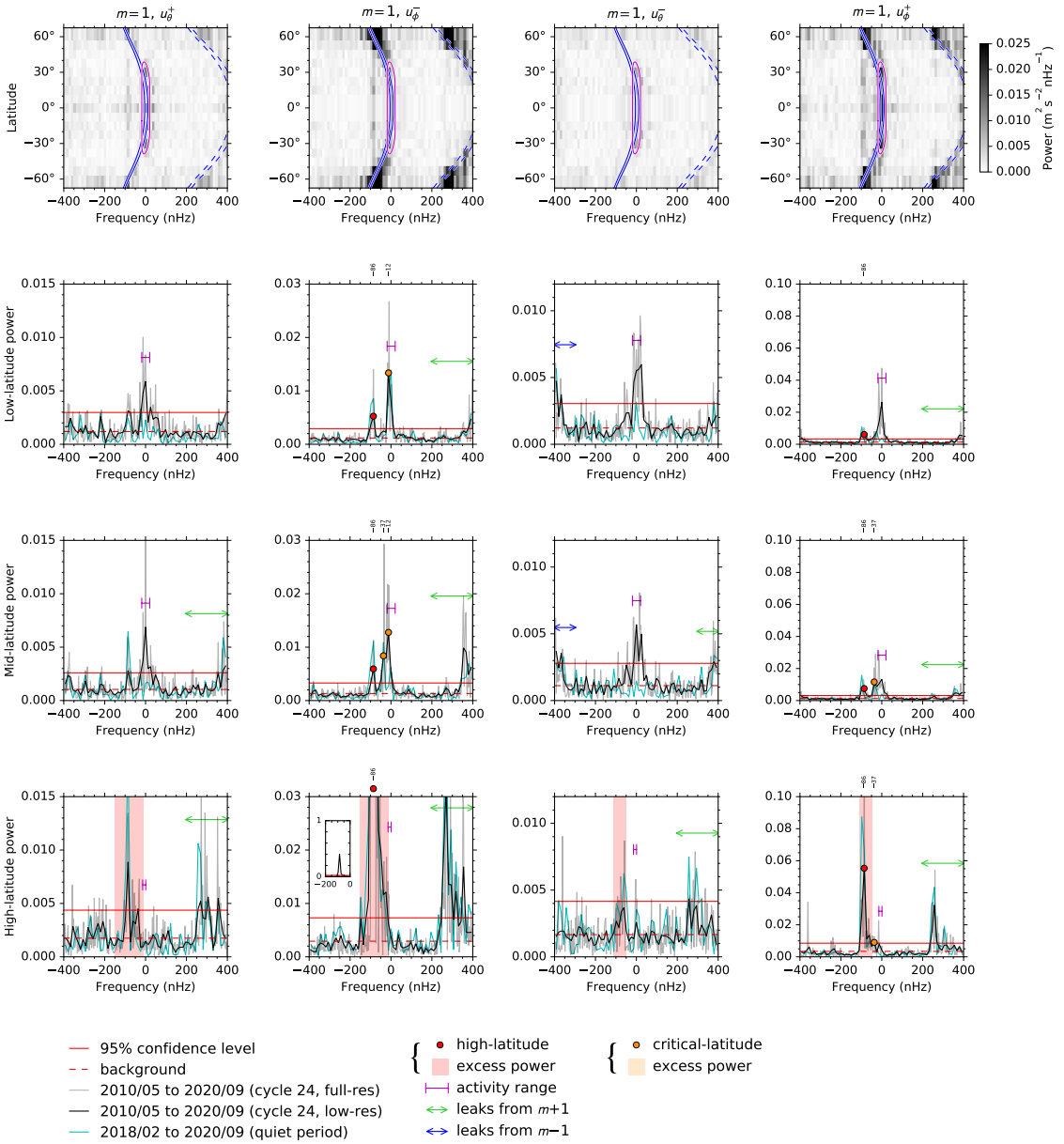

Figure 2.10: Power spectra for $m = 1$. (**Top row**) Power for the four components u_θ^+, u_ϕ^-, u_θ^-, and u_ϕ^+. The purple contours delineate the regions where inflows into active regions produce excess power (see Fig. 2.9). The two blue curves show $m(\Omega - \Omega_{\text{Carr}})/2\pi$ at the surface and at $r = 0.95R_\odot$. (**Second row**) Power spectral density averaged over $0° - 30°$. The gray curves show the power spectra at full resolution (3.06 nHz), and the black curves show them at a quarter of the resolution. The 95% confidence levels are shown by the red horizontal lines. The cyan curves are for the quiet-Sun period only (2.6 years from 4 February 2018 to 6 September 2020). (**Third row**) Power spectral density averaged over $15° - 45°$. (**Fourth row**) Power spectral density averaged over $37.5° - 67.5°$. In the three lower rows, the dots and the shaded areas (see legend) indicate the significant peaks and the excess power ranges not related to magnetic activity, given in Table 2.1.

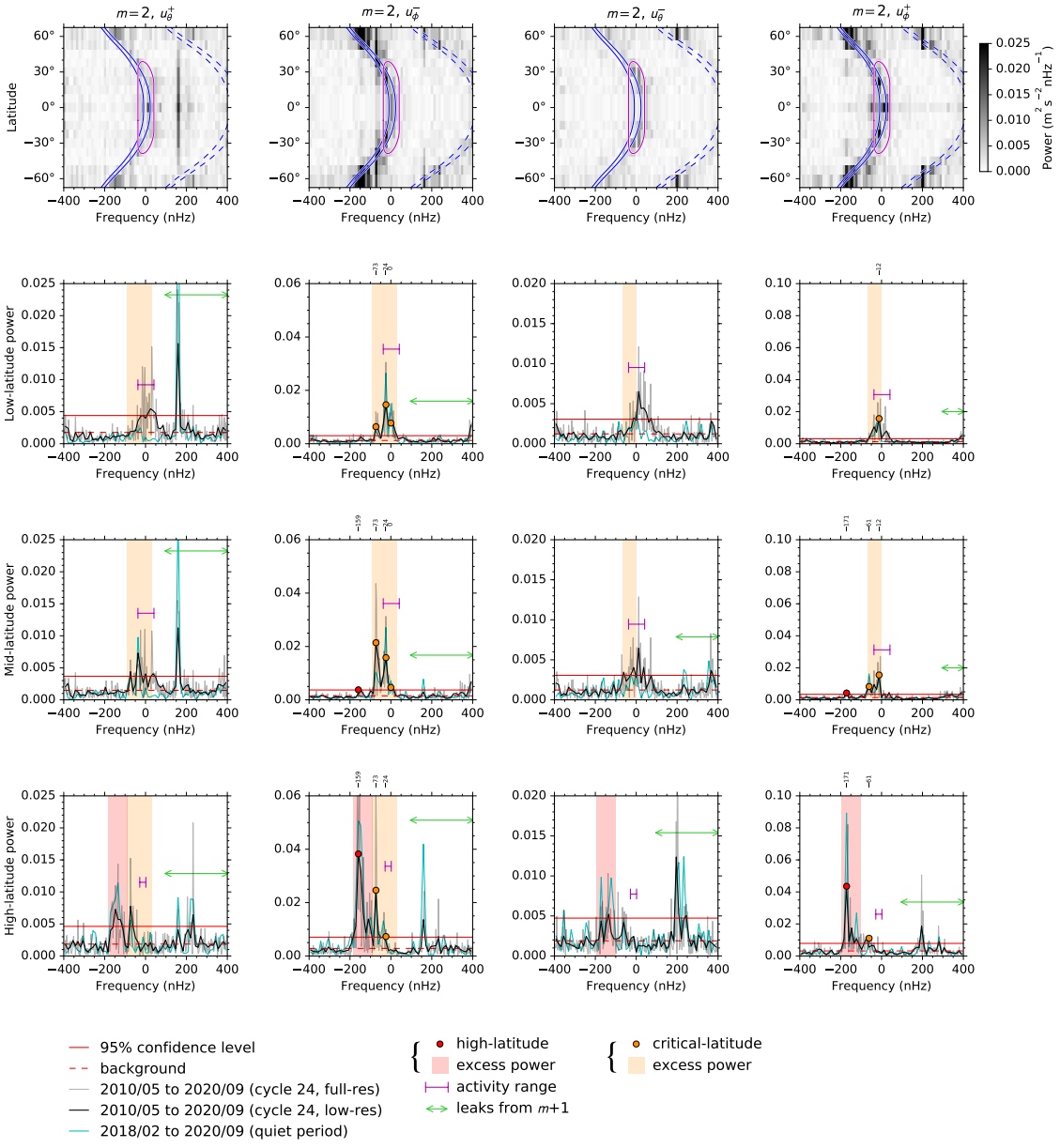

Figure 2.11: Same as Fig. 2.10, but for $m = 2$.

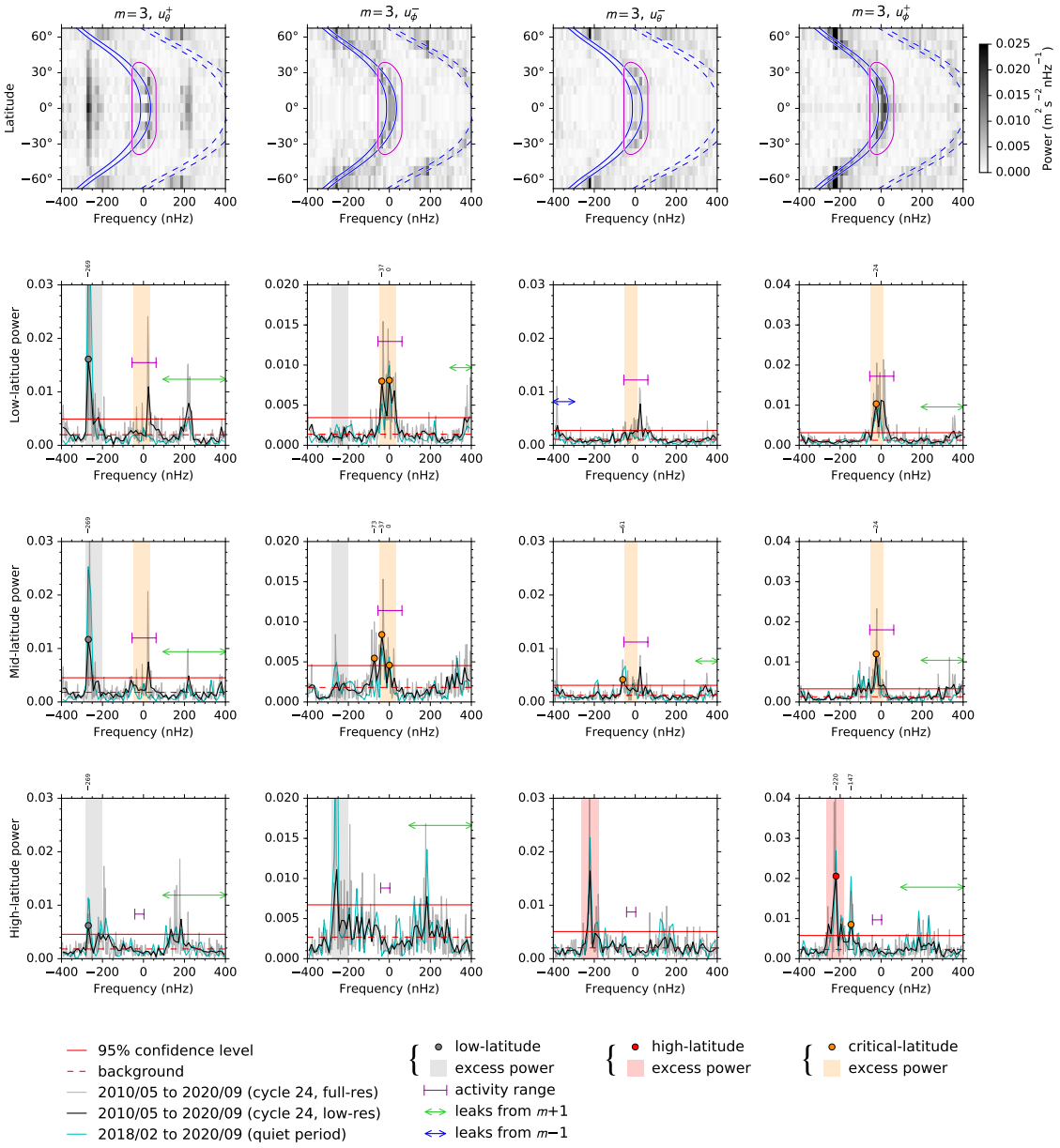

Figure 2.12: Same as Fig. 2.10, but for $m = 3$.

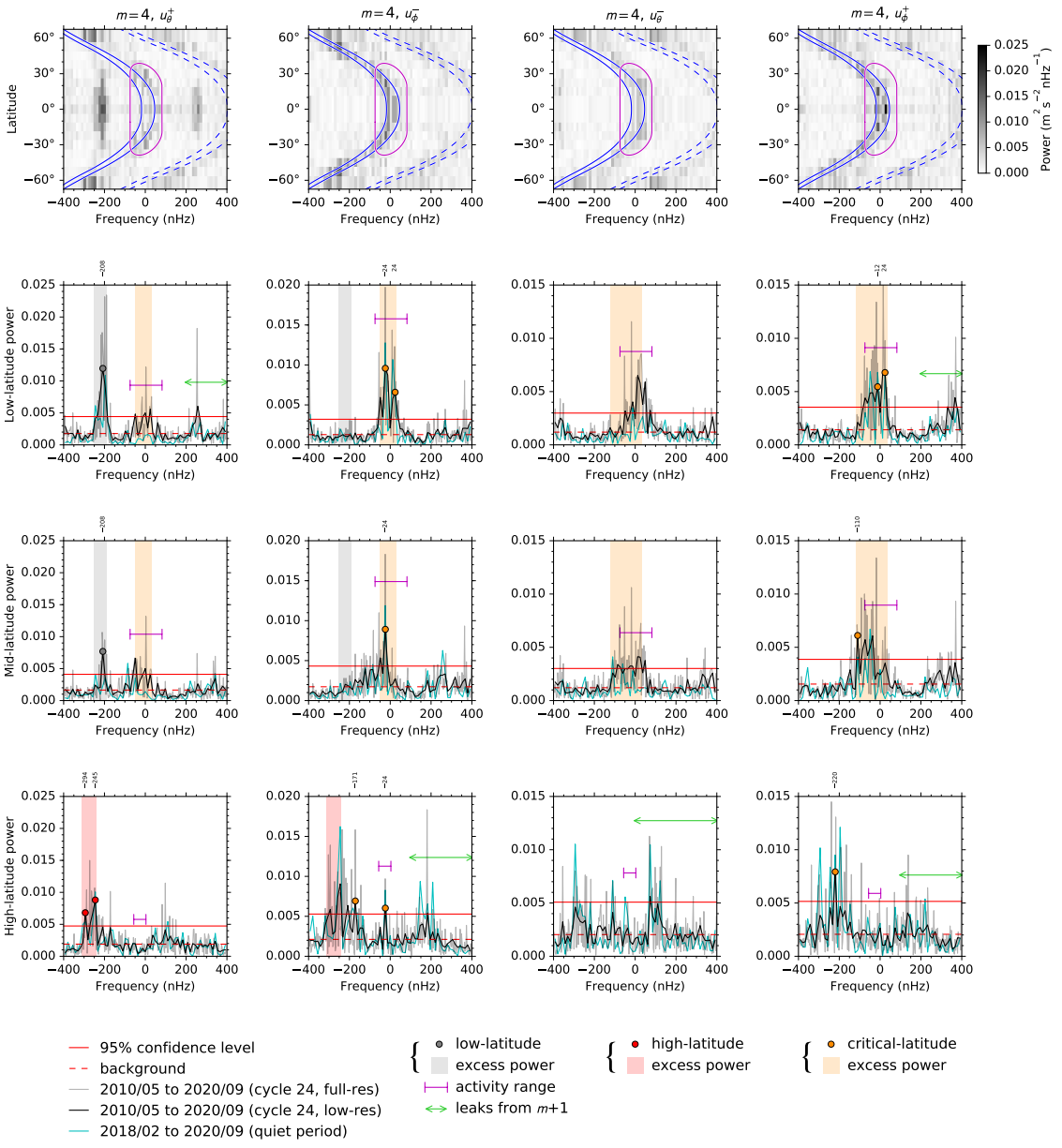

Figure 2.13: Same as Fig. 2.10, but for $m = 4$.

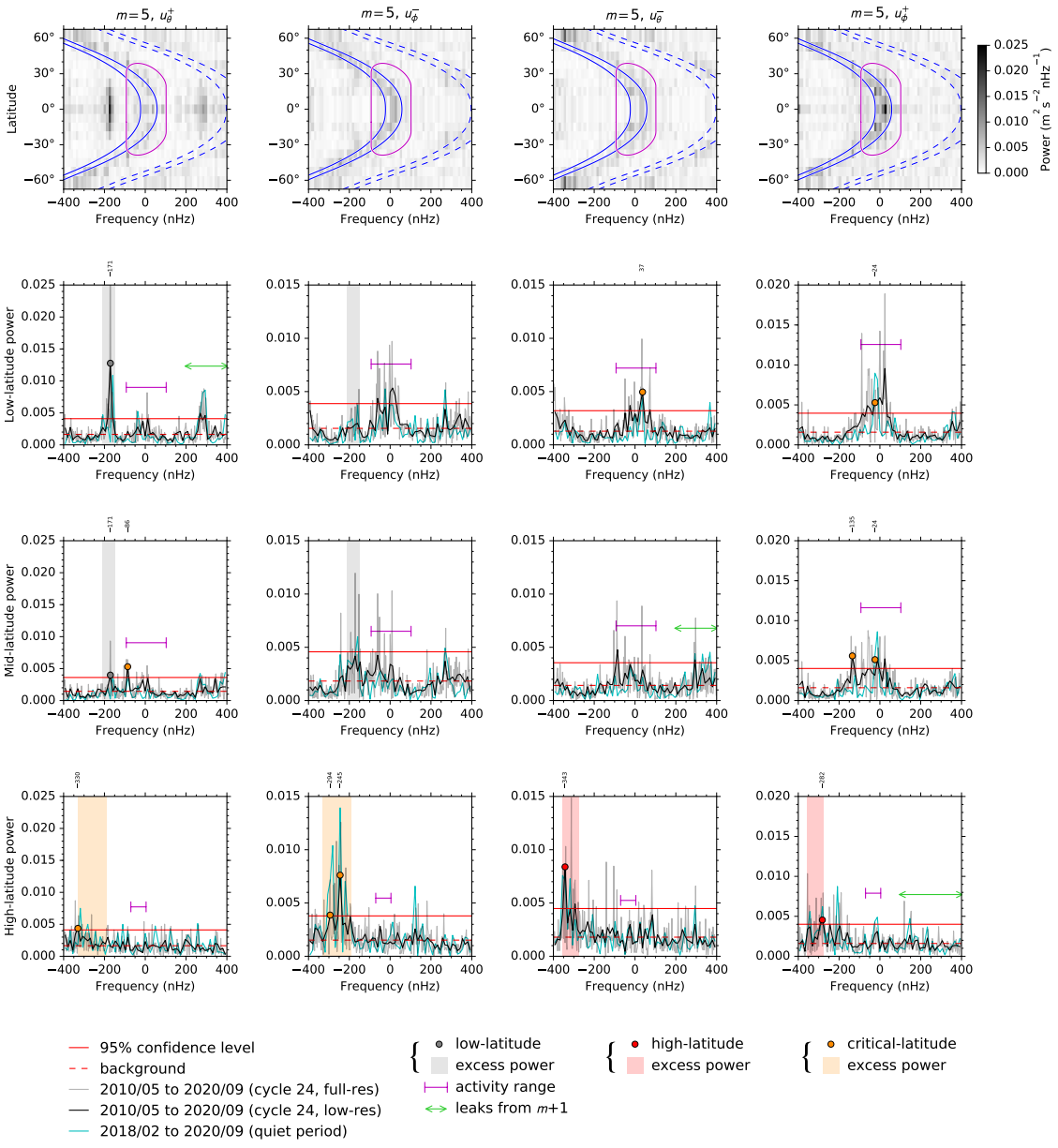

Figure 2.14: Same as Fig. 2.10, but for $m = 5$.

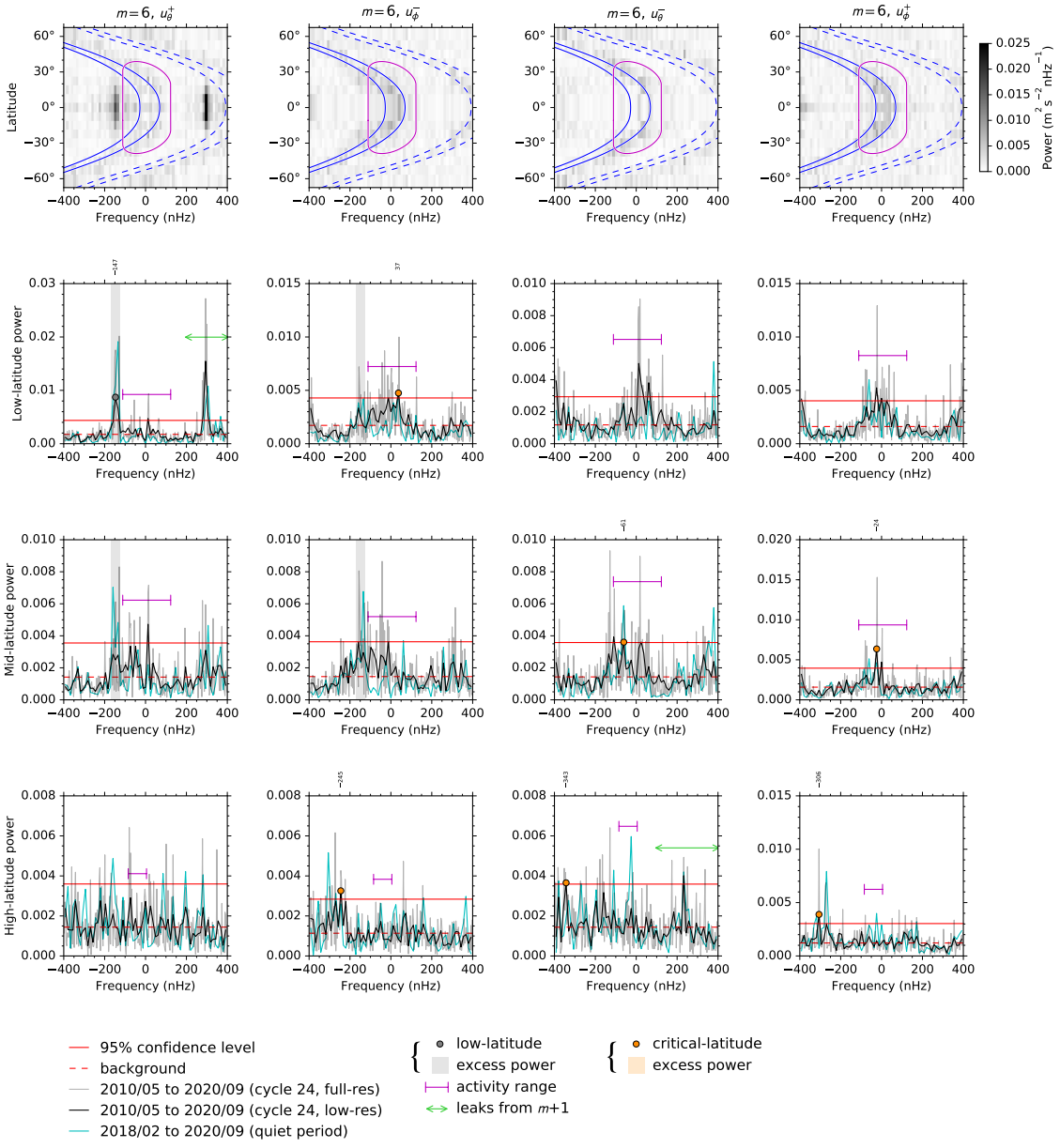

Figure 2.15: Same as Fig. 2.10, but for $m = 6$.

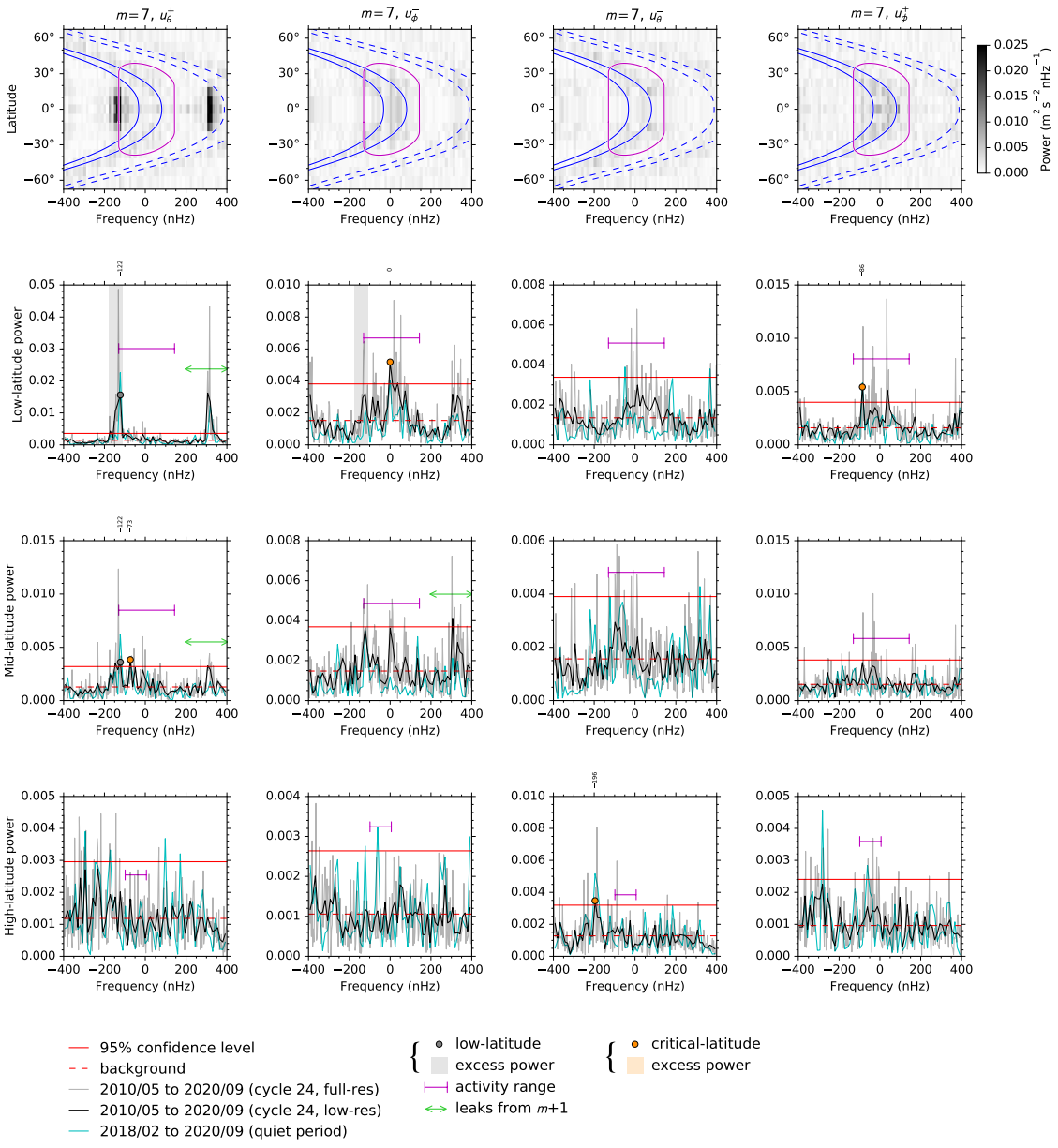

Figure 2.16: Same as Fig. 2.10, but for $m = 7$.

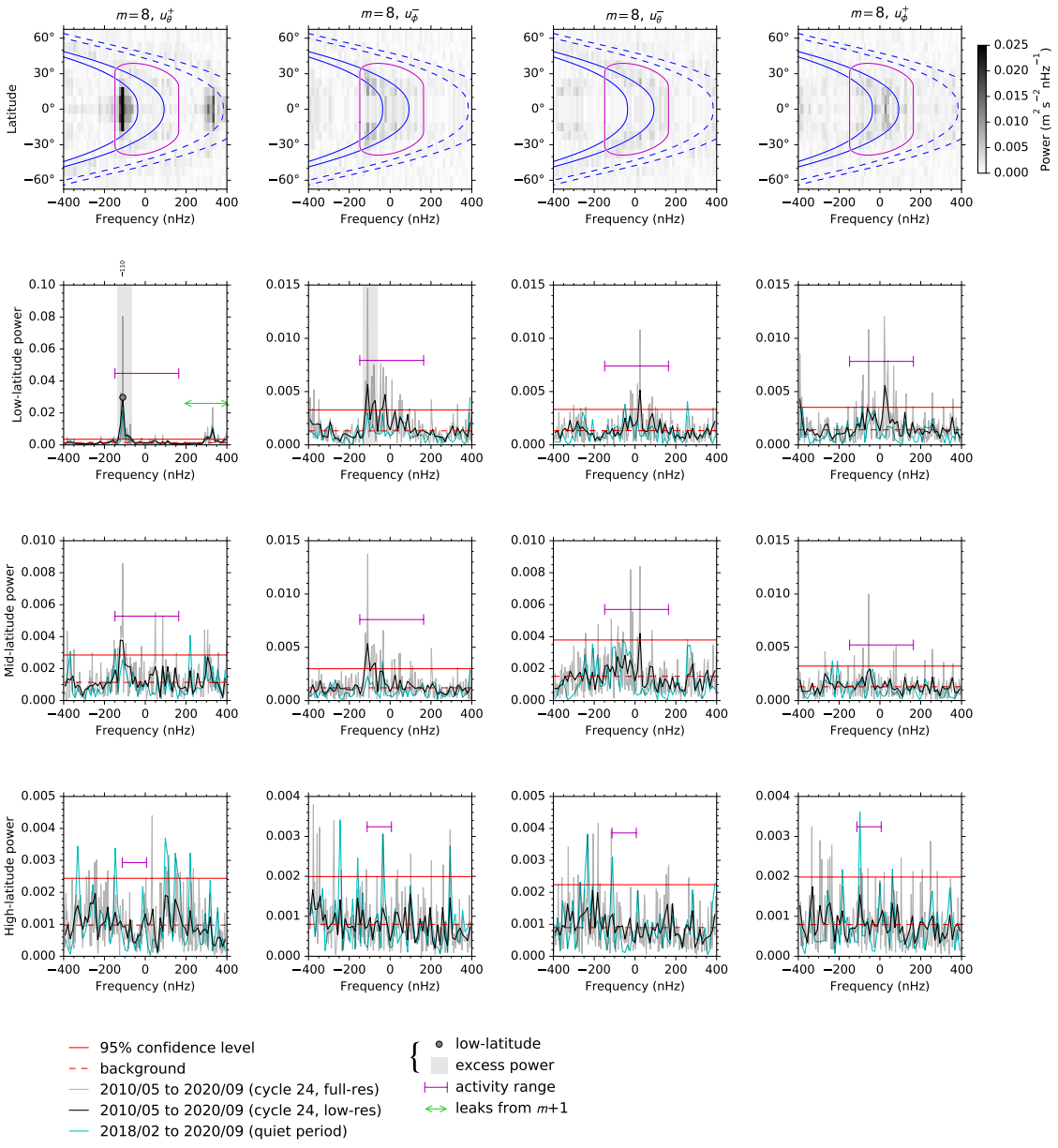

Figure 2.17: Same as Fig. 2.10, but for $m = 8$.

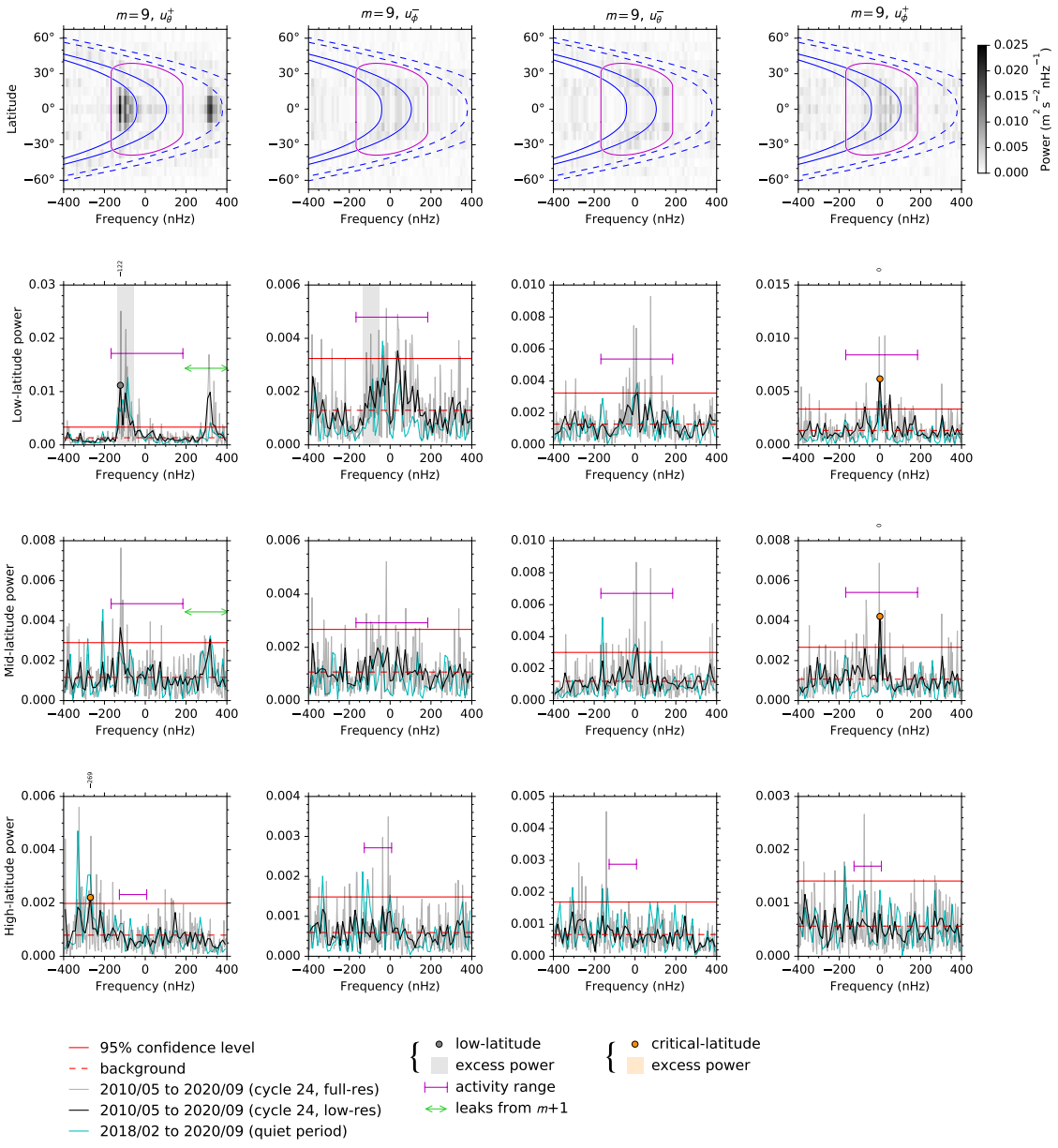

Figure 2.18: Same as Fig. 2.10, but for $m = 9$.

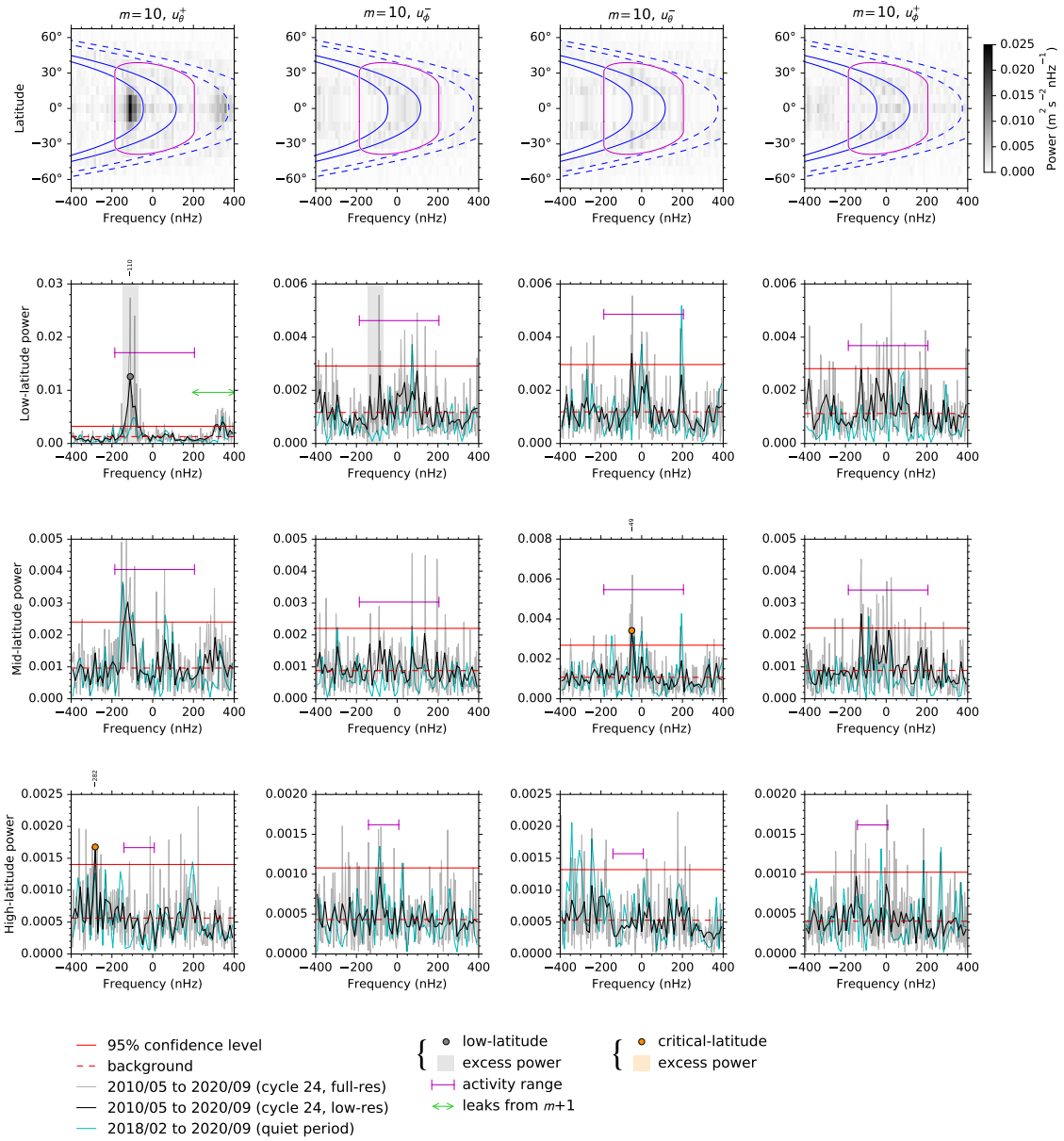

Figure 2.19: Same as Fig. 2.10, but for $m = 10$.

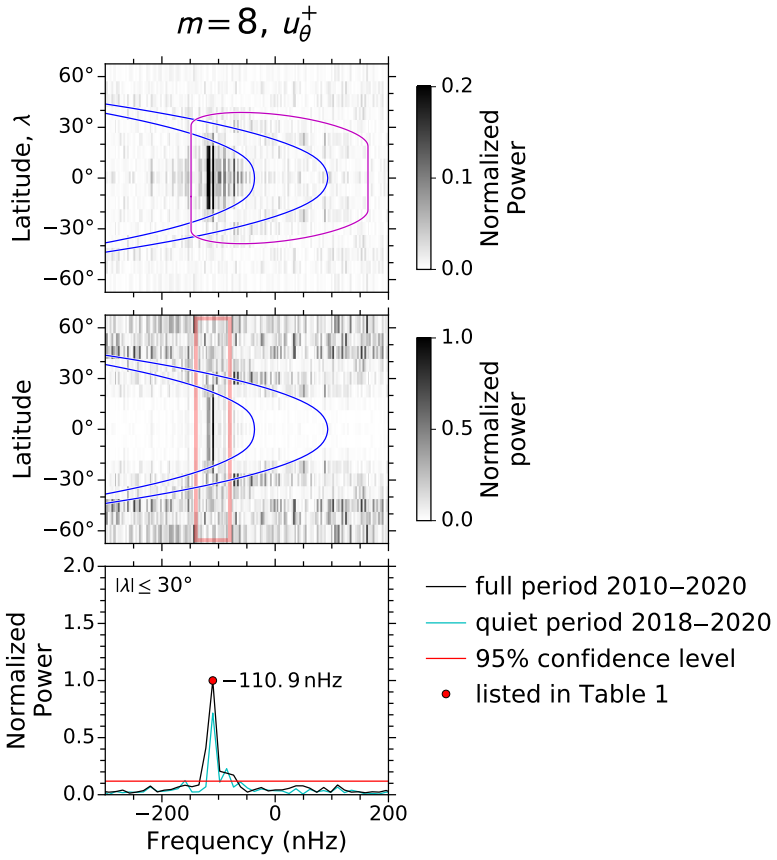

Figure 2.20: Same as Fig. 2.1, but for the $m = 8$ equatorial Rossby mode. In the top plot, it is important to notice the range of excess power at low latitudes, below the critical latitudes at the surface.

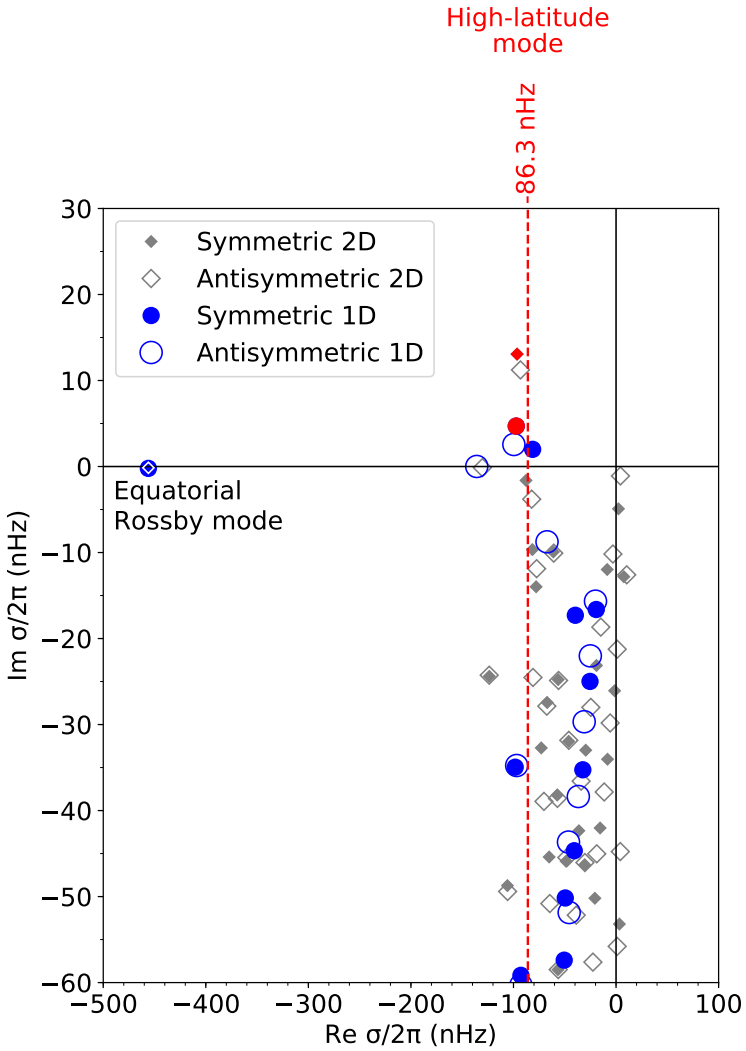

Figure 2.21: Eigenfrequencies in the complex plane for $m = 1$ from the 2D solver ($\delta = 0$, $\nu_t = 250$ km^2 s^{-1}) and the 1D solver ($\nu_t = 250$ km^2 s^{-1}). Modes with positive imaginary frequencies are self-excited (unstable). The red vertical line shows the observed frequency of the high-latitude symmetric mode at −86.3 nHz. The red symbols indicate the modes from the models, which have frequencies and surface eigenfunctions close to those observed.

3 Linear analysis of low-frequency modes in the convection zone

Abstract

On the one hand, several types of global-scale inertial modes of oscillation have been observed on the Sun. They include the equatorial Rossby modes, critical-latitude modes, and high-latitude modes. On the other hand, the columnar convective modes (predicted by simulations; also known as banana cells or thermal Rossby waves) remain elusive. We aim to investigate the influence of turbulent diffusivities, non-adiabatic stratification, differential rotation, and a latitudinal entropy gradient on the linear global modes of the rotating solar convection zone. We solve numerically for the eigenmodes of a rotating compressible fluid inside a spherical shell. The model takes into account the solar stratification, turbulent diffusivities, differential rotation (determined by helioseismology), and the latitudinal entropy gradient. As a starting point, we restrict ourselves to a superadiabaticity and turbulent diffusivities that are uniform in space. We identify modes in the inertial frequency range including the columnar convective modes, as well as modes of mixed character. The corresponding mode dispersion relations and eigenfunctions are computed for azimuthal orders $m \leq 16$. The three main results are as follows. Firstly, we find that, for $m \gtrsim 5$, the radial dependence of the equatorial Rossby modes with no radial node ($n = 0$) is radically changed from the traditional expectation (r^m) for turbulent diffusivities $\gtrsim 10^{12}$ cm^2 s^{-1}. Secondly, we find mixed modes, i.e. modes that share properties of the equatorial Rossby modes with one radial node ($n = 1$) and the columnar convective modes, which are not substantially affected by turbulent diffusion. Thirdly, we show that the $m = 1$ high-latitude mode in the model is consistent with the solar observations when the latitudinal entropy gradient corresponding to a thermal wind balance is included (baroclinally unstable mode). To our knowledge, this work is the first realistic eigenvalue calculation of the global modes of the rotating solar convection zone. This calculation reveals a rich spectrum of modes in the inertial frequency range, which can be directly compared to the observations. In turn, the observed modes can inform us about the solar convection zone.

This chapter reproduces the article *Theory of solar oscillations in the inertial frequency range: Linear modes of the convection zone* by Y. Bekki, R.H. Cameron, and L. Gizon, published in Astronomy and Astrophysics 662, A16 (2022). DOI: https://doi.org/10.1051/0004-6361/202243164. Contribution: Y. Bekki did most of the work.

3.1 Introduction

Using 10 years of observations from the Helioseismic and Magnetic Imager (HMI) onboard the Solar Dynamics Observatory (SDO), Gizon et al. (2021) discovered that the Sun supports a large number of global modes of inertial oscillations. The restoring force for these inertial modes is the Coriolis force, and thus the modes have periods comparable to the solar rotation period ($\sim$ 27 days). The inertial modes can potentially be used as a tool to probe the interior of the Sun, because they are sensitive to properties of the deep convection zone that the p modes are insensitive to. In order to achieve this goal, we need a better understanding of the mode physics.

3.1.1 Solar inertial modes

The low frequency modes of solar oscillation have been described in a rotating frame (angular velocity $\Omega_{\rm ref}$). Because the Sun is essentially symmetric about its rotation axis, the velocity of each mode in the rotating frame has the form $\boldsymbol{v}(r,\theta)\exp\left[\mathrm{i}(m\phi-\omega t)\right]$, where r is the radius, θ is the colatitude, ϕ is the longitude, m is the azimuthal order, and ω is the mode eigenfrequency. Gizon et al. (2021) provide all observed eigenfrequencies ω for each m, and the eigenfunctions (v_θ and v_ϕ at the surface) for a few selected modes.

The first family of inertial modes observed on the Sun consists of the quasi-toroidal equatorial Rossby modes (Löptien et al. 2018). They are analogous to the sectoral r modes described by, e.g., Papaloizou and Pringle (1978), Smeyers et al. (1981), and Saio (1982). On the Sun these modes have $3 \le m \le 15$ with a well-defined dispersion relation close to $\omega = -2\Omega_{\rm ref}/(m+1)$, where ω is the mode angular frequency and $\Omega_{\rm ref}/2\pi = 453.1$ nHz is the equatorial rotation rate at the surface. For positive m, a negative ω indicates retrograde propagation. There have been several follow-up studies that confirm these observations (e.g., Liang et al. 2019, Hanasoge and Mandal 2019, Proxauf et al. 2020, Mandal and Hanasoge 2020, Hanson et al. 2020, Mandal et al. 2021, Gizon et al. 2021). Using a one-dimensional β-plane model with a parabolic shear flow and viscosity, Gizon et al. (2020b) show that these modes, among others, are affected by differential rotation and are trapped between the critical latitudes where the phase speed of a mode is equal to the local rotational velocity. Fournier et al. (2022) extended this model to a spherical geometry using a realistic differential rotation model and found that some Rossby modes can be unstable for $m \le 3$.

Gizon et al. (2021) also report a family of modes at mid-latitudes that are localized near their critical latitudes. Several tens of critical-latitude modes have been identified in the range $m \le 10$. Another family of inertial modes introduced by the Sun's differential rotation are the high-latitude modes (Gizon et al. 2021). The highest amplitude mode ($\sim$ 10 - 20 m s^{-1} above 50° latitude) is the $m = 1$ mode with north-south antisymmetric longitudinal velocity v_ϕ with respect to the equator. This $m = 1$ mode was identified by Gizon et al. (2021) using linear calculations in two-dimensional model, which are further discussed in this chapter and Fournier et al. (2022). It corresponds to the spiral-like velocity feature reported at high latitudes by Hathaway et al. (2013), although it was there reported as giant-cell convection.

The equatorial-Rossby and high-latitude modes involve mostly toroidal motions with a radial velocity which is small compared to the horizontal velocity components. Non-

toroidal inertial modes have also been theoretically studied, mainly for incompressible fluids. These modes tend to be localized onto so-called attractors, closed periodic orbits of rays reflecting off the spherical boundaries (Maas and Lam 1995, Rieutord and Valdettaro 1997, Rieutord et al. 2001, Rieutord and Valdettaro 2018, Sibgatullin and Ermanyuk 2019). They are also strongly affected by critical latitudes when differential rotation is included (e.g., Baruteau and Rieutord 2013, Guenel et al. 2016).

3.1.2 Columnar convective modes

In numerical simulations of solar-like rotating convection, equatorial convective columns aligned with the rotation axis are prominent (e.g., Miesch et al. 2008, Bessolaz and Brun 2011, Matilsky et al. 2020). They are known as "Busse columns" (after Busse 1970), or "thermal Rossby waves", or "banana cells" in the literature. We call them "columnar convective modes" in the rest of this paper. These convective columns propagate in the prograde direction owing either to the "topographic β-effect" originating from the geometrical curvature (e.g., Busse 2002) or to the "compressional β-effect" originating from the strong density stratification (Ingersoll and Pollard 1982, Evonuk 2008, Glatzmaier et al. 2009, Evonuk and Samuel 2012, Verhoeven and Stellmach 2014). Glatzmaier and Gilman (1981) numerically derived the dispersion relation and the radial eigenfunctions of these convective modes using a one-dimensional cylinder model. They showed that the fundamental ($n = 0$) mode is the fastest of these prograde propagating modes with an eigenfunction that is localized near the surface, where the compressional β-effect is strongest.

In the parameter regime of the various numerical simulations, the columnar convective modes are the structures that are the most efficient to transport thermal energy upward under the rotational constraint (e.g., Gilman 1986, Miesch et al. 2000, Brun et al. 2004, Miesch et al. 2008, Käpylä et al. 2011, Gastine et al. 2013, Hotta et al. 2015b, Featherstone and Hindman 2016a, Matilsky et al. 2020, Hindman et al. 2020). Furthermore, it is often argued that these convective modes play a critical role in transporting the angular momentum equatorward to maintain the differential rotation of the Sun (e.g., Gilman 1986, Miesch et al. 2000, Balbus et al. 2009). The dominant columnar convective modes seen in simulations have not been detected in the velocity field at the surface of the Sun. However, we will show in this paper that some retrograde inertial modes have a mixed character and share some properties with columnar convection.

3.1.3 Focus of this study

In this paper, we study the properties of the equatorial Rossby modes, the high-latitude inertial modes, and the columnar convective modes in the linear regime. We are mainly interested in the effects of turbulent diffusion, solar differential rotation, and non-adiabatic stratification on these modes. Note that the critical-latitude modes, which are discussed by Fournier et al. (2022), will not be dealt with in depth in this paper.

Firstly, we will show that, when the turbulent viscosity is above approximately 10^{12} cm^2 s^{-1}, the equatorial Rossby modes with no radial node ($n = 0$) strongly depart from the expected r^m dependence and the radial vorticity at the surface is no longer maximum at the equator at azimuthal wavenumbers $m \gtrsim 5$. Secondly, we report a new class of modes

with frequencies close to that of the classical Rossby modes. They share properties of both equatorial Rossby modes and convective modes. Thirdly, we provide a physical explanation for the properties of the $m = 1$ high latitude modes in terms of the baroclinic instability due to the latitudinal entropy gradient in the convection zone.

The organization of the paper is as follows. In §3.2 we specify the linearized equations and solve the eigenvalue problem. The low-frequency modes are discussed in §3.3 for the inviscid, adiabatically stratified, and uniformly-rotating case. Then, the effects of turbulent diffusion and a non-adiabatically stratified background are discussed in §3.4 and §3.5. We discuss how the solar differential rotation and the associated baroclinicity affect the mode properties in §3.6. The results are summarized in §3.7.

3.2 Eigenvalue problem

In order to investigate the properties of various inertial modes in the Sun, a new numerical code has been developed. We consider the linearized fully-compressible hydrodynamic equations in a spherical coordinate (r, θ, ϕ).

3.2.1 Linearized equations

The linearized equations of motion, continuity, and energy conservation are:

$$\frac{\partial \boldsymbol{v}}{\partial t} = -\frac{\nabla p_1}{\rho_0} - \frac{\rho_1}{\rho_0} g \boldsymbol{e}_r - (\Omega - \Omega_0)\frac{\partial \boldsymbol{v}}{\partial \phi} - 2\Omega \boldsymbol{e}_z \times \boldsymbol{v} - r\sin\theta\, \boldsymbol{v}\cdot\nabla\Omega + \frac{1}{\rho_0}\nabla\cdot\mathcal{D}, \tag{3.1}$$

$$\frac{\partial \rho_1}{\partial t} = -\nabla\cdot(\rho_0 \boldsymbol{v}) - (\Omega - \Omega_0)\frac{\partial \rho_1}{\partial \phi}, \tag{3.2}$$

$$\frac{\partial s_1}{\partial t} = c_{\rm p}\delta\frac{v_r}{H_p} - \frac{v_\theta}{r}\frac{\partial s_0}{\partial \theta} - (\Omega - \Omega_0)\frac{\partial s_1}{\partial \phi} + \frac{1}{\rho_0 T_0}\nabla\cdot(\kappa\rho_0 T_0 \nabla s_1), \tag{3.3}$$

where, $\boldsymbol{v} = (v_r, v_\theta, v_\phi)$ is the 1st-order velocity perturbation. In this paper, we only consider the differential rotation for the mean flow and ignore meridional circulation. Thus, the background velocity is $\boldsymbol{U} = r\sin\theta(\Omega - \Omega_0)\boldsymbol{e}_\phi$. Here, Ω is a function of r and θ and denotes the rotation rate in the Sun's convection zone, and Ω_0 is the rotation rate of the observer's frame. Note that, in this paper, we start our by analysing the case without differential rotation for simplicity and study the linear modes in the uniformly-rotating Sun. In this case, Ω_0 represents the rotation rate of the unperturbed background state. For the case with the solar differential rotation, we choose to use the Carrington rotation rate $\Omega_0/2\pi = 456.0$ nHz.

The unperturbed model is given by p_0, ρ_0, T_0, g, and H_p which are the pressure, density, temperature, gravitational acceleration, and pressure scale height of the background state. The background is assumed to be spherically symmetric and in an adiabatically-stratified hydrostatic balance. All of these variables are functions of r alone. We use the same analytical model as Rempel (2005) and Bekki and Yokoyama (2017) for the background stratification which nicely mimics the solar model S (Christensen-Dalsgaard et al.

1996b):

$$g(r) = g_{\rm bc}\left(\frac{r}{r_{\rm min}}\right)^{-2}, \tag{3.4}$$

$$\rho_0(r) = \rho_{\rm bc}\left[1 + \frac{\gamma-1}{\gamma}\frac{r_{\rm min}}{H_{\rm bc}}\left(\frac{r_{\rm min}}{r} - 1\right)\right]^{1/\gamma-1}, \tag{3.5}$$

$$p_0(r) = p_{\rm bc}\left[1 + \frac{\gamma-1}{\gamma}\frac{r_{\rm min}}{H_{\rm bc}}\left(\frac{r_{\rm min}}{r} - 1\right)\right]^{\gamma/\gamma-1}, \tag{3.6}$$

$$T_0(r) = T_{\rm bc}\left[1 + \frac{\gamma-1}{\gamma}\frac{r_{\rm min}}{H_{\rm bc}}\left(\frac{r_{\rm min}}{r} - 1\right)\right], \tag{3.7}$$

where $\rho_{\rm bc}$, $p_{\rm bc}$, $T_{\rm bc}$, $g_{\rm bc}$ and $H_{\rm bc} = p_{\rm bc}/(\rho_{\rm bc} g_{\rm bc})$ are the values of density, pressure, temperature, and pressure scale height at the base of the convection zone. We use the solar values $\rho_{\rm bc} = 0.2$ g cm^{-3}, $p_{\rm bc} = 6\times10^{13}$ dyn cm^{-2}, $T_{\rm bc} = 1.82\times10^{6}$ K, $g_{\rm bc} = 5.2\times10^{4}$ cm s^{-2}, and $H_{\rm bc} = 0.0826 R_\odot$. The variables with subscript 1, p_1, ρ_1, and s_1, represent the 1st-order perturbations of pressure, density, and entropy that are associated with velocity perturbation $\boldsymbol{v}$. Here, to close the equations, the linearized equation of state is used

$$\frac{p_1}{p_0} = \gamma\frac{\rho_1}{\rho_0} + \frac{s_1}{c_{\rm v}}, \tag{3.8}$$

where $c_{\rm p} \approx 4.2\times10^{8}$ erg g^{-1} K^{-1} and $c_{\rm v} \approx 2.5\times10^{8}$ erg g^{-1} K^{-1} denote the specific heats at constant pressure and volume in the Sun's convection zone, respectively. The specific heat ratio is given as $\gamma\ (= c_{\rm p}/c_{\rm v}) = 5/3$.

Although the background is approximated to be adiabatic, we can still introduce a small deviation from the adiabatic stratification in terms of the superadiabaticity $\delta = \nabla - \nabla_{\rm ad}$, where $\nabla = {\rm d}\ln T/{\rm d}\ln p$ is the double-logarithmic temperature gradient. In the solar convection zone, superadiabaticity is estimated as $\delta \approx 10^{-6}$ (e.g., Ossendrijver 2003). Also, when the solar differential rotation is included, we may add a latitudinal entropy variation $\partial s_0/\partial\theta$ that is associated with the thermal wind balance of the differential rotation (e.g., Rempel 2005, Miesch et al. 2006, Brun et al. 2011).

We assume that the viscous stress tensor, $\mathcal{D}$, is given by

$$\mathcal{D}_{ij} = \rho_0\nu\left[\mathcal{S}_{ij} - \frac{2}{3}(\nabla\cdot\boldsymbol{v})\delta_{ij}\right], \tag{3.9}$$

where δ_{ij} is the Kronecker-delta and $\mathcal{S}_{ij}$ denotes the deformation tensor given in the spher-

ical coordinate as

$$\mathcal{S}_{rr} = 2\frac{\partial v_r}{\partial r}, \tag{3.10}$$

$$\mathcal{S}_{\theta\theta} = \frac{2}{r}\left(\frac{\partial v_\theta}{\partial \theta} + v_r\right), \tag{3.11}$$

$$\mathcal{S}_{\phi\phi} = \frac{2}{r\sin\theta}\left(\frac{\partial v_\phi}{\partial \phi} + v_r \sin\theta + v_\theta \cos\theta\right), \tag{3.12}$$

$$\mathcal{S}_{r\theta} = \mathcal{S}_{\theta r} = \frac{1}{r}\frac{\partial v_\phi}{\partial \theta} + \frac{\partial v_\theta}{\partial r} - \frac{v_\theta}{r}, \tag{3.13}$$

$$\mathcal{S}_{r\phi} = \mathcal{S}_{\phi r} = \frac{1}{r\sin\theta}\frac{\partial v_r}{\partial \phi} + \frac{\partial v_\phi}{\partial r} - \frac{v_\phi}{r}, \tag{3.14}$$

$$\mathcal{S}_{\theta\phi} = \mathcal{S}_{\phi\theta} = \frac{1}{r}\left\{\frac{1}{\sin\theta}\frac{\partial v_\theta}{\partial \phi} + \left(\frac{\partial v_\phi}{\partial \theta} - v_\phi\frac{\cos\theta}{\sin\theta}\right)\right\}. \tag{3.15}$$

ν and κ are the viscous and thermal diffusivities, respectively.

3.2.2 Eigenvalue problem

We assume that the ϕ and t dependence of all the perturbations $\boldsymbol{v}$, ρ_1, p_1, and s_1 is given by the waveform $\exp[\mathrm{i}(m\phi - \omega t)]$, where m is the azimuthal order (an integer) and ω is the complex angular frequency. With this representation, Eqs. (3.1)–(3.3) give

$$\begin{aligned}\omega v_r = &-\mathrm{i}\frac{\partial}{\partial r}\left[C_\mathrm{s}^2\left(\frac{\rho_1}{\rho_0} + \frac{s_1}{c_\mathrm{p}}\right)\right] + \mathrm{i}\frac{g}{c_\mathrm{p}}s_1 + 2\mathrm{i}\Omega\sin\theta v_\phi \\ &+m(\Omega - \Omega_0)v_r + \frac{\mathrm{i}}{\rho_0}(\nabla\cdot\mathcal{D})_r,\end{aligned} \tag{3.16}$$

$$\omega v_\theta = -\frac{\mathrm{i}}{r}\frac{\partial}{\partial\theta}\left[C_\mathrm{s}^2\left(\frac{\rho_1}{\rho_0} + \frac{s_1}{c_\mathrm{p}}\right)\right] + 2\mathrm{i}\Omega\cos\theta\, v_\phi + m(\Omega - \Omega_0)v_\theta + \frac{\mathrm{i}}{\rho_0}(\nabla\cdot\mathcal{D})_\theta, \tag{3.17}$$

$$\begin{aligned}\omega v_\phi = &-\frac{mC_\mathrm{s}^2}{r\sin\theta}\left(\frac{\rho_1}{\rho_0} + \frac{s_1}{c_\mathrm{p}}\right) - 2\mathrm{i}\Omega(v_r\sin\theta + v_\theta\cos\theta) + m(\Omega - \Omega_0)v_\phi \\ &-\mathrm{i}r\sin\theta\left(v_r\frac{\partial\Omega}{\partial r} + \frac{v_\theta}{r}\frac{\partial\Omega}{\partial\theta}\right) + \frac{\mathrm{i}}{\rho_0}(\nabla\cdot\mathcal{D})_\phi,\end{aligned} \tag{3.18}$$

$$\omega\rho_1 = -\mathrm{i}\rho_0\nabla\cdot\boldsymbol{v} + \mathrm{i}\frac{\rho_0}{H_\rho}v_r + m(\Omega - \Omega_0)\rho_1, \tag{3.19}$$

$$\omega s_1 = \mathrm{i}\frac{c_\mathrm{p}\delta}{H_p}v_r - \frac{\mathrm{i}}{r}\frac{\partial s_0}{\partial\theta}v_\theta + m(\Omega - \Omega_0)s_1 - \frac{\mathrm{i}}{\rho_0 T_0}\nabla\cdot(\kappa\rho_0 T_0\nabla s_1), \tag{3.20}$$

where $C_\mathrm{s} = (\gamma p_0/\rho_0)^{1/2}$ is the sound speed and $c_\mathrm{p} = \gamma c_\mathrm{v}$ is the constant specific heat at constant pressure. Here, the longitudinal velocity v_ϕ, density perturbation ρ_1, and entropy perturbation s_1 are out of phase with the meridional components of velocity (v_r and v_θ) in the inviscid limit ($\nu = \kappa = 0$).

Equations (3.16)–(3.20) can be combined into an eigenvalue problem

$$\omega\boldsymbol{V} = M\boldsymbol{V}, \tag{3.21}$$

where

$$\boldsymbol{V} = \begin{pmatrix} v_r \\ v_\theta \\ v_\phi \\ \rho_1 \\ s_1 \end{pmatrix} \tag{3.22}$$

and M is the linear differential operator represented by the right-hand side of the Eqs. (3.16)–(3.20). The operator M depends on azimuthal order m and the model parameters such as differential rotation $\Omega(r, \theta)$, superadiabaticity δ, and diffusivities ν and κ.

3.2.3 Boundary conditions

In this study, we confine our numerical domain from $r_{\rm min} = 0.71 R_\odot$ to $r_{\rm max} = 0.985 R_\odot$ in the radial direction to avoid the strong density stratification near the solar surface and gravity modes in the radiative interior. Because of viscosity, in this problem we have four second-order (in both the radial and latitudinal directions) PDEs and one first-order PDE. Equation (3.19) does not increase the order of the system as ρ_1 can be eliminated from the system without increasing the order of the other equations. Thus eight boundary conditions are required in the radial direction (four at the top, four at the bottom). At the top and bottom, we use impenetrable horizontal stress-free conditions for the velocity and assume there is no entropy flux ($\propto \kappa \partial s_1 / \partial r$) across the boundary:

$$v_r = 0, \quad \frac{\partial}{\partial r}\left(\frac{v_\theta}{r}\right) = \frac{\partial}{\partial r}\left(\frac{v_\phi}{r}\right) = 0, \quad \frac{\partial s_1}{\partial r} = 0. \tag{3.23}$$

All latitudes are covered in the numerical scheme, from the north pole ($\theta = 0$) to the south pole ($\theta = \pi$). We need another eight boundary conditions in the θ direction. For non-axisymmetric cases ($m \neq 0$), at the poles we impose

$$v_r = v_\theta = v_\phi = 0, \quad s_1 = 0, \tag{3.24}$$

to make the quantities single valued. For the axisymmetric case ($m = 0$), at both poles we assume instead

$$\frac{\partial v_r}{\partial \theta} = v_\theta = 0, \quad \frac{\partial}{\partial \theta}\left(\frac{v_\phi}{\sin\theta}\right) = 0, \quad \frac{\partial s_1}{\partial \theta} = 0. \tag{3.25}$$

3.2.4 Numerical scheme

We numerically solve the above eigenvalue problem using a finite differencing method in the meridional plane. We use a spatially-uniform grids. The grids for v_ϕ, ρ_1, and s_1 are staggered grids by half a grid point in radius for v_r and half a grid point in colatitude for v_θ (following Gilman 1975), as is illustrated in Fig. 3.1. Spatial derivatives are evaluated with a centered second-order accurate scheme. By converting the two dimensional grid (N_r, N_θ) into one dimensional array with the size $N_r N_\theta$ for all variables, $\boldsymbol{V}$ is defined as a one dimensional vector with size $\sim 5 N_r N_\theta$. Once the boundary conditions are properly set, M can be constructed as a two-dimensional complex matrix with the size approximately

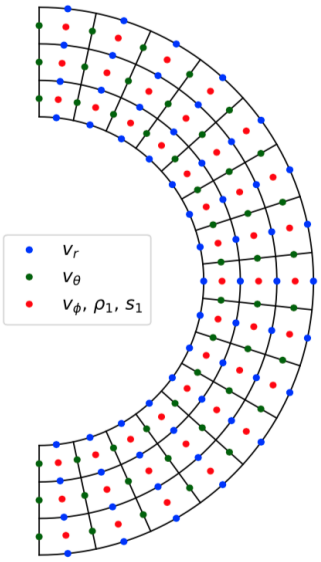

Figure 3.1: Layout of the staggered grid used to solve the eigenvalue equation. The grid locations where v_ϕ, ρ_1, and s_1 are defined are denoted by red circles. The blue and green circles represent the grid locations of v_r and v_θ, respectively. The grid resolution is reduced for a visualization purpose.

$(5N_rN_\theta \times 5N_rN_\theta)$. This method is similar to that of Guenther and Gilman (1985). In practice, each element of M can be computed by substituting a corresponding unit vector $\boldsymbol{V}$ into the right-hand side of the Eqs. (3.16)–(3.20). In most of the calculations, we use the grid resolution of $(N_r, N_\theta) = (16, 72)$. We have also carried out higher-resolution calculations with $(N_r, N_\theta) = (24, 180)$ for a uniform rotation case to check the grid convergence of the results. When the grid resolution is increased, the total number of eigenmodes increases accordingly. The additional modes have higher radial and latitudinal wavenumbers and are more finely structured. For the interpretation of the large-scale modes which have been observed on the Sun, the results are converged with $(N_r, N_\theta) = (16, 72)$.

We use the LAPACK routines (Anderson et al. 1999) to numerically compute the eigenvalues and eigenvectors of $M(m, \nu, \kappa, \delta, \Omega)$, corresponding to the mode frequencies ω and the eigenfunctions $(v_r, v_\theta, v_\phi, \rho_1, s_1)$ of linear modes in the Sun. In this study, we limit the range of azimuthal orders to $m \geq 0$ and allow the real frequency to take a negative value. This means that $\Re[\omega] < 0$ corresponds to retrograde-propagating modes and $\Im[\omega] > 0$ corresponds to exponentially growing modes.

3.2.5 Example spectrum for uniform rotation

For each m, there are $5N_rN_\theta$ eigensolutions with frequencies ω and eigenfunctions $\boldsymbol{V}$. As an example, we show the typical distribution of the output eigenfrequencies in a complex plane for the case with $m = 1$, $\delta = 10^{-6}$ (weakly superadiabatic), and $\nu = \kappa = 2 \times 10^{12}$ cm^2 s^{-1} in Fig. 3.2. Note that the differential rotation is not included here for simplicity; the uniform rotation rate Ω is equal to the Carrington rotation rate Ω_0.

The modes belong to one of several regions in the complex eigenfrequency spectrum.

The modes seen in Fig. 3.2a are acoustic modes (p modes) slightly damped due to the viscous and thermal diffusion. On this plot, the effect of rotation is not visible to the eye. In the rest of this paper, we focus on the low-frequency modes in the inertial frequency range. Inertial oscillations are confined within the range $|\Re[\omega]| < 2\Omega_0$ (e.g., Greenspan et al. 1968). Figure 3.2b shows the spectrum of inertial modes in the complex plane. The sectoral Rossby mode with no radial node ($n = 0$) is easy to identify by comparison with the analytical frequency $\omega = -2\Omega_0/(m + 1)$. Owing to the slightly superadiabatic background ($\delta > 0$), we can see that some modes have positive imaginary frequencies ($\Im[\omega] > 0$) at very low frequencies and thus are unstable. These convective modes are shown in Fig. 3.2c.

When the background is weakly subadiabatic (e.g., $\delta = -10^{-6}$), all the modes become stable ($\Im[\omega] < 0$) and some inertial modes are partially mixed with gravity modes (g modes). When $\Omega_0 = 0$, the modes are either purely convective modes or purely g modes depending on the sign of δ as shown in Fig. 3.3. The frequency of the g modes depends on δ and, depending on Ω_0, can lie in the inertial range.

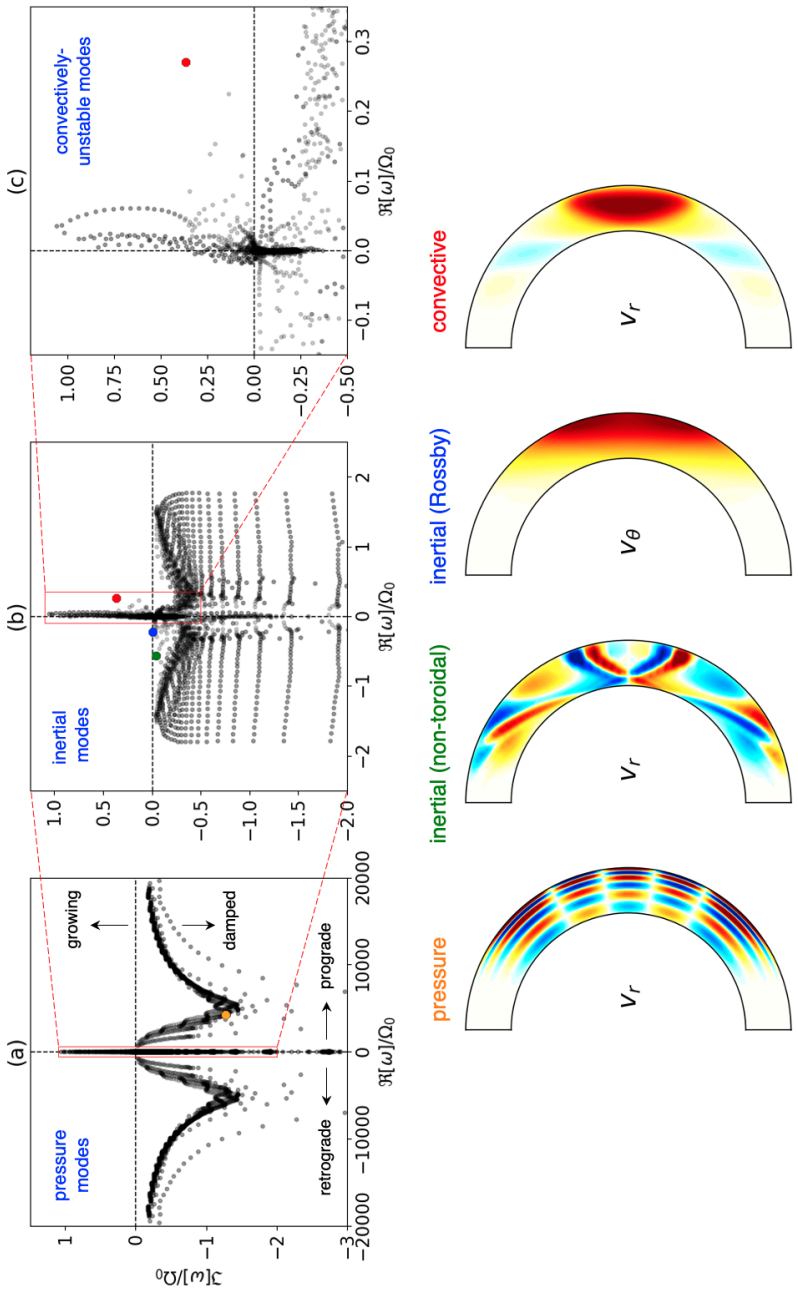

Figure 3.2: Upper panels: Complex eigenfrequencies ω in the co-rotating frame for $m = 8$ in the case of uniform rotation ($\Omega = \Omega_0$), a weakly superadiabatic stratification ($\delta = 10^{-6}$), and moderate turbulent viscous and thermal diffusivities ($\nu = \kappa = 10^{11}$ cm^2 s^{-1}). Panel (a): Real frequencies in the range ±10 mHz showing the acoustic modes (p modes). Panel (b): Zoom-in focusing on the inertial range $|\Re[\omega]| < 2\Omega_0$. The blue dot shows the sectoral Rossby mode with no radial nodes. Panel (c): Zoom-in focusing on the convectively-unstable modes ($\Im[\omega] > 0$). Lower Panels: Example eigenfunctions corresponding to the few modes highlighted in the upper panels.

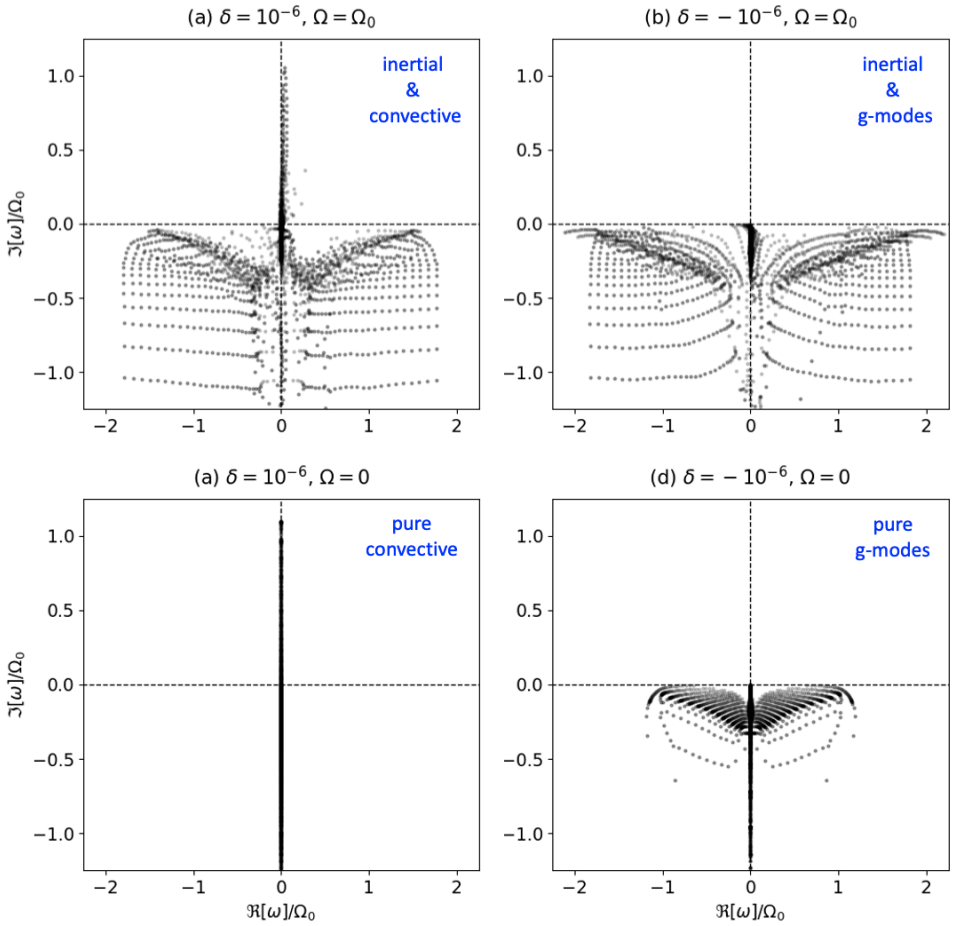

Figure 3.3: Eigenfrequency spectrum in the complex plane at $m = 8$ for (a) $\delta = 10^{-6}$, $\Omega = \Omega_0$, (b) $\delta = -10^{-6}$, $\Omega = \Omega_0$, (c) $\delta = 10^{-6}$, $\Omega = 0$, and (d) $\delta = -10^{-6}$, $\Omega = 0$, respectively. Here, Ω_0 is the Carrington rotation rate. Only inertial frequency range is shown. Upper and lower panels show the cases with and without uniform rotation. Left and right panels show the cases with superadiabatic and subadiabatic background. Panel (a) is the same as Fig. 3.2b.

3.3 Reference case: no diffusion, adiabatic stratification, uniform rotation

In this section, we report the results of an ideal case where turbulent viscous and thermal diffusivities are set to zero ($\nu = \kappa = 0$), the background is convectively neutral ($\delta = 0$), and no differential rotation is included ($\Omega(r, \theta) = \Omega_0$ and $\partial s_0/\partial\theta = 0$). We present the dispersion relations and eigenfunctions of various types of global-scale vorticity modes that might be relevant to the Sun. We will use the results of this ideal setup as references and the effects of turbulent diffusion, non-adiabatic stratification, and differential rotation will later be compared to these reference results.

In the inviscid case with uniform rotation, M is self adjoint, thus the physically-meaningful solutions must have real eigenfrequencies. We find about 10% of the eigenfrequencies to have a nonzero imaginary part; these correspond to numerical artifacts due to truncation errors, and the corresponding eigenfunctions have most of their power at high spatial frequencies. For the solutions with purely real eigenfrequencies, the eigenfunctions of v_r and v_θ have the same complex phase on each meridional plane, and those of v_ϕ, ρ_1 are 90° out of phase with respect to v_r and v_θ. In presenting the results in this section, we choose a meridional plane where v_r and v_θ are real.

In the following sections, we conduct a mode-by-mode analysis for the equatorial Rossby modes with no radial nodes ($n = 0$) and one radial node ($n = 1$), columnar convective modes (thermal Rossby waves) with both north-south symmetries, and the high-latitude modes with both north-south symmetries. Fundamental properties of these modes are summarized in Table 3.1. Their dispersion relations are presented in Table 3.2.

Table 3.1: Summary of the properties of the modes of the models discussed in this paper. Each row refers to a set of modes with different m values.

	Classification	peak location of kinetic energy	north-south symmetries v_r	v_θ	v_ϕ	propagation direction	sections discussed
	Equatorial Rossby ($n = 0$)	equator	A	S	A	retrograde	§ 3.3.1.1, § 3.4, § 3.6.1
	Equatorial Rossby ($n = 1$)	equator	A	S	A	retrograde	§ 3.3.1.2, § 3.6.1
"mixed"	Columnar convective (ζ_z-sym)	equator	S	A	S	prograde	§ 3.3.2.1, § 3.5
	Columnar convective (ζ_z-antisym)	equator	A	S	A	prograde	§ 3.3.2.2
	High latitude (ζ_z-sym)	near poles	S	A	S	retrograde	§ 3.3.3.1
	High latitude (ζ_z-antisym)	near poles	A	S	A	retrograde	§ 3.3.3.2, § 3.6.2

Note: The integer n denotes the number of radial nodes of v_θ at the equator for the Rossby modes. The north-south symmetries of the different components of the velocity are given in columns 3 to 6, where 'S' indicates the velocity component is symmetric across the equator and 'A' indicates the velocity component is antisymmetric across the equator. The propagation direction is for the uniformly rotating case, and is given in the rotating frame.

Table 3.2: Dispersion relations of the modes studied in this paper in the corotating frame for the case of uniform rotation ($\Omega = \Omega_0$), with $\nu = \kappa = 0$ and $\delta = 0$.

m	$\Re[\omega]/\Omega_0$					
	Equatorial Rossby modes		Columnar convective modes		High-latitude modes	
	$n = 0$	$n = 1$	v_ϕ sym.	v_ϕ asym.	v_ϕ sym.	v_ϕ asym.
0	–	−0.629	–	0.629	–	–
1	−0.999	−0.527	0.151	0.694	−0.303	−0.173
2	−0.666	−0.447	0.290	0.758	−0.293	−0.172
3	−0.499	−0.380	0.410	0.824	−0.258	−0.166
4	−0.399	−0.328	0.518	0.883	−0.216	−0.157
5	−0.333	−0.286	0.612	0.938	−0.181	−0.149
6	−0.285	−0.253	0.682	0.990	−0.161	−0.141
7	−0.249	−0.226	0.743	1.029	−0.144	−0.133
8	−0.222	−0.204	0.792	1.053	−0.131	−0.126
9	−0.199	−0.185	0.822	1.061	−0.121	−0.120
10	−0.181	−0.170	0.846	1.056	−0.111	−0.114
11	−0.166	−0.156	0.863	1.049	−0.103	−0.109
12	−0.153	−0.145	0.873	1.041	−0.096	−0.104
13	−0.142	−0.135	0.881	1.033	−0.092	−0.099
14	−0.133	−0.126	0.887	1.024	−0.089	−0.095
15	−0.124	−0.119	0.889	1.015	−0.085	−0.091
16	−0.117	−0.112	0.889	1.006	−0.083	−0.087

Note: For the equatorial Rossby modes, n denotes the number of radial nodes for v_θ at the equator. For the other two types modes, at fixed m, there are both modes with north-south symmetric and and antisymmetric v_ϕ. These different dispersion relations and their connections are plotted in Fig. 3.10.

3.3.1 Equatorial Rossby modes

In this section, we discuss the equatorial Rossby modes (r modes). The modes with no radial nodes ($n = 0$) and one radial node ($n = 1$) are reported.

3.3.1.1 $n = 0$ modes

In order to extract the $n = 0$ equatorial Rossby mode at each m, we apply the following procedure to the computed eigenfunctions $\boldsymbol{V}$. The latitudinal and longitudinal velocities at the surface are projected onto a basis of associated Legendre polynomials:

$$v_\theta(r_{\max}, \theta) = \sum_{l=0}^{l_{\max}} a_{l-m} P_l^m(\cos\theta), \tag{3.26}$$

$$v_\phi(r_{\max}, \theta) = \sum_{l=0}^{l_{\max}} b_{l-m} P_l^m(\cos\theta), \tag{3.27}$$

where $l_{\max} = 2N_\theta/3 - 1 = 47$. We also compute the number of radial nodes, n, of v_θ at the equator. We select the modes that satisfy all of the following three criteria:

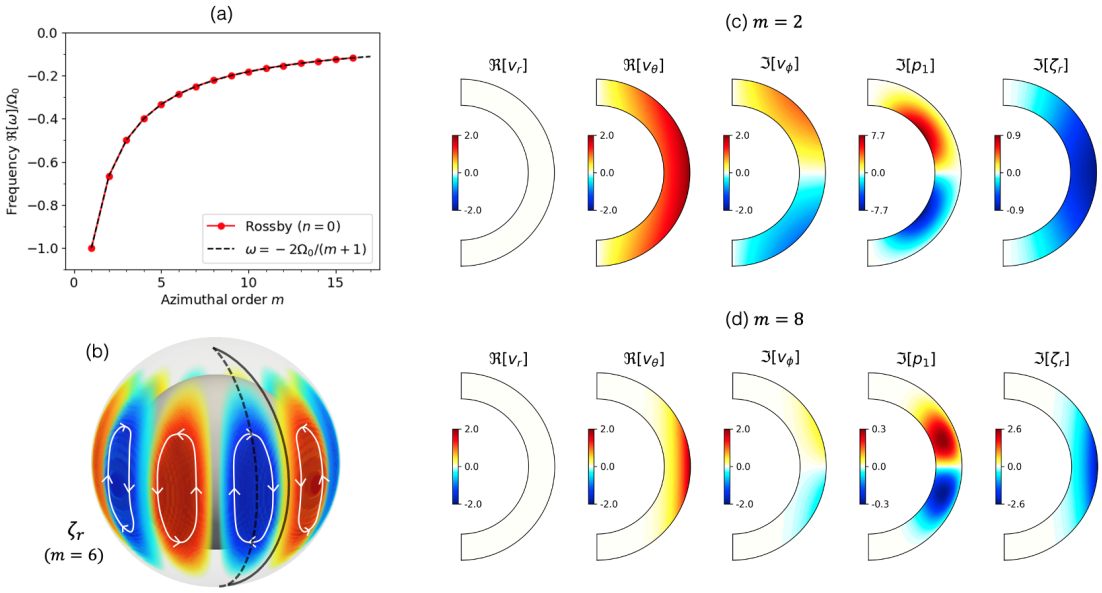

Figure 3.4: Dispersion relation and eigenfunctions of the equatorial Rossby modes without radial nodes in the case of uniform rotation, no viscosity, and adiabatic stratification. (a) Dispersion relation from the calculated modes (red). Overplotted black dashed line represents the theoretical dispersion relation of the sectoral ($l = m$) Rossby modes $\omega = 2\Omega_0/(m+1)$. (b) Schematic illustration of flow structure of the mode with m=6. The red and blue volume rendering shows the structure of $\Re[\zeta_r(r,\theta)\exp(\mathrm{i}m\phi - \mathrm{i}\omega t)]$. The black solid curve shows the meridional plane at $\phi = 0$ and at $t = 0$ where v_r and v_θ are purely real and v_ϕ, p_1 and ζ_r are purely imaginary. The black dashed line denotes the meridional plane at $\phi = -\pi/2m$ where v_ϕ, p_1 and ζ_r are real. (c) Meridional cuts of the $m = 2$ eigenfunctions for the velocity $\boldsymbol{v}(r,\theta)\exp[\mathrm{i}(m\phi - \omega t)]$, the pressure $p_1(r,\theta)\exp[\mathrm{i}(m\phi - \omega t)]$, and the radial vorticity $\zeta_r(r,\theta)\exp[\mathrm{i}(m\phi - \omega t)]$. The solutions are shown in the meridional plane at $\phi = 0$ and $t = 0$. The units of the color bars are m s^{-1} for the three velocity components, 10^5 dyn cm^{-2} for the pressure, and 10^{-8} s^{-1} for the vorticity. The eigenfunctions are normalized such that the maximum of $|v_\theta|$ is 2 m s^{-1}. (d) The same as panel (c) but for $m = 8$.

- The $l = m$ component of v_θ is dominant ($|a_0| > |a_j|$ for all $j > 0$),
- the $l = m + 1$ component of v_ϕ is dominant ($|b_1| > |b_j|$ for all $j \neq 1$),
- and the number of radial nodes of v_θ is zero at the equator, $n = 0$.

Figure 3.4a shows the dispersion relation of the selected $n = 0$ equatorial Rossby modes for this ideal setup for $m = 1 - 16$. It should be noted that these modes are the only type of inertial modes where a simple analytical solution can be found in the inviscid, uniformly-rotating limit (e.g., Saio 1982). Therefore, we use this analytical solution to verify our code. The red points and black dashed lines represent the computed eigenfrequencies in our model and the theoretically-expected dispersion relation, $\omega = -2\Omega_0/(m+1)$, respectively. We find that the differences in the normalized frequencies are less than 10^{-2} at all m.

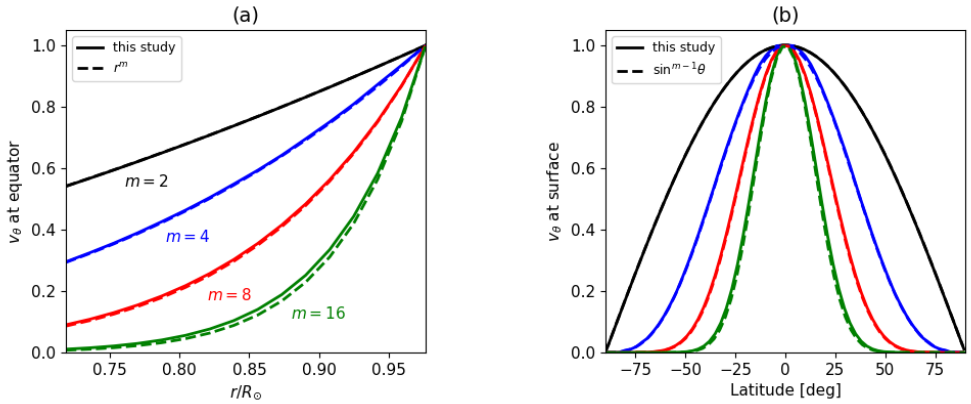

Figure 3.5: (a) Radial structure of the eigenfunction of v_θ at the equator for the $n = 0$ equatorial Rossby modes in the inviscid, uniformly rotating, and adiabatically stratified case. Overplotted dashed lines represent theoretically-predicted radial dependence $v_\theta \propto r^m$. The eigenfunctions are normalized to unity at the surface $r = r_{\rm max}$. (b) Latitudinal structure of the eigenfunction of v_θ at the surface. Dashed lines are the theoretical solution in the form of legendre-polynomials $v_\theta \propto \sin^{m-1}\theta$. All the eigenfunctions are normalized at the equator.

The typical flow structure of this mode is schematically illustrated in Fig. 3.4b where the volume rendering of the radial vorticity ζ_r is shown by red and blue. Figures 3.4c and d show the real eigenfunctions for $m = 2$ and 8, respectively. The eigenfunctions are normalized such that the maximum of v_θ is 2 m s^{-1} at the surface. The amplitude of radial velocity v_r is about 10^3 times smaller than those of horizontal velocities v_θ and v_ϕ, implying that the fluid motion is essentially toroidal. We find that using a higher resolution leads to even smaller v_r. The pressure perturbation p_1 is positive (negative) where the radial vorticity ζ_r is negative (positive) in the northern (southern) hemisphere, which is consistent with the modes being in geostrophic balance. As m increases, the $n = 0$ equatorial Rossby modes are shifted to the surface and to the equator. The horizontal eigenfunction of ζ_r becomes more elongated in latitude, which means that v_θ becomes much stronger than v_ϕ to keep the mass conservation horizontally.

Figure 3.5a shows the radial structure of the eigenfunctions of v_θ at the equator for selected azimuthal orders m. Solid and dashed lines compare our results with the analytical solution $v_\theta \propto r^m$. It is seen that computed eigenfunctions exhibit the r^m dependence that agree with the analytical solutions. We also confirm the same r^m dependence for the eigenfunctions of v_θ in the middle latitudes (not shown). For higher m, the radial eigenfunction shows a slight deviation (within a few percent error) from the analytical solution. This is possibly due to the stress-free boundary condition, $\partial(v_\theta/r)/\partial r = 0$, at the top and bottom boundaries, which conflicts with the r^m dependence. Figure 3.5b shows the latitudinal eigenfunctions of v_θ at the surface. Again, an agreement can be seen between our results and the analytical solutions $v_\theta \propto \sin^{m-1}\theta$.

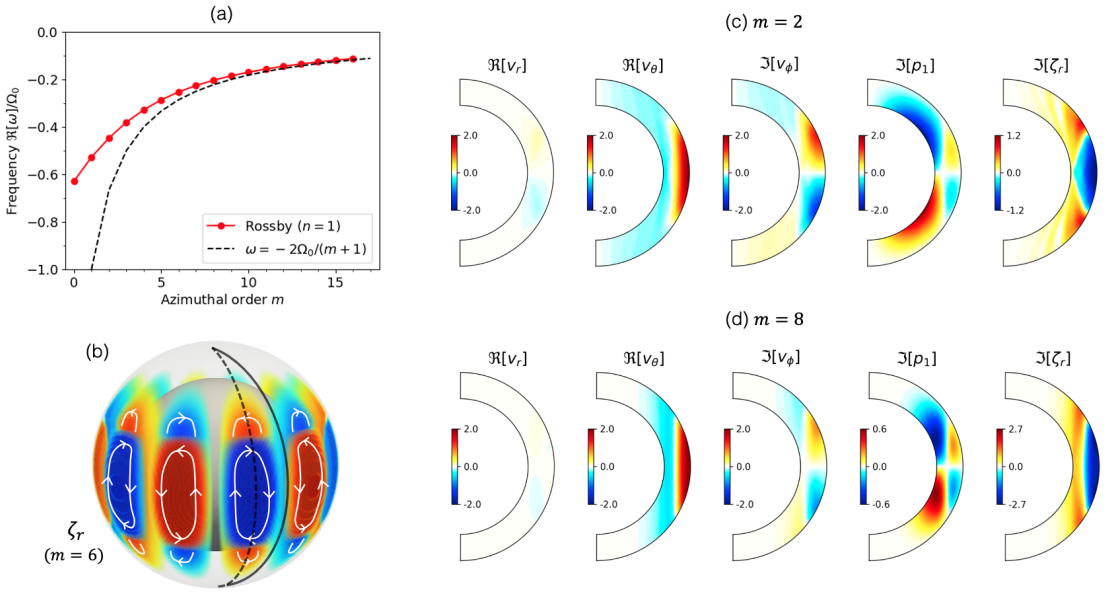

Figure 3.6: Dispersion relation and eigenfunctions of the equatorial Rossby modes with one radial node ($n = 1$) in the inviscid, uniformly rotating, adiabatically stratified case. The same notation as Fig. 3.4 is used.

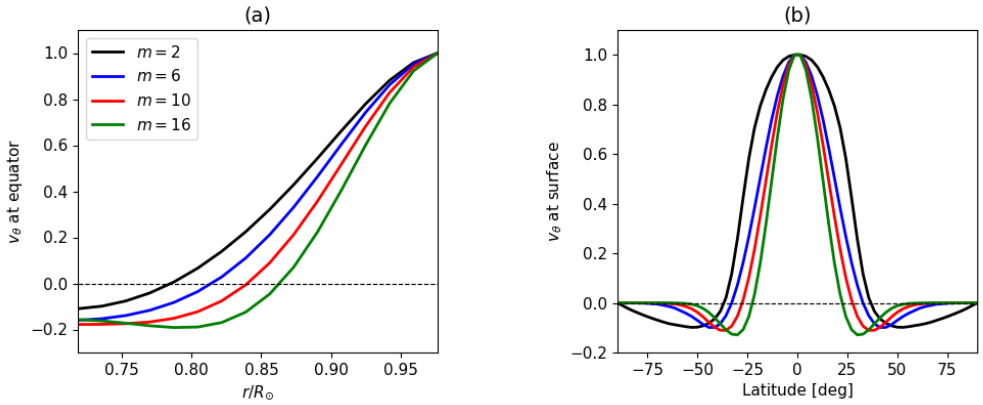

Figure 3.7: (a) Radial structure of the eigenfunction of v_θ at the equator of the $n = 1$ equatorial Rossby modes in the inviscid, uniformly rotating, adiabatically stratified case. The eigenfunctions are normalized to unity at the surface $r = r_{\max}$. (b) Latitudinal structure of the eigenfunction of v_θ at the surface normalized at the equator.

3.3.1.2 $n = 1$ modes

The equatorial Rossby modes with one radial node ($n = 1$) can be selected by applying the following filters for latitudinal and longitudinal velocity eigenfunctions:

- The $l = m$ component of v_θ is dominant at the surface,
- the $l = m + 1$ component of v_ϕ is dominant at the surface,
- and the number of radial nodes of v_θ is one at the equator.

Figure 3.6a shows the dispersion relation of the selected $n = 1$ equatorial Rossby modes for $0 \leq m \leq 16$. It should be noted that we successfully identify the axisymmetric mode ($m = 0$) at $\Re[\omega] = -0.63\Omega_0$. This $m = 0$ mode is an equatorially-trapped axisymmetric inertial mode. It will be shown later in §3.3.2.2 that this mode is connected to a prograde-propagating columnar convective mode. The $n = 1$ Rossby modes propagate in a retrograde direction with slower phase speed than that of $n = 0$ Rossby modes at low m. However, for $m \geq 8$, the mode frequencies become so close to those of $n = 0$ modes that they are almost indistinguishable.

Figure 3.6b shows a schematic sketch of typical flow motion of the $n = 1$ equatorial Rossby mode. Figures 3.6c and d further shows the obtained eigenfunctions of $n = 1$ equatorial Rossby modes plotted in the same way as in Fig. 3.4. It is clearly shown that v_θ has a nodal plane in the middle convection zone at the equator which extends in the direction of the rotation axis. One of the most striking consequences of the existence of the radial node is that substantial v_r is involved owing to the radial shear of v_θ. Therefore, unlike the $n = 0$ modes, the associated fluid motions are no longer purely toroidal and become essentially three-dimensional.

Figure 3.7a shows the radial structure of the eigenfunctions of v_θ at the equator for selected m. It is clearly seen that the location of the radial node shifts towards the surface as m increases. Figure 3.7b shows the latitudinal structure of the eigenfunctions of v_θ at the surface. The eigenfunctions peak at the equator and change their sign in the middle latitudes ($25^\circ - 50^\circ$) and decay at higher latitudes.

3.3.2 Columnar convective modes

In this section, we carry out a similar mode-by-mode analysis for the columnar convective modes (thermal Rossby waves) with both hemispheric symmetries. Here, we define the north-south symmetry based on the eigenfunction of z-vorticity ζ_z. The "banana cel" convection pattern can be essentially regarded as the north-south symmetric part of these convective modes. We will also show that the north-south ζ_z-antisymmetric modes are essentially mixed with the $n = 1$ equatorial modes.

3.3.2.1 North-south ζ_z-symmetric modes

North-south ζ_z-symmetric columnar convective modes can be selected by applying the following filters on the velocity eigenfunctions:

- The $l = m$ component of v_ϕ is dominant at the surface,
- the $l = m + 1$ component of v_θ is dominant at the surface.
- the number of radial nodes of v_r is zero at the equator,
- and the number of radial nodes of v_ϕ is one at the equator.

Figure 3.8a shows the dispersion relation of the selected north-south ζ_z-symmetric columnar convective modes. For comparison, we overplot in black dashed line the dispersion relation derived from the one-dimensional cylinder model of Glatzmaier and Gilman

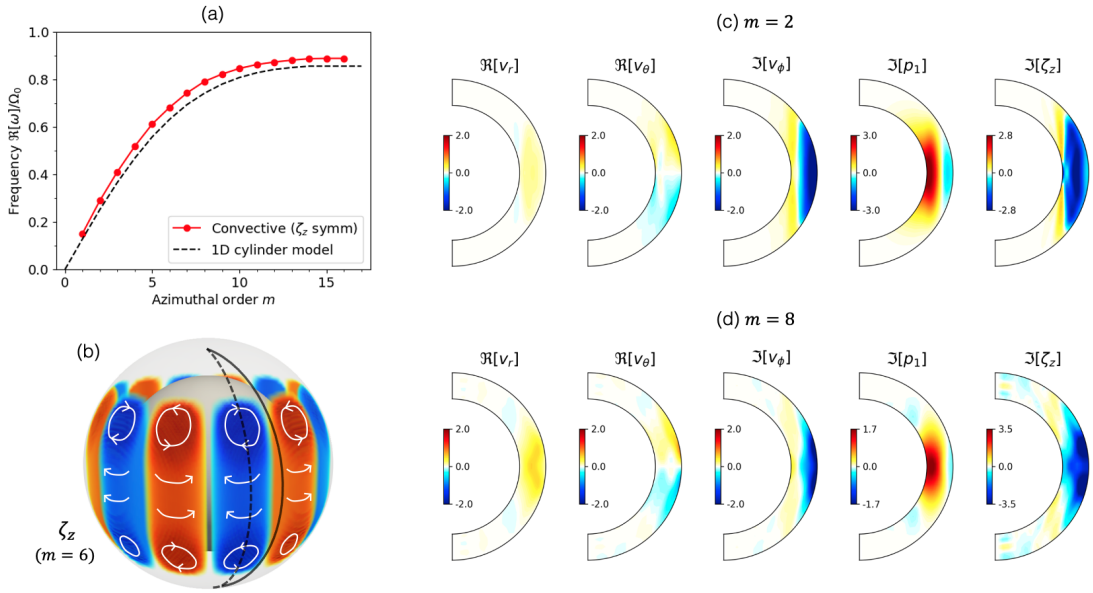

Figure 3.8: Dispersion relation and eigenfunctions of the north-south ζ_z-symmetric columnar convective modes in the case of uniform rotation, no viscosity, and adiabatic stratification. (a) Dispersion relation of the north-south ζ_z-symmetric columnar convective modes in red points. For comparison, dispersion relation analytically derived using one-dimensional cylinder model by Glatzmaier and Gilman (1981) is overplotted in black dashed line. (b) Schematic illustration of flow structure of the mode. Red and blue volume rendering shows the structure of $\Re[\zeta_z(r,\theta)\exp(\mathrm{i}m\phi - \mathrm{i}\omega t)]$ for $m = 6$ at $t = 0$. (c) Meridional cuts of the $m = 2$ eigenfunctions for the velocity $\boldsymbol{v}(r,\theta)\exp[\mathrm{i}(m\phi - \omega t)]$, the pressure $p_1(r,\theta)\exp[\mathrm{i}(m\phi - \omega t)]$, and the z-vorticity $\zeta_r(r,\theta)\exp[\mathrm{i}(m\phi - \omega t)]$. The solutions are shown in the meridional plane at $\phi = 0$ and $t = 0$ where v_r and v_θ are purely real and v_ϕ, p_1 and ζ_z are purely imaginary. The units of velocity, pressure, and vorticity are m s^{-1}, 10^5 dyn cm^{-2}, and 10^{-8} s^{-1}, respectively. The eigenfunctions are normalized such that maximum of $|v_\phi|$ is 2 m s^{-1}. (d) The same as panel (c) but for $m = 8$.

(1981) (their figure 2). Qualitatively, they both show similar features: Columnar convective modes propagate in a prograde direction at all m. The modes are almost non-dispersive at low m (≤ 7), but at higher m, the mode frequencies become almost constant at $\Re[\omega] \approx 0.85\Omega_0$. Quantitatively, our model produces the mode frequencies slightly higher (less than 10%) than that of the one-dimensional cylinder model. This difference likely comes from the spherical geometry of our model: Our model takes into account both compressional and topographic β-effects that both lead to a prograde phase propagation, whereas only compressional β-effect is included in the cylinder model of Glatzmaier and Gilman (1981).

Figures 3.8c and d show example eigenfunctions of the north-south ζ_z-symmetric columnar convective modes. The flow structure is dominantly characterized by the longitudinal velocity shear outside the tangential cylinder, leading to a strong z-vorticity (where z is a coordinate in the direction of the rotation axis). Substantial radial motions are involved where v_ϕ converges or diverges in longitudes, as schematically illustrated in Fig. 3.8b. Owing to the spherical curvature of the top boundary, equatorward (poleward)

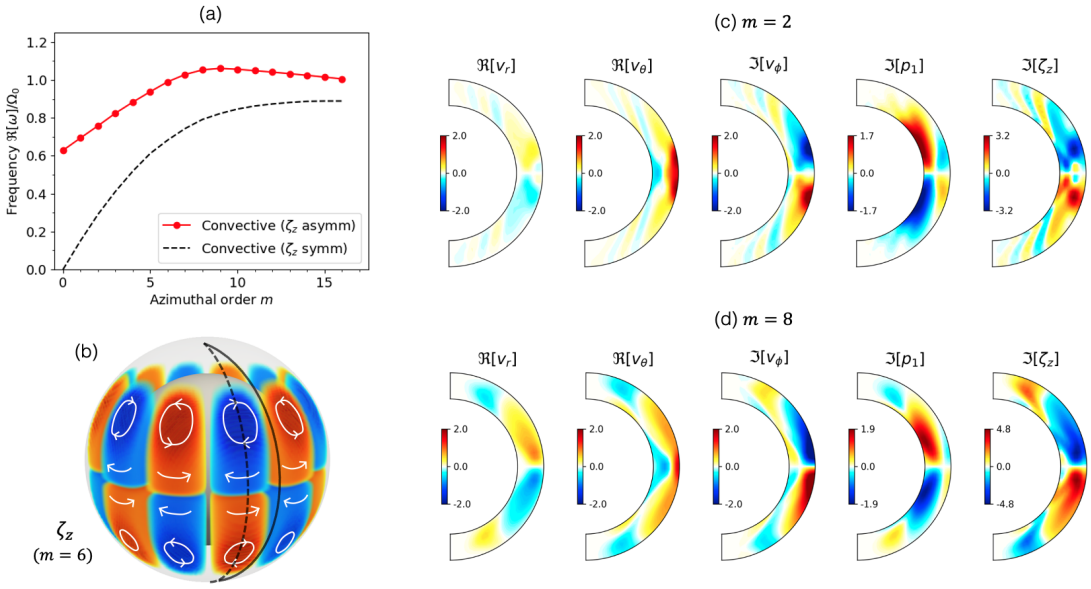

Figure 3.9: Dispersion relation and eigenfunctions of the north-south ζ_z-antisymmetric columnar convective modes in the inviscid, uniformly rotating, adiabatically stratified case. The same notation as Fig. 3.8 is used. In panel (a), the dispersion relation of the north-south ζ_z-symmetric columnar convective modes is shown in black dashed line for comparison.

latitudinal flows are involved where radial flows are outward (inward). The z-vortex tubes outside the tangential cylinder are often called as Taylor columns or Busse columns in the geophysical context (Busse 1970, 2002) or Banana cells in the solar context (Miesch et al. 2000). The pressure perturbation p_1 is generally positive (negative) where z-vorticity ζ_z is negative (positive), as the modes are in geostrophic balance. As m increases, the modes are more concentrated towards the surface and towards the equator.

3.3.2.2 North-south ζ_z-antisymmetric modes

North-south ζ_z-antisymmetric columnar convective modes can be selected by filtering out the eigenfunctions that satisfy the followings:

- The $l = m$ component of v_θ is dominant at the surface,
- the $l = m + 1$ component of v_ϕ is dominant at the surface,
- and the number of radial nodes of v_θ is one at the equator.

The dispersion relation of the ζ_z-antisymmetric columnar convective modes is shown in Fig. 3.9a. For comparison, we also show the dispersion relation of the ζ_z-symmetric modes in black dashed line. The modes propagate in a prograde direction with faster phase speed than that of the ζ_z-symmetric modes. At high m, the dispersion relation asymptotically approaches that of the ζ_z-symmetric modes.

Figures 3.9c and d show the example eigenfunctions of the north-south ζ_z-antisymmetric columnar convective modes. The flow structure is dominantly characterized by z-vortex

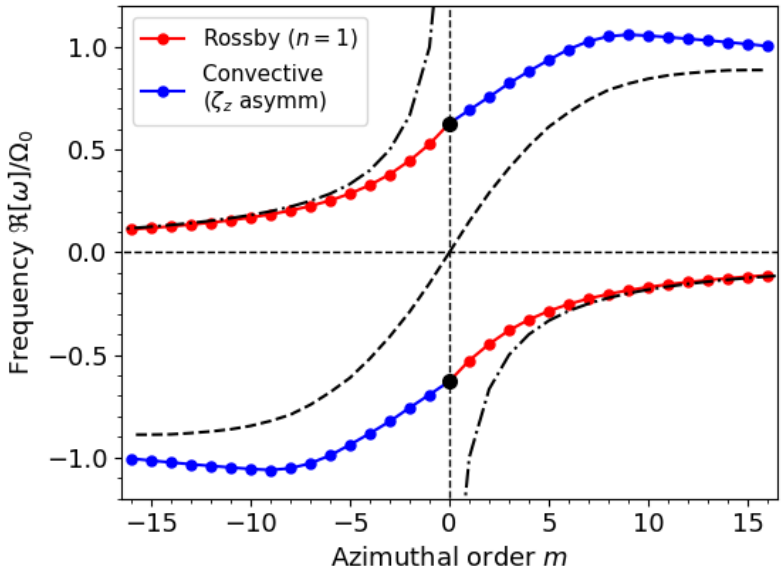

Figure 3.10: Dispersion relation of the "mixed modes" between the $n = 1$ equatorial Rossby modes (red) and the north-south ζ_z-antisymmetric columnar convective modes (blue) in the inviscid, uniformly rotating, adiabatically stratified case. The black points denote the axisymmetric mode at $m = 0$. Black solid dashed and dot-dashed lines represent the dispersion relation of the $n = 0$ equatorial Rossby modes and north-south ζ_z-symmetric columnar convective modes.

tubes that are antisymmetric across the equator. It should be noted that strong latitudinal motions are involved at the equator at the surface.

We find that the eigenfunctions of the $m = 0$ mode are the complex conjugate of the $n = 1$ equatorial Rossby mode, which means that these two modes are identical at $m = 0$ (note the phase speed does no longer matter for the non-propagating axisymmetric mode). To better illustrate this point, we show in Fig. 3.10 the dispersion relations of these two modes in the full $(m, \Re[\omega])$ domain extended to negative azimuthal orders. It is seen that the dispersion relations of these two modes connects across $m = 0$ and form a single continuous curve. This implies that these two modes are essentially mixed with each other: The $n = 1$ equatorial Rossby modes and the north-south ζ_z-antisymmetric columnar convective modes should be regarded as retrograde and prograde branches of the "mixed" (Rossby) modes. It is instructive to note that this mode mixing can be understood as analogous to the so-called Yanai waves which are mixed modes between retrograde-propagating Rossby modes and prograde-propagating inertial-gravity modes (Matsuno 1966, Vallis 2006).

The flow structure itself of the ζ_z-antisymmetric columnar convective mode has been recognized to be convectively-unstable in the previous literature (Lorenzani and Tilgner 2001, Tilgner 2007). However, its relation to the $n = 1$ equatorial Rossby modes has never been reported.

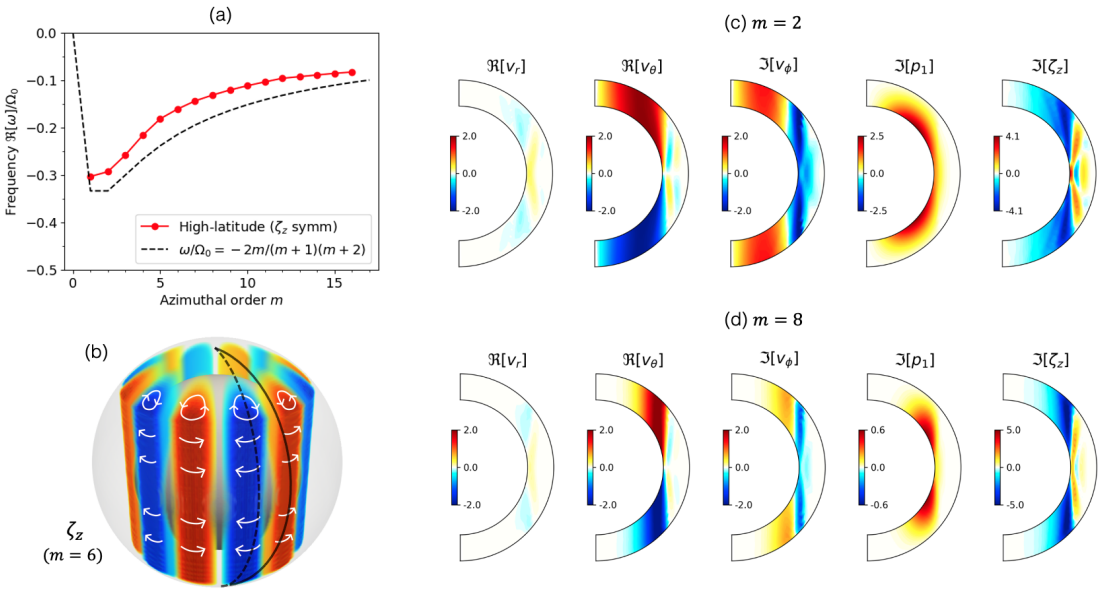

Figure 3.11: Dispersion relation and eigenfunctions of the high-latitude modes (topographic Rossby waves) with north-south symmetric ζ_z in the inviscid, uniformly rotating, adiabatically stratified case. The same notation as Fig. 3.8 is used. In panel (a), the dispersion relation of the $l = m + 1$ Rossby modes is shown in black dashed line.

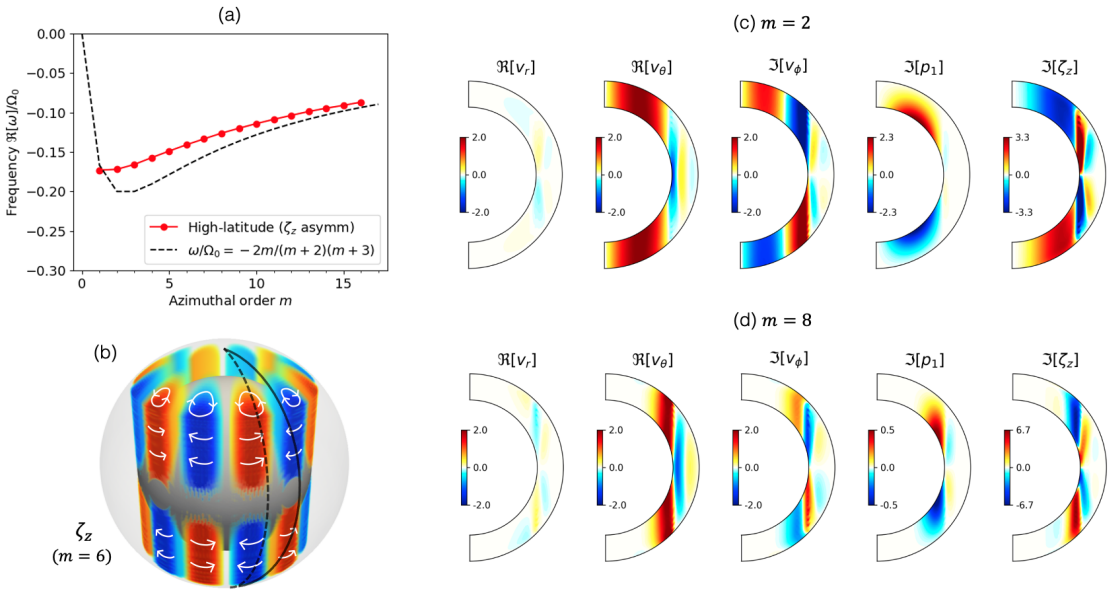

Figure 3.12: Dispersion relation and eigenfunctions of north-south ζ_z-antisymmetric high-latitude modes in the inviscid, uniformly rotating, adiabatically stratified case. The same notation as Fig. 3.11 is used. In panel (a), the dispersion relation of the $l = m + 2$ Rossby mode is shown in black dashed line.

3.3.3 High latitude modes

In this subsection, we present the eigenmodes of the high-latitude inertial modes with both hemispheric symmetries. In the absence of solar differential rotation and the latitudinal entropy gradient, the modes exist as pure topographic Rossby waves originating from the topographic β-effect of the lower spherical boundary (See Appendix 3.8 for more detail). Note that, here the north-south symmetry is defined based on the eigenfunction of z-vorticity ζ_z.

3.3.3.1 North-south ζ_z-symmetric modes

To discuss these modes, it is useful to introduce a cylindrical coordinate system (ϖ, ϕ, z). In this coordinate system, the tangent cylinder is located at $\varpi = r_{\rm min}$, i.e., it is the cylinder aligned with the rotation axis which touches the radiative interior at the equator. North-south ζ_z-symmetric high-latitude modes can be selected by applying the following criteria:

- The kinetic energy is predominantly inside the tangential cylinder, i.e., $E_{\rm in}/E_{\rm CZ} > 0.5$ where $E_{\rm in}$ and $E_{\rm CZ}$ are the volume-integrated kinetic energies inside the tangent cylinder and in the entire convection zone, respectively.
- The $l = m + 1$ component of v_θ is dominant at the bottom of the convection zone.
- The number of z-nodes of v_θ is zero at $\varpi = 0.5 R_\odot$.

Figure 3.11a shows the dispersion relation of the north-south ζ_z-symmetric high-latitude modes. Although the high-latitude modes have many similar properties to the columnar convective modes, it is found that the high-latitude modes are much more dispersive than the columnar convective modes at low m. The dispersion relation is found to be roughly approximated by the non-sectoral Rossby modes' dispersion relation with one latitudinal node ($l = m + 1$), as shown in the black dashed line in Fig. 3.11a. This is because the horizontal flows at the bottom boundary behave like the $l = m + 1$ (classical) Rossby modes. Note, however, that this is not regarded as the mode mixing as discussed in §3.3.2.2:

Figures 3.11c and d show example eigenfunctions of the ζ_z-symmetric high-latitude modes. The fluid motion is predominantly characterized by z-vortices inside the tangential cylinder in both hemispheres, as schematically illustrated in the Fig. 3.11b. The power of ζ_z peaks at the tangential cylinder $\varpi = r_{\rm min}$ where the topographic β-effect is the most significant. Note that the longitudinal velocity v_ϕ extends slightly outside the cylinder. Again, $\Im[p_1]\Im[\zeta_z] < 0$ follows from the mode being in geostrophic balance.

3.3.3.2 North-south ζ_z-antisymmetric modes

North-south ζ_z-antisymmetric high-latitude modes are selected using the following filters:

- The kinetic energy is predominantly inside the tangential cylinder.
- the $l - m = 1$ (or 3) component of v_ϕ is dominant at the bottom of the convection zone,
- and the number of z-nodes is zero for v_θ at $\varpi = 0.5 R_\odot$.

The example modes are presented in Fig. 3.12. The eigenfunctions show very similar properties of the high-latitude modes discussed in Fig. 3.11 except for the north-south symmetry. It should be pointed out that there exists a latitudinal flow along the tangential cylinder and across the equator. The dispersion relation of the ζ_z-antisymmetric high-latitude modes are found to be similar to that of $l = m + 2$ Rossby modes, as shown in Fig. 3.12a.

3.4 Effect of turbulent diffusion

So far, we have discussed the results for an inviscid case. In this section, we examine the effects of viscous and thermal diffusion arising from turbulent mixing of momentum and entropy in the Sun (e.g., Rüdiger 1989). Let us start our discussion by estimating the impact of the turbulent diffusion on (classical) Rossby modes. The oscillation period of the equatorial Rossby mode at the azimuthal order m is given by

$$P_{\rm Ro} = \left| \frac{2\pi}{\omega_{\rm Ro}} \right|, \quad \text{where} \quad \omega_{\rm Ro} = -\frac{2\Omega_0}{m+1}. \tag{3.28}$$

On the other hand, typical diffusive time scale can be estimated as

$$\tau_{\rm diff} = \frac{l_m^2}{\nu}, \quad \text{with} \quad l_m = \frac{R_\odot}{m}, \tag{3.29}$$

where l_m denotes the typical length scale of the Rossby mode. Figure 3.13 compares $P_{\rm Ro}$ and $\tau_{\rm diff}$ as functions of m. Two representative values of turbulent diffusitivies in the solar convection zone $\nu = 10^{12}$ and 10^{13} cm^2 s^{-1} are shown (e.g., Ossendrijver 2003). When $P_{\rm Ro} \ll \tau_{\rm diff}$, viscous diffusion is almost negligible. However, if $P_{\rm Ro} \gtrsim \tau_{\rm diff}$, diffusion can have a dominant effect on the Rossby modes. For a given turbulent diffusivity ν, the critical azimuthal order $m_{\rm crit}$ can be defined as

$$m_{\rm crit} = \left(\frac{R_\odot \Omega_0}{\pi \nu} \right)^{1/3}. \tag{3.30}$$

The Rossby modes are dominated by diffusive effects for $m > m_{\rm crit}$. Figure 3.13 implies that the Rossby modes in the Sun are substantially affected by the turbulent diffusion especially for $m \geq 5 - 6$.

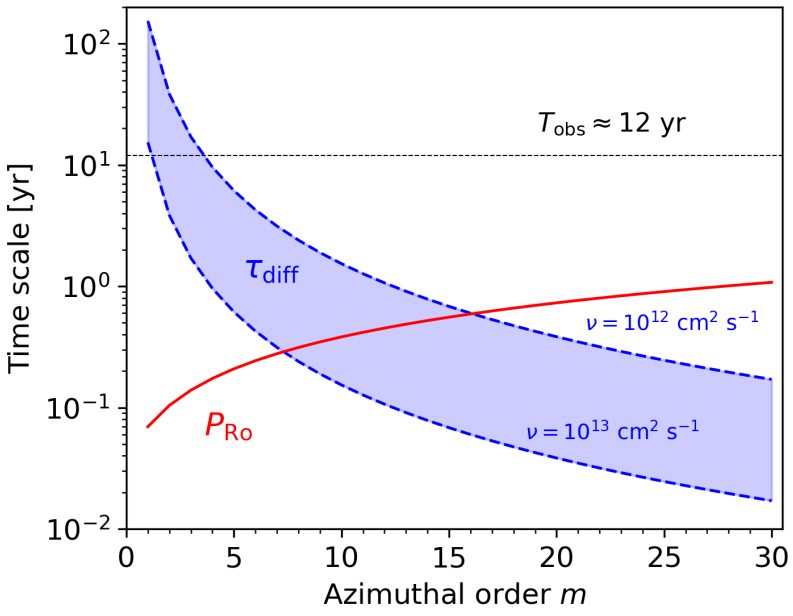

Figure 3.13: Comparison between the oscillation periods of Rossby modes $P_{\rm Ro}$ and the diffusive time scale $\tau_{\rm diff}$ for two representative values of turbulent diffusivities $\nu = 10^{12}$ and 10^{13} cm^2 s^{-1}. The horizontal black dashed line represents the length of the SDO/HMI observational record $T_{\rm obs} \approx 12$ years.

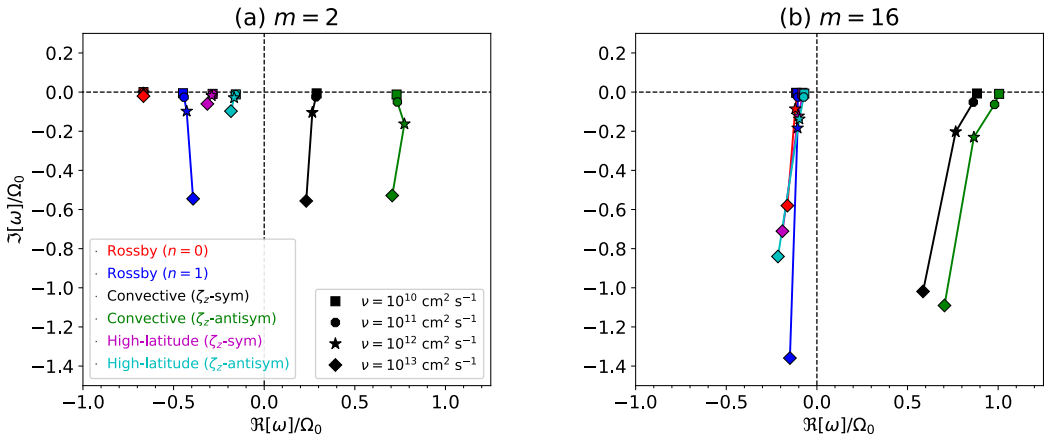

Figure 3.14: Eigenfrequency spectra of the low-frequency vorticity modes in a complex plane with different values of diffusivities for (a) $m = 2$ and (b) $m = 16$. Different colors represent different classes of inertial modes. Different symbols represent different values of the viscous and thermal diffusivities. In all cases, rotation is uniform and the stratification is adiabatic.

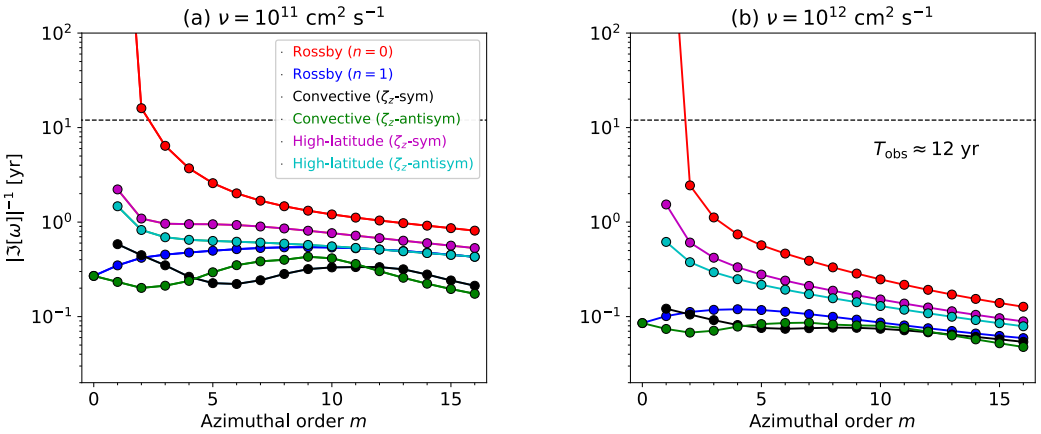

Figure 3.15: e-folding lifetimes of various low-frequency modes for a viscous diffusivity (a) $\nu = 10^{11}$ cm^2 s^{-1} and (b) $\nu = 10^{12}$ cm^2 s^{-1}. Note that all the modes selected here are stable modes ($\Im[\omega] < 0$). Different colors represent different types of inertial modes. The horizontal black dashed line shows the length of the SDO/HMI observational record ($T_{\rm obs} \approx 12$ yr as of today). In both cases, rotation is uniform and the stratification is adiabatic. The lifetimes of the convective modes and high-latitude modes are very sensitive to the radial and latitudinal entropy gradients, a point which is discussed in § 3.5 and § 3.6.2.

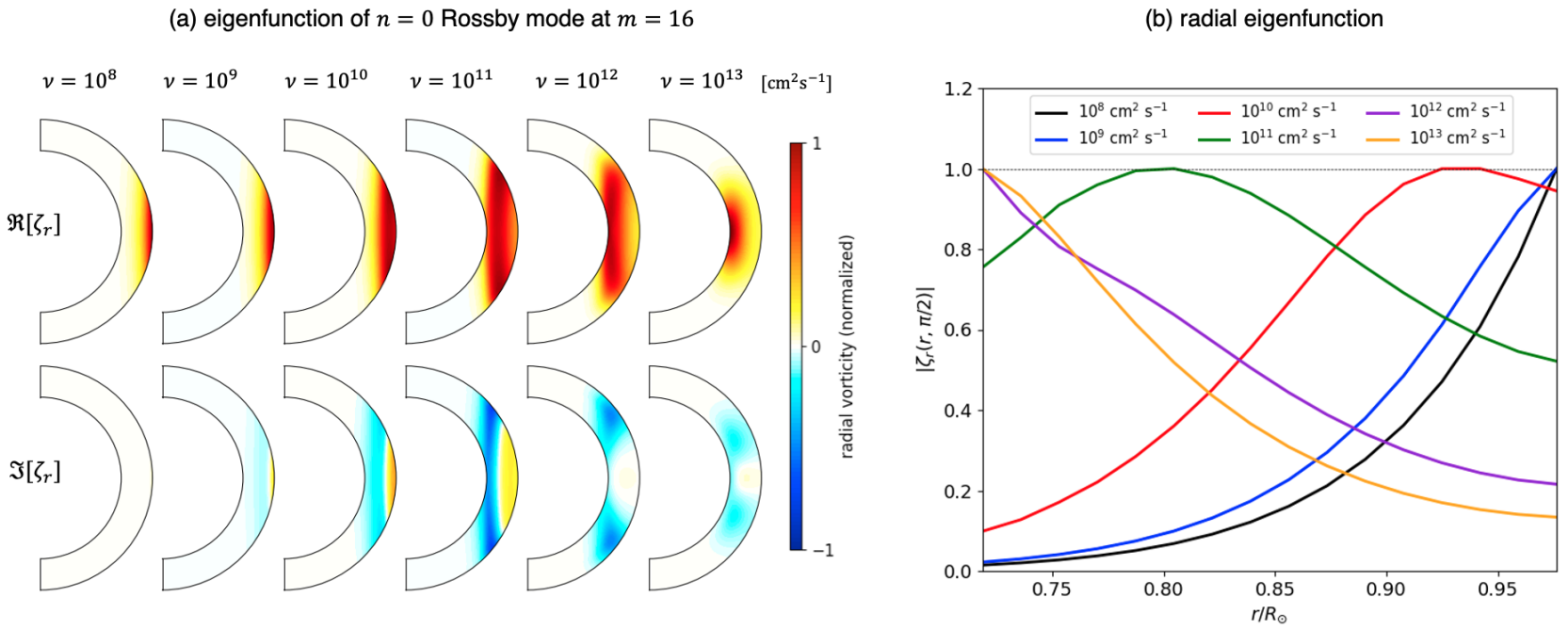

Figure 3.16: (a) Meridional eigenfunctions of radial vorticity ζ_r of the $n = 0$ equatorial Rossby mode at $m = 16$ for different values of viscous diffusivities ν. Upper and lower panels show the normalized real and imaginary eigenfunctions, respectively. (b) Radial eigenfunctions of $|\zeta_r|$ at the equator (normalized by their maximum amplitudes). Different colors represent different values of diffusivities. In all cases, rotation is uniform and the stratification is adiabatic.

In this paper, we carry out a set of calculations of uniformly-rotating adiabatic fluid with varying diffusivities; $\nu = 10^9, 10^{10}, 10^{11}, 10^{12}$, and 10^{13} cm^2 s^{-1}. For simplicity, we fix the Prandtl number to unity so that $\kappa = \nu$. Now, both the eigenfrequencies and eigenfunctions are complex. Figure 3.14 shows the eigenfrequencies of the six types of Rossby modes discussed in § 3.3 for different viscous diffusivities in a complex plane. Figures 3.14a-c show the cases for $m = 2, 8$, and 16, respectively. In general, the modes are damped by diffusion so that the imaginary frequencies are shifted towards more negative values. At small m (e.g. $m = 2$), diffusion tends to act predominantly on the columnar convective modes with both symmetries and $n = 1$ equatorial Rossby modes, whereas the $n = 0$ Rossby modes and the high-latitude modes remain almost unaffected. At large m (e.g. $m = 16$), however, all the modes are damped to a similar degree. Note that a strong diffusion modifies not only the imaginary part but also the real part of the mode frequencies.

Now, let us focus on the $n = 0$ equatorial Rossby modes to see how eigenfunctions are affected by the viscous diffusion. Figure 3.16a shows the real (top row) and imaginary (bottom row) eigenfunctions of radial vorticity ζ_r at $m = 16$ for different values of viscous diffusivities ν. As ν increases, the $n = 0$ equatorial Rossby modes are shifted towards the base of the convection zone. This is clearly illustrated in Fig. 3.16b where the absolute amplitudes of radial vorticity at the equator are shown as functions of radius. When ν becomes sufficiently large, the radial eigenfunction substantially deviates from the well-known r^m dependence. This can be explained as follows: With the moderate diffusion included, the radial force balance between Coriolis force and pressure gradient force is no longer maintained. Consequently, radial flows are driven and the diffusive momentum flux becomes directed radially inward. In fact, the confinement of the $n = 0$ equatorial Rossby modes near the base is also seen in rotating convection simulations where the diffusion can be significantly enhanced by turbulent convection (see § 4.5.2).

3.5 Effect of non-adiabatic stratification

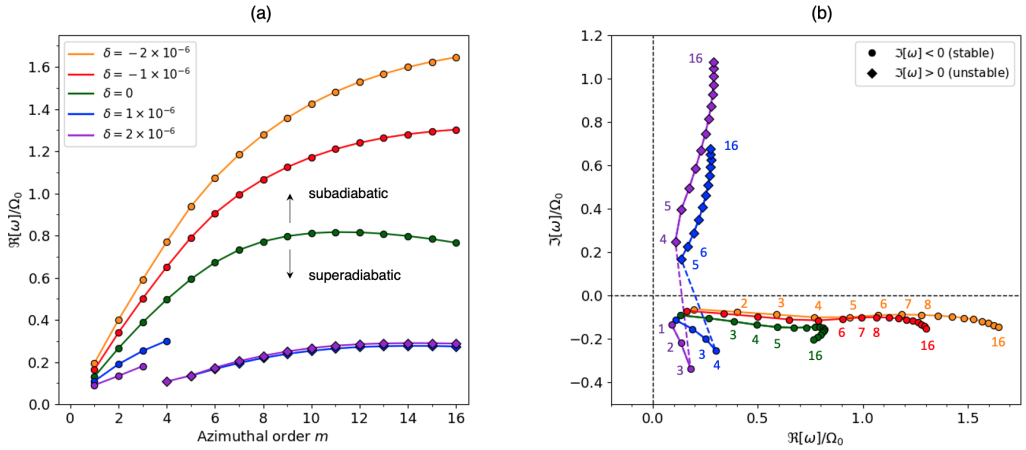

Figure 3.17: (a) Dispersion relations of the north-south ζ_z-symmetric columnar convective modes with different background superadiabaticity values δ. Different colors represent different values of superadiabaticity. Circles and diamonds denote the stable ($\Im[\omega] < 0$) and unstable ($\Im[\omega] > 0$) modes, respectively. (b) Eigenfrequencies plotted on a complex plane. Each circle (diamond) represent a mode with azimuthal order m, which is labelled with small integers from $m = 1$ to 16. In all cases, rotation is uniform and the diffusivities are set $\nu = \kappa = 10^{12}$ cm^2 s^{-1}.

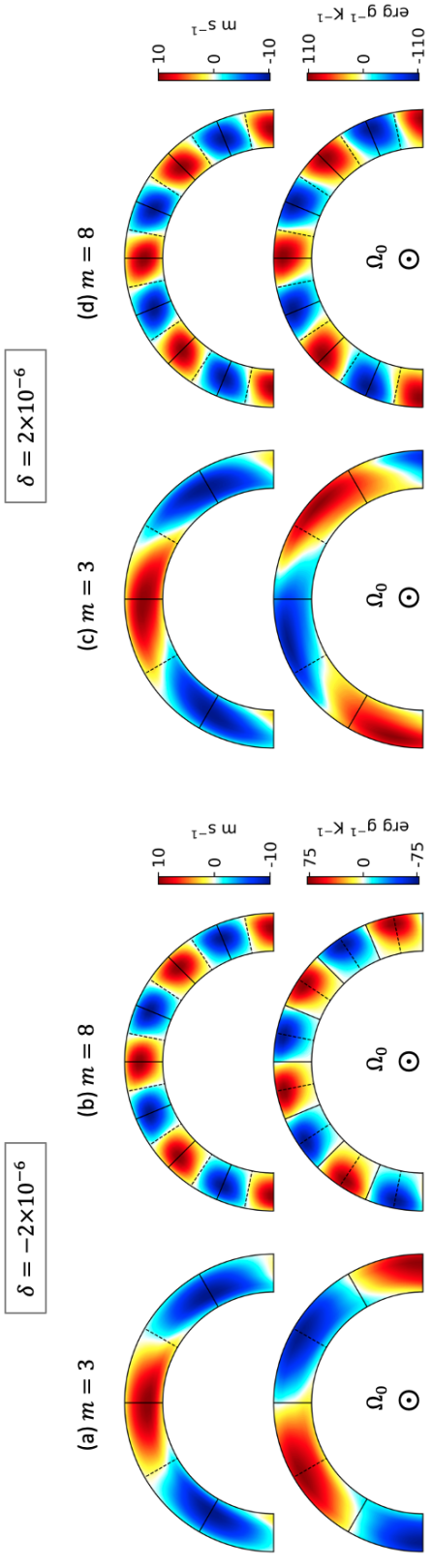

Figure 3.18: Radial velocity v_r (upper plots) and entropy perturbation s_1 (lower plots) of the columnar convective modes along the rotational axis displayed in the equatorial plane for subadiabatic and superadiabatic background. Panels (a) and (b) show the cases with subadiabatic background $\delta = -2 \times 10^{-6}$ for $m = 3$ and $m = 8$, respectively. Panels (c) and (d) are the same plots for superadiabatic background $\delta = 2 \times 10^{-6}$. The eigenfunctions are normalized such that the maximum radial velocity is 10 m s^{-1} at the equator. In all cases, rotation is uniform and the diffusivities are set $\nu = \kappa = 10^{12}$ cm^2 s^{-1}.

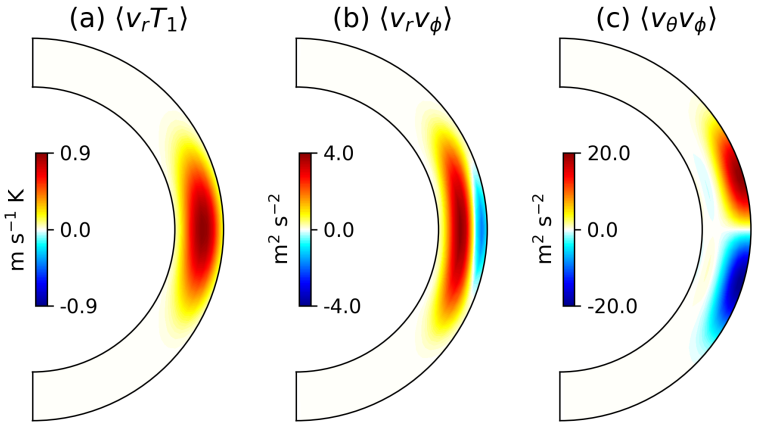

Figure 3.19: Transport properties of thermal energy and angular momentum by the north-south ζ_z-symmetric columnar convective modes for $m = 16$. (a) Correlation between radial velocity velocity and temperature perturbation $\langle v_r T_1 \rangle$, (b) Reynolds stress between radial and longitudinal velocities $\langle v_r v_\phi \rangle$, and (c) Reynolds stress between latitudinal and longitudinal velocities $\langle v_\theta v_\phi \rangle$. The background is weakly superadiabatic ($\delta = 2 \times 10^{16}$), rotation is uniform, and moderate diffusivities are used ($\nu = \kappa = 10^{12}$ cm^2 s^{-1}). The eigenfunctions are normalized such that the maximum radial velocity is 10 m s^{-1} at the equator.

In this section, the effects of non-adiabatic stratification are investigated. While theoretical model of the Sun conventionally assume a slightly positive superadiabaticity value $0 < \delta \lesssim 10^{-6}$ (e.g., Ossendrijver 2003), recent numerical simulations of solar convection imply that the lower half of the convection zone might be slightly subadiabatic (Hotta 2017, Käpylä et al. 2017, Bekki et al. 2017, Karak et al. 2018, Käpylä et al. 2019). To this end, we vary the superadiabaticity from weakly subadiabatic to weakly superadiabatic, $\delta = -2 \times 10^{-6}, -10^{-6}, 0, 10^{-6}, 2 \times 10^{-6}$, while keeping the diffusivities fixed ($\nu = \kappa = 10^{12}$ cm^2 s^{-1}). The solar differential rotation and latitudinal entropy gradient are not included. Since the entropy perturbation is generated by the radial flow, in this section, we focus on the (north-south ζ_z-symmetric) columnar convective modes where strong radial motions are involved.

Figure 3.17a shows the dispersion relations of the ζ_z-symmetric columnar convective modes for different δ. As the background becomes more subadiabatic (superadiabatic), the mode frequencies become higher (lower), i.e., the modes propagate in a prograde direction with faster (slower) phase speed. When δ is sufficiently large, the imaginary mode frequencies become positive, i.e., the modes become convectively unstable. This is clearly manifested in Fig. 3.17b where the mode frequencies are plotted in a complex plane. Each points denote each mode with the associated azimuthal order labelled nearby. The stable and unstable modes are distinguished by circles and diamonds, respectively. For $\delta > 0$ (blue and purple), a sudden transitions occurs from stable to unstable branches (at $m = 5$ and 4). The critical azimuthal order for this transition depends on the superadiabaticity δ via the Rayleigh number criterion for the convective instability.

The changes in the dispersion relation can be understood by considering whether the buoyancy force acts as a restoring force or the opposite. Figures 3.18a and b present

the snapshots of v_r and s_1 in an equatorial plane seen from the north pole for weakly subadiabatic background ($\delta = -2 \times 10^{-6}$) for $m = 3$ and 8, respectively. It is seen that the phase with positive s_1 is always ahead of the phase with positive v_r in longitude, leading to a negative correlation between $\Re[v_r]$ and $\Im[s_1]$. This physically means that, in this case, the buoyancy force acts as an additional restoring force for prograde-propagating columnar convective modes. In other words, these modes share a property of prograde-propagating g modes. Consequently, the mode frequencies become higher for $\delta < 0$. The opposite situation happens for $\delta > 0$. Figures 3.18c and d show the same equatorial cuts of v_r and s_1 for weakly superadiabatic background. When m is not large enough for the convective instability to occur, it is seen that the phase with positive s_1 is behind the phase with positive v_r in longitude, leading to a positive correlation between $\Re[v_r]$ and $\Im[s_1]$. Therefore, the buoyancy force acts against the original restoring force of the compressional β-effect, which weakens the prograde propagation of columnar convective modes. As a consequence, the mode frequencies become lower for $\delta > 0$. Figure 3.18d shows the case where m is sufficiently large and the mode becomes convectively unstable. It is obviously seen that the phases of v_r and s_1 now coincide and they both have the same sign at each phase, leading to $\langle v_r s_1 \rangle > 0$.

Figure 3.19 further shows the transport properties of thermal energy and angular momentum by convectively-unstable columnar convective modes. Shown is the case with $\delta = 2 \times 10^{-6}$ and for $m = 16$. Positive $\langle v_r T_1 \rangle$ in Fig. 3.19a manifests that the enthalpy flux is transported upward. The Reynolds stress components $\langle v_r v_\phi \rangle$ and $\langle v_\theta v_\phi \rangle$ are representatives of the radial and latitudinal angular momentum fluxes, respectively. It is shown that the columnar convective modes can transport the angular momentum radially upward in the bulk of the convection zone and eqautorward near the surface. This agrees with the results found in the rotating convection simulation (see § 4.5.1).

3.6 Effect of solar differential rotation

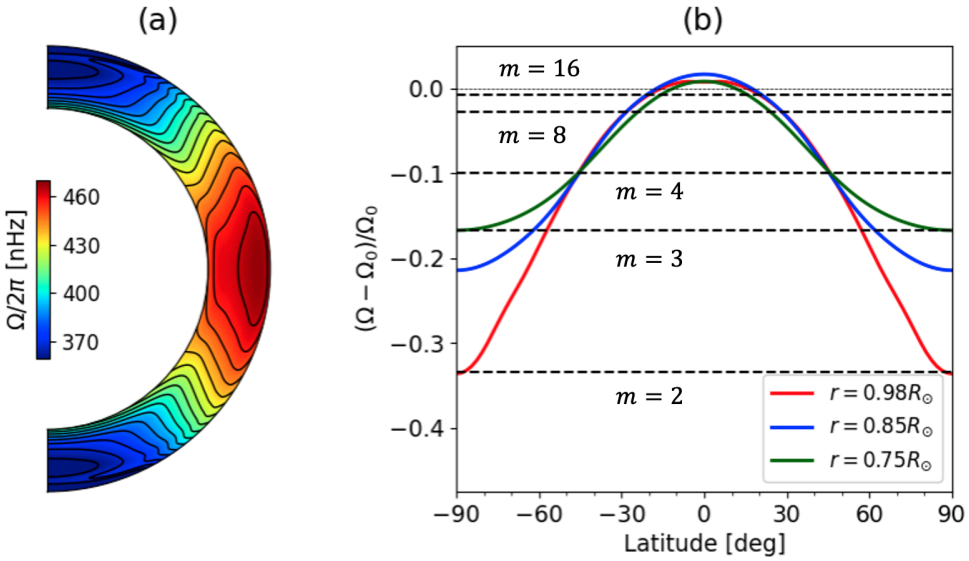

Figure 3.20: Solar differential rotation profile used in this study. (a) Differential rotation $\Omega(r, \theta)$ in a meridional plane, deduced from the global helioseismology (Larson and Schou 2018). (b) Latitudinal profiles of differential rotation at different depths. Horizontal dashed lines indicate the theoretically-expected phase speed of the sectoral ($l = m$) classical Rossby modes for selected azimuthal orders $m = 2, 3, 4, 8, 16$. The observing frame is chosen to be the Carrington frame rotating at $\Omega_0/2\pi = 456.0$ nHz.

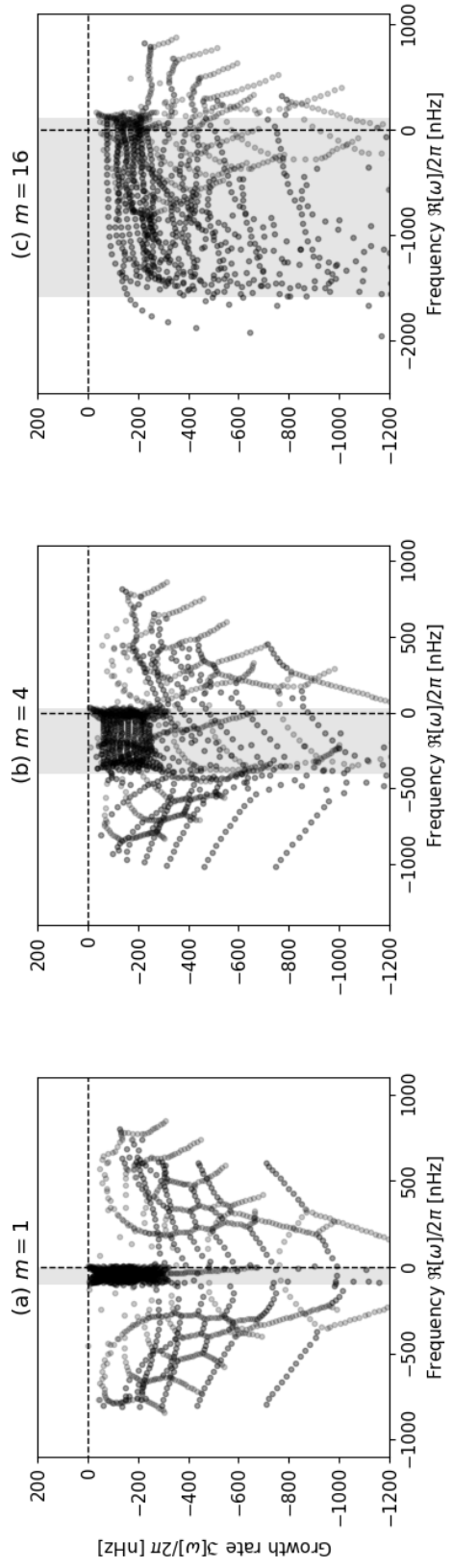

Figure 3.21: Eigenfrequencies of inertial modes under the solar differential rotation in the complex plane for (a) $m = 1$, (b) $m = 4$, and (c) $m = 16$. The diffusivity is set to $\nu = 10^{12}$ cm^2 s^{-1} and the background is assumed to be adiabatic, $\delta = 0$. The shaded areas indicate the frequency range associated with the surface differential rotation, i.e., $m(\Omega_{\rm pole} - \Omega_0) < \Re[\omega] < m(\Omega_{\rm eq} - \Omega_0)$.

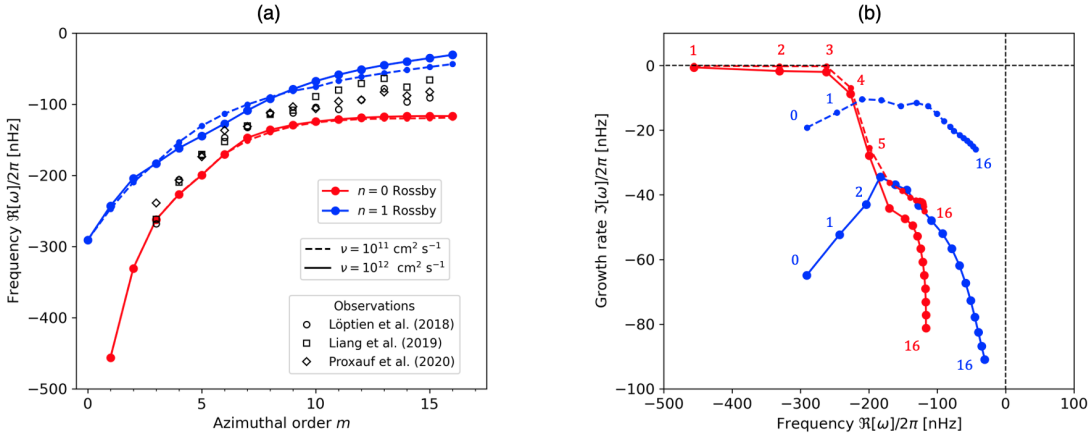

Figure 3.22: (a) Dispersion relations of the equatorial Rossby modes for the cases with solar differential rotation. Red and blue curves represent the modes with no radial nodes ($n = 0$) and one radial node ($n = 1$), respectively. Solid and dashed lines denote the cases with weak diffusion ($\nu = 10^{11}$ cm^2 s^{-1}) and strong diffusion ($\nu = 10^{12}$ cm^2 s^{-1}), respectively. For comparison, the observed Rossby mode frequencies reported in Löptien et al. (2018), Liang et al. (2019), and Proxauf et al. (2020) are plotted by white hexagons and squares. All the presented frequencies are measured in the Carrington frame rotating at $\Omega_0 = 456.0$ nHz. (b) Eigenfrequencies plotted on a complex plane similarly to Fig. 3.17b. Each point represents a mode with azimuthal order m, which is labelled with small integers from $m = 1$ to 16.

Finally, in this section, we take into account the effects of solar differential rotation. For prescribing $\Omega(r, \theta)$, we use the data obtained from global helioseismology inversions from MDI and HMI (Larson and Schou 2018) as shown in Fig. 3.20a. Note that the observational data is truncated at $r = r_{\rm min}$ and $r_{\rm max}$, and therefore, the effects of strong radial shear layers such as tachocline and the near surface shear layer of the Sun are not included. The observing frame is chosen to be Carrington frame with the rotation rate $\Omega_0 = 456.0$ nHz. Figure 3.20b shows the latitudinal profiles of the differential rotation at different depths. Horizontal dashed lines indicate the estimated phase speed of the $n = 0$ equatorial Rossby modes, $-2\Omega_0/[m(m+1)]$, for selected m values. For $m > 2$, there emerge critical latitudes where the phase speed of the Rossby mode matches with the differential rotation speed. As discussed in Gizon et al. (2020b), turbulent viscous diffusion is required to get rid of the singularities at the critical latitudes, leading to a formation of viscous critical layers with the typical thickness $\delta_{\rm crit}$ given by

$$\frac{\delta_{\rm crit}}{R_\odot} \approx \left(\frac{\nu}{m \Omega_0 R_\odot^2} \right)^{1/3} . \tag{3.31}$$

Figure 3.21 shows the distribution of eigenfrequencies of the global-scale inertial modes in a complex plane for selected m. Shown in shaded area represent the range of mode frequencies where differential rotation can have a strong impact by producing the critical layers. As higher m, the number of eigenmodes that are affected by differential rotation increases: In fact, most of the retrograde-propagating inertial modes are affected by critical latitudes at higher m (see Fig. 3.21c).

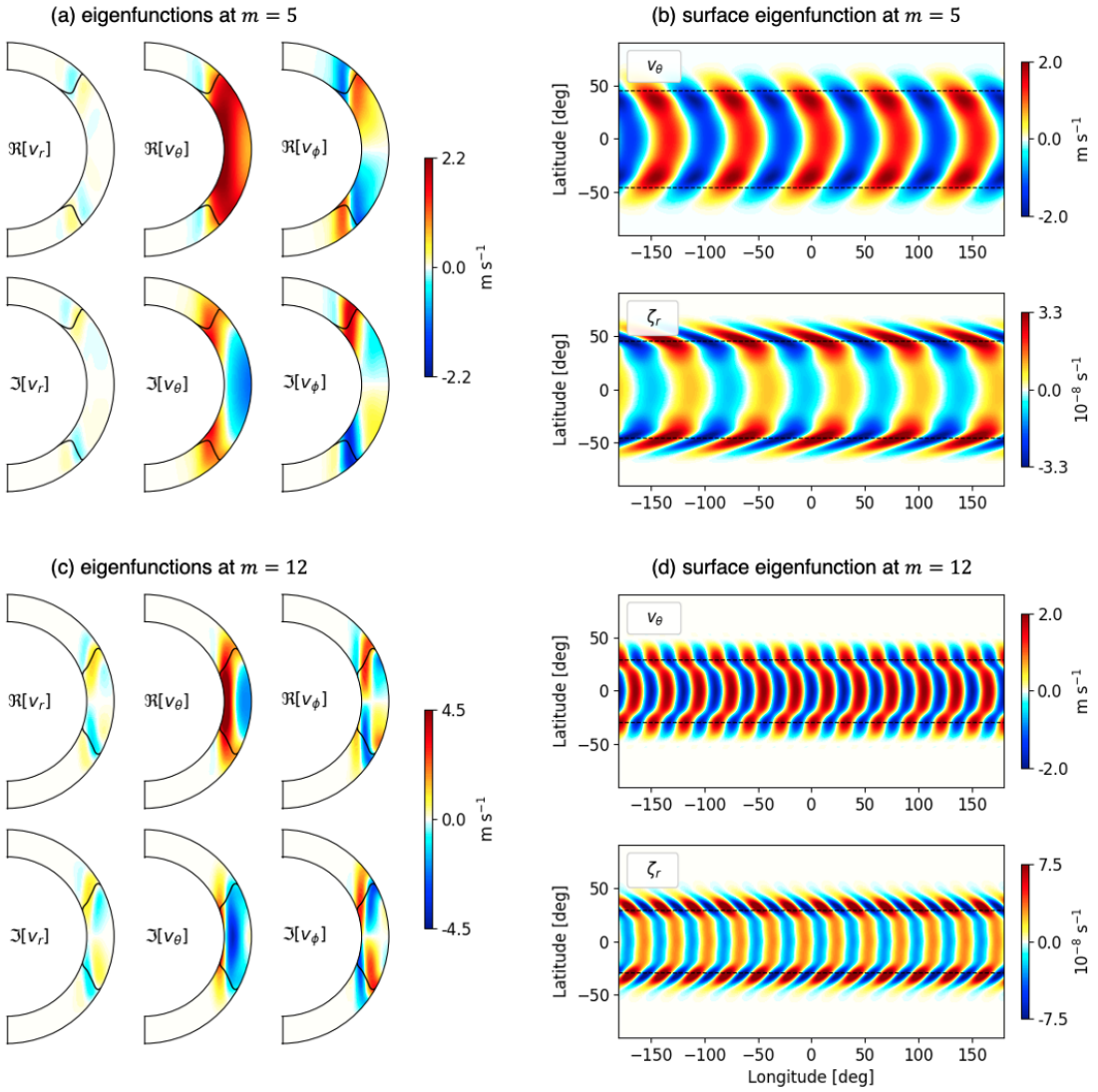

Figure 3.23: Eigenfunctions of the equatorial Rossby modes with no radial nodes ($n = 0$). (a) Real (upper) and imaginary (lower) eigenfunctions of three components of velocity shown in a meridional plane for $m = 5$. The eigenfunctions are normalized such that the maximum latitudinal velocity is 2 m s^{-1} at the surface. The solid black line indicates the location of the critical latitudes where the phase speed of a Rossby modematches to the differential rotation sped. (b) Horizontal eigenfunctions of latitudinal velocity v_θ (upper) and radial vorticity ζ_r (lower) at the surface $r = 0.985R_\odot$ for $m = 5$. The horizontal black dashed lines indicate the location of the critical latitudes at the surface. (c) and (d) are the counterparts of the panels (a) and (b) for $m = 12$.

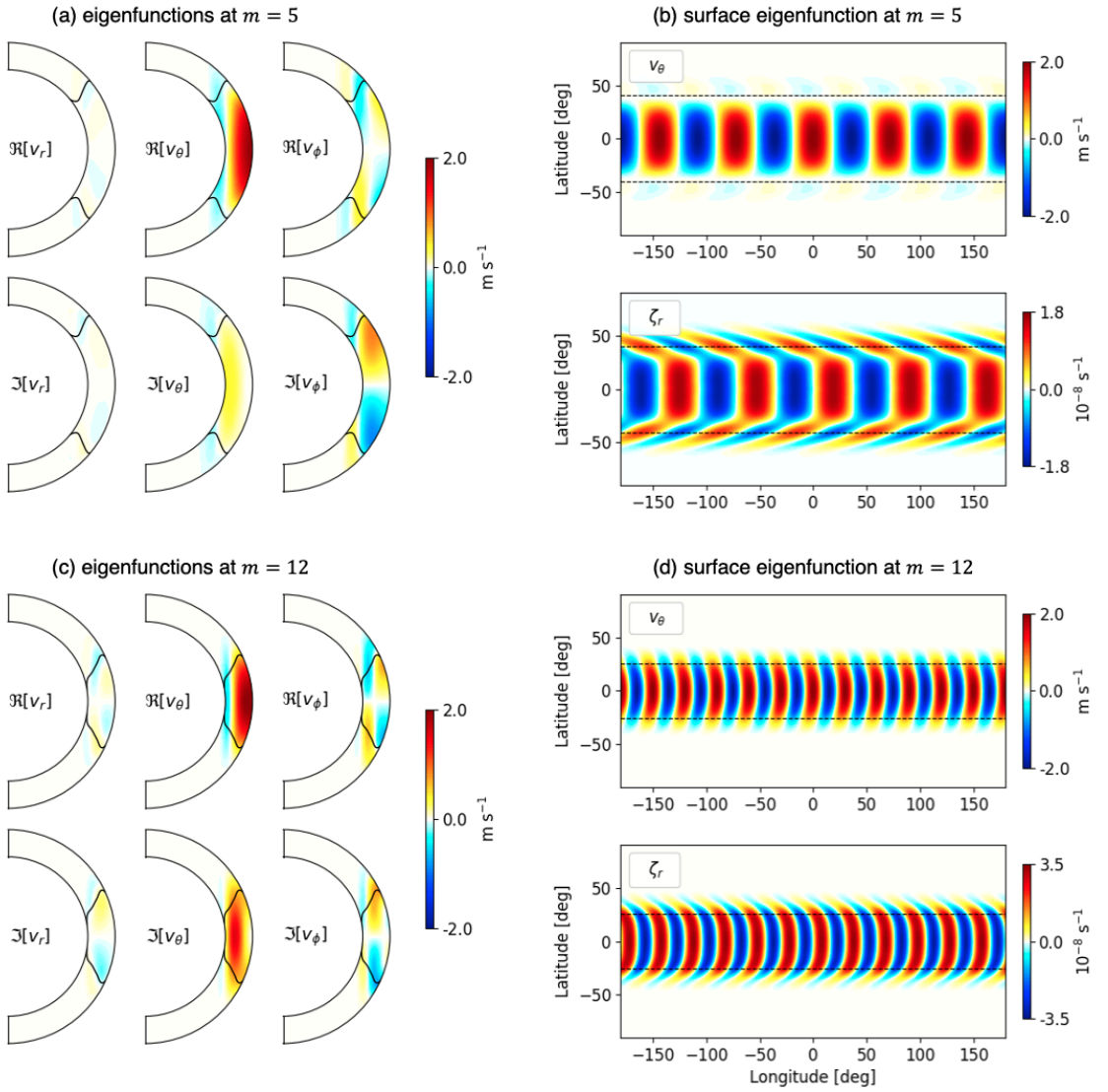

Figure 3.24: The same as Fig. 3.23 but for the equatorial Rossby modes with one radial node ($n = 1$).

3.6.1 Rossby modes with viscous critical layers

In this section, we carry out a set of calculations for $\nu = 10^{11}$ and 10^{12} cm^2 s^{-1} with the differential rotation included to study how the equatorial Rossby modes are affected by the viscous critical layers. For the sake of simplicity, the background is set to be perfectly adiabatic and the latitudinal entropy variation $\partial s_0/\partial\theta$ is switched off.

Figure 3.22a shows the dispersion relation of the equatorial Rossby modes with $n = 0$ (red) and $n = 1$ (blue) for weak (dashed) and strong (solid) viscous diffusivities, respectively. Shown in white circles, squares, and diamonds are the frequencies of the Rossby modes observed on the Sun (Löptien et al. 2018, Liang et al. 2019, Proxauf et al. 2020). The viscous diffusivity value is found to have a rather small effect on the real part of their eigenfrequencies. At $m = 3$, the observed frequency agrees almost perfectly with the $n = 0$ equatorial Rossby mode's frequency. However, for $m > 3$, the observed frequen-

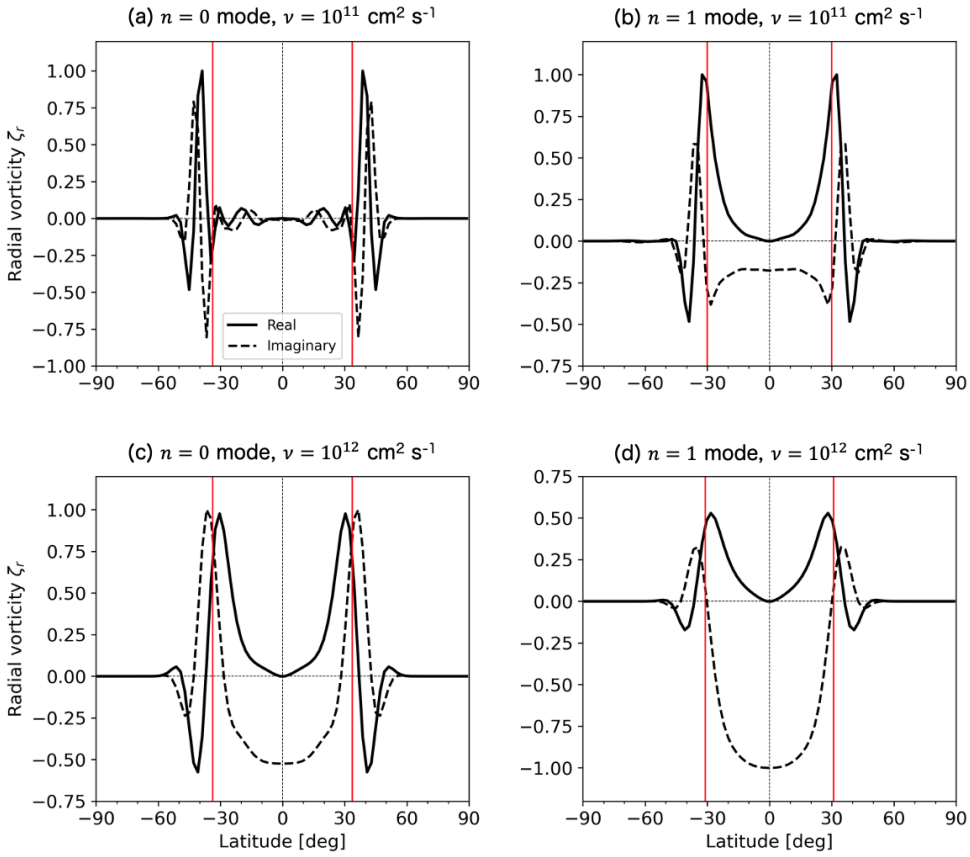

Figure 3.25: Radial vorticity ζ_r eigenfunctions at the surface ($r = 0.985R_\odot$) for $m = 8$. Left and right panels show the cases for the equatorial Rossby modes with no radial nodes ($n = 0$) and with one radial node ($n = 1$). Upper and lower panels show the cases with weak diffusion ($\nu = 10^{11}$ cm^2 s^{-1}) and strong diffusion ($\nu = 10^{12}$ cm^2 s^{-1}). Black solid and dashed lines represent real and imaginary eigenfunctions, respectively. The real part of the eigenfunctions are defined to be zero at the equator. The vertical red lines denote the location of critical latitudes where the phase speed of a Rossby mode is equal to the differential rotation velocity.

cies lie in between the frequencies of $n = 0$ and $n = 1$ modes. Figure 3.22b shows the computed eigenfrequencies in a complex plane. Unlike the $n = 1$ modes, the $n = 0$ modes are substantially damped only for $m \geq 4$, which is likely owing to the emergence of the critical latitudes that significantly modify the $n = 0$ modes' eigenfunctions.

Figure 3.23 shows the velocity eigenfunctions of the $n = 0$ modes for the case with $\nu = 10^{12}$ cm^2 s^{-1}. Figures 3.23a and c show meridional cuts through the eigenfunctions for $m = 5$ and 12, respectively. As already discussed in § 3.4, the latitudinal velocity is confined close to the base of the convection zone. With differential rotation included, they are further trapped in the equatorial region bounded by the viscous critical layers. Unlike the uniformly-rotating case, strong radial and longitudinal flows are driven around the critical latitudes, which leads to strong concentrations of z-vorticity there. Figures 3.23b and d show the latitudinal velocity v_θ (top rows) and radial vorticity ζ_r (bottom rows) at the top of the domain. They both have a similar chevron-like inclination towards the equator.

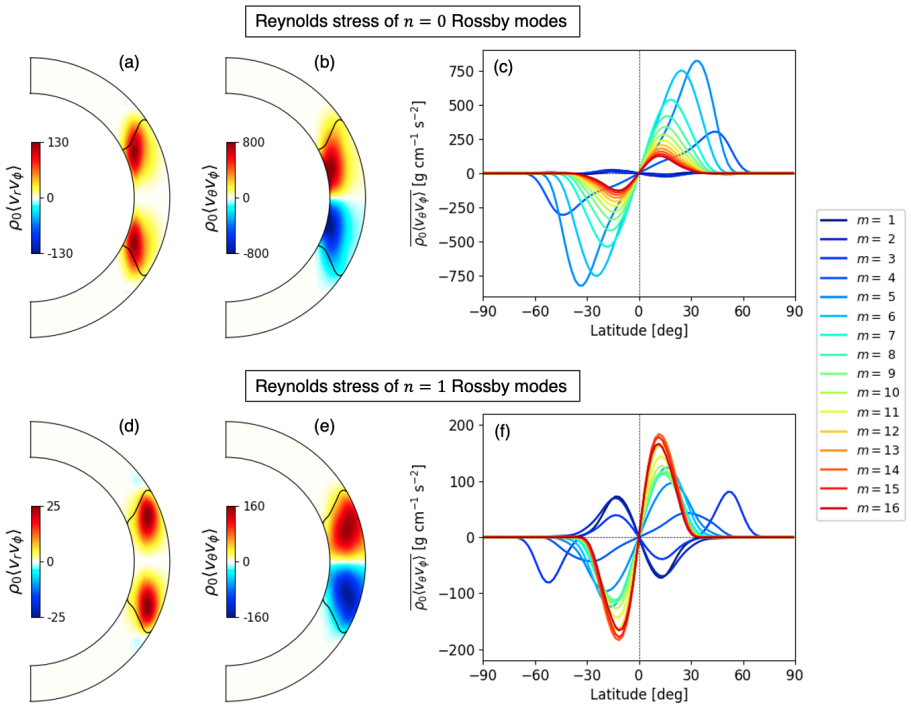

Figure 3.26: Reynolds stress components (a)(d) $\rho_0\langle v_r v_\phi\rangle$ and (b)(e) $\rho_0\langle v_\theta v_\phi\rangle$ associated with the equatorial Rossby modes for $m = 8$. The units are g cm^{-1} s^{-2}. Black solid lines denote the location of critical latitudes at each height. The eigenfunctions are normalized such that the maximum horizontal velocity at the top boundary is 2 m s^{-1}. Panels (c) and (f) show the horizontal Reynolds stress averaged over radius $\overline{\rho_0\langle v_\theta v_\phi\rangle}$ where the overbar denotes the radial average. Different colors represent different azimuthal orders. Upper and lower panels show the cases for $n = 0$ modes and $n = 1$ Rossby modes, respectively.

However, ζ_r has prominent power peaks around the critical layers.

Figure 3.24 is the same figure as Fig. 3.23 but for the $n = 1$ equatorial Rossby modes. Unlike the $n = 0$ modes, the eigenfunctions of v_θ (and ζ_r) peak at the surface and at the equator. Although the critical layers exist similarly to the $n = 0$ modes, they are found to have a rather limited impact on the $n = 1$ Rossby modes.

To see the diffusivity dependence, we show ζ_r at the surface for weak (top rows) and strong viscous diffusivities (bottom rows) in Fig. 3.25. The left and right panels are for the $n = 0$ and $n = 1$ equatorial Rossby modes, respectively. The solid and dashed lines denote the real and imaginary parts, and the vertical red line indicates the location of the critical latitudes. The phase is defined such that $\Re[\zeta_r] = 0$ at the equator and the maximum amplitudes are normalized to unity. Substantial structure is observed associated with the viscous critical layers. In general, this structure becomes broader and weaker as the viscosity ν is increased. It is also seen that amplitudes of the imaginary parts of the eigenfunctions are larger for $n = 0$ modes than for $n = 1$ modes.

Next, let us examine the impact of the net angular momentum transport by the equatorial Rossby modes under the influences of solar differential rotation. Figures 3.26a and b show the Reynolds stress components $\langle v_r v_\theta\rangle$ and $\langle v_\theta v_\theta\rangle$ for $n = 0$ modes at $m = 8$. The Reynolds stresses become substantially non-zero near the viscous critical layers. It

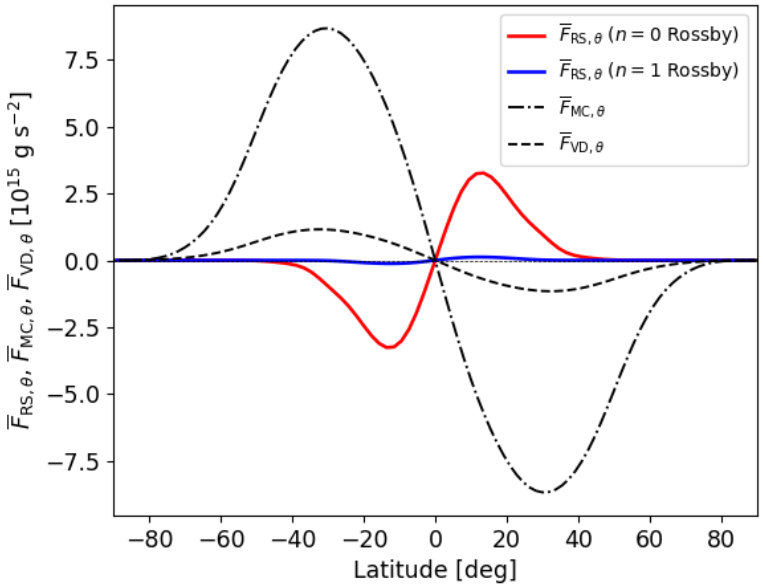

Figure 3.27: Radially averaged latitudinal angular momentum fluxes. Solid, dot-dashed, and dashed lines represent the angular momentum fluxes associated with the Reynolds stress of the equatorial Rossby modes $F_{\mathrm{RS},\theta}$, advection by meridional circulation $F_{\mathrm{MC},\theta}$, and diffusion by turbulent viscosity $F_{\mathrm{VD},\theta}$, defined by the Eqs. (3.33)–(3.35). Red and blue lines represent the equatorial Rossby modes with no radial nodes ($n = 0$) and with one radial node ($n = 1$), respectively. Here, eigenfunctions are normalized such that the maximum horizontal velocity amplitude at the surface is 2 m s^{-1}.

is striking that even $n = 0$ mode, which in the case of uniform rotation is toroidal and non-convective, can transport the angular momentum radially upward around the viscous critical layers. Latitudinally, the angular momentum is transported equatorward in both hemispheres. Figure 3.26c shows the $\langle v_\theta v_\theta \rangle$ at the surface for all m. It is seen that the correlations become small as m increases because the $n = 0$ modes are more and more confined closer to the base of the convection zone. The counterparts for $n = 1$ modes are shown in Fig. 3.26d–f. It is clear that the $n = 1$ modes also transport angular momentum radially upward and equatorward at higher m. However, unlike the $n = 0$ modes, the Reynolds stress $\langle v_\theta v_\theta \rangle$ peaks slightly below the surface. Therefore, the correlation at the surface becomes more prominant as m increases, as shown in Fig. 3.26f.

It is instructive to examine how significant the angular momentum transport by these equatorial Rossby modes can be in the Sun. To this end, we consider the so-called gyroscopic pumping equation (e.g., Elliott et al. 2000, Miesch and Hindman 2011)

$$\nabla \cdot (\boldsymbol{F}_{\mathrm{RS}} + \boldsymbol{F}_{\mathrm{MC}} + \boldsymbol{F}_{\mathrm{VD}}) = 0, \tag{3.32}$$

where $\boldsymbol{F}_{\mathrm{RS}}$, $\boldsymbol{F}_{\mathrm{MC}}$, and $\boldsymbol{F}_{\mathrm{VD}}$ are the angular momentum fluxes transported by the Reynolds stress, meridional circulation, and turbulent viscous diffusion, respectively. They are de-

fined by

$$\boldsymbol{F}_{\rm RS} = \rho_0 r \sin\theta \, \langle v_\phi \boldsymbol{v}_{\rm m} \rangle, \tag{3.33}$$

$$\boldsymbol{F}_{\rm MC} = \rho_0 (r \sin\theta)^2 \Omega \, \boldsymbol{v}_{\rm m}, \tag{3.34}$$

$$\boldsymbol{F}_{\rm VD} = -\rho_0 \nu (r \sin\theta)^2 \, \nabla\Omega, \tag{3.35}$$

where $\boldsymbol{v}_{\rm m}$ is the meridional flow. Figure 3.27 shows the each term of the latitudinal component of the Eq. (3.32) averaged over radius. The eigenfunctions are normalized such that the maximum horizontal velocity amplitude at the surface is 2 m s^{-1}, as inferred from observations (Löptien et al. 2018). To estimate $F_{{\rm MC},\theta}$ (black dot-dashed line), we use the observational meridional circulation data obtained by Gizon et al. (2020a). For $F_{{\rm VD},\theta}$ (black dashed line), we assume the spatially-uniform viscosity of $\nu = 10^{12}$ cm^2 s^{-1}. It is shown that the equatorward angular momentum transport by the Reynolds stress is balanced by the poleward transport by meridional flow and by turbulent diffusion. The amplitude of $F_{{\rm RS},\theta}$ associated with $n = 1$ modes are found to be almost negligible, whereas that of $n = 0$ modes is substantial and accounts for about 30 – 40 % of the other two contributions $F_{{\rm MC},\theta} + F_{{\rm VD},\theta}$. The difference between the $n = 0$ and $n = 1$ modes comes from that fact that the velocity eigenfunctions of the $n = 1$ modes peak at the surface, whereas those of the $n = 0$ modes peak near the base. Therefore, when the eigenfunctions are normalized by the surface velocity speed, only $n = 0$ modes become important for the convection zone dynamics. Some caution must be given here as the eigenfunctions can also be highly sensitive to various model parameters (such as ν and δ), and thus, a different set of parameters might lead to a different angular momentum balance. Furthermore, the model assumes that the diffusivities are uniform and isotropic, which will also affect the eigenfunctions. Nonetheless, it is suggested that the equatorial Rossby modes might potentially play a role in transporting the angular momentum equatorward in the Sun.

3.6.2 Effect of baroclinicity on high-latitude inertial modes

We assume the solar differential rotation is in thermal wind balance; where the deviation from the Taylor-Proudman's state is balanced by the latitudinal entropy variation (e.g., Rempel 2005, Miesch et al. 2006, Brun et al. 2011). In other words, the solar convection zone is essentially baroclinic. Since the high-latitude modes (topographic Rossby waves) are located at high latitudes, they are subject to the imposed baroclinicity in the convection zone and potentially become unstable (Knobloch and Spruit 1982, Spruit and Knobloch 1984, Kitchatinov 2013, Gilman and Dikpati 2014).

In this section, we study the effect of baroclinicity in the convection zone on the high-latitude inertial modes by varying the amplitude of the imposed latitudinal entropy gradient. Of particular interest is this effect on the $m = 1$ mode with north-south antisymmetric ζ_z. Here, we assume the latitudinal dependence of the background entropy profile is

$$\frac{\partial s_0}{\partial \theta} = -|\Delta_\theta s| \, \sin 2\theta, \tag{3.36}$$

where $\Delta_\theta s = s_{0,{\rm eq}} - s_{0,{\rm pole}} (< 0)$ represents the entropy difference between the cooler equator and the hotter poles. For simplicity, the radial dependence is ignored (s_0 is uniform in radius and thus convectively neutral). We use moderately viscous and thermal diffusivities $\nu = \kappa = 10^{12}$ cm^2 s^{-1}.

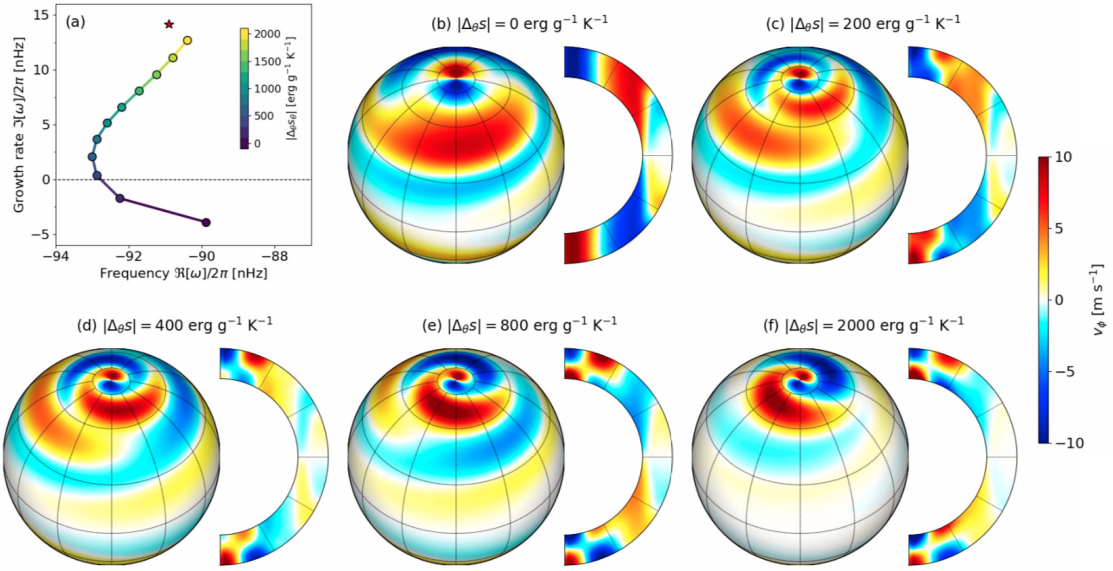

Figure 3.28: (a) Eigenfrequencies of north-south ζ_z-antisymmetric high-latitude mode (topographic Rossby mode) at $m = 1$ for different amplitudes of the latitudinal entropy variation $\Delta_\theta s$. The red star is for the case with a realistic latitudinal entropy gradient that depends on position, estimated by the Eq. (3.37). The solar differential rotation is included. The background stratification is adiabatic ($\delta = 0$) and the diffusivities are set to $\nu = \kappa = 10^{12}$ cm^2 s^{-1}. (b)-(f) Eigenfunctions of the longitudinal velocity v_ϕ at the surface ($r = 0.985 R_\odot$) and at the central meridian for some selected Δs_θ. The eigenfunctions are normalized so that the maximum flow amplitudes at the surface is $v_\phi = 10$ m s^{-1}.

Figure 3.28a shows the eigenfrequencies of the $m = 1$ north-south ζ_z-antisymmetric high-latitude modes in a complex plane with varying $|\Delta_\theta s|$ from 0 to 2000 erg g^{-1} K^{-1}. It is shown that, as the baroclinicity is increased, the modes become unstable ($\Im[\omega] > 0$). In this sense, these modes can also be called baroclinic (Rossby) modes. Figures 3.28b–f show the eigenfunctions of v_ϕ both at the surface and at the central meridian for different values of $\Delta_\theta s$. It is clearly seen that, as $|\Delta_\theta s|$ increases and the high-latitude mode becomes more and more baroclinically unstable, it begins to exhibit a spiralling flow structure around the poles. The spatial extent and the tilt of this spiral agree strikingly well with the observations, see Hathaway and Upton (2021) and Gizon et al. (2021).

In order to assess if the baroclinicity in the Sun is large enough for the baroclinic instability to occur, we estimate the latitudinal entropy variation using the helioseismically-constrained differential rotation profile using,

$$\frac{g}{c_\mathrm{p}} \frac{\partial s_0}{\partial \theta} = r^2 \sin\theta \, \frac{\mathrm{d}(\Omega^2)}{\mathrm{d}z}. \tag{3.37}$$

With this realistic baroclinicity included in our model (Eq. 3.20), we find that the $m = 1$ high-latitude mode is self-excited: The growth rate is $\Im[\omega]/2\pi = 14.1$ nHz, which translates into the growing time scale of 4.3 months. This may explain why the high-latitude flow feature on the Sun has a much larger flow amplitude than the equatorial Rossby modes. Its mode frequency is $\Re[\omega]/2\pi = -90.9$ nHz (measured in the Carrington

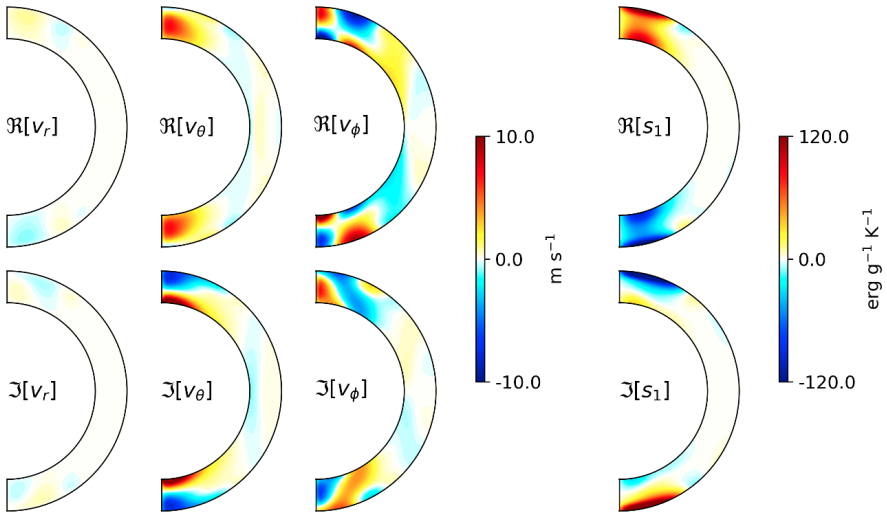

Figure 3.29: Eigenfunctions of v_r, v_θ, v_ϕ, and s_1 of the $m = 1$ north-south ζ_z-antisymmetric high-latitude inertial mode with the solar differential rotation and the corresponding latitudinal entropy gradient (Eq. 3.37) included. The background stratification is adiabatic ($\delta = 0$) and the diffusivities are set to $\nu = \kappa = 10^{12}$ cm^2 s^{-1}. The eigenfunctions are normalized such that the maximum v_ϕ is 10 m s $^{-1}$ at the surface.

frame), which is close to the observed propagation frequency of the high-latitude flow feature of −86.3 nHz (Gizon et al. 2021). The eigenfunctions of this $m = 1$ mode are shown in Fig. 3.29. The mode is characterized by its dominant z-vortical motion and is quasi-toroidal (the vertical flow is about 10 times weaker than the horizontal ones). It is clearly seen that, unlike the case without baroclinicity, a strong entropy perturbation is associated with this mode.

3.7 Summary

In this paper, we have presented a linear modal analysis of the oscillations of the solar convection zone at low frequencies. Our main findings are summarized as follows.

One effect of turbulent diffusion is to radically change the radial force balance of the $n = 0$ equatorial Rossby modes. The modes are confined closer to the base of the convection zone and their eigenfunctions deviate strongly from the well-known r^m radial dependence. When the solar differential rotation is taken into account, viscous critical layers are formed in latitudes where the phase speed of the equatorial Rossby mode is equal to the differential rotation speed. Strong radial and longitudinal flows are present in the viscous critical layers and the eigenfunctions are complex, implying non-zero Reynolds stresses.

We find "mixed Rossby modes" which share properties of the $n = 1$ equatorial Rossby modes and the north-south ζ_z-antisymmetric columnar convective modes. Unlike the $n = 0$ equatorial Rossby modes, these "mixed modes" are almost unaffected by the presence of solar differential rotation and strong viscous diffusivity. The retrograde frequencies of the observed Rossby modes of the Sun have values in between the model eigenfrequencies of

the $n = 0$ and $n = 1$ modes for $m \geq 5$ (see Fig. 3.22a).

We have further demonstrated that the $m = 1$ high-latitude mode can be explained in terms of a topographic Rossby mode modified by differential rotation and a latitudinal entropy gradient. When these are taken into account, the mode is baroclinically unstable and the eigenfunction at the surface matches the observations with the correct geometry, including the correct sense for the spiral seen in v_ϕ.

Several simplifying assumptions were made in this study. For instance, the viscous and thermal diffusivities, ν and κ, and the superadiabaticity δ were all assumed to be spatially uniform, which is not realistic. Moreover, we set the bottom and top boundaries at $(r_{\rm min}, r_{\rm max}) = (0.71R_\odot, 0.985R_\odot)$ and thus both the tachocline and the near-surface shear layer of the Sun were excluded from our model. Future work will be to include the radiative interior and the photosphere and to allow for a radial dependence of ν, κ and δ. In addition, it will be important to compare the present results to modes extracted from three-dimensional numerical simulations of rotating convection in the strongly non-linear regime. The aim is to have a physical understanding of all the modes in the low-frequency spectrum and thus a reliable identification of the observed modes, including the critical-latitude modes.

Acknowledgements

We thank A.C. Birch and B. Proxauf for helpful discussions. YB did most of the work, RHC and LG provided supervision. YB is a member of the International Max-Planck Research School for Solar System Science at the University of Göttingen. We acknowledge support from ERC Synergy Grant WHOLE SUN 810218. YB is the beneficiary of a long-term scholarship program for degree-seeking graduate students abroad from the Japan Student Services Organization (JASSO).

3.8 Appendix

3.8.1 Potential vorticity conservation and β-effects

Rossby waves are inertial waves in a rotating fluid that are rooted in the conservation law of potential vorticity (Ertel 1942, Green 1970, Müller 1995). In this appendix, we explain the physical picture of Rossby wave propagation in a uniformly-rotating shell on the basis of potential vorticity conservation, which might be unfamiliar to solar physics community. The potential vorticity Π is defined as (Müller 1995, Miesch 2005),

$$\Pi = \frac{(\boldsymbol{\zeta} + 2\boldsymbol{\Omega}_0) \cdot \nabla s}{\rho}, \tag{3.38}$$

where $\boldsymbol{\zeta} = \nabla \times \boldsymbol{v}$ is the vorticity, $\boldsymbol{\Omega}_0$ is the uniform angular velocity, and s is the specific entropy. Thus, Π denotes the component of absolute vorticity (sum of fluid and planetary vorticities) perpendicular to an isentropic surface per unit density. It can be shown that Π is materially conserved,

$$\frac{D\Pi}{Dt} = 0, \tag{3.39}$$

in the idealized case where dissipation, the Lorentz force, and internal radiative heating can all be ignored. Several types of Rossby waves can be derived from this conservation law, each based on a particular "β effect".

Planetary β-effect

First, let us consider ideal situations. For instance, if the entropy is constant over a spherical surface then

$$\frac{D}{Dt}(\zeta_r + 2\Omega_0 \sin\theta) = 0, \tag{3.40}$$

holds for fluid motions on this spherical surface (toroidal). The main terms of the linearized equation are then

$$\frac{\partial \zeta_r}{\partial t} \approx \beta v_\theta, \tag{3.41}$$

where

$$\beta = \frac{2\Omega_0 \sin\theta}{r}, \tag{3.42}$$

is the so-called planetary β-effect of the classical Rossby wave and encapsulates the latitudinal dependence of the tangential component of the Coriolis force (e.g., Vallis 2006). The wave propagation mechanism may be explained as follows. Consider a vortex with $\zeta_r > 0$. In the retrograde (prograde) side of the edge of the vortex, we have southward flow, i.e., $v_\theta > 0$ (northward flow, $v_\theta < 0$). Thus, the vortex shrinks (broadens) on the retrograde (prograde) side of the vortex according to Eq. (3.41) because $\beta > 0$ at all latitudes. Owing to the change in the vortex size (Rossby radius) associated with v_θ, the

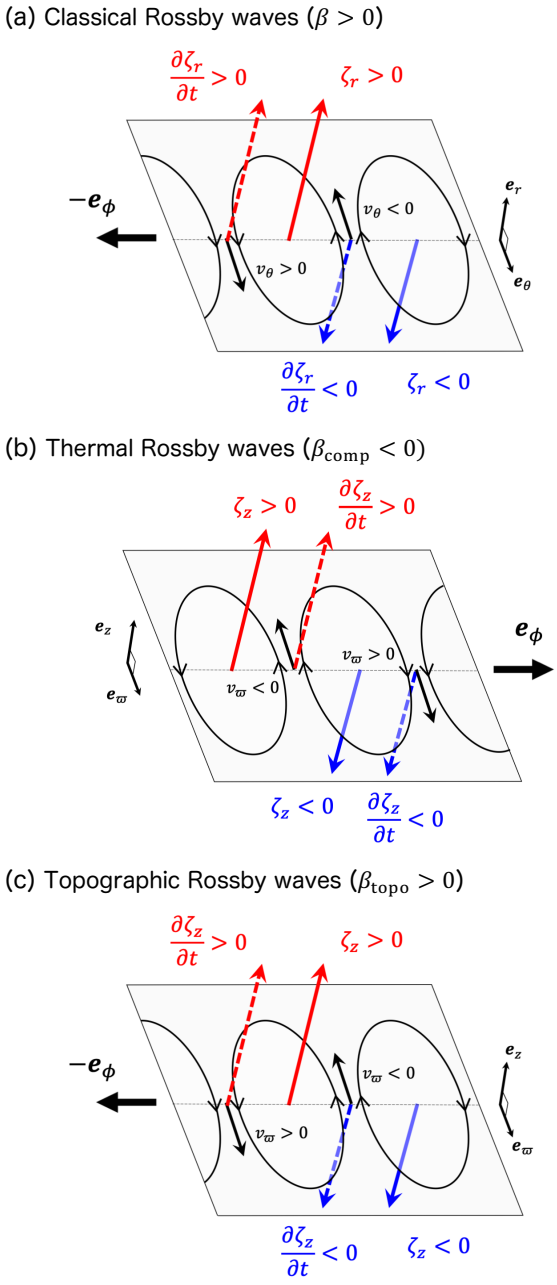

Figure 3.30: Schematic illustration explaining the propagation mechanism of Rossby waves. The planes in panels (a), (b) and (c) are the planes inside the sphere shown in Fig. 3.31. (a) Classical Rossby waves are radial vorticity waves such that $\partial\zeta_r/\partial t \approx \beta v_\theta$ with $\beta > 0$. The propagation direction (retrograde, $-\boldsymbol{e}_\phi$) is denoted by the thick black arrow. (b) Thermal Rossby waves are z-vorticity waves such that $\partial\zeta_z/\partial t \approx \beta_{\mathrm{comp}} v_\varpi$ with $\beta_{\mathrm{comp}} < 0$ outside the tangent cylinder, propagating in a prograde direction. (c) Topographic Rossby waves are z-vorticity waves such that $\partial\zeta_z/\partial t \approx \beta_{\mathrm{topo}} v_\varpi$ with $\beta_{\mathrm{topo}} > 0$ inside the tangent cylinder, propagating in a retrograde direction.

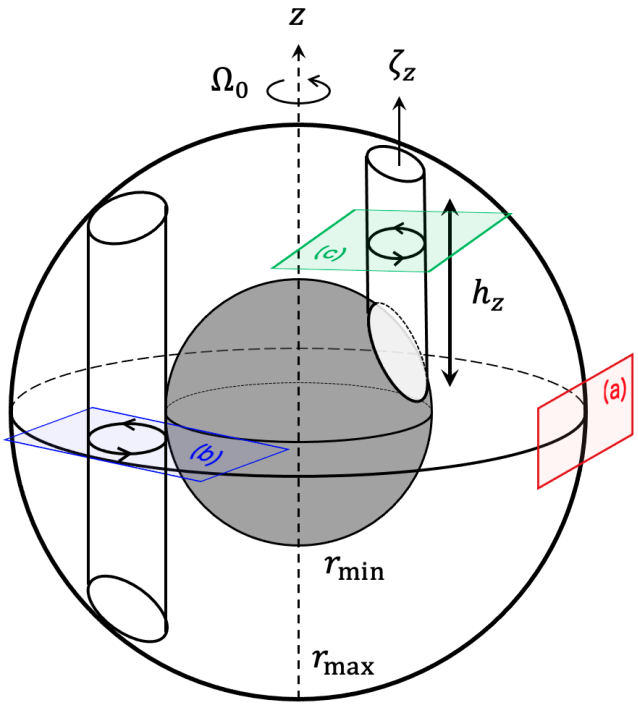

Figure 3.31: Sketch illustrating a z-vortex tube inside the tangential cylinder. The red, blue, and green planes show the locations of classical Rossby waves, thermal Rossby waves, and topographic Rossby waves discussed in Fig. 3.30.

vortex propagates in a retrograde (opposite to rotation) direction. The same discussion applies to the negative vortex $\zeta_r < 0$ as well. This is also schematically illustrated in Fig. 3.30a.

Compressional β-effect

Next, we discuss the propagation mechanism of z-vorticity waves. We adopt a cylindrical coordinate system ($\varpi = r\sin\theta$, ϕ, z) and consider a vortex tube in the z-direction inside the convection zone as illustrated in Fig. 3.31. Assuming that the specific entropy is uniform over the equatorial plane ($\varpi\phi$-plane), z-component (parallel to the rotational axis) of the potential vorticity becomes a conserved quantity,

$$\frac{D}{Dt}\left(\frac{\zeta_z + 2\Omega_0}{\rho}\right) = 0. \tag{3.43}$$

Now, for the sake of simplicity, let us also assume that the density is dominantly stratified in the ϖ-direction outside the tangential cylinder. We can then linearize Eq. (3.43) to obtain

$$\frac{\partial \zeta_r}{\partial t} \approx \beta_{\rm comp} v_\varpi, \tag{3.44}$$

where

$$\beta_{\rm comp} = 2\Omega_0 \frac{{\rm d}\ln\rho}{{\rm d}\varpi}, \tag{3.45}$$

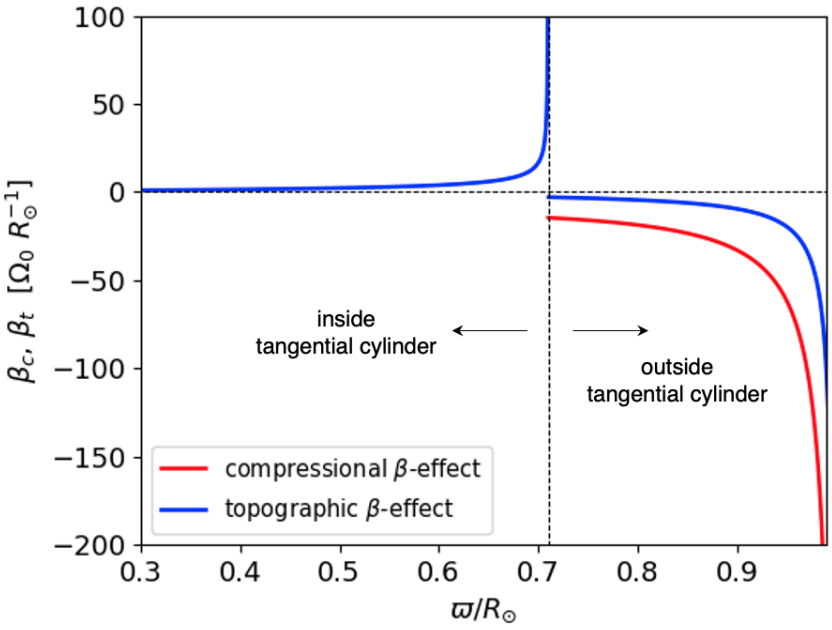

Figure 3.32: (Red) Compressional β-effect coefficients $\beta_{\rm comp}$ defined by the Eq. (3.45) outside the tangential cylinder at the equator, and (Blue) topographic β-effect coefficients defined by the Eq. (3.49) inside the tangential cylinder. Vertical dotted line denotes the location of the base of the convection zone.

is called "compressional" β-effect. This effect originates from the background density stratification (Glatzmaier et al. 2009, Verhoeven and Stellmach 2014): when the background density changes, the fluid vorticity ζ_z is forced to change in order to conserve local angular momentum. The type of wave originating from the compressional β-effect is sometimes called the "compressional Rossby wave" (Ong and Roundy 2020). However, it is more often referred to as a "thermal Rossby wave" in the solar literature (Miesch 2005, Miesch et al. 2008, Verhoeven and Stellmach 2014, Matilsky et al. 2020) since it is in many cases thermally driven. Given that $\beta_{\rm comp}$ is negative outside the tangential cylinder, these waves propagate in a prograde direction near the equator, as schematically illustrated in Fig. 3.30b.

Topographic β-effect

Last, we consider the z-vorticity waves inside the tangential cylinder. Since their fluid motions can be approximated to be toroidal, we restrict our discussion to incompressible fluids in this section. The Eq.(3.43) is now reduced to

$$\frac{D}{Dt}\left(\zeta_z + 2\Omega_0\right) = 0. \tag{3.46}$$

The vertical height h_z of the cylinder inside the convection zone can be expressed as a function of ϖ

$$h_z = \sqrt{r_{\rm max}^2 - \varpi^2} - \sqrt{r_{\rm min}^2 - \varpi^2}, \tag{3.47}$$

where $r_{\rm min}$ and $r_{\rm max}$ are the radii of the lower and upper spherical boundaries, respectively. We now integrate the Eq.(3.46) over z-direction in the convection zone assuming that velocity is independent of z (thus the Taylor-Proudman's constraint is satisfied inside the tangential cylinder), obtaining

$$\frac{\partial \zeta_z}{\partial t} \approx \beta_{\rm topo} v_\varpi, \tag{3.48}$$

where

$$\beta_{\rm topo} = 2\Omega_0 \frac{{\rm d} \ln h_z}{{\rm d}\varpi}, \tag{3.49}$$

is called "topographic" β-effect. This effect comes from the curvature of the lower and upper spherical shells. Owing to the impenetrable boundary condition at the top and bottom, z-vortex tubes are forced to stretch or shorten when displaced cylindrically inwards or outwards in ϖ direction, which brings perturbations in the z-vorticity ζ_z. The type of Rossby wave originating from the topographic β-effect is called a "topographic Rossby wave" (e.g., Vallis 2006). Inside the tangential cylinder, β_t is positive as shown in Fig. 3.32. Therefore, topographic Rossby waves propagate in a retrograde direction as illustrated in Fig. 3.30c.

4 Amplitudes of equatorial vorticity modes from a nonlinear rotating convection simulation

Abstract

Several types of inertial modes have been detected on the Sun. Properties of these inertial modes have been studied in the linear regime but have not been studied in nonlinear simulations of solar rotating convection. Comparing the nonlinear simulations, the linear theory, and the solar observations is important to better understand the differences between the models and the real Sun. We wish to detect and characterize the modes present in a nonlinear numerical simulation of solar convection, in particular to understand the amplitudes and lifetimes of the modes. We developed a code with a Yin-Yang grid to carry out fully-nonlinear numerical simulations of rotating convection in a spherical shell. The stratification is solar-like up to the top of the computational domain at 0.96 $R_\odot$. The simulations cover a duration of about 15 solar years, which is more than the observational length of the Solar Dynamics Observatory (SDO). Various large-scale modes at low frequencies (comparable to the solar rotation frequency) are extracted from the simulation. Their characteristics are compared to those from the linear model and to the observations. Among other modes, both the equatorial Rossby modes and the columnar convective modes are seen in the simulation. The columnar convective modes, with north-south symmetric longitudinal velocity v_ϕ, contain most of the large-scale velocity power outside the tangential cylinder and substantially contribute to the heat and angular momentum transport near the equator. Equatorial Rossby modes with no radial node ($n = 0$) are also found: They have the same spatial structures as the linear eigenfunctions. They are stochastically excited by convection and have the amplitudes of a few m s^{-1} and mode linewidths of about 20–30 nHz, which are comparable to those observed on the Sun. We also confirm the existence of the "mixed Rossby modes" between the equatorial Rossby modes with one radial node ($n = 1$) and the columnar convective modes with north-south antisymmetric v_ϕ in our nonlinear simulation, as predicted by the linear eigenmode analysis. We also see the high-latitude mode with $m = 1$ in our nonlinear simulation but its amplitude is much weaker than that observed on the Sun.

This chapter reproduces the article *Theory of solar oscillations in the inertial frequency range: Amplitudes of equatorial modes from a nonlinear rotating convection simulation* by Y. Bekki, R.H. Cameron, and L. Gizon, published in Astronomy and Astrophysics 666, A135 (2022). DOI: https://doi.org/10.1051/0004-6361/202244150. Contribution: Y. Bekki did most of the work.

4.1 Introduction

Large-scale convection in the Sun is still poorly understood (e.g., Hanasoge et al. 2012, Gizon and Birch 2012). Numerical simulations are unable to explain how thermal energy and angular momentum are transported inside the Sun's convection zone in a way that is consistent with the observations (e.g., Karak et al. 2018, Nelson et al. 2018). This problem is often called the "convective conundrum" and is regarded as one of the most important open questions in solar physics (e.g., O'Mara et al. 2016, Brandenburg 2016, Hanasoge et al. 2020, Vasil et al. 2021).

Recent observations indicate that a significant component of the large-scale non-axisymmetric solar flows are due to inertial modes of oscillation (Löptien et al. 2018, Gizon et al. 2021). The restoring force for these global-scale low-frequency modes of oscillation is the Coriolis force, and thus their oscillation periods are comparable to the solar rotation period ($\approx$ 27 days). In addition to the high-frequency acoustic modes, these inertial modes are expected to be useful as a tool to probe the interior of the Sun (Gizon et al. 2021, Bekki et al. 2022b).

The inertial modes observed and identified on the Sun include the equatorial Rossby modes, the high-latitude modes, and the critical-latitude modes (Löptien et al. 2018, Gizon et al. 2021, Bekki et al. 2022b, Fournier et al. 2022). The high-frequency retrograde modes recently reported by Hanson et al. (2022) are also likely inertial modes. Simplified theoretical studies have been carried out in the linear regime under the assumption of uniform rotation (Provost et al. 1981, Saio 1982, Wolff and Blizard 1986, Damiani et al. 2020) and in the case of differential rotation (Baruteau and Rieutord 2013, Gizon et al. 2020b, Bekki et al. 2022b, Fournier et al. 2022). However, there has been no study in the fully-nonlinear regime where turbulent convection strongly interacts with these inertial modes. Nonlinear simulations are also required in order to understand the excitation mechanism and the amplitudes of these modes.

Another interesting type of large-scale vorticity modes that might be relevant to the Sun are columnar convective modes (or "thermal Rossby waves"). They have been repeatedly predicted in numerical models of solar rotating convection (e.g., Gilman and Glatzmaier 1981, Glatzmaier 1984, Miesch et al. 2000, 2008) but they have not been observed on the Sun. A recent linear eigenmode analysis has revealed that the equatorial Rossby modes with one radial node ($n = 1$) share properties with the columnar convective modes with north-south antisymmetric z-vorticity (Bekki et al. 2022b), where z is the coordinate along the rotational axis. These so-called "mixed Rossby modes" have not yet been studied using nonlinear rotating convection simulations.

In this paper, we identify and characterize properties of these low-frequency modes of oscillation in a numerical simulation of solar-like rotating convection and study how they are affected by turbulent convection. We extract these modes from a fully nonlinear simulation and compare their mode properties such as dispersion relations and eigenfunctions with those of the linear eigenmodes reported by Bekki et al. (2022b). In addition, we look at mode amplitudes which cannot be discussed in the linear regime.

The organization of the paper is as follows. In §4.2, we shortly review previous studies on the various types of solar inertial modes. In §4.3, our numerical model is explained in detail. We also describe the analysis method for extracting the global-scale modes of oscillation from a temporal series of simulation data. We report the extracted columnar

convective modes in §4.5.1, and the equatorial Rossby modes in §4.5.2. The newly-discovered mixed Rossby mode is presented in §4.5.3. In all cases, the extracted modes are compared with the results of linear eigenmode analysis. The transport properties by these modes are discussed in §4.6. Finally, possible implications are discussed with concluding remarks in §4.7.

4.2 Inertial modes on the Sun

In this paper we will primarily focus on the equatorial Rossby modes (§ 4.2.1), the columnar convective modes (§ 4.2.2), and the "mixed Rossby modes" (§ 4.2.3). The other inertial modes discussed in § 4.2.4 are beyond the scope of the current paper.

4.2.1 Equatorial Rossby modes

The classical Rossby modes (Rossby 1939, 1940) are modes of radial vorticity originating from the planetary β-effect. In the case of a uniformly-rotating sphere, these modes propagate in the retrograde direction (opposite to rotation) in a co-rotating frame. They are essentially incompressible modes and the associated motion is quasi-toroidal. In the solar and stellar context, they are also commonly known as r modes (e.g., Papaloizou and Pringle 1978, Saio 1982).

The existence of these Rossby modes on the Sun is well established (Löptien et al. 2018, Hanasoge and Mandal 2019, Liang et al. 2019, Proxauf et al. 2020, Mandal and Hanasoge 2020, Hanson et al. 2020, Hathaway and Upton 2021, Gizon et al. 2021, Mandal et al. 2021). They are observed for azimuthal orders in the range $3 \leq m \leq 15$ and follow the dispersion relation of the classical sectoral ($l = m$) Rossby modes, where m is the azimuthal order and l is the spherical degree. It is found that these equatorial Rossby modes contribute a significant fraction of the large-scale horizontal velocity power at low latitudes.

4.2.2 Columnar convective modes

Another type of modes with large-scale vorticity, which might be relevant to the Sun, are the columnar convective modes. These modes are prograde-propagating convective columns that are strongly rotationally-constrained and are thus aligned parallel to the rotation axis (e.g., Unno et al. 1989). They are also known as "thermal Rossby waves" particularly among the geophysical fluid dynamics community because they are thermally (convectively) driven and they result from the conservation of potential vorticity (Busse 1970, 2002). When the term "thermal Rossby waves" was first introduced by Busse and Or (1986), an incompressible fluid was considered and thus the propagation frequency of these convective modes is purely set by the "topographic β effect" originating from the curvature of the spherical boundaries. However, when it comes to highly-stratified compressible fluids such as the interiors of the Sun and stars, there is an additional β effect, namely, the "compressional β effect" originating from the strong background density stratification (Glatzmaier and Gilman 1981, Ingersoll and Pollard 1982, Evonuk 2008, Glatzmaier et al. 2009, Evonuk and Samuel 2012, Verhoeven and Stellmach 2014,

Ong and Roundy 2020). In the solar and stellar physics community, the term "thermal Rossby waves" has been sometimes used to describe the prograde-propagating convective columns whose propagation frequencies are in fact affected by both the topographic and compressional β effects (Miesch et al. 2008). In order to avoid this ambiguity, we will follow the convention of Bekki et al. (2022b) and will primarily use the term "columnar convective modes" in this paper.

In numerical simulations of solar-like rotating convection simulations, the columnar convective modes can be seen as north-south aligned downflow lanes across the equator at the surface (e.g., Miesch et al. 2008, Bessolaz and Brun 2011, Matilsky et al. 2020). They are often called "banana cells" and are regarded as the most efficient convective structure in terms of the thermal energy transport under the rotational constraint (e.g., Miesch et al. 2000, Brun et al. 2004, Miesch et al. 2008, Käpylä et al. 2011, Gastine et al. 2013, Hotta et al. 2015a, Featherstone and Hindman 2016a, Hindman et al. 2020). Furthermore, they are also believed to play a significant role in transporting the angular momentum equatorward to maintain the differential rotation (e.g., Gilman 1986, Miesch et al. 2000, Balbus et al. 2009, Matilsky et al. 2020). However, despite their significance, the columnar convective modes have never been successfully detected on the Sun. It still remains unclear whether they really exist in the deep convection zone and are not visible at the surface for some reason, or if they are simply absent in the Sun.

The dispersion relation and eigenfunctions of the columnar convective modes were first derived by Glatzmaier and Gilman (1981) using a one-dimensional cylinder model, and recently, by Bekki et al. (2022b) using a more realistic two-dimensional model of the solar convection zone. A local analysis of these modes has also been carried out by Hindman and Jain (2022) in the context of low-mass stars. As far as the authors recognize, however, there is no such a study that compares the linear dispersion relation and eigenfunctions of the columnar convective modes with those found in a fully-nonlinear simulation of rotating convection of the Sun.

4.2.3 Mixed Rossby modes

Using the linear model of solar inertial oscillations, Bekki et al. (2022b) have recently found that the equatorial Rossby modes with one radial node ($n = 1$) and the columnar convective modes with north-south antisymmetric z-vorticity ζ_z are mixed with each other. This newly-discovered "mixed Rossby mode" has a dispersion that asymptotically (at large azimuthal wavenumbers m) approaches to that of the equatorial Rossby mode with no radial node ($n = 0$) for the retrograde-propagating part ($\omega < 0$) and to that of the north-south ζ_z-symmetric columnar convective modes for the prograde-propagating part ($\omega > 0$). Here, ω is the frequency measured in the rotating frame. Due to this mode mixing, the $n = 1$ equatorial Rossby modes (retrograde-propagating "mixed Rossby modes") become partially convective and have substantial radial motions. This is in contrast to the $n = 0$ modes where fluid motions are quasi-toroidal. Therefore, it is expected that the "mixed Rossby modes" might play a role in transporting thermal energy and angular momentum in the Sun's convection zone.

4.2.4 Other inertial modes

At higher latitudes (above 60°), modes with $1 \leq m \leq 4$ were also detected, which were shown to be global modes of inertial oscillation of the full convection zone. In particular, the $m = 1$ high-latitude mode can be observed at all latitudes (with much smaller amplitude) with the exact same frequency. This $m = 1$ mode has the largest amplitude and is associated with a spiralling flow pattern in the longitudinal velocity around the poles. It is the explanation for the observations reported by Hathaway et al. (2013) and Bogart et al. (2015). The dispersion relation and the eigenfunctions of the high-latitude modes can be well reproduced by a linear analysis of inertial oscillations in a realistic solar convection zone model (Bekki et al. 2022b).

At middle latitudes, additional retrograde inertial modes with $m \leq 10$ have been observed near their critical latitudes, where the mode angular frequencies are equal to the differential rotation rate (Gizon et al. 2021). Some of these mid-latitude modes have been identified in the linear model of Bekki et al. (2022b), see e.g. the $m = 2$ mode reported by Gizon et al. (2021). A one-dimensional linear analysis of modes on differentially rotating spheres by Fournier et al. (2022) also predicts such critical-latitude modes to be present.

Furthermore, Hanson et al. (2022) have recently reported additional low-amplitude modes of north-south antisymmetric vorticity near the equator that propagate in a retrograde direction with $8 \leq m \leq 14$. These modes are also likely inertial modes, according to the simplified linear analysis by Triana et al. (2022). Whether these modes are also present in the more realistic solar models remains to be studied.

4.3 Methods

4.3.1 Numerical model of rotating convection

We have developed a code to solve three-dimensional fully-compressible hydrodynamic equations in a rotating spherical shell. With the reduced-speed of sound approximation, the hydrodynamic equations are expressed in a spherical coordinate (r, θ, ϕ) as (e.g., Hotta et al. 2014b):

$$\frac{\partial \rho_1}{\partial t} = -\frac{1}{\xi^2}\nabla \cdot (\rho_0 \boldsymbol{v}), \tag{4.1}$$

$$\frac{\partial \boldsymbol{v}}{\partial t} = -\boldsymbol{v}\cdot\nabla\boldsymbol{v} - \frac{\nabla p_1}{\rho_0} - \frac{\rho_1}{\rho_0} g\boldsymbol{e}_r + 2\boldsymbol{v}\times\Omega_0 + \frac{1}{\rho_0}\nabla\cdot\mathcal{D}, \tag{4.2}$$

$$\begin{aligned}\frac{\partial s_1}{\partial t} = &-\boldsymbol{v}\cdot\nabla s_1 + \frac{1}{\rho_0 T_0}\nabla\cdot(\rho_0 T_0 \kappa \nabla s_1) \\ &+\frac{1}{\rho_0 T_0}(\mathcal{D}\cdot\nabla)\cdot\boldsymbol{v} + \frac{1}{\rho_0 T_0}(Q_{\rm heat} + Q_{\rm cool}),\end{aligned} \tag{4.3}$$

$$\frac{p_1}{p_0} = \gamma\frac{\rho_1}{\rho_0} + \frac{s_1}{c_{\rm v}}. \tag{4.4}$$

Here, $\xi = 100$ denotes a factor by which the background sound speed is reduced to relax the severe CFL condition (Rempel 2005, Hotta et al. 2014b). The quantities with subscript 0, p_0, ρ_0, T_0, and g_0, represent the pressure, density, temperature, and gravitational

acceleration of the time-independent background which is in an adiabatically-stratified hydrostatic equilibrium. Also, Ω_0 denotes the rotation rate of the rigidly-rotating radiative core and we use the solar value of $\Omega_0/2\pi = 431.3$ nHz. We use the same solar-like background stratification model as Rempel (2005) and Bekki and Yokoyama (2017) from $r_{\rm min} = 0.71R_\odot$ to $r_{\rm max} = 0.96R_\odot$ where $R_\odot$ is the solar radius. The variables v, ρ_1, p_1, and s_1 represent perturbations from the background reference state. The equations are fully nonlinear, however the Eq. (4.4) assumes that these perturbations are not too large to prevent us from linearizing the equation of state. As is usual, c_v denotes the specific heat at constant volume and the ratio of specific heats is given by $\gamma = 5/3$.

The viscous stress tensor, $\mathcal{D}$, is given by

$$\mathcal{D}_{ij} = \rho_0 \nu \left[\mathcal{S}_{ij} - \frac{2}{3}(\nabla \cdot \boldsymbol{v})\delta_{ij} \right], \tag{4.5}$$

where $\mathcal{S}$ is the deformation tensor. See Fan and Fang (2014) for the expression of this tensor in spherical coordinates. The coefficients ν and κ are respectively the eddy viscosity and the eddy thermal diffusivity, which model the unresolved subgrid-scale turbulent motions. In this study, we use the spatially-uniform turbulent viscosity $\nu = 10^{12}$ cm^2 s^{-1} and omit thermal diffusivity $\kappa = 0$. This enhances the effective Prandtl number and thus mimics the highly-magnetized convection (Hotta et al. 2015b, Bekki et al. 2017).

The internal heating and cooling terms, $Q_{\rm heat}$ and $Q_{\rm cool}$, are specified similarly to Karak et al. (2018): The radiative heating is assumed to be proportional to the difference of the background pressure from its surface value,

$$Q_{\rm heat} = \alpha \left[p_0(r) - p_0(r_{\rm max}) \right], \tag{4.6}$$

where the normalization factor α is determined so that

$$L_* = 4\pi \int_{r_{\rm min}}^{r_{\rm max}} r^2 Q_{\rm heat}(r) dr, \tag{4.7}$$

where L_* is the luminosity. The functional form of $Q_{\rm heat}$ gives a good approximation of the radiative flux computed from the solar temperature and opacity values of Model S (Featherstone and Hindman 2016a). The radiative cooling at the surface is assumed to have a thickness comparable to the local pressure scale height H_p, and thus is given by

$$Q_{\rm cool} = -\frac{1}{r^2}\frac{\partial}{\partial r}(r^2 F_{\rm sf}), \tag{4.8}$$

where the surface cooling flux $F_{\rm sf}$ is specified as

$$F_{\rm sf} = \frac{L_*}{4\pi r^2} \exp\left[-\left(\frac{r - r_{\rm max}}{H_p(r_{\rm max})} \right)^2 \right]. \tag{4.9}$$

In this study, we reduce the luminosity from the solar value $L_\odot = 3.84 \times 10^{33}$ erg s^{-1} by a factor of 20, i.e., $L_* = L_\odot/20$. By doing so, we reduce the convective Rossby number Ro ($\propto L_*^{1/3}$), which helps to produce a solar-like differential rotation (with a faster equator and slower poles) in a rotating convection simulation (Gastine et al. 2013, Fan and Fang 2014, Hotta et al. 2015a, Käpylä et al. 2014).

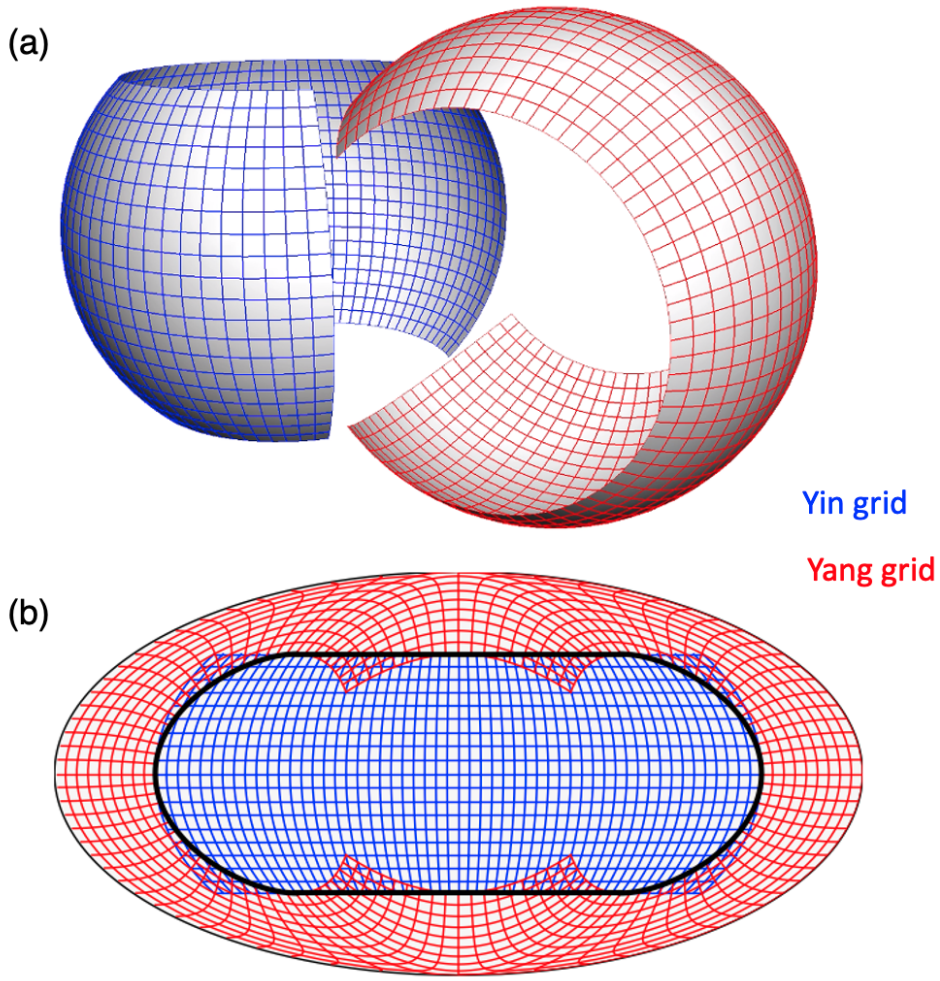

Figure 4.1: Yin-Yang grid used in our simulation. (a) Three-dimensional view of the Yin and Yang grids. Blue and red lines show Yin and Yang coordinates, respectively. (b) Mollweide projection of the Yin-Yang grid. The black thick curve denotes the location where the horizontal boundary condition is set in our code.

We solve the Eqs. (4.1)–(4.3) using a fourth-order centered-differencing method for spatial derivatives and a four-step Runge-Kutta scheme for the time integration (e.g., Vögler et al. 2005). To minimize numerical artifacts while allowing us to operate at as low a thermal diffusivity as possible, we use the slope-limited artificial diffusion presented in Rempel (2014) for entropy s_1. In order to compute in a full-spherical shell while avoiding the coordinate singularity at the poles, a Yin-Yang grid is adopted (Kageyama and Sato 2004). The Yin and Yang grids are defined so that they cover a full spherical surface in a way shown in Fig. 4.1. The grids extend in latitudes ($\pi/4 < \theta < 3\pi/4$) and longitudes ($-3\pi/4 < \phi < 3\pi/4$), respectively. However, unlike the method proposed in Kageyama and Sato (2004), we set the boundary condition on the curve C,

$$C : -\pi < \phi < \pi,\ \theta = \pi/4, 3\pi/4, \tag{4.10}$$

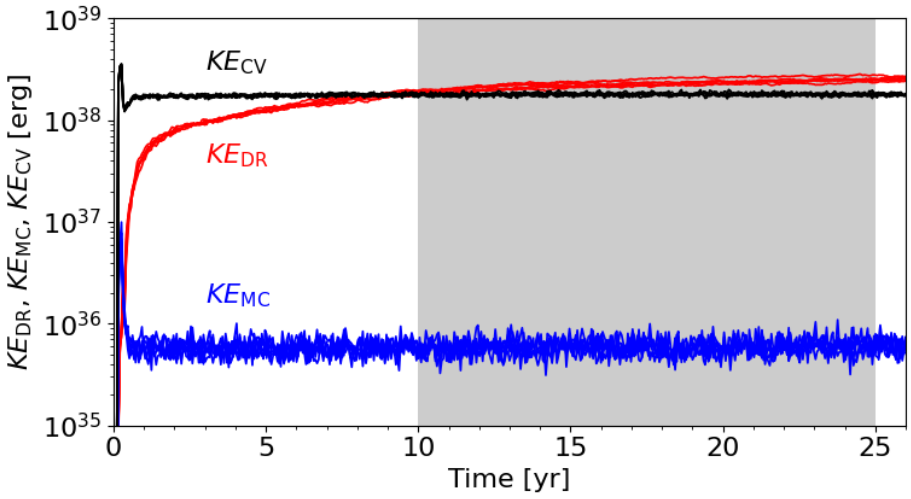

Figure 4.2: Temporal evolution of the volume-integrated kinetic energies; (red) Kinetic energy of the differential rotation $\mathrm{KE_{DR}}$, (blue) kinetic energy of the meridional circulation $\mathrm{KE_{MC}}$, and (black) kinetic energy of the non-axisymmetric flows $\mathrm{KE_{CV}}$. The results from the total 6 runs starting with different initial conditions are shown. The grey shaded are denotes the duration which we use for our spectral analysis.

and on the curve C',

$$C' : \begin{cases} \theta' = \cos^{-1}\left[\sin\theta \sin\phi\right] \\ \phi' = \tan^{-1}\left[-\cos\theta/(\sin\theta\cos\phi)\right] \end{cases} \tag{4.11}$$

where $(\theta, \phi) \in C$. By doing so, the overlapping regions are excluded from our numerical domain. The location where the boundary condition is set on a spherical surface is shown in a thick black curve in Fig. 4.1b. Both the upper and lower radial boundaries are assumed to be impenetrable and stress-free, and the radial gradient of entropy is assumed to vanish there. The grid resolution is $72(N_r)\times96(N_\theta)\times288(N_\phi)\times2$(Yin and Yang). The simulation is initiated from a small random fluctuation in s_1. To check whether the results are sensitive to the initial perturbations, we carry out 6 different simulation runs with different random initial fluctuations. Each simulation run corresponds to about 25 solar years, and we analyze the 15 years of data after the differential rotation becomes statistically stationary, as shwon in Fig. 4.2. The data is saved at a time cadence of about 4.7 days. Most results shown in the following sections are averages over 6 realizations (of 15 years each) to improve the signal-to-noise ratio.

4.3.2 Extracting modes from simulations

We begin with the simulations where each physical variable is only given for discrete values of r, θ, ϕ, and t. We extract the eigenfunctions of the large-scale low-frequency modes of oscillation from the simulation data using a singular-value decomposition (SVD) similar to what was done by Proxauf et al. (2020). To sketch the method, we consider

$q_\alpha(r,\theta,\phi,t)$ to be any of the physical variables, v_r, v_θ, v_ϕ, s_1, or p_1. We Fourier transform these variables to obtain

$$\tilde{q}_\alpha(r,\theta,m,\omega) = \int q_\alpha(r,\theta,\phi,t)\, e^{\mathrm{i}(\omega t - m\phi)}\, dt\, d\phi, \tag{4.12}$$

where m is the azimuthal order and ω is the angular frequency. With this definition, the phase speed ω/m is positive in the direction of rotation (prograde) and it is negative in the direction opposite to rotation (retrograde). In the following, we choose m to be positive with no loss of generality. Each m is analyzed independently.

Among the set of variables $\{q_\alpha\}$, we choose a particular physical variable q_β to target a particular mode. For example, we choose $q_\beta = u_\phi$ for the columnar convective modes and $q_\beta = u_\theta$ for the equatorial Rossby modes and the "mixed Rossby modes". Since our main focus is on the modes that peak near the equator, we consider the latitudinal average

$$\tilde{q}_{\beta,\mathrm{eq}}(r,m,\omega) = \frac{6}{\pi}\int_{\pi/2-\pi/12}^{\pi/2+\pi/12} \tilde{q}_\beta(r,\theta,m,\omega)\, d\theta \tag{4.13}$$

over a narrow band of latitudes covering 15° on either side of the equator. Given the mode frequency, ω_{mode}, for which we want to extract the eigenfunctions, we limit the domain of analysis to the frequency range $[\omega_1,\omega_2] \ni \omega_{\mathrm{mode}}$ and to an appropriate radius range $[r_1,r_2]$ in which the mode has significant power, in order to reduce the contamination from the neighboring modes. For each fixed m, the quantity $\tilde{q}_{\beta,\mathrm{eq}}$ is then decomposed according to the SVD as

$$\tilde{q}_{\beta,\mathrm{eq}}(r,m,\omega) = \sum_k \sigma_k^\beta(m) U_k^\beta(r,m) V_k^{\beta,H}(m,\omega), \tag{4.14}$$

where the σ_k are the singular values, U_k and V_k are the left and right singular vectors, and H denotes the conjugate transpose. The vectors V_k are normalized such that $V_k^H V_{k'} = \delta_{kk'}$. The decomposition is ordered such that the first singular value is dominant over the other values. For each mode, we keep only the first of the right singular vectors, V_0, from the SVD. Using V_0^β derived from q_β, the spatial dependence of a mode is calculated for all the other variables q_α according to

$$q_{\alpha,\mathrm{mode}}(r,\theta,m) = \sum_{\omega'=\omega_1}^{\omega_2} \tilde{q}_\alpha(r,\theta,m,\omega') V_0^\beta(m,\omega'). \tag{4.15}$$

These spatial functions are approximations to a mode's eigenfunctions, and can be compared to the eigenfunctions from the linear analysis. The amplitude of a mode extracted using the above equation is an estimate of the root-mean-square (rms) of this mode in the frequency range $\omega_1 \le \omega \le \omega_2$, according to the Parseval's theorem.

4.3.3 Linear eigenvalue solver

The modes extracted from the nonlinear rotating convection simulation will be compared to the linear eigenmodes of oscillation in the Sun. For solving the linearized problem, we use the code developed in Chapter 3. The differences from the Bekki et al.

(2022b)'s setup are follows: The lower and upper boundaries are changed to $(r_{\rm min}, r_{\rm max}) = (0.71R_\odot, 0.96R_\odot)$ corresponding to those of the nonlinear simulation. We also impose the differential rotation (the axisymmetric background mean flow) taken from the nonlinear simulation (Fig. 4.3a). However, we do not take into account the meridional circulation which has a much smaller impact on inertial modes than the differential rotation (Gizon et al. 2020b, Fournier et al. 2022). For simplicity, the background is adiabatic ($\delta = 0$) and spatially-uniform viscosity of 10^{12} cm^2 s^{-1} is included.

4.4 General results

4.4.1 Rossby number regime

Let us first evaluate the parameter regime of our nonlinear rotating convection simulation. To do so, we compute the volume-averaged rms velocity in the simulation (fluctuations with respect to the mean flows) defined by

$$\bar{v}_{\rm rms}^2 = \frac{1}{V}\int_V \left[(v_r - \langle v_r\rangle)^2 + (v_\theta - \langle v_\theta\rangle)^2 + (v_\phi - \langle v_\phi\rangle)^2\right] dV, \tag{4.16}$$

where $\langle\rangle$ denotes the azimuthal average and the integral is taken over the volume of the whole convection zone, V. We obtain $\bar{v}_{\rm rms} = 37.1$ m s^{-1}, which is smaller than that of previous simulations of solar global convection by a factor of about 3 (e.g., Miesch et al. 2008). This is due to the fact that the luminosity is reduced by a factor of 20 from the solar value in our simulation.

The rotational influence on convection can be measured by the Rossby number

$$\mathrm{Ro} = \frac{\bar{v}_{\rm rms}}{2\Omega_0(r_{\rm max} - r_{\rm min})}. \tag{4.17}$$

We obtain Ro = 0.04, indicating that our simulation is operating in a strongly rotationally-constrained regime. Thanks to this low Ro, we successfully obtain the solar-like differential rotation (with faster equator and slower poles); see Gastine et al. (2013). Whether the Rossby number in our simulation takes a realistic value is an open question: The Rossby number in the Sun's convection zone is one of the most important unknown global parameters, which bears on the solar convective conundrum.

4.4.2 Axisymmetric mean flows

Figures 4.3a and b show the time-averaged profiles of the axisymmetric mean flows, i.e., differential rotation and meridional circulation, respectively. For the parameters we used, the differential rotation is solar-like although its amplitude is much weaker than that of the real Sun (e.g., Howe 2009). The reference rotation rate of $\Omega_0/2\pi = 431.3$ nHz roughly corresponds to the middle-latitude rotation rate ($\approx 40°$) at the surface. The meridional flow tends to be multiple-cellular structure at low latitudes but is largely counter-clockwise (clockwise) in the northern (southern) hemisphere at higher latitudes: The flow at high latitudes is poleward (equatorward) at the surface (base of the convection zone) (e.g., Featherstone and Miesch 2015).

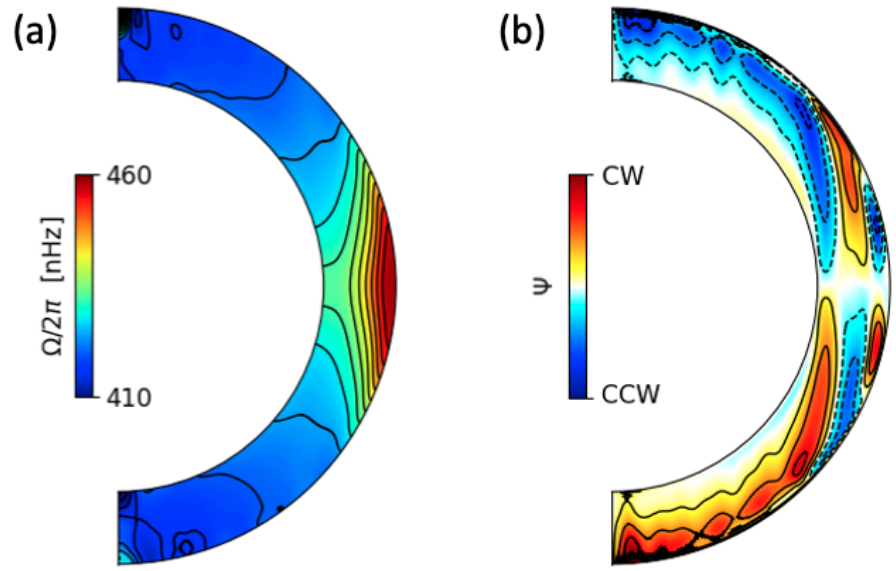

Figure 4.3: Temporally-averaged profile of (a) the differential rotation $\Omega(r,\theta) = \Omega_0 + \langle v_\phi \rangle / r \sin\theta$, and (b) the streamlines of the meridional circulation $\boldsymbol{v}_\mathrm{m} = (\langle v_r \rangle, \langle v_\theta \rangle)$. Here, $\langle\rangle$ denotes the longitudinal average. The meridional flow stream function Ψ is defined by $\rho_0 \boldsymbol{v}_\mathrm{m} = \nabla \times (\Psi \boldsymbol{e}_\phi)$. The Red (blue) indicates the circulation is clockwise (counter-clockwise), i.e., the flow is poleward near the surface at high latitudes in both hemispheres.

4.5 Low-frequency modes found in our simulation

4.5.1 Columnar convective modes

Figures 4.4a and b show temporal snapshots of the non-axisymmetric components of radial velocity v_r and longitudinal velocity v_ϕ near the surface $r = 0.95 R_\odot$, respectively. The convective structure at high latitudes can be characterized by granular cells consisting of broad upflows and narrow downflows (e.g., Spruit et al. 1990). Near the equator, we can clearly see the north-south aligned lanes of radial and longitudinal velocities. They are often called "banana cells" and have been repeatedly reported in previous numerical simulations of rotating convection (Miesch et al. 2000, Käpylä et al. 2011, Gastine et al. 2013, Guerrero et al. 2013, Hotta et al. 2015a, Featherstone and Hindman 2016a, Käpylä et al. 2019, Matilsky et al. 2019, 2020). We will show that these "banana-cell" features can be identified as the columnar convective modes largely originating from the compressional β-effect (Glatzmaier and Gilman 1981, Glatzmaier et al. 2009, Verhoeven and Stellmach 2014, Bekki et al. 2022b).

Figure 4.5a shows the equatorial power spectrum ($m - \omega$ diagram) of the longitudinal velocity near the top boundary $|\tilde{v}_{\phi,\mathrm{eq}}(0.95R_\odot, m, \omega)|^2$. The dispersion relationship for the columnar convective modes from the linear eigenmode calculation are overplotted in red. The frequencies are given for a frame rotating with Ω_0. A clear power ridge can be

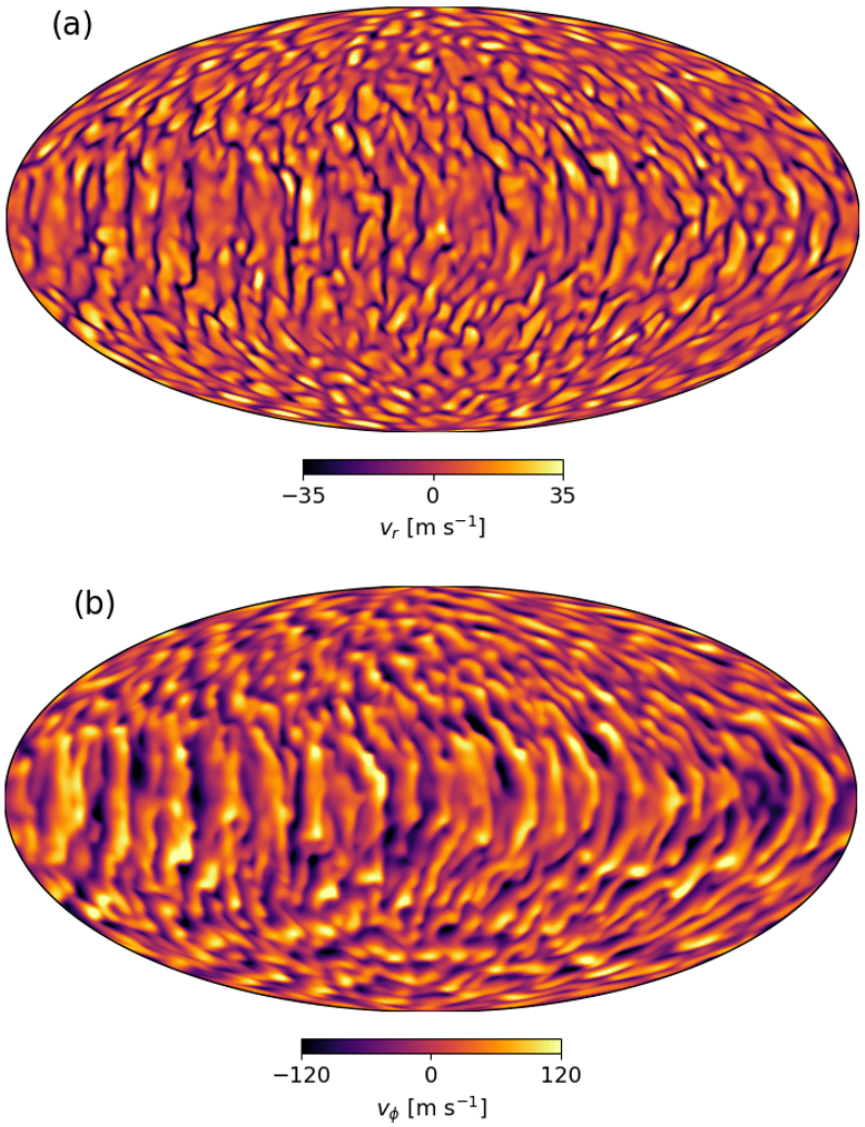

Figure 4.4: Snapshots of the convective pattern in our simulation near the top boundary $r = 0.95R_\odot$. Panels (a) and (b) show the radial velocity v_r and non-axisymmetric component of the longitudinal velocity v_ϕ.

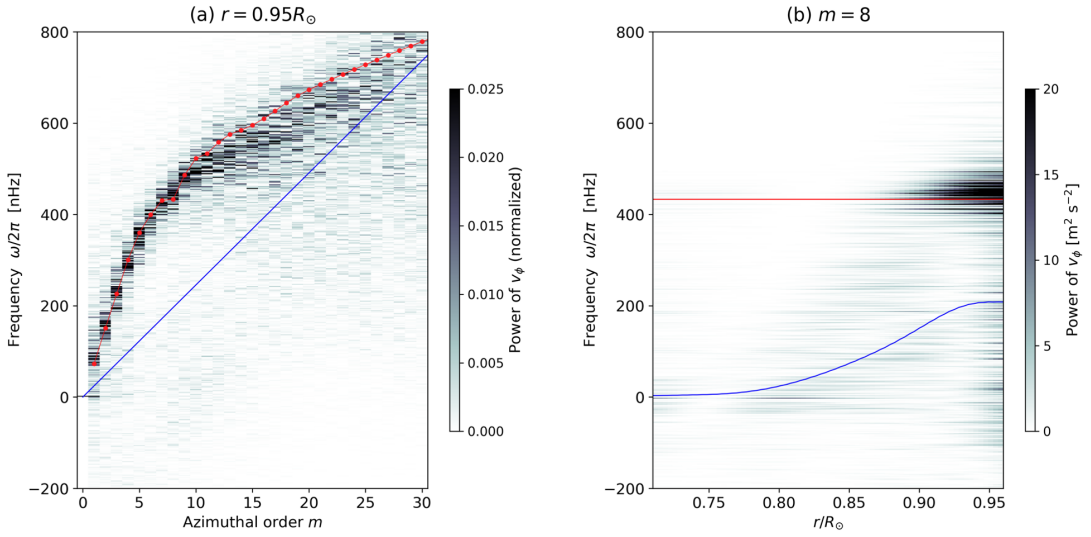

Figure 4.5: (a) Power spectrum of longitudinal velocity v_ϕ near the top boundary $r = 0.95R_\odot$, averaged over the equatorial band (±15 deg). The power is normalized at each m. The spectrum is computed in a frame rotating at $\Omega_0/2\pi = 431.3$ nHz (the rotation rate of the radiative interior). The blue line represents the advective speed by the local differential rotation, $m\,[\Omega(r, \pi/2) - \Omega_0]$. Overplotted in red represents the dispersion relation of the columnar convective modes from the linear eigenmode calculation. Panel (b) shows the same equatorial power spectrum at fixed azimuthal order $m = 8$ as a function of depth. The blue line is again the local advection frequency and the red line is the eigenfrequency from the linear analysis.

observed in Fig. 4.5a, matching that from the linear analysis for $m \lesssim 10$. The frequency of this power ridge is positive in the frame rotating with the local differential rotation rate (denoted by blue solid line), implying that the convective modes are propagating in a prograde direction (Miesch et al. 2008, Bessolaz and Brun 2011). Figure 4.5b shows the same equatorial power spectrum at fixed azimuthal order $|\tilde{v}_{\phi,\mathrm{eq}}(r, m = 8, \omega)|^2$. The strong longitudinal velocity power is localized near the surface where the compressional β-effect ($\propto H_\rho^{-1}$ where H_ρ is the density scale height) is the strongest (e.g., Glatzmaier and Gilman 1981). At $m = 8$, the mode has a linewidth of 30 nHz and a corresponding decaying timescale of 122 days.

We used the method described in § 4.3.2 to extract the spatial structure of the columnar convective modes for azimuthal orders $1 \leq m \leq 39$ [1]. To extract the modes, we calculated $V_0(\omega)$ in Eq. (4.15) based on the equatorial spectrum of longitudinal velocity near surface. Figure 4.6 shows the three-dimensional spatial patterns of the convective columnar modes found in our simulation for selected m. For visualization purposes, the non-axisymmetric components of pressure perturbation p_1 are shown. We note that the positive (negative) pressure perturbation p_1 is associated with negative (positive) z-vorticity ζ_z of the modes due to the strong constraint of geostrophic balance (e.g., Matilsky et al. 2020). It is clearly

[1]The maximum azimuthal order in our grid resolution is 192. However, we restrict our analysis to large-scale modes in a range $0 \leq m \leq 39$.

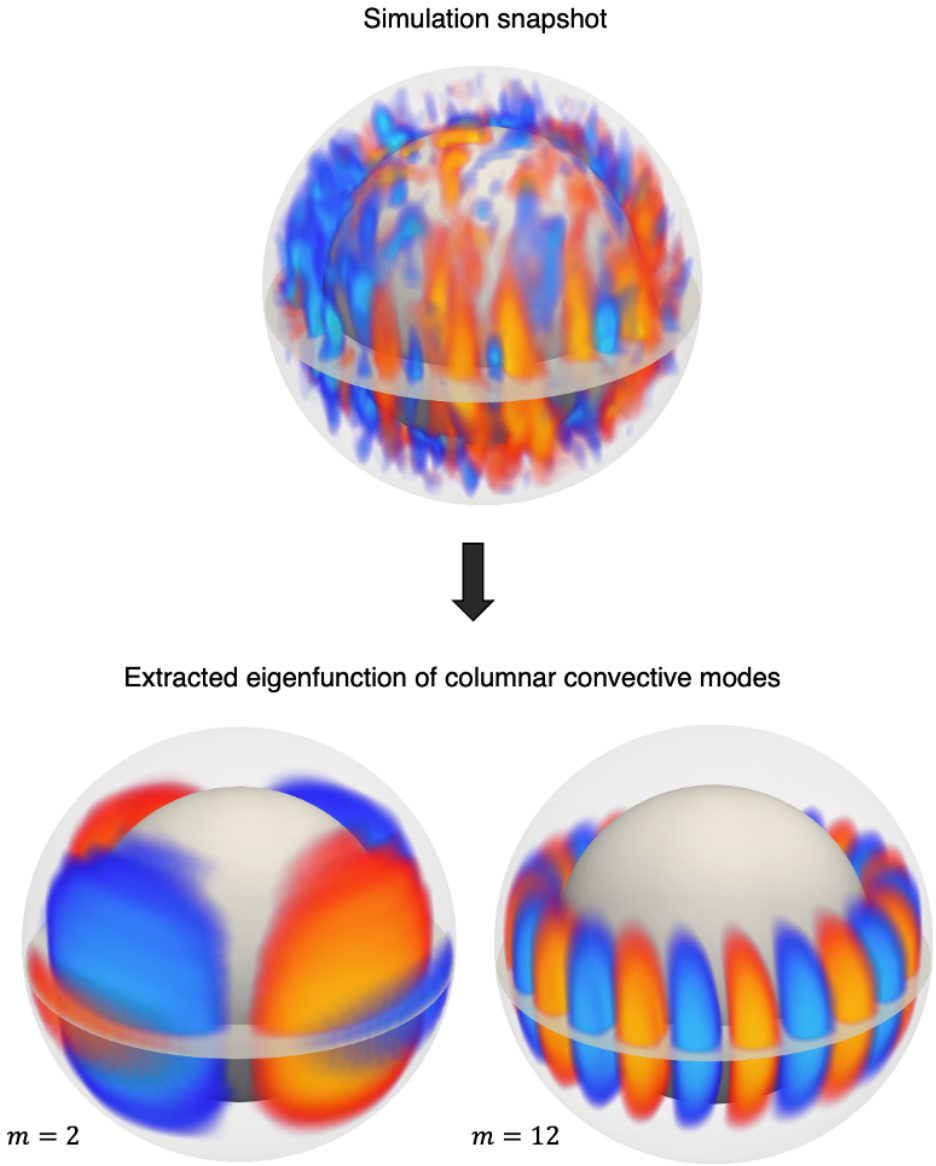

Figure 4.6: (Left) A snapshot of the pressure perturbation (non-axisymmetric component) from the nonlinear simulation shown as a 3D volume rendering. Red/yellow and blue/cyan parts correspond to the regions with positive and negative pressure perturbations, respectively. (Right) Eigenfunctions of pressure perturbation of the conlumnar convective modes extracted from the simulation data using SVD. The cases with $m = 2$ and $m = 12$ are shown.

seen that the columnar convective modes are characterized by the north-south aligned columns across the equatorial plane.

Figure 4.7 shows the extracted eigenfunctions of the convective columnar modes for $m = 2$, in comparison with the results of the linear analysis. The real eigenfunctions of v_r and v_θ and the imaginary eigenfunctions of v_ϕ and p_1 are shown in Fig. 4.7a. Fig-

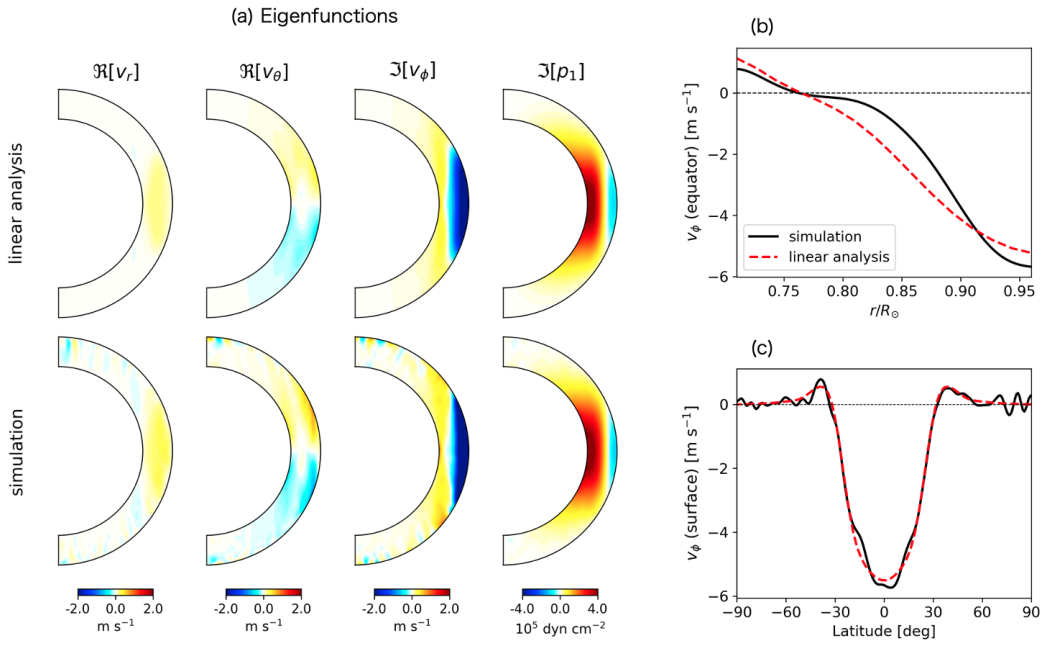

Figure 4.7: Plots of the spatial eigenfunctions $q_{\alpha,\mathrm{mode}}(r,\theta,m)$ for the ζ_z-symmetric columnar convective modes with $m = 2$. By definition, modes are of the form $q_{\alpha,\mathrm{mode}}(r,\theta,m)\exp\left[\mathrm{i}(m\phi-\omega t)\right]$ where q_α is either v_r, v_θ, v_ϕ, or p_1. (a) Meridional cuts of the radial velocity v_r, latitudinal velocity v_θ, longitudinal velocity v_ϕ, and pressure perturbation p_1 extracted from the convection simulation (lower penals) and obtained from our linear calculation (upper panels). (b) Radial dependence of the eigenfunction v_ϕ at the equator. Black solid and red dashed lines represent that of simulation and linear calculation. (c) Latitudinal eigenfunction of v_ϕ at the surface normalized near the equator.

ures 4.7b and c further compare the radial and latitudinal structures of the extracted mode at the equator and at the surface, respectively. Note that the eigenfunctions extracted from the simulations are realizations of random processes, and therefore contain noise. The noise is visible at small spatial scales, however particularly at large scales, a great agreement can be seen between the eigenfunctions from the simulation and those of the linear analysis. Therefore, the columnar convective modes are unambiguously identified in our simulations. The modes can be clearly characterized by a dominant z-vorticity ζ_z that is confined outside the tangential cylinder as described in detail in Bekki et al. (2022b). As m increases, the eigenfunctions are more and more confined towards the surface and towards the equator (not shown).

4.5.2 Equatorial Rossby modes

In this section, we present the same modal analysis for the equatorial Rossby modes (r modes) where radial vorticity ζ_r is symmetric across the equator. In this study, we use the latitudinal velocity v_θ near the equator for our spectral analysis which is a good representative of the equatorial Rossby modes. Figures 4.8a and b show the equatorial power spectra ($m-\omega$ diagram) of latitudinal velocity near the base $|\tilde{v}_{\theta,\mathrm{eq}}(0.715R_\odot,m,\omega)|^2$

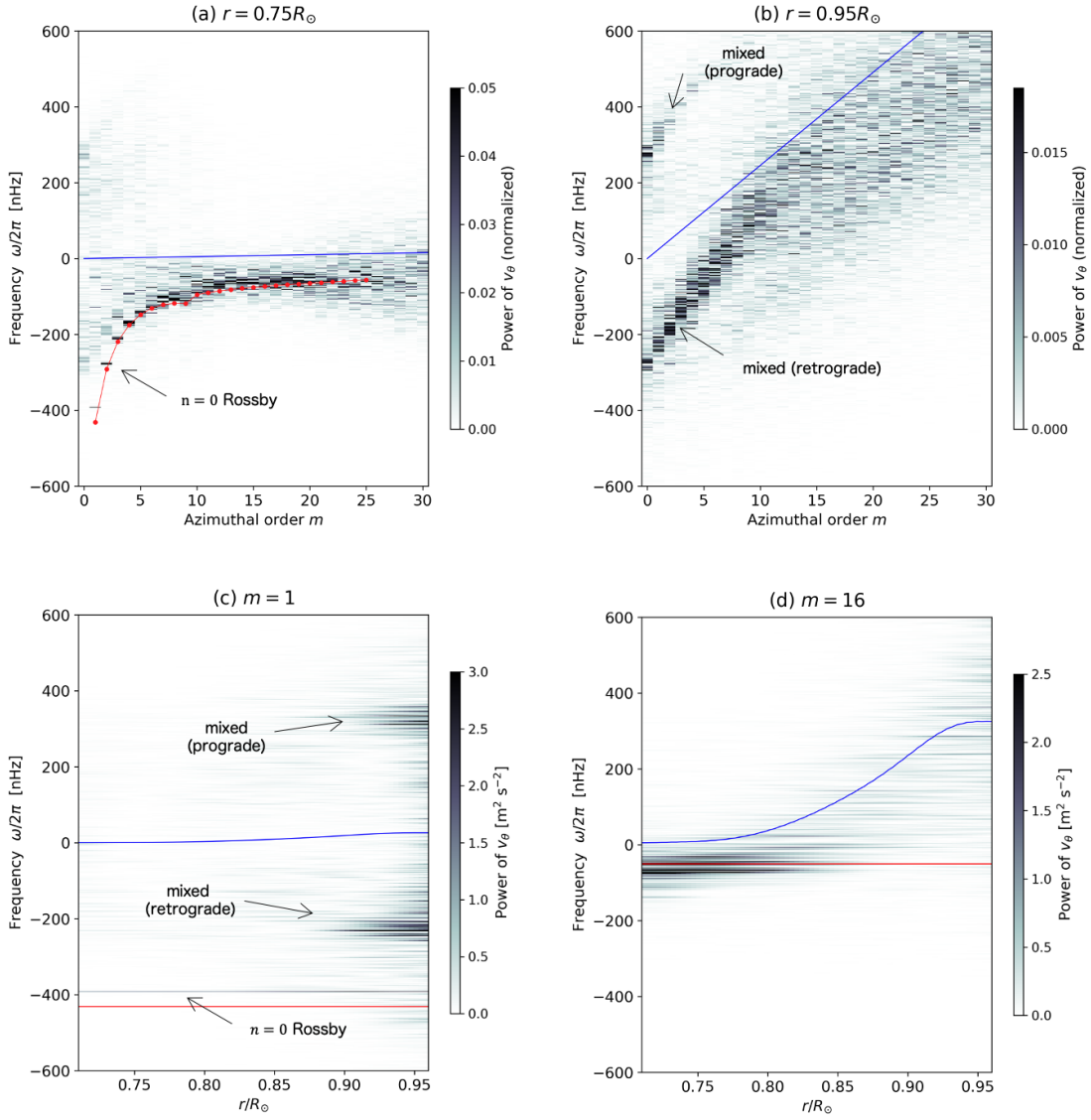

Figure 4.8: Power spectra of latitudinal velocity v_θ near the equator (averaged over ±15 deg). Panels (a) and (b) show the $m - \omega$ diagram near the base ($r = 0.75R_\odot$) and near the surface ($r = 0.95R_\odot$), respectively. The power is normalized at each m. The spectra are computed in a frame rotating at $\Omega_0/2\pi = 431.3$ nHz. Overplotted in red line in panel (a) represents the dispersion relation of the equatorial Rossby mode with no radial node ($n = 0$) obtained from the linear calculation. The blue line represents the advection frequency of the equatorial differential rotation, $m\,[\Omega(r, \pi/2) - \Omega_0]$, at each height. Panels (c) and (d) show the power spectra at fixed azimuthal order $m = 1$, and $m = 16$, respectively.

and near the surface $|\tilde{v}_{\theta,\mathrm{eq}}(0.95R_\odot, m, \omega)|^2$, respectively. The dispersion relation of the equatorial Rossby modes with no radial node ($n = 0$) obtained from our linear analysis are shown in red points in Fig. 4.8a. A clear power ridge can be seen along the linear dispersion relation near the base, whereas two distinct ridges are found in the surface power spectrum (denoted as "mixed prograde" and "mixed retrograde" in Fig.4.8b).

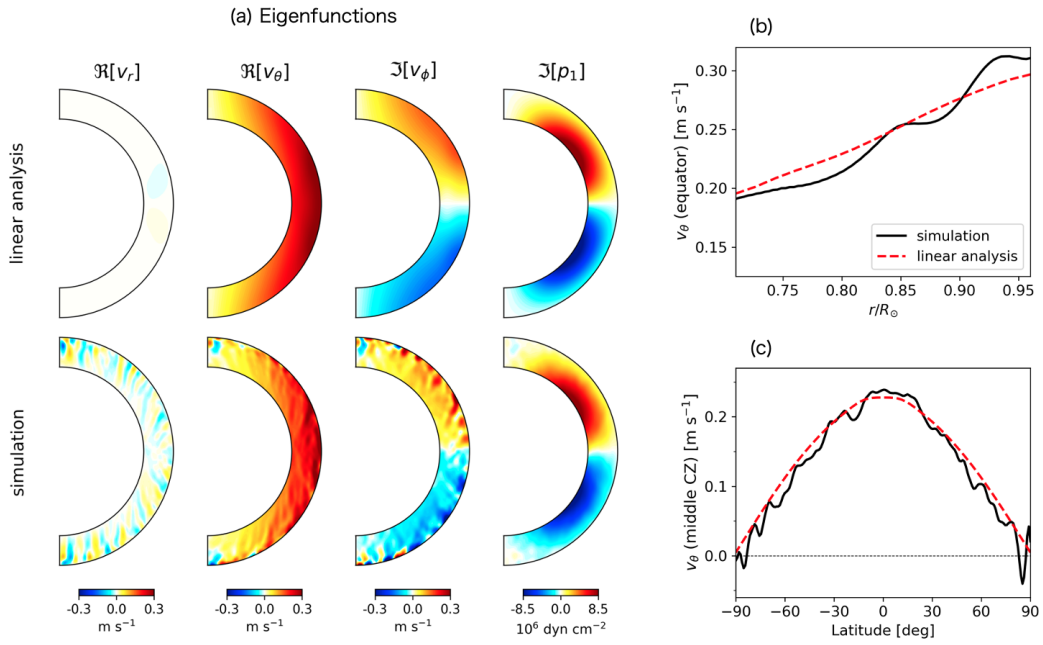

Figure 4.9: Eigenfunctions of the equatorial Rossby mode with no radial node ($n = 0$) for $m = 2$. (a) Meridional eigenfunctions extracted from the simulation (lower panels) and those obtained from the linear analysis (upper panels). The same notation is used as in Fig. 4.7a. (b) Radial eigenfunction of v_θ at the equator. Black solid and red dashed lines represent the results from simulation and linear calculation, respectively. (c) Latitudinal eigenfunction of v_θ in the middle convection zone.

Figures 4.8c and d show the same equatorial power spectra of v_θ at fixed azimuthal orders $|\tilde{v}_{\theta,eq}(r, m = 1, \omega)|^2$ and $|\tilde{v}_{\theta,eq}(r, m = 16, \omega)|^2$, respectively. As shown in Fig. 4.8c, three distinct modes exist at low-m regime;

- A retrograde-propagating mode that exists globally in radius at $\omega/2\pi \approx -395$ nHz. Its mode frequency is close to the theoretical eigenfrequency of the $n = 0$ Rossby mode predicted in linear analysis (denoted by red line) and is independent of height. This mode is undoubtedly identified as the $n = 0$ equatorial Rossby mode and will be discussed in §4.5.2.1.

- A retrograde-propagating mode localized near the surface at $\omega/2\pi \approx -230$ nHz is also seen. This mode is identified as the equatorial Rossby mode with one radial node ($n = 1$) and will be discussed in §4.5.3.

- A prograde-propagating mode localized near the surface at $\omega/2\pi \approx 320$ nHz is also apparent. This mode is identified as the north-south ζ_z-antisymmetric columnar convective mode and will also be discussed in §4.5.3.

At higher m, on the other hand, most of the power is concentrated near the bottom convection zone at frequencies close to those of the $n = 0$ Rossby modes from the linear analysis (denoted by red line) as shown in Fig. 4.8d. Properties of these high-m Rossby modes will be discussed in §4.5.2.2.

4.5.2.1 Rossby modes with $n = 0$ and $m \leq 4$

At low m, equatorial Rossby modes can be unambiguously found in our simulation. Figure 4.9a shows the extracted eigenfunctions of $m = 2$ mode as an example. The associated flow motion is mostly r-vortical and quasi-toroidal, i.e., $v_r \approx 0$. Geostrophical balance is well established by positive (negative) p_1 in a region where ζ_r is negative (positive) in the northern (southern) hemisphere. The radial component of the Coriolis force is balanced by the radial pressure gradient force. For $m \leq 4$, almost all the power is in real part of the eigenfunction of v_θ ($\Re[v_\theta]$) and the imaginary part for v_ϕ ($\Im[v_\phi]$): The other components of the eigenfunctions (for example $\Im[v_\theta]$ or $\Re[v_\phi]$) are small and consistent with noise. For comparison, we also show the eigenfunctions of $m = 2$ equatorial Rossby mode with no radial node ($n = 0$) obtained from our linear calculation in the uppper panel of Fig. 4.9a. A very good agreement can be seen between the extracted eigenfunctions from the nonlinear simulation and those of the linear calculation. Figures 4.9b and c further compare the radial and latitudinal structures of the eigenfunction of v_θ. The radial eigenfunction roughly shows a monotonic increase towards the surface as expected from the analytical solution for the ideal case of inviscid and uniformly-rotating sphere, $v_\theta \propto r^m$ (e.g., Saio 1982). Similarly, the latitudinal eigenfunction also roughly follows the analytical solution for the ideal case, $v_\theta \propto \sin^{m-1}\theta$.

It is noteworthy that the $m = 1$ equatorial Rossby mode shown in Fig. 4.8c has a flow vorticity that is uniform in the frame of the mode and points in a direction perpendicular to the solar rotation axis. This particular mode is often called the "spin-over inertial mode" (e.g., Greenspan et al. 1968) and has been extensively studied in the context of planetary cores (e.g., Triana et al. 2012, Rekier 2022).

We also note that these equatorial Rossby modes at low m are very long-lived. For instance, the $m = 4$ mode has a linewidth of 7.5 nHz and the corresponding lifetime of about 500 days. The modes with $m < 4$ have much longer lifetimes as their linewidths are too small to be well resolved and to be fitted with Lorentzian.

4.5.2.2 Rossby modes with $n = 0$ and $m > 4$

As m increases, the eigenfunctions of the $n = 0$ equatorial Rossby modes significantly deviate from the well-known analytical expression of, $v_\theta \propto r^m \sin^{m-1}\theta$. Figure 4.10 shows the eigenfunctions at $m = 24$ that is extracted from the convection simulation along the power ridge shown in Fig. 4.8a. We emphasize that the eigenfunctions become essentially complex, with the complex phase for each variable being a function of r and θ. For large azimuthal order m, the modes cease to be quasi-toroidal, i.e., the radial motions become substantial and the modes are partially convectively driven. This can be confirmed by the fact that, in Fig. 4.10, v_r and s_1 have the same sign at the same phase in both hemispheres. The transport properties of thermal energy will later be discussed in detail in § 4.6.2.

It is also found that the $n = 0$ Rossby modes are more and more confined towards the base of the convection zone as m increases. This is clearly illustrated in Fig. 4.12 where the normalized eigenfunctions of $\Re[v_\theta]$ at the equator are plotted against radius for different m. For $m \geq 4$, the radial eigenfunctions become decreasing functions in radius, which clearly disagrees with the analytical solution of Rossby modes in the ideal case (uniform rotation and no viscosity) (Saio 1982). In the ideal case, r^m dependence is required in order to balance the radial component of the Coriolis force by the radial pressure

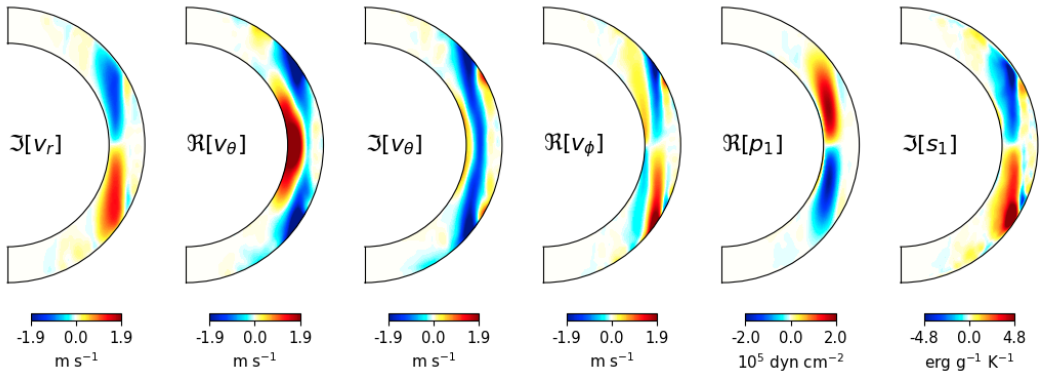

Figure 4.10: Extracted eigenfunctions of the $n = 0$ equatorial Rossby modes at $m = 24$. Eigenfunctions of radial velocity (imaginary) $\Im[v_r]$, latitudinal velocity (both real and imaginary) $\Re[v_\theta]$, $\Im[v_\theta]$, longitudinal velocity (real) $\Re[v_\phi]$, pressure perturbation (real) $\Re[p_1]$, and entropy perturbation (imaginary) $\Im[s_1]$ are shown from left to right. The real and imaginary phases are determined in a way that $\Re[v_\theta]$ at the base takes its maximum at the equator.

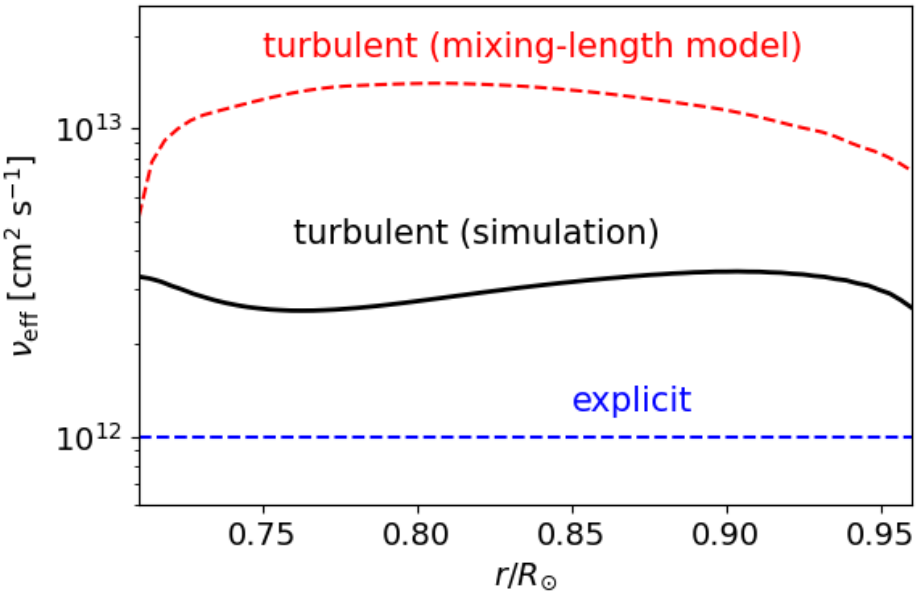

Figure 4.11: Radial profiles of the effective diffusivity due to small-scale convective motions $\nu_{\rm eff}$ (black solid). For comparison, the explicit viscosity used in the simulation and the turbulent diffusivity estimated based on the mixing-length model (Muñoz-Jaramillo et al. 2011) are also shown by blue and red dashed lines.

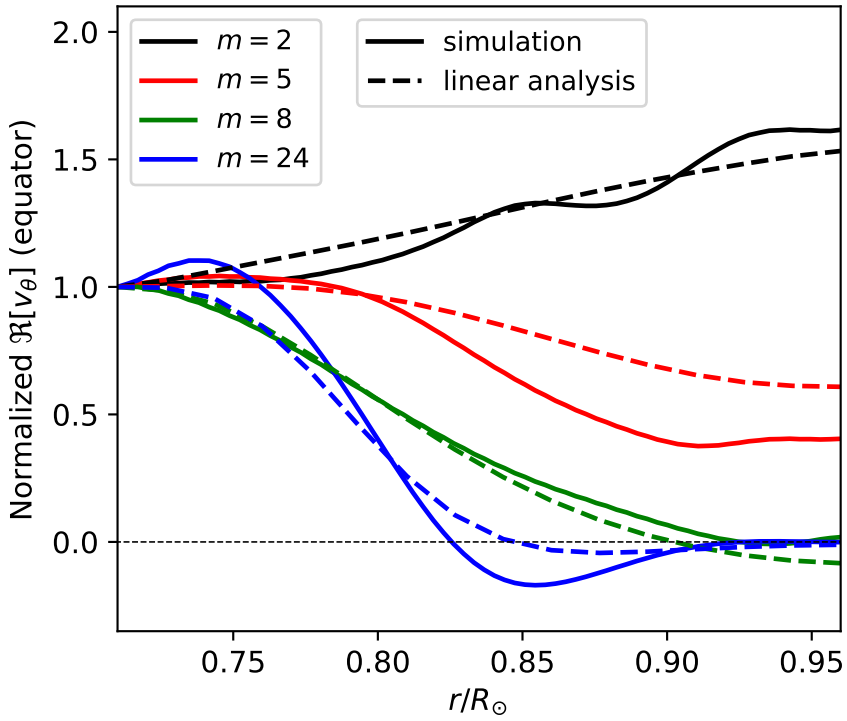

Figure 4.12: Radial structure of the real eigenfunctions of latitudinal velocity $\Re[v_\theta]$ at the equator. The eigenfunctions are normalized to unity at the base. Different colors represent different azimuthal orders m. Solid and dashed lines denote those extracted from the nonlinear simulation and from the linear eigenmode calculation, respectively.

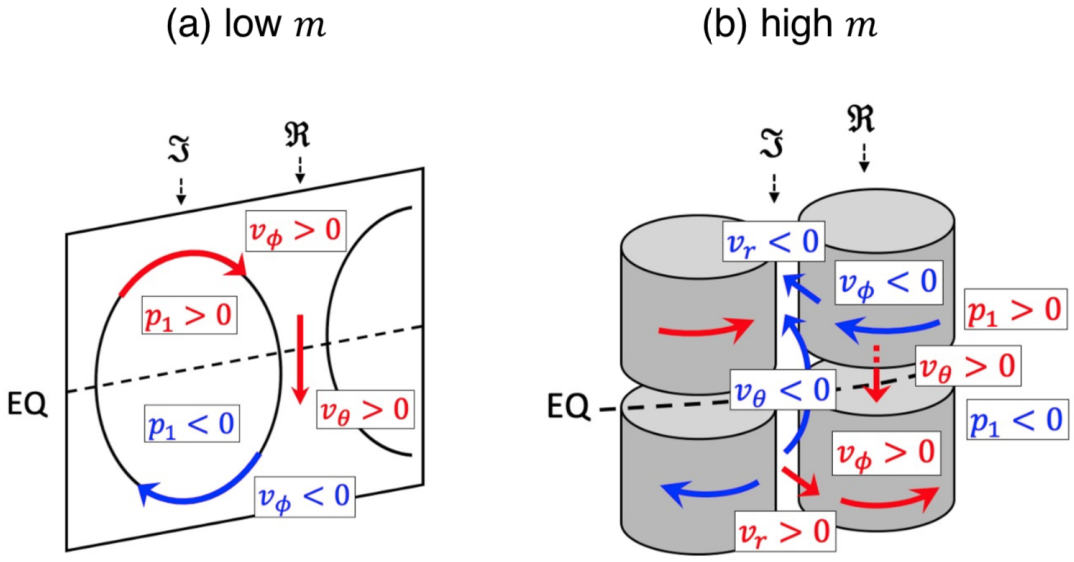

Figure 4.13: Schematic illustration of the flow structure of the $n = 0$ equatorial Rossby modes at (a) low-m and (b) high-m regimes.

gradient. We attribute this discrepancy to the strong viscous diffusion in our simulation: When strong diffusivity is present, the radial force balance is drastically changed. This has already been pointed out by Bekki et al. (2022b) who showed, in the linear regime, that the eigenfunctions of $n = 0$ Rossby modes tend to be localized near the base of the convection zone when the turbulent viscosity is above $\approx 10^{12}$ cm^2 s^{-1}. To confirm this, we show in Fig. 4.12 the results from our linear calculations by dashed lines that can well explain this trend. In fact, the effective diffusivity in our nonlinear simulation is substantially enhanced by the turbulent (eddy) momentum mixing by the convective flows. In Fig. 4.11, we estimate the turbulent diffusivity due to the small-scale convective motions in the simulation to be $\approx 3 \times 10^{12}$ cm^2 s^{-1} throughout the convection zone, which is larger than the explicit viscosity value of 10^{12} cm^2 s^{-1}. Therefore, the effective viscosity is dominated by the eddy diffusion due to the stochastic convective motions on resolved scales. For more detailed discussions on the effect of turbulent diffusion on Rossby modes, see § 5 in Bekki et al. (2022b).

Figure 4.10 also reveals that, at high m, the flow motions are characterized by z-vortices along with the tangential cylinder, as manifested by the eigenfunctions of $\Im[v_r]$, $\Im[v_\theta]$, and $\Re[v_\phi]$. The essential difference from the columnar convective modes discussed in §4.5.1 is here that ζ_z is north-south antisymmetric across the equator. This is schematically illustrated in Fig. 4.13. These modes should also be distinguished from the prograde-propagating "mixed Rossby modes" (that we will discuss in § 4.5.3) where the power is strongly localized near the surface and not at the tangential cylinder.

Note that these high-m equatorial Rossby modes have generally broader linewidths (thus shorter lifetimes) than those with low m. For instance, the mode with $m = 15$ has a linewidth of about 25 nHz. This is in fact comparable to those observed in the Sun (the linewidth of the $m = 15$ mode observed on the Sun is reported to be $\approx$ 10–40 nHz, see Löptien et al. 2018, Liang et al. 2019, Proxauf et al. 2020).

4.5.3 Mixed Rossby modes

Figure 4.14a shows the same equatorial power spectrum near the surface as Fig. 4.8b except that we extend the spectrum to negative azimuthal orders ($m < 0$) considering the symmetry with respect to the origin; $|\tilde{v}_{\theta,\mathrm{eq}}(-m, -\omega)|^2 = |\tilde{v}_{\theta,\mathrm{eq}}(m, \omega)|^2$. We also show the equatorial power spectrum of the north-south antisymmetric component of v_ϕ in Fig. 4.14b. Note that both Fig. 4.14a and b have the same symmetry and thus represent the same modes. This enables us to better see the connection between the two distinct power ridges that are each denoted by "mixed (retrograde)" and "mixed (prograde)": These two oppositely-propagating modes form a single continuous power ridge across $m = 0$, implying that they are essentially mixed with each other. The axisymmetric mode ($m = 0$) is considered to be an inertial mode trapped inside the spherical shell (e.g., Rieutord et al. 2001, Rieutord and Valdettaro 2018) and has an oscillation frequency of about $\omega/2\pi \approx \pm 280$ nHz.

Figure 4.15a shows the extracted eigenfunctions of the retrograde-propagating mode at $m = 2$. The retrograde-propagating mode can be classified as an equatorial Rossby mode with one radial node $n = 1$ in the middle convection zone as depicted in Fig. 4.15b. We note that the nodal plane is more cylindrical than radial outside the tangential cylinder. The associated motion is dominantly r-vortical near the surface, but unlike the $n = 0$ equa-

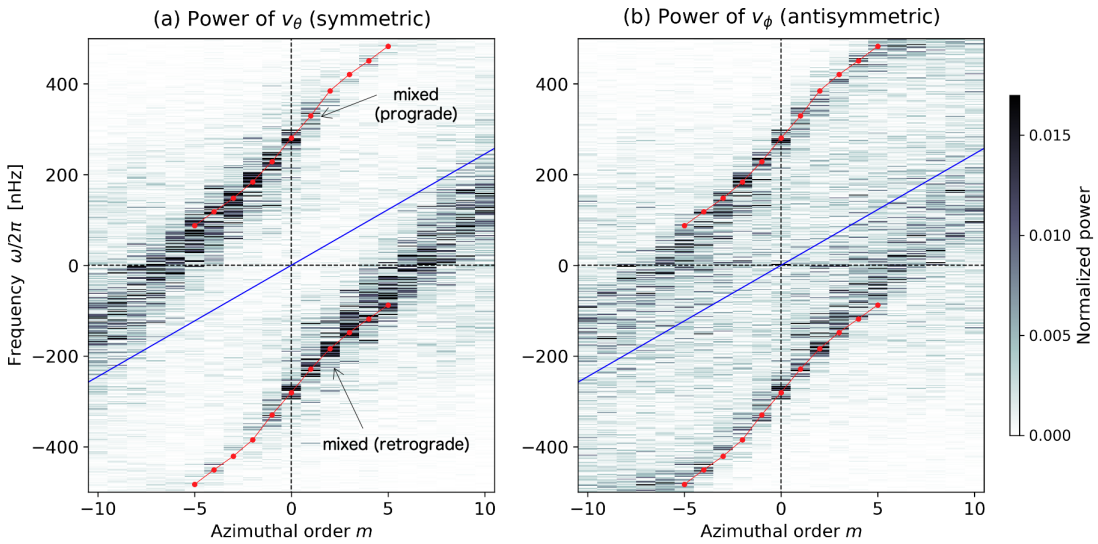

Figure 4.14: Power spectra of horizontal velocities near the surface extended to negative azimuthal orders ($m < 0$). (a) Equatorial power spectrum of north-south symmetric component of v_θ near the top boundary $r = 0.95R_\odot$, which is the same as Fig. 4.8b. The power is normalized at each m. Shown in red points are the frequencies of the "mixed Rossby modes" obtained from our linear analysis. The blue line represents the advection frequency of the equatorial differential rotation, $m\,[\Omega(0.95R_\odot, \pi/2) - \Omega_0]$. (b) Equatorial power spectrum of north-south antisymmetric component of v_ϕ near the top boundary $r/R_\odot = 0.95$.

torial Rossby modes, non-negligible radial velocities are involved. Similarly, the extracted eigenfunctions of the prograde-propagating mode at $m = 2$ are shown in Figure 4.16a. The prograde-propagating mode can be classified as a north-south ζ_z-antisymmetric columnar convective mode as illustrated in Fig. 4.16b. Given that both of these modes follow the same dispersion relationship, we call them "mixed Rossby modes" in this paper.

The existence of the "mixed Rossby modes" was first pointed out in Bekki et al. (2022b). Their dispersion relation asymptotically approaches to that of $n = 0$ equatorial Rossby mode for large m with negative ω (retrograde modes) and to that of the north-south ζ_z-symmetric columnar convective mode for large m with positive ω (prograde modes). The coupling between these two oppositely-propagating modes can be understood by analogy to the well-known mixed Rossby-gravity waves (sometimes called Yanai waves) in the geophysical context (e.g., Matsuno 1966, Vallis 2006) whose dispersion relation is asymptotic to that of classical Rossby waves for large m with negative ω (retrograde) and asymptotic to that of inertia-gravity waves for large m with positive ω (prograde).

To further support the identification of these mixed Rossby modes, we compute the dispersion relation and the corresponding eigenfunctions using the linear eigenvalue solver. The computed dispersion relation is shown by red points in Fig. 4.14 for $m \leq 5$, which nicely agrees with the power ridge in the simulated spectrum. We also show in Fig. 4.15a and Fig. 4.16a the eigenfunctions of the $n = 1$ equatorial Rossby mode and the north-south ζ_z-antisymmetric columnar convective mode at $m = 2$ obtained from the linear

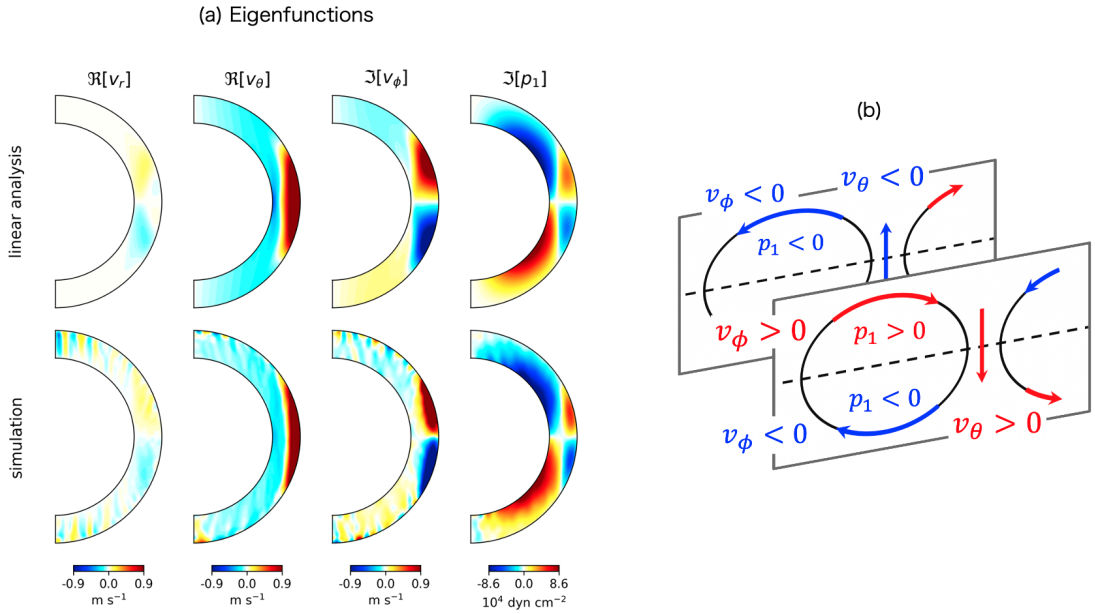

Figure 4.15: (a) Eigenfunctions of the retrograde-propagating mixed Rossby mode ($n = 1$ equatorial Rossby mode) at $m = 2$. Lower and upper panels show the results extracted from the simulation and those obtained from the linear analysis. (b) Schematic illustration of this mode.

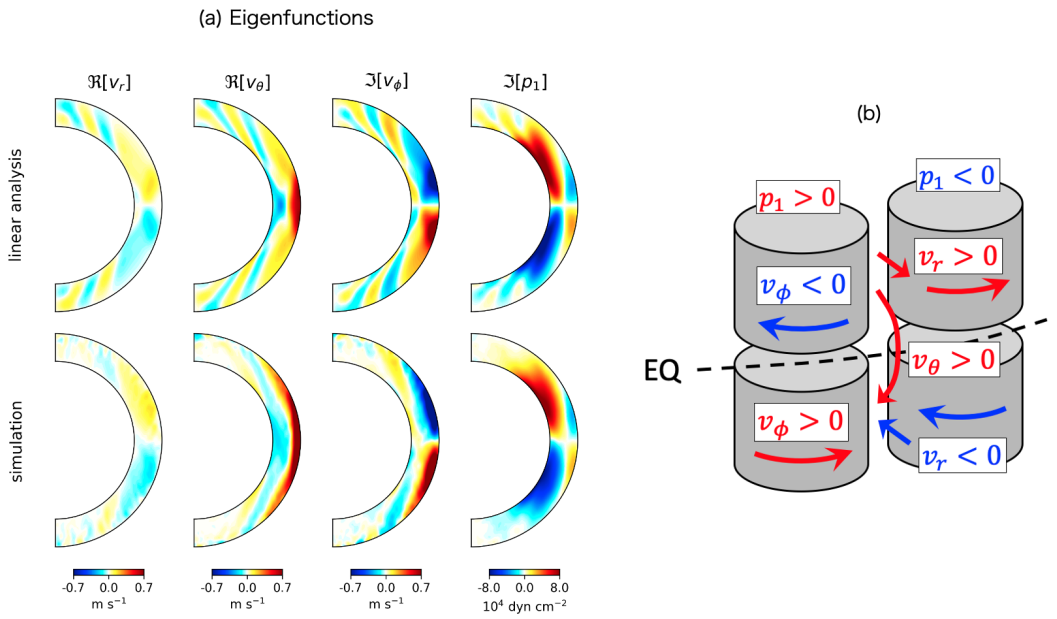

Figure 4.16: (a) Eigenfunctions of the prograde-propagating mixed Rossby mode (north-south ζ_z-antisymmetric columnar convective mode) at $m = 2$. Lower and upper panels show the results extracted from the simulation and those obtained from the linear analysis. (b) Schematic illustration of this mode.

calculation. The agreement between the simulation and linear theory is striking.

4.6 Transport properties of low-frequency modes

4.6.1 Mode amplitudes

So far, we have investigated the eigenfunctions and eigenfrequencies of the north-south ζ_z-symmetric columnar convective modes, the $n = 0$ equatorial Rossby modes, and the "mixed Rossby modes". In this section, we discuss how significant these modes are for transport processes in our nonlinear simulation.

Figure 4.17a shows the spectra of the maximum horizontal velocity $v_\mathrm{h} = \sqrt{v_\theta^2 + v_\phi^2}$ of the equatorial modes near the surface. It is clearly seen that the north-south ζ_z-symmetric columnar convective modes are the most dominant in power: They account for about $10 - 30$ % of the total velocity power of the simulation near the surface (black dashed line). When observed at the surface, the $n = 0$ equatorial Rossby modes are much weaker than the columnar convective modes and the "mixed Rossby modes". Nonetheless, their amplitudes are comparable to those observed on the Sun (Liang et al. 2019, Gizon et al. 2021) This may imply that these equatorial Rossby modes are both excited and damped by the turbulent convective motions.

Figure 4.17b shows, on the other hand, the spectra of the volume-integrated kinetic energies of these modes. It is shown that, despite the weak amplitudes in the surface spectrum, the total kinetic energy of the $n = 0$ equatorial Rossby modes become significant: It is much larger than that of the mixed modes for $m > 6$, and become comparable to that of the ζ_z-symmetric columnar convective modes for $m \geq 10$. This reflects the fact the $n = 0$ Rossby modes are concentrated near the base of the convection zone at high m where the background density is substantial. As shown in the 2nd column of Table 4.1, the ζ_z-symmetric columnar convective modes and the $n = 0$ Rossby modes have about 7% and 6% of the total fluctuating ($m \neq 0$) kinetic energy of the simulation, respectively.

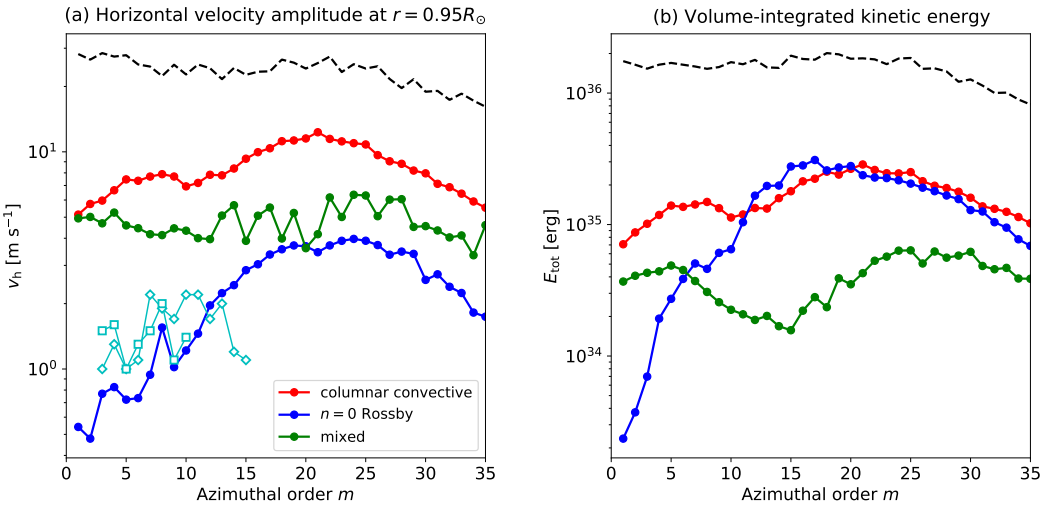

Figure 4.17: (a) Maximum horizontal velocity v_h of the equatorial modes near the top boundary $r = 0.95R_\odot$ at each azimuthal order m. Red, blue, and green points represent the ζ_z-symmetric columnar convective modes, $n = 0$ equatorial Rossby modes, and the mixed Rossby modes, respectively. Black dashed line represents the overall power of the convection simulation (including modes at high latitudes and stochastic convective motions). Cyan diamonds and squares denote the (rms) horizontal velocity amplitudes of the observed Rossby modes near the solar surface obtained by Liang et al. (2019) and Gizon et al. (2021), respectively. (b) Spectra of volume-integrated kinetic energy of the equatorial modes.

Table 4.1: Amplitudes and lifetimes of the equatorial vorticity modes in our simulation

Classification		kin. energy $E_{\mathrm{mode}}/E_{\mathrm{all}}$ [%]	v_{max} [m s^{-1}]		τ_{mode} [days]	
			$m = 2$	$m = 16$	$m = 2$	$m = 16$
Columnar convective (ζ_z-sym)		7.12	5.75	9.96	78.4	30.4
Equatorial Rossby ($n = 0$)		6.07	0.48	3.68	> 903	164.7
Columnar convective (ζ_z-antisym)	mixed	1.18	1.99	1.31	56.9	20.6
Equatorial Rossby ($n = 1$)	mixed	0.51	3.03	0.92	90.2	11.2

Note: Each row refers to a set of modes with different m values. Shown in 2nd column are the volume-integrated kinetic energies of each mode integrated over m (E_{mode}) normalized by the total fluctuating kinetic energy E_{all}. Shown in 3rd and 4th columns are the maximum flow amplitudes v_{max} of the extracted modes at $m = 2$ and $m = 16$, respectively. Shown in 5th and 6th columns are the e-folding lifetimes $\tau_{\mathrm{mode}} = 2/\Gamma_{\mathrm{mode}}$ of the $m = 2$ and $m = 16$ modes, where $\Gamma_{\mathrm{mode}}/2\pi$ is the mode linewidth (full width at half maximum).

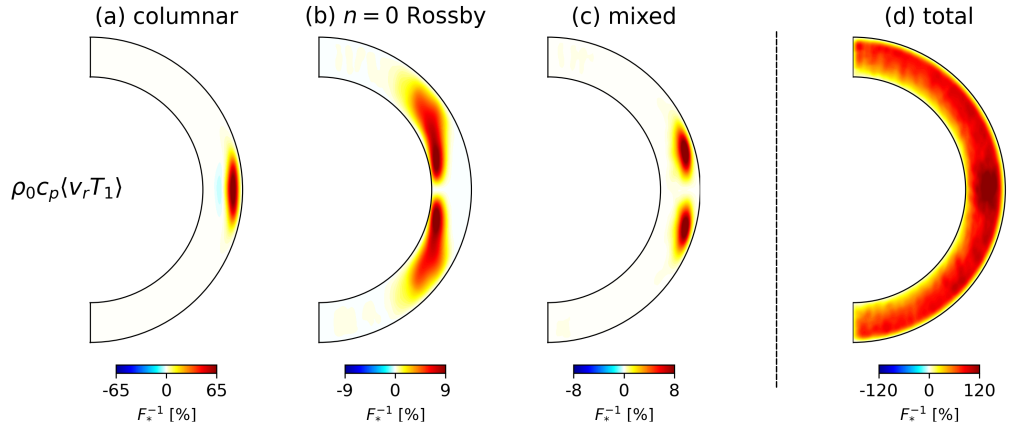

Figure 4.18: Enthalpy fluxes F_e associated with the extracted modes in our simulations summed over $m = 1 - 39$. Panels (a), (b), and (c) show those of the ζ_z-symmetric columnar convective modes, the $n = 0$ equatorial Rossby modes, and the mixed Rossby modes, respectively. In panel (d), the total enthalpy flux (including other modes and small-scale convection) is shown. The fluxes are normalized by the injected energy flux $F_* = L_*/(4\pi r^2)$.

4.6.2 Thermal energy transport

To examine the properties of the thermal energy transport, we compute the (radial) enthalpy flux F_e for each extracted mode as

$$F_\mathrm{e} = \rho_0 c_\mathrm{p} \langle v_r T_1 \rangle, \tag{4.18}$$

where $\langle\rangle$ denotes the longitudinal average and T_1 is temperature perturbation

$$T_1 = \left[\frac{\gamma - 1}{\gamma} \frac{p_1}{p_0} + \frac{s_1}{c_p} \right] T_0. \tag{4.19}$$

Figures 4.18a, b, and c show meridional distributions of the enthalpy flux F_e for the three extracted vorticity modes summed over $m = 1 - 39$. We note that all of these modes transport the thermal energy radially upward. The ζ_z-symmetric columnar convective modes transport about 65% of what is required in the upper convection near the equator. The $n = 0$ Rossby modes and the mixed modes can transport about $8 - 9\%$ of the required thermal energy in the lower and upper convection zone, respectively, outside the tangential cylinder.

This is a striking result because the $n = 0$ Rossby modes are believed to be quasi-toroidal and cannot contribute to the thermal energy transport in the linear theory for the simplified case with uniformly rotation, no turbulent diffusion, and adiabatic background stratification (e.g., Saio 1982, Damiani et al. 2020). We find that, under the influence of strong turbulent diffusion and superadiabatic background, the $n = 0$ equatorial Rossby modes become partially convective especially at high m.

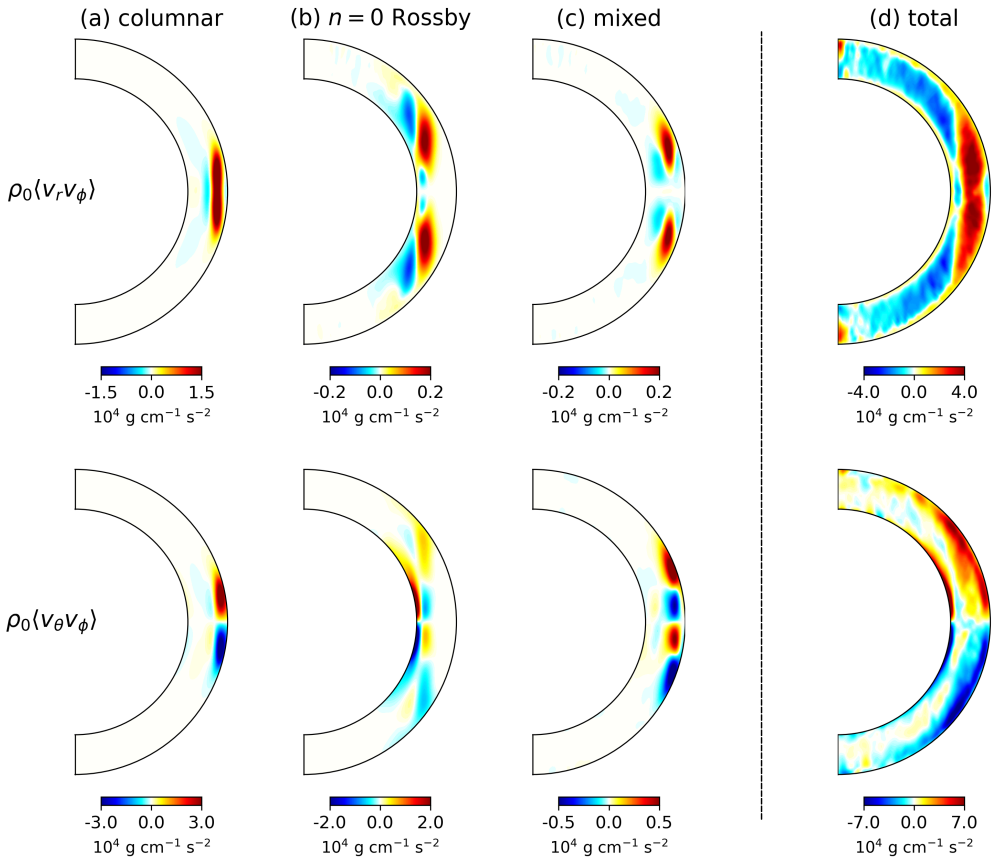

Figure 4.19: Reynolds stresses associated with the extracted modes in our simulations summed over $m = 1-39$. Panels (a), (b), and (c) show those of the ζ_z-symmetric columnar convective modes, the $n = 0$ equatorial Rossby modes, and the mixed Rossby modes, respectively. In panel (d), the total Reynolds stresses (including other modes and small-scale convection) is shown. Upper and lower panels correspond to $\rho_0\langle v_r v_\phi\rangle$ and $\rho_0\langle v_\theta v_\phi\rangle$.

4.6.3 Angular momentum transport

These equatorial vorticity modes also transport the angular momentum. Figures 4.19a, b, and c show the Reynolds stresses $\rho_0\langle v_r v_\phi\rangle$ (upper panels) and $\rho_0\langle v_\theta v_\phi\rangle$ (lower panels) summed over all m values for the extracted ζ_z-symmetric columnar convective modes, $n = 0$ equatorial Rossby modes, and the "mixed Rossby modes", respectively. These terms are proportional to the radial and latitudinal components of the convective angular momentum flux. For comparison, we show the total Reynolds stresses in our simulation (which include contributions from the other modes and small-scale convection) in Fig. 4.19d.

As for radial transport of the angular momentum, the dominant contribution is from the ζ_z-symmetric columnar convective modes that is about 8 times bigger than those from the $n = 0$ Rossby modes and the "mixed Rossby modes". The radially-upward angular momentum flux by the columnar convective modes accounts for about 37% of the total amount in the upper half of the convection zone near the equator. The positive

$\langle v_r v_\phi \rangle$ outside the tangential cylinder is a common feature of convection simulation in a strongly rotationally-constrained regime (Gastine et al. 2013, Fan and Fang 2014, Hotta et al. 2015a, Matilsky et al. 2020).

On the other hand, the angular momentum is preferentially transported equatorward in our simulation, as manifested by positive (negative) $\langle v_\theta v_\phi \rangle$ in the northern (southern) hemisphere in Fig. 4.19d lower panel. Our analysis reveals that both the ζ_z-symmetric columnar convective modes and the $n = 0$ Rossby modes contribute to this net equatorward angular momentum transport by about $30 - 40\%$ near the surface and at the base, respectively. The "mixed Rossby modes" turn out to be rather insignificant for the net angular momentum transport in the latitudinal direction.

4.7 Summary and discussion

In this paper, we report a mode-by-mode analysis of the low-frequency equatorial vorticity modes in a fully-nonlinear simulation of solar-like rotating convection. This study was motivated by the recent observational discovery of various types of inertial modes on the Sun (Löptien et al. 2018, Gizon et al. 2021) and the consequent theoretical study on these modes in a linear regime (Bekki et al. 2022b).

Based on the equatorial velocity power spectra, we have successfully identified and characterized several types of equatorial modes in our simulation. For each mode, eigenfunctions are extracted using the SVD method. We have also carried out the linear eigenmode analysis with the simulated differential rotation included. The computed linear dispersion relations and eigenfunctions are compared with the simulated power spectra and the extracted eigenfunctions. Our work provides a technique for subsequent numerical studies of low-frequency inertial modes in nonlinear convection simulations.

We have successfully identified the ζ_z-symmetric columnar convective modes, the $n = 0$ equatorial Rossby modes, and the "mixed Rossby modes". Table 4.1 summarizes the modes identified in this paper. Although we have mainly focused on these equatorial modes in this paper, we have also checked that the high-latitude modes are found to exist in our simulation as well (see Appendix 4.8.5).

Our major findings can be summarized as follows. The north-south ζ_z-symmetric columnar convective modes have the highest power in our simulation. They originate primarily from the compressional β-effect near the surface and thus can be well characterized by the dispersion relation similar to that of Glatzmaier and Gilman (1981). They transport a significant fraction of enthalpy upward and are the dominant term in the angular momentum transport near the equator.

Our analysis reveals that, at high m, the equatorial Rossby modes with no radial nodes ($n = 0$) have eigenfunctions that deviate from that of the uniformly-rotating and inviscid case ($r^m \sin^m \theta$). As m increases, we find that these modes are more and more confined near the base of the convection zone. We argue that this is due to the strong diffusion arising from the turbulent convective motions on resolved scales, which breaks the radial force balance between the pressure gradient and the Coriolis force and drives radial flows (Bekki et al. 2022b). We find that these equatorial Rossby modes are the longest-lived modes in our simulation.

Mode mixing between the equatorial Rossby modes and the columnar convective

modes is found in our nonlinear simulations, as predicted by the linear analysis of Bekki et al. (2022b). The surface power spectrum of the north-south symmetric v_θ can be characterized by two oppositely-propagating modes that form a single well-defined power ridge across $m = 0$. The retrograde and prograde modes for $m > 0$ can be identified as the $n = 1$ equatorial Rossby modes and the north-south ζ_z-antisymmetric columnar convective modes, respectively. We call them "mixed Rossby modes" following Bekki et al. (2022b). An analogy can be drawn between these "mixed modes" and the Yanai waves (mixed Rossby-gravity waves) where the retrograde-propagating Rossby waves and prograde-propagating gravity waves (Kelvin waves) are mixed with one another (e.g., Vallis 2006). The existence of the "mixed Rossby modes" has important implications. One of these follow from its frequency which is very close to that of the $n = 0$ equatorial Rossby mode at $m \geq 5$ (see Fig. 10 in Bekki et al. 2022b). Therefore, it is possible that the observed Rossby modes on the Sun could be $n = 1$ modes rather than $n = 0$ modes as is typically assumed.

The nonlinear simulations contain a wealth of information about many more modes of oscillations in the inertial frequency range. In fact, the analysis method reported in this paper can be used in the future to study the $m = 1$ high-latitude inertial mode (Gizon et al. 2021, Bekki et al. 2022b) and the $l = m + 1$ high-frequency retrograde modes (Hanson et al. 2022).

Acknowledgements

We thank A. Birch and B. Proxauf for helpful discussions. Y. B. is enrolled in the International Max-Planck Research School for Solar System Science at the University of Göttingen (IMPRS). Y .B. also acknowledges a financial support from long-term scholarship program for degree-seeking graduate students abroad from the Japan Student Services Organization (JASSO). We acknowledge a support from ERC Synergy Grant WHOLE SUN 810218. All the numerical computations were performed at GWDG and the Max-Planck supercomputer RZG in Garching.

4.8 Appendix

4.8.1 Spatio-temporal discretization scheme

The same numerical scheme as Vögler et al. (2005) is used. Suppose that a partial equation describing the time evolution of a quantity Q is written as

$$\frac{\partial Q}{\partial t} = -\frac{\partial \mathcal{F}(Q)}{\partial x} + \mathcal{S}(Q), \tag{4.20}$$

where $\mathcal{F}$ and $\mathcal{S}$ are the x-directed flux function and the source function, respectively. Time integration is conducted in a following 4-step manner to compute the value at $t = (n+1)\Delta t$,

$$Q_i^{n+1/4} = Q_i^n - \frac{\Delta t}{4\Delta x}(\tilde{\mathcal{F}}^n_{i+1/2} - \tilde{\mathcal{F}}^n_{i-1/2}) + \frac{\Delta t}{4}\mathcal{S}^n, \tag{4.21}$$

$$Q_i^{n+1/3} = Q_i^n - \frac{\Delta t}{3\Delta x}(\tilde{\mathcal{F}}^{n+1/4}_{i+1/2} - \tilde{\mathcal{F}}^{n+1/4}_{i-1/2}) + \frac{\Delta t}{3}\mathcal{S}^{n+1/4}, \tag{4.22}$$

$$Q_i^{n+1/2} = Q_i^n - \frac{\Delta t}{2\Delta x}(\tilde{\mathcal{F}}^{n+1/3}_{i+1/2} - \tilde{\mathcal{F}}^{n+1/3}_{i-1/2}) + \frac{\Delta t}{2}\mathcal{S}^{n+1/3}, \tag{4.23}$$

$$Q_i^{n+1} = Q_i^n - \frac{\Delta t}{\Delta x}(\tilde{\mathcal{F}}^{n+1/2}_{i+1/2} - \tilde{\mathcal{F}}^{n+1/2}_{i-1/2}) + \Delta t\mathcal{S}^{n+1/2}. \tag{4.24}$$

Here, i denotes the index of the grid position along a spatial direction x, and $\tilde{\mathcal{F}}_{i+1/2}$ represents the numerical flux evaluated at the cell boundary as

$$\tilde{\mathcal{F}}_{i+1/2} = \frac{-\mathcal{F}_{i+2} + 7\mathcal{F}_{i+1} + 7\mathcal{F}_i - \mathcal{F}_{i-1}}{12}. \tag{4.25}$$

The source functions are calculated with fourth-order accuracy using the first and second spatial derivatives,

$$\left(\frac{\partial Q}{\partial x}\right)_i = \frac{-Q_{i+2} + 8Q_{i+1} - 8Q_{i-1} + Q_{i-2}}{12\Delta x}, \tag{4.26}$$

$$\left(\frac{\partial^2 Q}{\partial x^2}\right)_i = \frac{-Q_{i+2} + 16Q_{i+1} - 30Q_i + 16Q_{i-1} - Q_{i-2}}{12\Delta x^2}. \tag{4.27}$$

4.8.2 Slope-limited artificial diffusion

We use the slope-limited (strongly non-linear) artificial diffusion proposed by Rempel (2014). The artificial viscous term is added after the 4-step Runge-Kutta time integration,

$$Q_i^{\mathrm{new}} = Q_i + \frac{\Delta t}{\Delta x}(\tilde{f}_{i+1/2} - \tilde{f}_{i-1/2}), \tag{4.28}$$

where $\tilde{f}_{i+1/2}$ denotes the numerical artificial diffusive flux at the cell interface. In order to minimize the numerical diffusions on the resolved scale and to obtain an effective cutoff at the grid scale, the numerical diffusive flux is determined in the following manner. First, we reconstruct the values at the cell interface $i + 1/2$ that are extrapolated from left and right sides based on the discrete solutions u_i as

$$Q^L_{i+1/2} = Q_i + \Delta Q_i/2, \tag{4.29}$$

$$Q^R_{i+1/2} = Q_{i+1} - \Delta Q_{i+1}/2. \tag{4.30}$$

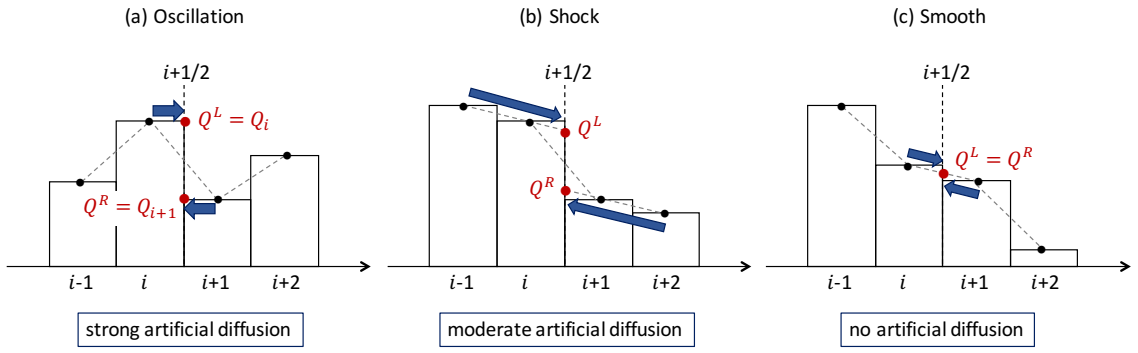

Figure 4.20: Schematic diagram explaining how to reconstruct the values at the cell interfaces, extracted from both sides, for (a) an oscillatory region where the solution is locally non-monotonic, (b) a shock region where the solution is locally monotonic but has a jump, and (c) a region where the solution is monotonic and is sufficiently smooth.

Here, ΔQ_i denotes the reconstruction slope for the ith cell and given by

$$\Delta Q_i = \mathrm{minmod}\left[\frac{Q_{i+1} - Q_{i-1}}{2}, 2(Q_{i+1} - Q_i), 2(Q_i - Q_{i-1})\right], \tag{4.31}$$

where minmod selects the variable whose amplitude is the smallest among three if all of their signs are the same, whereas it returns zero when any of them has a different sign from the others. As a result, $Q^R_{i+1/2} - Q^L_{i+1/2}$ becomes the largest possible value $Q_{i+1} - Q_i$ when a discrete solution shows a zigzag structure whereas $Q^R_{i+1/2} - Q^L_{i+1/2}$ vanishes if the discrete structure is sufficiently smooth. This is clearly illustrated in Fig. 4.20.

The Numerical diffusive fluxes are given so that it becomes essentially proportional to a difference between the two extrapolated values at the cell interface as

$$\tilde{f}_{i+1/2} = -\frac{c_{i+1/2}}{2}\Phi_{\mathrm{h}}\left[Q^R_{i+1/2} - Q^L_{i+1/2}, Q_{i+1} - Q_i\right] \cdot (Q^R_{i+1/2} - Q^L_{i+1/2}). \tag{4.32}$$

Here, an adjustment factor Φ_{h} is further introduced to minimize the diffusion. We use the functional form of Φ_{h} given by

$$\Phi_{\mathrm{h}}(a, b) = \begin{cases} \max\left[0, 1 + h\,(a/b - 1)\right] & (ab > 0) \\ 0 & (ab < 0). \end{cases} \tag{4.33}$$

Here, a parameter h controls the degree of diffusion. For example, a choice of $h = 0$ (and thus $\Phi_h = 1$) reduces to that of Lax-Friedrich scheme. For $0 < h < 1$, the scheme becomes less diffusive than Lax-Friedrich scheme since Φ_{h} returns a value smaller than 1 for smooth regions, i.e., $|(Q^R_{i+1/2} - Q^L_{i+1/2})/(Q_{i+1} - Q_i)|$ is small. For $h > 1$, Φ_h begins to return 0 for sufficiently smooth regions, i.e., $|(Q^R_{i+1/2} - Q^L_{i+1/2})/(Q_{i+1} - Q_i)| < 1 - 1/h$. This is clearly illustrated in Fig. 4.21. In all of our calculations, we set $h = 1.5$.

The slope-limited artificial diffusion described above is applied to the momentum $\rho_0 \boldsymbol{v}$ after the final Runge-Kutta time integration. The kinetic energy dissipated by the artificial diffusion $\tilde{Q}_{\mathrm{D}}$ is converted to the internal energy to keep the global energy conservation well. This is given by

$$\tilde{Q}_{\mathrm{D}} = -\tilde{f}_{ij}(\rho_0 \boldsymbol{v})\frac{\partial v_i}{\partial x_j}, \tag{4.34}$$

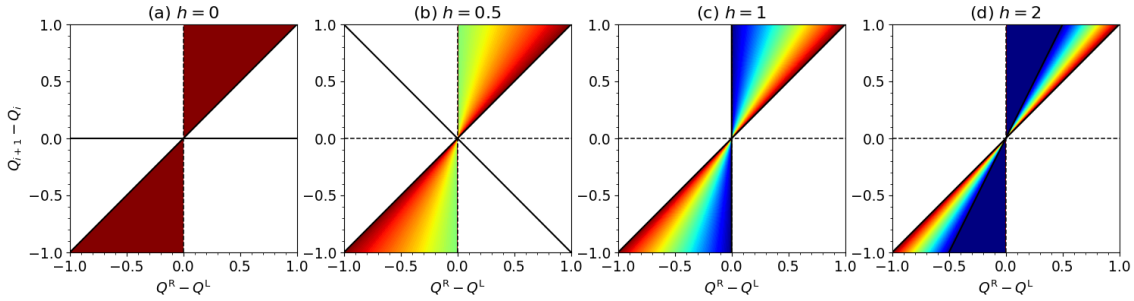

Figure 4.21: Dependence of Φ_h on h parameter. Blue and red color scale linearly corresponds 0 and 1, respectively. As h increases, Φ_h is switched on only when $Q^{\mathrm{R}} - Q^{\mathrm{L}} \approx Q_{i+1} - Q_i$, i.e., the solution is highly oscillatory.

where $\tilde{\boldsymbol{f}}$ denotes the artificial diffusive momentum flux.

4.8.3 Implementation of the Yin-Yang grid

In this appendix, we briefly explain how to transform vectors and tensors between Yin and Yang grids. The transformation matrix (metric tensor) $\mathcal{M}$ is defined as

$$\boldsymbol{e}_{\bar{\beta}} = \mathcal{M}^{\alpha}_{\bar{\beta}} \boldsymbol{e}_{\alpha}, \tag{4.35}$$

where $\boldsymbol{e}_{\alpha}$ and $\boldsymbol{e}_{\bar{\beta}}$ are the unit vectors of the Yin (denoted by subscripts without bar) and Yang grids (denoted by subscripts with bar), respectively. In the spherical coordinate, the above equation can be expressed as (Kageyama and Sato 2004),

$$\left(\boldsymbol{e}_{\bar{r}}, \boldsymbol{e}_{\bar{\theta}}, \boldsymbol{e}_{\bar{\phi}}\right) = \left(\boldsymbol{e}_{r}, \boldsymbol{e}_{\theta}, \boldsymbol{e}_{\phi}\right) \begin{pmatrix} 1 & 0 & 0 \\ 0 & -\sin\phi \sin\bar{\phi} & -\cos\bar{\phi}/\sin\theta \\ 0 & \cos\bar{\phi}/\sin\theta & -\sin\phi\sin\bar{\phi} \end{pmatrix}. \tag{4.36}$$

This leads to a useful formula of Yin-Yang transformation,

$$\begin{aligned} \bar{r} &= r, \\ \bar{\theta} &= \cos^{-1}\left(\sin\theta \sin\phi\right), \\ \bar{\phi} &= \tan^{-1}\left(-\frac{\cos\theta}{\sin\theta\cos\phi}\right). \end{aligned} \tag{4.37}$$

Note that the transformation matrix $\mathcal{M}$ is orthogonal, meaning that the Yin-Yang transformation is symmetric and complemental with each other,

$${}^{t}\mathcal{M} = \mathcal{M}^{-1}. \tag{4.38}$$

Since a vector $\boldsymbol{V}$ is invariant with respect to the choice of the coordinate;

$$\boldsymbol{V} = V^{\alpha}\boldsymbol{e}_{\alpha} = V^{\bar{\beta}}\boldsymbol{e}_{\bar{\beta}}, \tag{4.39}$$

the vector transformation can be easily derived as

$$V^{\bar{\beta}} = \mathcal{M}^{\bar{\beta}}_{\alpha} V^{\alpha}. \tag{4.40}$$

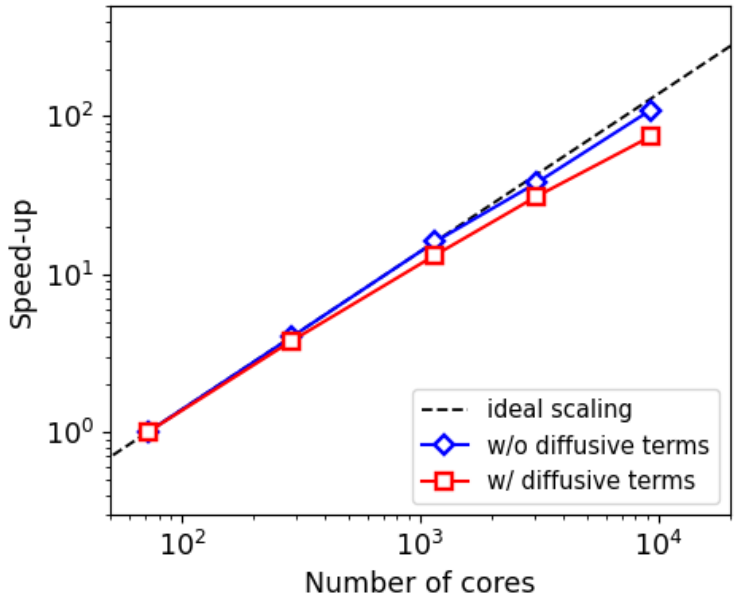

Figure 4.22: Result of the strong-scaling test. Shown is the relative speed-up as a function of number of cores. Red and blue points indicate the simulations with and without the viscous terms. Black dashed line represent the ideal scaling.

In the spherical coordinate, this can be expressed as

$$\begin{pmatrix} V^{\bar{r}} \\ V^{\bar{\theta}} \\ V^{\bar{\phi}} \end{pmatrix} = \begin{pmatrix} 1 & 0 & 0 \\ 0 & -\sin\phi \sin\bar{\phi} & -\cos\phi/\sin\bar{\theta} \\ 0 & \cos\phi/\sin\bar{\theta} & -\sin\phi\sin\bar{\phi} \end{pmatrix} \begin{pmatrix} V^{r} \\ V^{\theta} \\ V^{\phi} \end{pmatrix}. \tag{4.41}$$

In the same way, the tensor transformation can be derived as follows. Let us consider a second-order tensor $\mathcal{T}$,

$$\mathcal{T} = \mathcal{T}^{\alpha\beta} \boldsymbol{e}_\alpha \otimes \boldsymbol{e}_\beta = \mathcal{T}^{\bar{\gamma}\bar{\delta}} \boldsymbol{e}_{\bar{\gamma}} \otimes \boldsymbol{e}_{\bar{\delta}}. \tag{4.42}$$

Substituting the Eq.(4.35), we have

$$\mathcal{T}^{\bar{\gamma}\bar{\delta}} = \mathcal{T}^{\alpha\beta} \mathcal{M}^{\bar{\gamma}}_{\alpha} \mathcal{M}^{\bar{\delta}}_{\beta}. \tag{4.43}$$

The Eq.(4.43) can be used to set the boundary condition of the viscous stress tensor or determining the Λ-effect tensor in the simulation code.

4.8.4 Code performance

Since our code is designed to avoid the global communications among cores as much as possible, it is expected to hold a high MPI parallel efficiency. In this appendix, we carry out performance benchmark tests to evaluate the code's strong scaling: The elapsed CPU time used to finish 300 steps of time integration is measured with an increasing number of cores, while fixing the total problem size to $(N_r, N_\theta, N_\phi) = (144, 768, 1536)$. The scaling

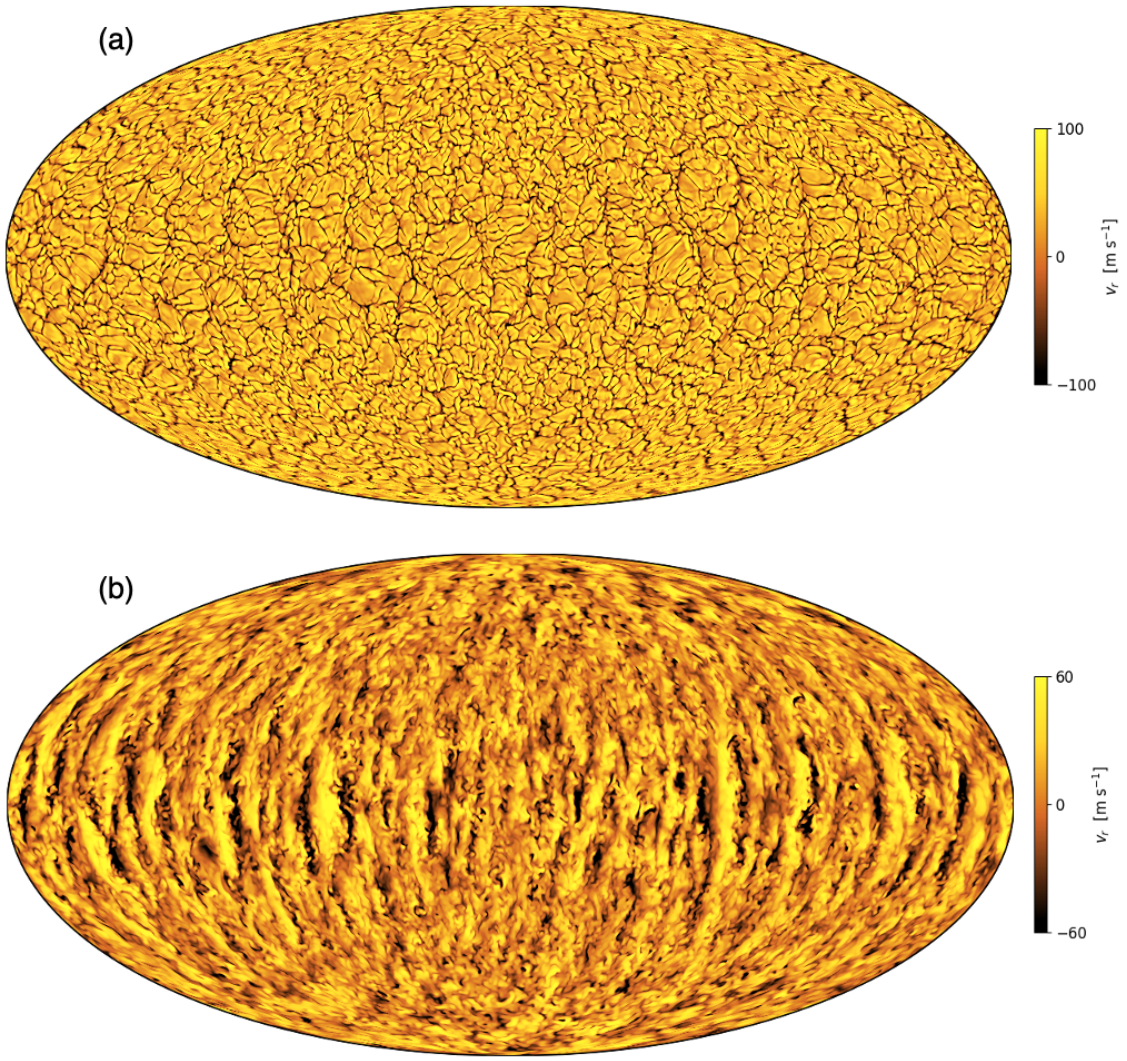

Figure 4.23: Mollweide-projected view of radial velocity at (a) $r = 0.99R_\odot$ and at (b) $r = 0.92R_\odot$ from our high-resolution calculation.

tests have been carried out at the COBRA HPC system at the Max Planck Computing and Data Facility (MPCDF). We use Intel compiler version 19.1 and Intel MPI version 19.7. Figure 4.22 shows the result of the performance test for the cases with and without the explicit viscous and thermal diffusion. When the explicit diffusion is excluded (and only the artificial diffusion is used), the code scales almost perfectly up to 10^4 cores. However, it is shown that the use of explicit diffusion makes the code slightly inefficient. This is because we set the boundary condition on the viscous stress tensor in the code as well.

To demonstrate a high performance of our code, we show a snapshot of the high-resolution simulation of rotating convection in Figure 4.23. Although the scale of convection at the surface becomes much smaller than the low-resolution simulation discussed in §4.5.1, the existence of thermal Rossby waves ('banana' cells) can still be confirmed.

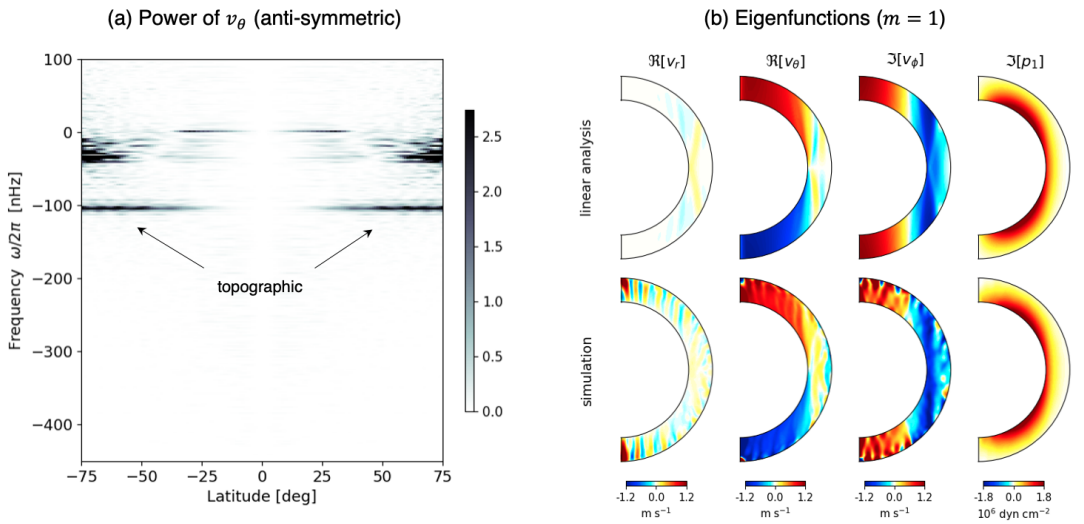

Figure 4.24: (a) Power spectrum of nouth-south anti-symmetric component of latitudinal velocity at the base of the convection zone $r = 0.71R_\odot$ at $m = 1$ as a function of latitude. The high-latitude power associated with topographic Rossby mode is denoted by white arrows at $\omega/2\pi \approx -105$ nHz. (b) Extracted eigenfunctions of topographic Rossby mode (with north-south symmetric for ζ_z) at $m = 1$. Upper and lower panels show the eigenfunctions extracted from simulation and that of linear analysis, respectively.

4.8.5 High-latitude modes

In this appendix, we demonstrate that the high-latitude modes (topographic Rossby modes), as well as traditional equatorial Rossby modes and columnar convective modes, exist in our simulation predominantly at $m = 1$. For $m = 2$ and 3, the power still exists but is getting substantially weaker. Figure 4.24a shows the power spectrum of north-south symmetric component of v_θ at the base of the convection zone $r = 0.71R_\odot$ at $m = 1$ as a function of latitude. The power of topographic Rossby mode can be seen at $\omega/2\pi \approx -105$ nHz from middle to high latitudes. The extracted eigenfunctions of this mode are shown on the upper panels of Fig.4.24b and are compared with the results of linear analysis (lower panels). The associated flow is dominantly z-vortical and is strongly confined inside the tangential cylinder. This mode can be called as 'north-south symmetric high-latitude mode' because ζ_z is symmetric across the equator. The product of ζ_z and p_1 is negative throughout the domain, showing that the mode is in geostrophic balance.

In addition to the symmetric modes, we also identified the north-south anti-symmetric high-latitude modes in our simulation. Figure 4.25a shows the same power spectrum as Fig. 4.24a but for symmetric component of v_θ between the hemispheres. The power resides at $\omega/2\pi \approx -48$ nHz in high latitudes (above ± 50 deg) whereas the equatorial Rossby mode (r mode) exists at $\omega/2\pi \approx -400$ nHz in low latitudes. Figure 4.25b shows the extracted eigenfunctions of anti-symmetric high-latitude mode at $m = 1$. Unlike the symmetric mode, ζ_z is dissected between the hemispheres. However, there exists a latitudinal velocity at the equator, which can correlate the vortices between the hemispheres.

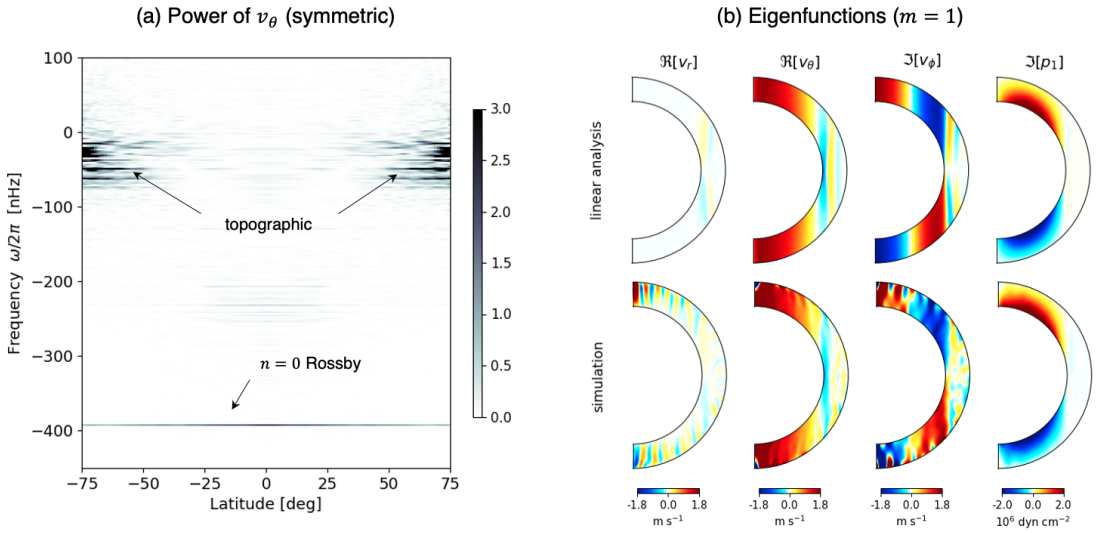

Figure 4.25: (a) Power spectrum of north-south symmetric component of latitudinal velocity at the base of the convection zone $r = 0.71R_\odot$ at $m = 1$ as a function of latitude. High-latitude mode power exists at the frequency of about -48 nHz, whereas the equatorial Rossby power can be seen at the frequency of about -400 nHz. (b) The same as Fig. 4.24(b) but for the high-latitude mode with north-south anti-symmetric for ζ_z.

5 Baroclinic instability as an origin of the high-latitude inertial modes in the Sun

Abstract

Recent observations show that, at high latitudes, the large-scale flow on the Sun is dominated by a retrograde-propagating spiraling pattern with the azimuthal order $m = 1$. However, the physical origin of this flow feature is still unknown. The aim of this study is to demonstrate that the observed high-latitude flow feature can be explained in terms of the baroclinically-induced Rossby modes. We first carry out a linear analysis of the eigen oscillations of the Sun including the latitudinal entropy gradient in the solar convection zone. It is shown that baroclinic instability occurs at high latitudes when the latitudinal entropy gradient is included. The eigenfunctions at the surface show a spiral pattern which is in a good agreement with the observations. The dispersion relation of the most unstable baroclinic modes agree well with the observed mode frequencies for $1 \leq m \leq 4$. We further conduct a set of nonlinear simulations where the thermal wind is artificially forced and show that the baroclinic instability leads to an efficient equatorward transport of the thermal energy. In the nonlinear phase, the most dominant baroclinic mode always turns out to be the $m = 1$ mode with the north-south anti-symmetric longitudinal velocity. It is also demonstrated that the baroclinic instability serves as an inherent mechanism to regulate the amplitudes of latitudinal differential rotation (and the entropy variation) in the solar convection zone. We emphasize for the first time a significance of the baroclinic instability on the large-scale flow dynamics in the solar convection zone.

5.1 Introduction

In the outer 30% of the Sun, thermal convection occurs on various spatial and temporal scales. On small scales, granulation and supergranulation are robustly observed at the surface (e.g., Nordlund et al. 2009). On the other hand, large-scale convection in the Sun is rather poorly understood. It is generally predicted that large-scale convective motions are strongly rotationally-constrained and tend to exist in the form of the columnar convective modes (thermal Rossby waves) (Glatzmaier and Gilman 1981, Busse 2002, Miesch et al.

This chapter reproduces a draft paper prepared by Y. Bekki, R. Cameron, and L. Gizon. Contribution: Y. Bekki did most of the work.

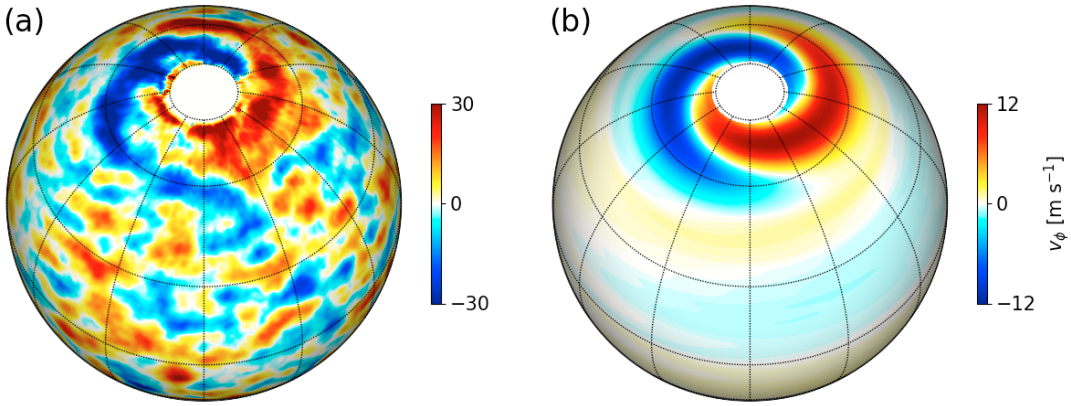

Figure 5.1: Observed spiralling pattern of the longitudinal velocity v_ϕ at high latitudes. (a) A temporal snapshot of the non-axisymmetric v_ϕ on the solar surface at 2018/12/30 00^h:00^m:00^s UT. The flow data is obtained by the local correlation tracking of supergranulation seen in the HMI data (Hathaway and Upton 2021). (b) The surface eigenfunction of v_ϕ for the $m = 1$ high-latitude inertial mode extracted from the 10-year time series of HMI data. The flow data is obtained by the ring-diagram analysis (Gizon et al. 2021).

2008), also known as "banana-cell" convection (e.g., Elliott et al. 2000). However, these large-scale convective patterns have never been successfully observed (Gizon et al. 2021).

Recent observational studies have revealed that the large-scale flow pattern on the Sun falls into two distinct regimes (Hathaway and Upton 2021, Gizon et al. 2021). First, at low latitudes, Rossby modes (r modes) have been unambiguously detected (Löptien et al. 2018, Liang et al. 2019, Hanasoge and Mandal 2019, Proxauf et al. 2020, Mandal and Hanasoge 2020). The observed properties of the equatorial Rossby modes in the Sun are theoretically investigated in both linear (Damiani et al. 2020, Gizon et al. 2020b, Bekki et al. 2022b) and nonlinear regimes (Chapter 4).

At high latitudes, on the other hand, observations have found the longitudinal flow features that spiral around the poles (Hathaway et al. 2013, Bogart et al. 2015, Hathaway and Upton 2021, Gizon et al. 2021). We show in Fig. 5.1 an example of this flow feature obtained by supergranulation tracking at the solar surface. The velocity power predominantly lies at the azimuthal order $m = 1$, and the flow pattern propagates in a retrograde direction with respect to the Carrington frame. They have relatively large velocity amplitudes of about $9 - 12$ m s^{-1} (Howe et al. 2015, Hathaway and Upton 2021, Gizon et al. 2021). The associated Reynolds stresses become positive (negative) near the north (south) poles, implying that they can substantially contribute to the equatorward angular momentum transport at high latitudes.

Despite their significance on the convection zone dynamics, the physical origin of these high-latitude flow features remains largely uncertain. Hathaway et al. (2013), Hathaway and Upton (2021) claimed that they likely represent the giant convection cells advected by differential rotation in the deep convection zone. Indeed, Gilman (1975) has shown that the most unstable convective modes at high latitudes exhibit spiralling patterns using the linear model of rotating Bouussinesq convection. However, these features are not well reproduced in solar-like rotating convection simulations in a spherical shell.

In this paper, we alternatively propose the baroclinic instability as a possible physical origin for the observed large-scale high-latitude flow features in the Sun.

Baroclinic instability is an instability of thermal wind in a stratified rotating fluid. In the Earth's atmosphere, this instability plays a critical role in controlling the weather at middle latitudes (e.g., Vallis 2006, Holton and Hakim 2013). Moreover, in the Venus atmosphere, the baroclinic instability is often considered crucial for sustaining the observed "streak" structure of the clouds (Kashimura et al. 2019).

In the solar convection zone, the non-Taylor-Proudman differential rotation is considered to be maintained by the latitudinal entropy gradient via the thermal wind balance (Kitchatinov and Ruediger 1995, Rempel 2005, Miesch et al. 2006, Brun et al. 2011, Hotta 2018), and thus should be essentially unstable for baroclinic instability. Historically, it has long been believed that baroclinic instability is strongly suppressed when the background is convectively unstable (Knobloch and Spruit 1982, Spruit and Knobloch 1984). Thus, the main focus has been on the stability of the solar tachocline both in hydrodynamic (Gilman and Dikpati 2014, Gilman 2016) and in magnetohydrodynamic regimes (Gilman 2015, 2017). Similar stability analyses have also been conducted for the stellar radiative interiors with weak radial differential rotation (Kitchatinov 2013, 2014). However, recent numerical experiments indicate that the baroclinic instability can still occur and grow even in the presence of vigorous small-scale convection (Callies and Ferrari 2018).

In this paper, we claim that the observed large-scale high-latitude flow features result from the baroclinic instability in the Sun. To this end, we carry out a set of numerical experiments in both linear and nonlinear regimes: In the linear regime, the basic properties (dispersion relations and eigenfunctions) of the baroclinically-unstable modes are investigated and compared with the observations. Then, we carry out a set of nonlinear simulations of the large-scale flows in a spherical shell to study how the instability develops and saturates inside the solar convection zone.

5.2 Linear stability analysis of baroclinic modes

In this section, we discuss the baroclinically-unstable modes in the solar convection zone in the linear regime.

5.2.1 Numerical methods

For the linear analysis of baroclinic instability in the Sun, we use the numerical code developed and described by Chapter 3 (Bekki et al. 2022b). We seek for the low-frequency eigenmodes under the influences of solar differential rotation and associated the background entropy gradient. The linearized equations of mass, motion, entropy, and state are

given in a spherical coordinate as

$$\frac{D\rho_1}{Dt} = -\nabla\cdot(\rho_0\boldsymbol{v}), \tag{5.1}$$

$$\frac{D\boldsymbol{v}}{Dt} = -\frac{\nabla p_1}{\rho_0} - \frac{\rho_1}{\rho_0}g\boldsymbol{e}_r + 2\boldsymbol{v}\times\Omega\boldsymbol{e}_z - r\sin\theta\boldsymbol{v}\cdot\nabla\Omega + \frac{1}{\rho_0}\nabla\cdot\mathcal{D}_{\rm vis}, \tag{5.2}$$

$$\frac{Ds_1}{Dt} = -v_r\frac{\partial s_0}{\partial r} - \frac{v_\theta}{r}\frac{\partial s_0}{\partial\theta} + \frac{1}{\rho_0 T_0}\nabla\cdot(\kappa\rho_0 T_0\nabla s_1), \tag{5.3}$$

$$\frac{p_1}{p_0} = \gamma\frac{\rho_1}{\rho_0} + \frac{s_1}{c_{\rm v}}. \tag{5.4}$$

Here $D/Dt = \partial/\partial t + (\Omega - \Omega_0)\partial/\partial\phi$ denotes the material derivative and $\Omega_0/2\pi = 456$ nHz is the Carrington rotation rate. $\boldsymbol{v} = (v_r, v_\theta, v_\phi)$ denotes the velocity perturbation and p_1, ρ_1, and s_1 are the perturbations of pressure, density, and entropy with respect to the background quantities (denoted by subscript 0). We use the same solar background model as Bekki et al. (2022b), which mimics the standard internal model S (Christensen-Dalsgaard et al. 1996a). c_v is the heat capacity per unit mass at constant volume and $\gamma = 5/3$ is the specific heat ratio. $\mathcal{D}_{\rm vis}$ represents the viscous stress tensor,

$$\mathcal{D}_{\rm vis} = \rho_0\nu\left[\mathcal{S} - \frac{2}{3}(\nabla\cdot\boldsymbol{v})\boldsymbol{I}\right], \tag{5.5}$$

where ν is viscous diffusivity and $\mathcal{S}$ denotes the velocity deformation tensor. For simplicity, we use the spatially constant viscous and thermal diffusivities with $\nu = \kappa = 10^{12}$ cm^2 s^{-1}.

For prescribing the differential rotational in the convection zone $\Omega(r,\theta)$, we use the solar observational data inferred from global helioseismology (Larson and Schou 2018). Note, however, that we slightly modified the rotational profile at high latitudes where the measurements are not reliable, following the method described in Karak and Cameron (2016). Figure 5.2a shows the profile of the differential rotation used in our linear analysis.

$\partial s_0/\partial r$ and $\partial s_0/\partial\theta$ represent radial and latitudinal deviations from the adiabatic background, respectively. Note that the deviation is assumed to be very small ($\approx 10^{-6}$) so that we can still use the adiabatic description for the background pressure, density, and temperature. In order to distinguish the baroclinic modes from the convective modes, we set the background to be convectively-neutral by omitting the radial entropy gradient ($\partial s_0/\partial r = 0$) in this study. On the other hand, the latitudinal entropy gradient $\partial s_0/\partial\theta$ is estimated based on the thermal wind balance in the convection zone (e.g., Kitchatinov and Ruediger 1995, Rempel 2005, Miesch et al. 2006, Brun et al. 2011),

$$\frac{g}{c_p}\frac{\partial s_0}{\partial\theta} = r^2\sin\theta\frac{\partial\Omega^2}{\partial z}, \tag{5.6}$$

as shown in Fig. 5.2b.

The numerical domain extends from the base of the convection zone $r = 0.71R_\odot$ to $r = 0.985R_\odot$ and both radial boundaries are assumed to be impenetrable and stress-free. At both poles ($\theta = 0, \pi$), we set all variables to zero; $\boldsymbol{v} = \rho_1 = s_1 = 0$. We seek for

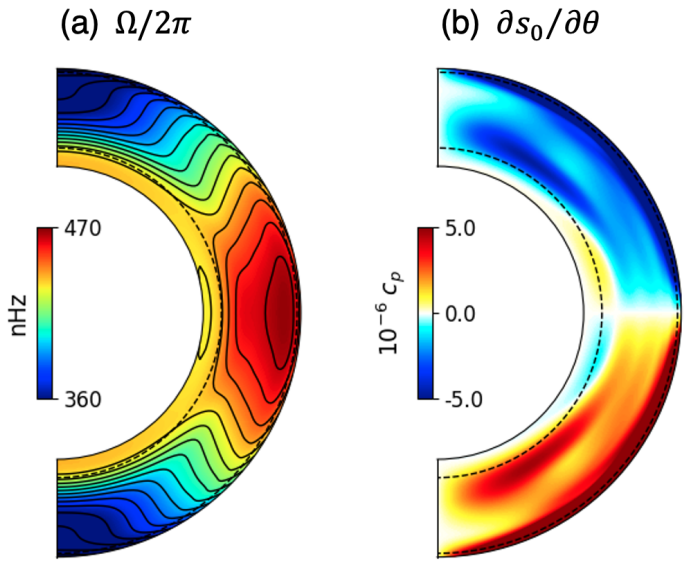

Figure 5.2: (a) Differential rotation in the Sun deduced from the global helioseismology (Larson and Schou 2018) used in the linear analysis. The rotational profiles near the poles are corrected using the analytical model. The data is available online. (b) Latitudinal entropy gradient estimated by the Eq.(5.6). Dotted lines denote the location of the top and bottom boundaries used in our linear eigensolver.

solutions of the linearized equations assuming that the perturbations are proportional to $\propto \exp\left[i(m\phi - \omega t)\right]$, where m is azimuthal order and ω is frequency. The spatial derivatives are evaluated with second-order finite-differences by 16 grid points in radial and by 72 grid points in latitudinal directions. The above Eqs (5.1)-(5.3) are combined in a matrix form into a complex eigenvalue problem, which is numerically solved using the LAPACK routine. For mode details about the linear eigen-solver, refer to Chapter 3.

5.2.2 Results

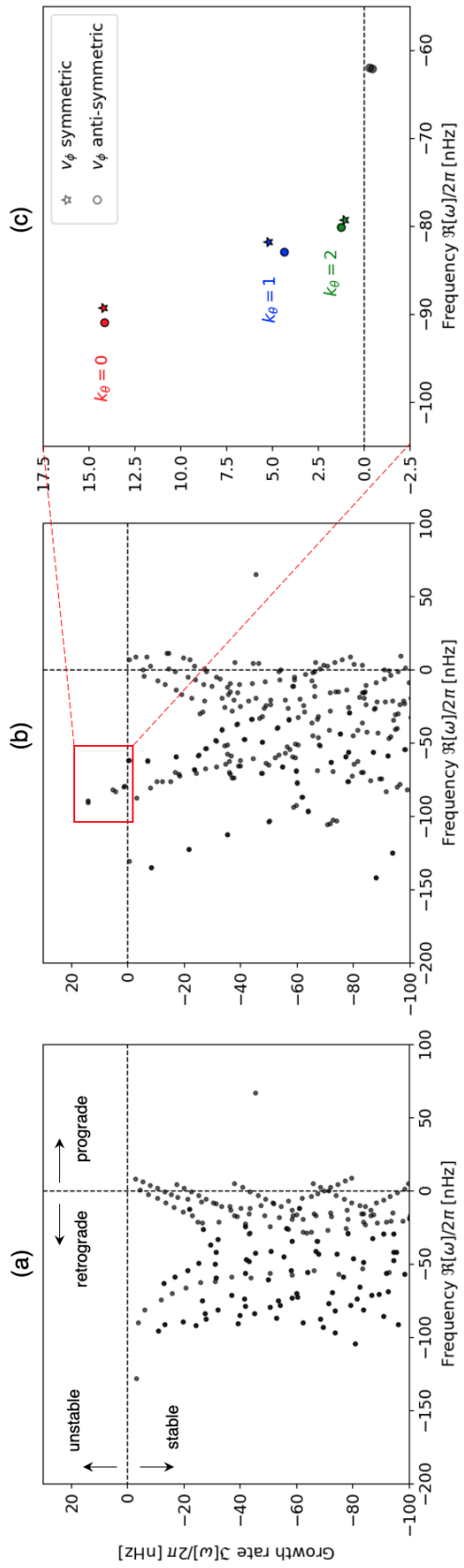

Figure 5.3: Distibution of eigenfrequencies obtained in the linear calculation in a complex domain at $m = 1$. (a) The case without the latitudinal entropy gradient $\partial s_0/\partial\theta$. (b) The case with the latitudinal entropy gradient. (c) The zoom-in of the panel (b), focusing on the baroclinically-unstable modes. Star and diamonds represent the modes whose v_ϕ eigenfunctions are north-south symmetric and anti-symmetric, respectively. Red, blue, and green markers denote the modes with the number of latitudinal nodes at high-latitude $k_\theta = 0$, 1, and 2, respectively.

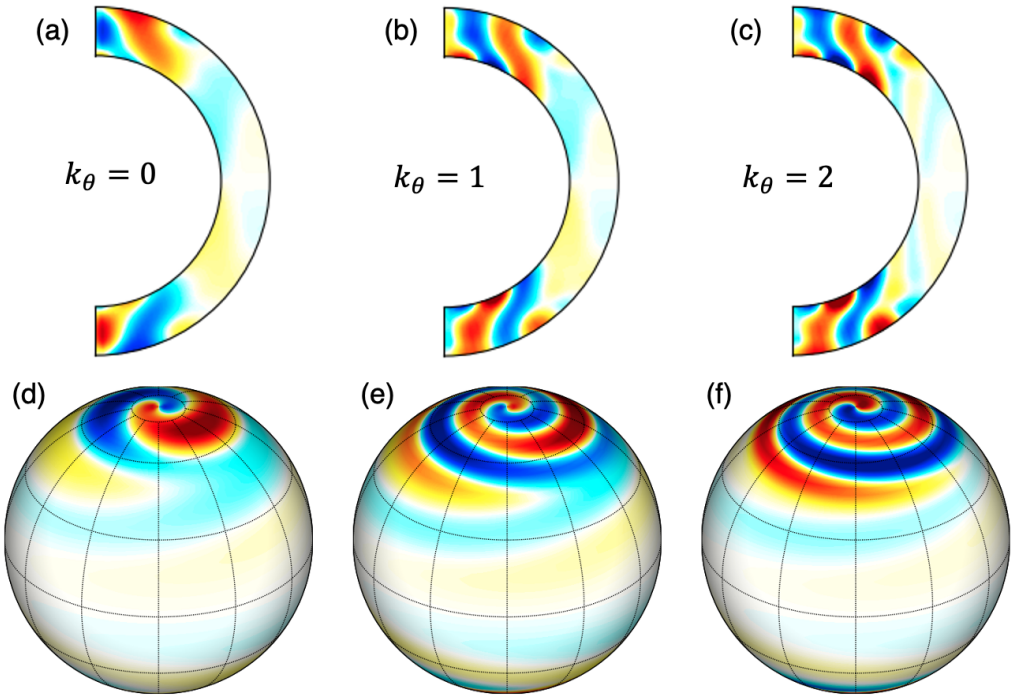

Figure 5.4: Eigenfunctions of azimuthal velocity v_ϕ of the baroclinically-unstable modes with north-south anti-symmetric v_ϕ. Top, middle, and bottom rows show the modes with $k_\theta = 0$, 1, and 2, respectively. Left and right panels are the meridional eigenfunctions at the central meridian and the sphertical eigenfunctions at the surface $r = 0.985R_\odot$, respectively.

To assess the impact of the latitudinal entropy variation on the stability of the linear system, we first carry out two case studies with and without the baroclinic term, $-v_\theta(\partial s_0/\partial\theta)/r$, in the equation of entropy (5.3). Figures 5.3a and b compare the distribution of low-frequency eigenmodes in the complex frequency domain at $m = 1$. Note that positive (negative) frequency $\Re[\omega]$ corresponds to prograde (retrograde) propagation and positive (negative) growth rate $\Im[\omega]$ represents instability (damping). It is clearly shown that some modes become unstable only when the latitudinal entropy gradient is included, as indicated by red square in Fig. 5.3b. Figure 5.3c shows a zoom-in of Fig. 5.3b, focusing on the unstable (growing) modes. As will be shown later, these unstable modes represent the baroclinic instability and are classified by the number of latitudinal nodes per hemisphere $k_y = 0$ (red), $k_y = 1$ (blue), and $k_y = 2$ (green). The fastest growing mode always turns out to be the one with $k_y = 0$. It is also shown that the modes with both north-south symmetries (denoted by stars and circles) appear as pairs at similar frequencies and growth rates with each other.

Figure 5.4 shows the eigenfunctions of the baroclinically-unstable modes with north-south anti-symmetry at $m = 1$ extracted from the Fig. 5.3c for different k_y. Shown in left and right panels are the meridional eigenfunctions at $\phi = 0°$ (central meridian) and the surface eigenfunctions of the longitudinal velocity v_ϕ, respectively. All the modes are confined inside the tangential cylinder, and thus, are visible only in high latitudes at the surface. It is also clearly manifested that, regardless of k_y, the baroclinically-unstable

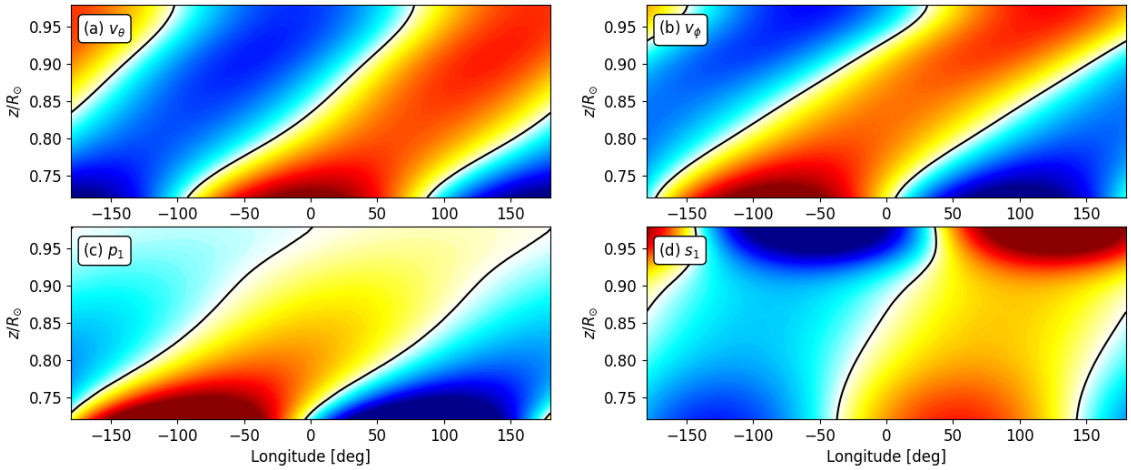

Figure 5.5: Eigencuntions of (a) latitudinal velocity, (b) longitudinal velocity v_ϕ, (c) pressure perturbation p_1, and (d) entropy perturbation s_1 of the north-south antisymmetric $k_\theta = 0$ mode. Shoen are the cut at the fixed cylindrical radius $r \sin\theta = 0.15 R_\odot$ in the northern hemisphere. The units are arbitrary.

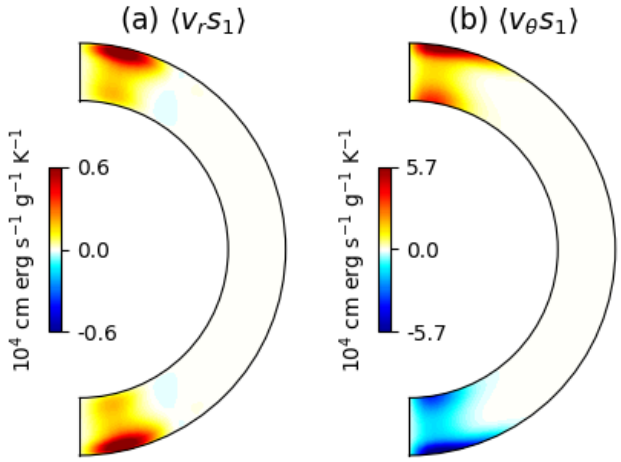

Figure 5.6: Correlations between velocity and entropy perturbations (a,c) $\langle v_r s_1 \rangle$ and (b,d) $\langle v_\theta s_1 \rangle$ of the $k_\theta = 0$ mode. Top and bottom rows correspond to the modes with (a,b) north-south anti-symmetric and (c,d) north-south symmetric longitudinal velocity v_ϕ. The eigenfunctions are normalized such that the maximum v_ϕ is 10 m s^{-1} at the surface as inferred from observations.

modes have spiralling patterns around the poles similar to what is observed on the Sun. To probe the depth and longitudinal dependence, we show in Fig. 5.5 the longitude-height plots of longitudinal velocity v_ϕ, pressure perturbation p_1, and entropy perturbation s_1 of the $m = 1$ and $k_y = 0$ mode at fixed cylindrical radius $r \sin\theta = 0.15 R_\odot$ in the northern hemisphere. The contours of v_ϕ and p_1 are both strongly tilted eastward in longitudes, whereas the contours of s_1 show much more modest inclination. This structure is the characteristic feature of the baroclinic mode discussed in §5.5.1. We have also confirmed that the modes with $k_y \geq 1$ exhibit the same properties of tilted structures (not shown).

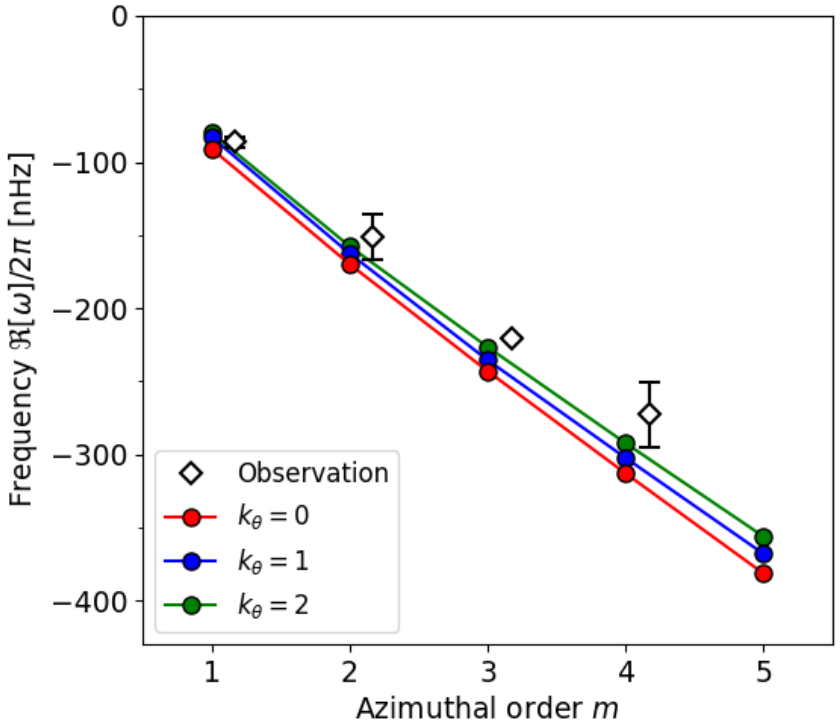

Figure 5.7: Dispersion relations of the baroclinically-unstable modes with $k_\theta = 0$ (red), $k_\theta = 1$ (blue), and $k_\theta = 2$ (green). White diamonds refer to the observations (Gizon et al. 2021).

Figure 5.6 shows the correlations between the velocity and entropy perturbation, $\langle v_r s_1 \rangle$ and $\langle v_\theta s_1 \rangle$, for the $k_y = 0$ mode with north-south anti-symmetric v_ϕ at $m = 1$. Note that the eigenfunctions are normalized such that the maximum amplitude of v_ϕ at the surface is 10 m s^{-1}. Positive $\langle v_r s_1 \rangle$ implies that the radial motions associated with the baroclinically-unstable mode are mostly buoyantly-driven. Positive (negative) $\langle v_\theta s_1 \rangle$ in northern (southern) hemisphere indicates the equatorward heat transport, which leads to an alleviation of the latitudinal entropy difference of the initial state. In other words, the potential energy of the thermal wind balanced state is converted to the kinetic energy of the instability. Since the radial velocity is much weaker than the horizontal components (about 10%), the associated thermal energy transport is predominantly latitudinal. Nonetheless, it is striking to note that the heat can be transported radially outward by this instrability even when the background is convectively-neutral. In the nonlinear phase, this equatorward heat transport is expected to feedback on the mean thermal wind state so as to saturate the instability.

Figure 5.7 shows the dispersion relations of the baroclinic modes for a range of azimuthal order, $1 \leq m \leq 5$, in comparison with the observed frequencies of the high-latitude modes (Gizon et al. 2021). Different colors represent the modes with different k_y, and we only show the north-south anti-symmetric modes. It is revealed that the baroclinic modes are almost non-dispersive and their propagation frequencies are only slightly affected by the number of latitudinal nodes k_y. For $1 \leq m \leq 4$, the agreement on the propagation frequencies between our model and the observations is striking. Therefore,

we convincingly argue that the high-latitude flow pattern observed on the Sun should be regarded as baroclinically-unstable modes. At each m, the most unstable mode of the system is always given by $k_y = 0$. For growth rates, we find that the typical e-folding time scales are about one year for $m \leq 3$. It is also found that the growth rates tend to increase as m increases within the range of azimuthal orders investigated ($1 \leq m \leq 5$).

In summary, both propagation frequencies and eigenfunctions of the high-latitude flow feature observed on the Sun can be well reproduced by the baroclinically-unstable modes under the influences of solar differential rotation and the corresponding latitudinal entropy gradient.

5.3 Nonlinear simulations of large-scale flows in a spherical shell

Observations suggest that the observed high-latitude flow feature predominantly has an azimuthal order $m = 1$ and its symmetry is largely north-south symmetric (anti-symmetric) in v_θ (v_θ) (Hathaway and Upton 2021, Gizon et al. 2021). So far, we have discussed the linear eigenmodes of the baroclinic instability in the Sun. However, to address the final amplitudes of the baroclinic modes in a statistically stationary state, the study needs to be extended into a nonlinear regime. In this section, we study the nonlinear evolution of the baroclinic modes by explicitly solving the temporal evolution of the large-scale flows in a three-dimensional spherical shell.

5.3.1 Numerical model

Although the baroclinically-unstable modes grow by extracting the available potential energy of the axisymmetric thermal wind state, care must be taken that the potential energy is being continuously replenished in the Sun: The latitudinal entropy gradient is maintained either by the anisotropic heat transport of rotationaly-constraint turbulent convection (Kitchatinov and Ruediger 1995, Küker and Stix 2001, Hotta 2018) or by the interaction of meridional circulation and the weakly subadiabatic tachocline (Rempel 2005, Brun et al. 2011). Therefore, the model requires the external forcing term in addition to the nonlinear terms to sustain the thermal wind state of the solar differential rotation.

We use the hydrodynamic solver of the numerical code developed in Chapter 4. In fact, the model can be regarded as a three-dimensional realization of Rempel (2005)'s two-dimensional mean-field model of the solar differential rotation and meridional circulation. In this framework, we do not explicitly solve the small-scale thermal convection and only focus on the large-scale axisymmetric and non-axisymmetric flow patterns. The small-scale convective processes such as the convective angular momentum transport (Λ-effect, see Rüdiger 1989) are parameterized. Another key ingredient in our model is an inclusion of weakly subadiabatic layer beneath the lower convection zone (Bekki et al. 2017, Käpylä et al. 2017, Karak et al. 2018, Hotta 2017), which produces the latitudinal entropy gradient (Rempel 2005) and serves as an external energy injection source of the available potential energy for the instability.

The governing system equations are the mean-field hydrodynamic equations in a

three-dimensional spherical shell,

$$\frac{\partial \rho_1}{\partial t} = -\frac{1}{\xi^2}\nabla\cdot(\rho_0\boldsymbol{v}), \tag{5.7}$$

$$\frac{\partial \boldsymbol{v}}{\partial t} = -\boldsymbol{v}\cdot\nabla\boldsymbol{v} - \frac{\nabla p_1}{\rho_0} - \frac{\rho_1}{\rho_0}g\boldsymbol{e}_r + 2\boldsymbol{v}\times\Omega_0\boldsymbol{e}_z + \frac{1}{\rho_0}\nabla\cdot\boldsymbol{\mathcal{R}}, \tag{5.8}$$

$$\frac{\partial s_1}{\partial t} = \boldsymbol{v}\cdot\nabla s_1 + c_{\rm p}\delta\frac{v_r}{H_p} + \frac{1}{\rho_0 T_0}\nabla\cdot(\rho_0 T_0\kappa\nabla s_1) + \frac{1}{\rho_0 T_0}(\boldsymbol{\mathcal{R}}\cdot\nabla)\cdot\boldsymbol{v}, \tag{5.9}$$

where $\boldsymbol{v}$, p_1, ρ_1, and s_1 are the velocity, pressure, density, and entropy deviations from the background. We use the same background model as prescribed in §5.2.1. $H_p = p_0/(\rho_0 g)$ is the pressure scale height. $\delta = \nabla - \nabla_{\rm ad}$ denotes the superadiabaticity where ∇ is the double-logarithmic temperature gradient. As discussed above, the lower half of the convection zone is set weakly subadiabatic as

$$\delta = \frac{\delta_0}{2}\left[1 - \tanh\left(\frac{r - r_{\rm sub}}{d_{\rm sub}}\right)\right], \tag{5.10}$$

where $r_{\rm sub} = 0.725R_\odot$ is the height below which the stratification is weakly subadiabatic, and $d_{\rm sub} = 0.0125R_\odot$ is the transition thickness. The superadiabaticity in the overshooting layer δ_0 (< 0) is treated as a free parameter in this model. See Table. 5.1.

The Reynolds stress arising from the small-scale convective motions is decomposed into the turbulent diffusive part and the non-diffusive part (Λ-effect) as

$$\mathcal{R}_{ik} = \rho_0\nu\left[\left(\mathcal{S}_{ik} - \frac{2}{3}\delta_{ik}\nabla\cdot\boldsymbol{v}\right) + \Lambda_{ik}(1+\sigma'_{ik})\Omega_0\right], \tag{5.11}$$

where Λ_{ik} denotes a dimensionless tensor that specifies the amplitude and direction of the Λ-effect. In our model, differential rotation is primarily driven by the Λ-effect, which transports the angular momentum largely equatorward. σ'_{ik} represents the three-dimensional random fluctuation of the Λ-effect due to the unresolved turbulent convection. The random field σ'_{ik} is constructed at every time step (thus uncorrelated in time) by superposing 30 gaussians with amplitudes of $|\sigma'| < 2$. Note, therefore, the random forcing does not have a preferred azimuthal order m. For detail functional profiles for ν, κ, Λ_{ik}, and σ_{ik}, refer to § 6.2.2.

We numerically solve the Eqs (5.7) - (5.9) using the 4th-order centered-differencing method for space and 4-step Runge-Kutta scheme for time integration (Vögler et al. 2005). To avoid the severe CFL constraint for time step, the background sound speed is artificially reduced by a factor of $\xi = 100$ in the Eq. (5.7) (e.g., Hotta et al. 2012). The numerical domain extends from $r_{\rm min} = 0.65R_\odot$ up to $r_{\rm max} = 0.985R_\odot$, in middle of which lies the base of the convection zone $r_{\rm bc} = 0.71R_\odot$. At both radial boundaries, impenetrable and stress-free boundary condition is assumed. The Yin-Yang grid is avoid the singular points in a full spherical geometry (Kageyama and Sato 2004). The grid resolution used in this study is $72(N_r)\times 96(N_\theta)\times 288(N_\phi)\times 2$(Yin and Yang grids). Each simulations start from the zero initial condition.

Table 5.1: Summary of nonlinear simulations.

Case		δ_0	$\Delta_\theta\Omega/2\pi$ [nHz]	$\Delta_\theta s$ [erg g^{-1} K^{-1}]
1	...	-5×10^{-6}	72.6	296.7
2	...	-2×10^{-5}	124.4	797.1
3	...	-4×10^{-5}	157.9 $\rightarrow$ 86.4	1068.0 $\rightarrow$ 609.8

Note: δ_0 is the input free parameter. $\Delta_\theta\Omega$ denotes the latitudinal variation of the differential rotation between the poles and the equator at the surface. $\Delta_\theta s$ represents the latitudinal entropy variation. In Case 3, amplitudes of $\Delta_\theta\Omega$ and $\Delta_\theta s$ are substantially relaxed due to the baroclinic instability as denoted by $\rightarrow$ in the third row.

5.3.2 Results

We conduct three simulation runs (Cases 1-3) with varying δ_0, as summarized in Table.5.1. From Case 1 to 3, the stratification at the base of the convection zone becomes more and more subadiabatic. Figure 5.8 shows the profiles of differential rotation and entropy perturbation averaged over longitudes ($m = 0$), for Cases 1-3. It is clearly shown that, as the subadiabaticity is increased from Case 1 to Case 3, the generation of positive (negative) entropy perturbation by the radial meridional flow near the poles (equator) becomes more and more efficient, leading to an enhancement of the latitudinal entropy gradient in the convection zone (Rempel 2005). The latitudinal differential rotation becomes accordingly amplified from Case 1 to Case 3 via the thermal wind balance. The values of latitudinal variations of differential rotation $\Delta_\theta\Omega$ and entropy perturbation $\Delta_\theta s$ are given in the third and fourth columns of Table. 5.1. We emphasize that the increase of $\Delta_\theta s_1$ from the Case 1 to 3 means that the mean states become more and more subject to the baroclinic instability.

We find that the solutions of Case 1 and Case 2 are close to axisymmetric ($m = 0$), i.e., the flow motions are largely dominated by differential rotation (and meridional circulation). Although non-axisymmetric modes (such as p-modes, g-modes, and Rossby modes) are excited by random forcing in the Λ-effect, these non-axisymmetric perturbations are kept substantially small in power with respect to the mean ($m = 0$) part. In these two cases, differential rotation is driven and maintained by the Λ-effect and becomes almost stationary after $t \geq 10$ yr without experiencing any instability. In Case 3, however, we find that the solution qualitatively differs from those of Cases 1 and 2, i.e., a very strong differential rotation is generated as a mean ($m = 0$) state at an initial stage but then it undergoes a sudden distortion that is brought about by the non-axisymmetric ($m \neq 0$) disturbances. Consequently, the amplitude of the differential rotation is substantially weakened, as shown in Fig. 5.8c and d. It is also observed that the latitudinal variation of the mean entropy is correspondingly reduced, as shown in in Fig. 5.8g–h. This can be well explained by the baroclinic instability. As discussed in §5.5.1, the latitudinal entropy variation is a measure of the available potential energy stored in the mean ($m = 0$) state, and thereby, will be tapped by the baroclinic instability when it exceeds a threshold value. In our simulations, only in Case 3, the mean state becomes sufficiently baroclinic for the instability to occur: Baroclinic modes may exist in all runs, but they can

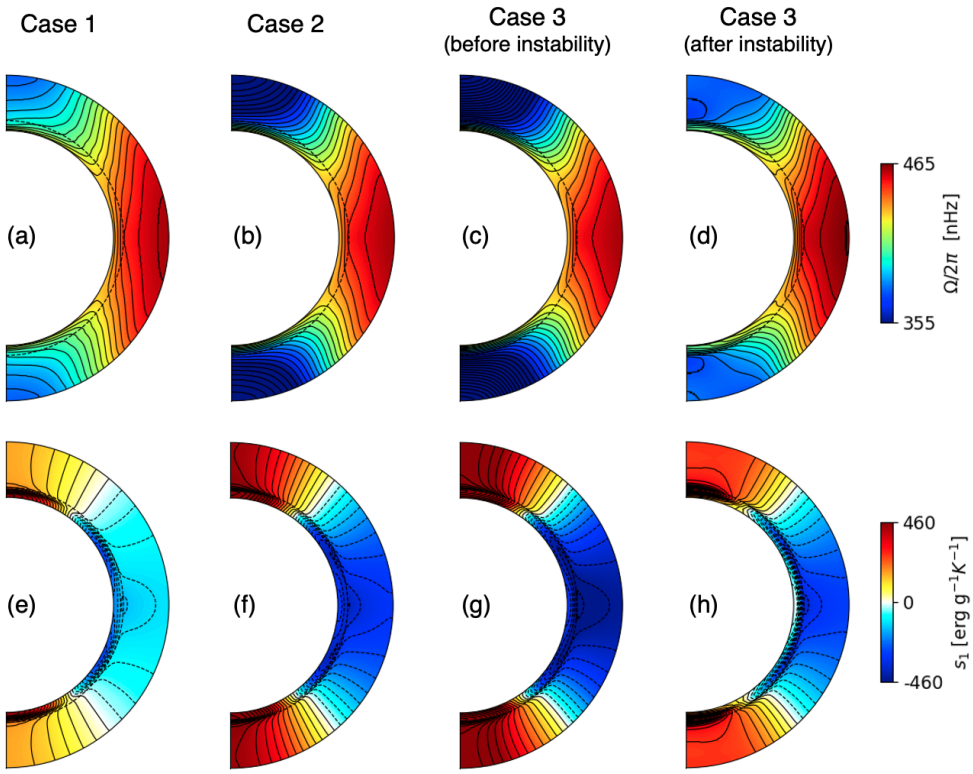

Figure 5.8: Profiles of temporally- and azimuthally-averaged (top, a-d) differential rotation Ω and (bottom, e-h) entropy perturbation s_1, for Cases 1-3 from left to right. Third and fourth columns show the results of case 3 before and after the baroclinic instability, respectively.

grow and become strong enough to have a substantial impact on the mean state only in Case 3. The threshold value of the latitudinal entropy difference across the poles and the equator is estimated as 10^3 erg g^{-1} K^{-1} (see Fig. 5.8 (g)), corresponding to the temperature difference of about 7.4 K.

Figure 5.9 shows snapshots of the non-axisymmetric components of the longitudinal velocity v_ϕ and the entropy perturbation s_1 at the surface $r = 0.985R_\odot$ for Cases 1-3 focusing on the structure around the north pole. In Case 1, non-axisymmetric perturbations are small in amplitudes and do have a preferred azimuthal order m. In Case 2, on the other hand, it is obvious that the $m = 1$ mode of perturbation becomes dominant in amplitudes with typical longitudinal velocity amplitude of about $v_\phi \approx 10 - 15$ m s^{-1}. Furthermore, a spiralling pattern around the pole is clearly seen on the surface flow map, just as suggested by observations and by our linear analysis in §5.2.2. It should also be noted that v_ϕ (or s_1) is predominantly north-south anti-symmetric whereas v_θ being symmetric (as will be discussed later). These properties are not limited to the snapshots shown in Fig. 5.9 but are found quite general. The non-axisymmetric flow pattern in Case 3 look very similar to that of Case 2 except for the amplitude: Qualitatively, they both are dominated by $m = 1$ north-south anti-symmetric mode and are spiralling westward around the poles. Quantitatively, however, the $m = 1$ perturbation in Case 3 is about 3 times greater than that of Case 2, which is large enough to affect the mean ($m = 0$) state.

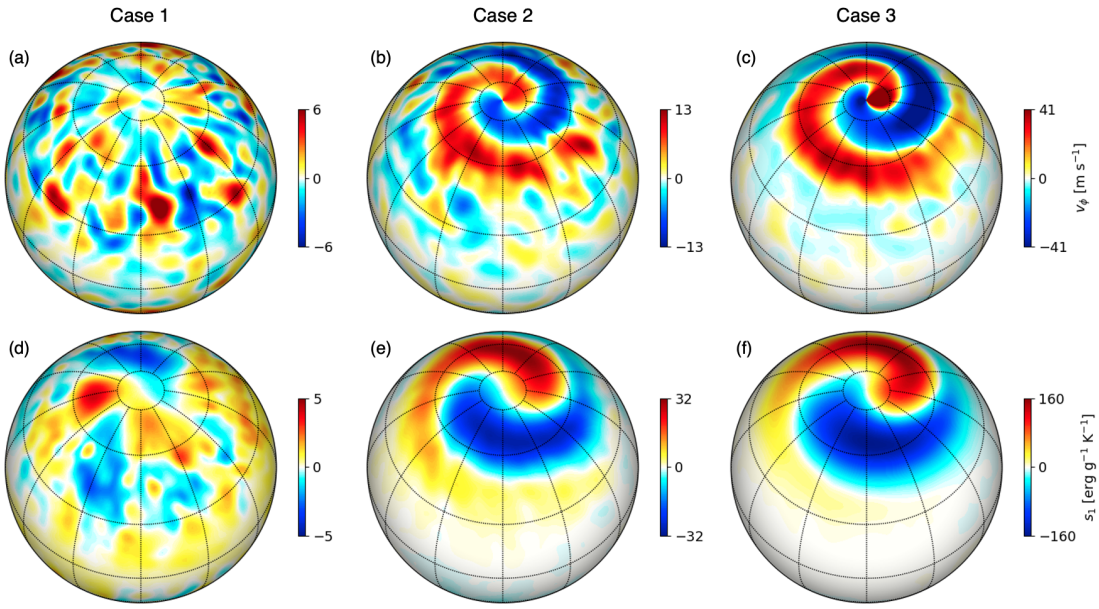

Figure 5.9: Snapshots of the non-axisymmetric components of (top, a-c) the longitudinal velocity v_ϕ and (bottom, d-f) entropy perturbation s_1 at the surface $r = 0.985R_\odot$ at $t = 30$ yr. Left, middle, and right panels correspond to the Case 1, 2, and 3, respectively.

To better support the above argument, we show in Fig. 5.10 the temporal evolution of the volume-integrated kinetic energies separately computed for different azimuthal orders ($0 \leq m \leq 3$) for different colors. The solid and dashed lines represent the modes consisting of $(v_r^+, v_\theta^-, v_\phi^+)$ and those of $(v_r^-, v_\theta^+, v_\phi^-)$, respectively, where the north-south symmetric (+) and anti-symmetric (−) velocities are defined as

$$v^\pm(r,\theta,\phi) = \frac{1}{2}\left[v(r,\theta,\phi) \pm v(r,\pi-\theta,\phi)\right]. \tag{5.12}$$

The black line represents the axisymmetric ($m = 0$) component, consisting of differential rotation and meridional circulation. The non-axisymmetric (m ($\neq$ 0)) perturbations are almost negligible in Case 1, and they own comparable power with each other. In Case 2, the mean flows are still by far dominant in power but we now clearly observe the $m = 1$ perturbation stands out. It is also noteworthy that this $m = 1$ mode is predominantly north-south anti-symmetric in v_ϕ. In Case 3, the non-axisymmetric perturbations grow significantly in power (up to about 10% of the kinetic energy of the mean differential rotation), causing an instability at around $t \approx 17$ yr, as indicated by the grey shaded area in Fig. 5.10. Once the instability occurs, there is a substantial amount of equatorward heat transport at high latitudes, leading to a reduction in the latitudinal entropy variation. Note that this accompanies an poleward transport of the angular momentum so as to keep the thermal wind balance of the differential rotation. The available potential energy of the mean state is consequently reduced, which in turn limits a further growth of the baroclinic modes. This so-called "baroclinic adjustment" (e.g., Stone 1978) takes place over about 5 years (18 yr $\lesssim t \lesssim$ 23 yr) in our numerical model. In the saturated phase, the mean state becomes statistically stationary ($t \gtrsim 30$ yr).

It is instructive to note that, in both Cases 2 and 3, the power of non-axisymmetric per-

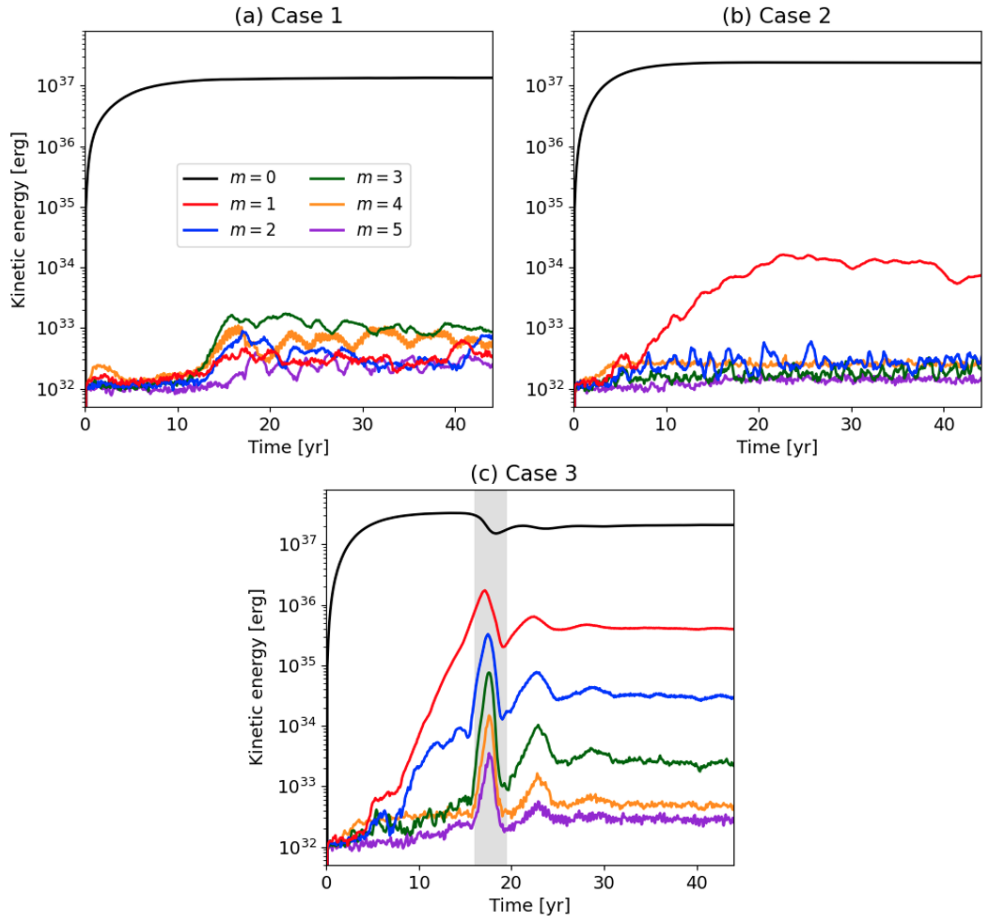

Figure 5.10: Temporal evolution of the volume-integrated kinetic energies associated with $m = 0$ (black), $m = 1$ (red), $m = 1$ (red), $m = 2$ (blue), $m = 3$ (green), $m = 4$ (orange), and $m = 5$ (purple) flow components. Panels (a), (b), and (c) show the Case 1, 2, and 3, respectively. Grey shaded area in the panel (c) denote the time where the instability occurs. Solid and dashed lines represent the modes with different north-south symmetries, $\int \rho_0(|v_r^{\pm}|^2 + |v_\theta^{\mp}|^2 + |v_\phi^{\pm}|^2)/2 \cdot dV$, where $v_{r,\theta,\phi}^{\pm}$ are defined in the Eq. (5.12).

turbations lies predominantly at $m = 1$ north-south anti-symmetric mode. To understand how this occurs, we have investigated the sensitivity of the baroclinic modes' growth rates to the latitudinal entropy variation in the linear regime. The results are briefly reported in an Appendix 5.5.2. It is shown that, as the latitudinal entropy variation $\Delta_\theta s$ is increased, the $m = 1$ north-south anti-symmetric mode is the first one to becomes unstable: The threshold value of $\Delta_\theta s$ for the baroclinic instability at $m = 1$ is about $300 - 400$ erg g^{-1} K^{-1} for the north-south anti-symmetric mode, whereas that of the north-south symmetric mode is about 800 erg g^{-1} K^{-1}. Although many simplifying assumptions are made in the linear calculation (such as fixed differential rotation, spatially-uniform diffusivities, adiabatic stratification in radial direction), this explains why the $m = 1$ north-south anti-symmetric mode becomes unstable first and able to grow in time.

In Case 3, the non-axisymmetric modes are excited at a wide range of azimuthal orders, even though the dominant mode is $m = 1$ and the power become weaker as m in-

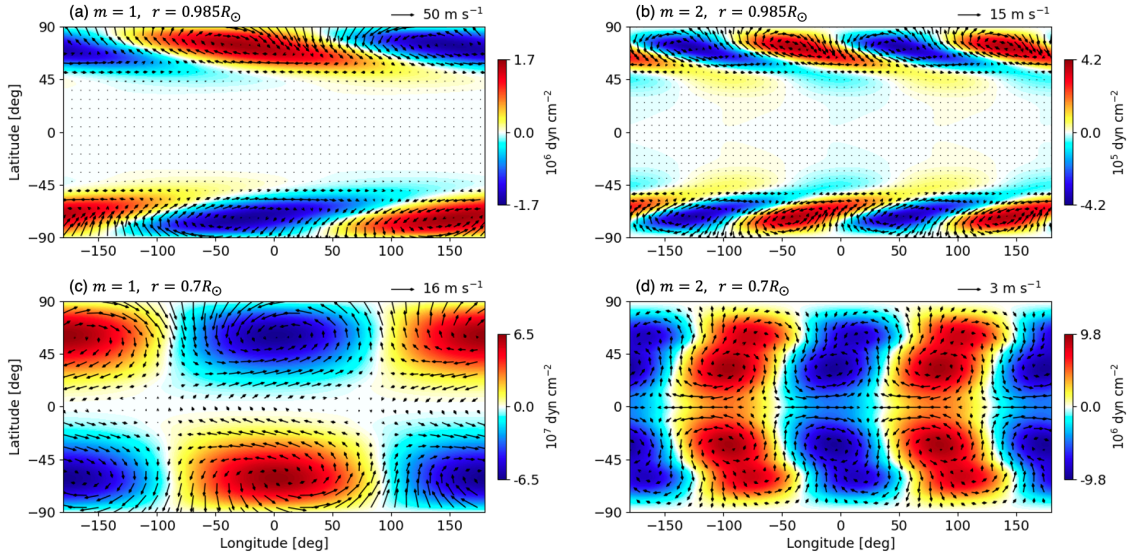

Figure 5.11: Snapshots of pressure perturbation p_1 (color contour) and the horizontal velocity (v_θ, v_ϕ) (vector fields) for Case 3 after the instability. Left and right panels represent the azimuthal order $m = 1$ and $m = 2$ components, respectively. Top and bottom rows show the horizontal cuts at the surface $r = 0.985R_\odot$ and at the base $r = 0.7R_\odot$.

creases. Interestingly, we empirically find that the modes are predominantly north-south symmetric (anti-symmetric) in v_ϕ when m is even (odd). Note that this symmetry selection rule is clearly shown in Fig. 5.10c for $1 \leq m \leq 3$ but it holds for $m \geq 4$ as well. In order to investigate the spatial structure and the dynamics of the baroclinic modes with both north-south symmetries, we show in Fig. 5.11 a snapshot of the pressure perturbation p_1 and the horizontal velocities (v_θ, v_ϕ) in a statistically stationary state of Case 3 for $m = 1$ (left panels) and $m = 2$ (right panels) components. Top and bottom rows show the horizontal (spherical) cuts at the surface $r = 0.985R_\odot$ and near the base of the convection zone $r = 0.7R_\odot$, respectively. It is generally confirmed that the positive (negative) pressure perturbations $p_1 > 0$ (< 0) are associated with negative (positive) radial vortices $\zeta_r < 0$ (> 0) in the northern (southern) hemisphere. This implies that the modes are in a geostrophical balance. The baroclinic modes are strongly confined at high latitudes ($> 45°$) near the surface, but as we go deeper in the convection zone, the vortices in each hemisphere are connected with each other across the equator, i.e., the latitudinal (longitudinal) flows are driven at the equator for $m = 1$ (2), by which the north-south symmetry is maintained. It should be noted that this structure resembles that of the topographic Rossby modes with both north-south symmetries discussed in detail in § 4.3 of Bekki et al. (2022b). In this sense, we consider the baroclinic modes could be regarded as topographic Rossby modes under the influence of thermal wind.

Kashimura et al. (2019) have reported that the baroclinic instability can lead to a formation of the global-scale spiralling flow pattern at $m = 1$ in the Venus atmosphere, which is mostly north-south symmetric. They have further argued that this north-south symmetry is likely to be maintained by the equatorial Kelvin waves. We must note here that the equatorial Kelvin waves do not exist in our simulations even for $m = 2$ where the structure is predominantly north-south symmetric. This is clearly manifested in Fig. 5.11d

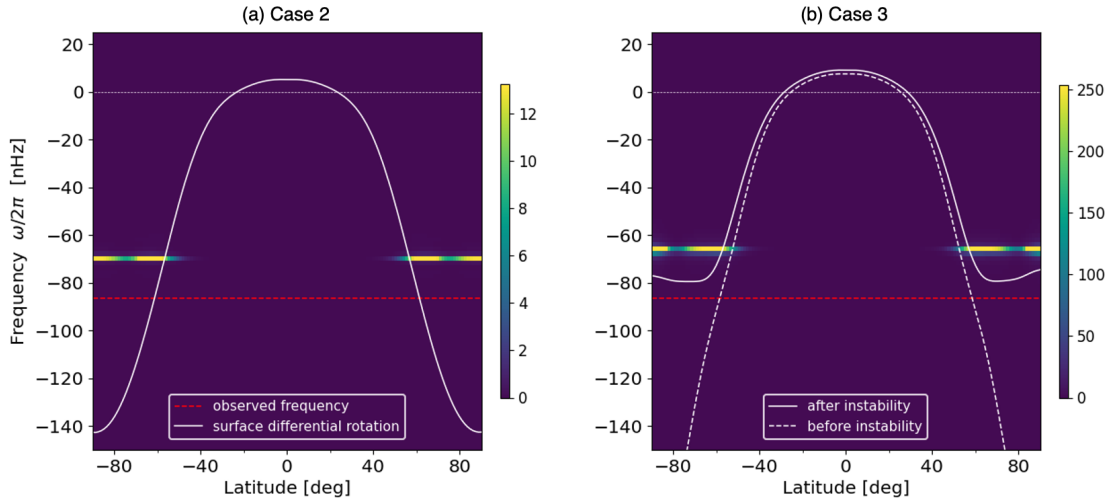

Figure 5.12: Power spectra of the north-south anti-symmetric v_ϕ at the surface $r = 0.985R_\odot$ as a function of latitude at $m = 1$ for (a) Case 2 and (b) Case 3, respectively. White lines denote the time-averaged latitudinal differential rotation at the surface. In Case 3, the differential rotation profiles before and after the instability are distinguished by dashed and solid lines. Red horizontal line denotes the observed frequency $\omega/2\pi = -86.3$ nHz.

where the positive (negative) v_ϕ at the equator is associated with negative (positive) pressure perturbation. We consider that this discrepancy comes from the relative thickness of the convective layer between the Sun and Venus. Since the solar convection zone is much thicker compared to its raius ($\approx 30\%$) than the Venus atmosphere ($\approx 1-2\%$), the topographic β-effect of the inner sphere is expected to become much more dominant.

Next, let us we examine the propagation frequencies of baroclinic modes in our nonlinear simulations. We use the 10-year-series of data (35 yr $< t <$ 45 yr) with the time cadence of about 4.7 days. Each variable is then Fourier transformed in time and longitude as

$$q(r,\theta,\phi;t) = \sum_m \sum_\omega \tilde{q}(r,\theta;m,\omega)\exp\left[i(m\phi-\omega t)\right], \tag{5.13}$$

where q takes either of v_r, v_θ, v_ϕ, s_1, ρ_1 or p_1. We consider the range of azimuthal order $0 \le m \le 5$ to focus on the large-scale flow features. Note that we choose a Carrington frame as a reference frame ($\Omega_{\rm ref}/2\pi = 456$ nHz) for the temporal Fourier transform. Figures 5.12a and b show the surface power spectra of the $m = 1$ longitudinal velocity as a function of latitude for the Cases 2 and 3, respectively. White lines represent the latitudinal differential rotation profiles at the surface, and the red dashed line denotes the observed frequency of the $m = 1$ high-latitude mode Gizon et al. (2021). The strong velocity power is located at high latitudes ($> 45°$) with a well-defined frequency peak. Despite the significant difference in the high-latitude differential rotation rates, the mode frequencies of Cases 2 and 3 are found strikingly close. The obtained propagation frequencies of the $m = 1$ mode in our simulations are $\omega/2\pi = -69.6$ nHz (Case 2), -65.8 nHz (Case 3) that roughly corresponds to the surface differential rotation rate at about $50-60°$ in latitude.

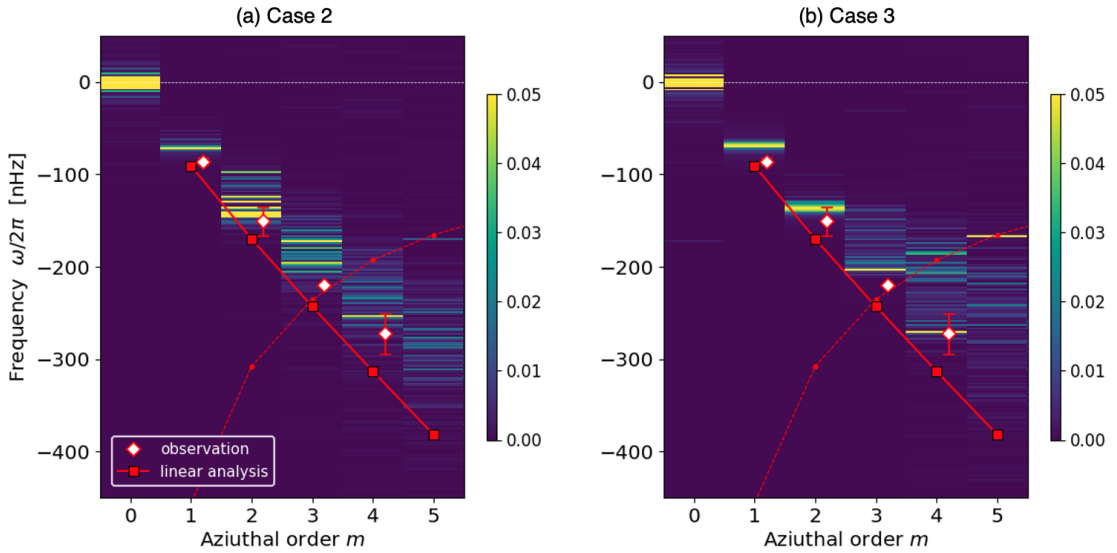

Figure 5.13: High-latitude power spectra ($k-\omega$ diagram) of the longitudinal velocity v_ϕ for (a) Case 2 and (b) Case 3. Shown are the spectra at the surface averaged over high-latitudinal band ($50^\circ - 90^\circ$) in both hemispheres. The power is normalized at each m. White diamonds and red points refer to the observations (Gizon et al. 2021) and the dispersion relation obtained from the linear analysis in § 5.2.2, respectively. Red dashed lines denote the dispersion relation of the sectoral Rossby modes of the Sun (Löptien et al. 2018).

Figures 5.13a and b show the high-latitude power spectra ($k-\omega$ diagram) of v_ϕ at the surface for Cases 2 and 3, respectively. Note that the power is averaged over the high-latitude band ($50^\circ - 90^\circ$) and normalized at each m. In both cases, well-defined power ridges can be seen in a negative frequency domain starting for $1 \leq m \leq 4$, and they are almost non-dispersive, as observed and also predicted in our linear calculation. For the sake of comparison, we show the dispersion relation of the most unstable ($k_y = 0$) baroclinic modes obtained from our linear calculation by red solid lines, and the observed mode frequencies by white diamonds. The mode frequencies in our nonlinear simulations are slightly lower (less retrograde) than those of the linear analysis (errors are less than 10%) but are generally in good agreement with the observations, especially in Case 3. For $m \geq 5$, we find that the power is more predominantly visible at the frequencies of the traditional Rossby modes (r modes), as denoted by red dashed lines.

At each m, the eigenfunctions of the baroclinic modes can be extracted from the nonlinear simulation data by performing the singular-value decomposition for the power spectrum. For a more detail description of this method, see § 4.3.2. Figure 5.14 shows the extracted eigenfunctions of the $m = 1$ baroclinic mode in the Case 2, where the top and the bottom panels show the real and imaginary parts, respectively. We note here that the eigenfunctions extracted from Case 3 are found to be almost identical to those of Case 2 except for the amplitudes (not shown). Generally, the eigenfunctions look similar to those of the $k_y = 0$ north-south anti-symmetric baroclinic mode obtained in the linear analysis: The flow motion is predominantly toroidal ($|v_r| \ll |v_\theta|, |v_\phi|$) and strongly confined inside the tangential cylinder. Th surface eigenfunctions exhibit a clear spiralling pattern around

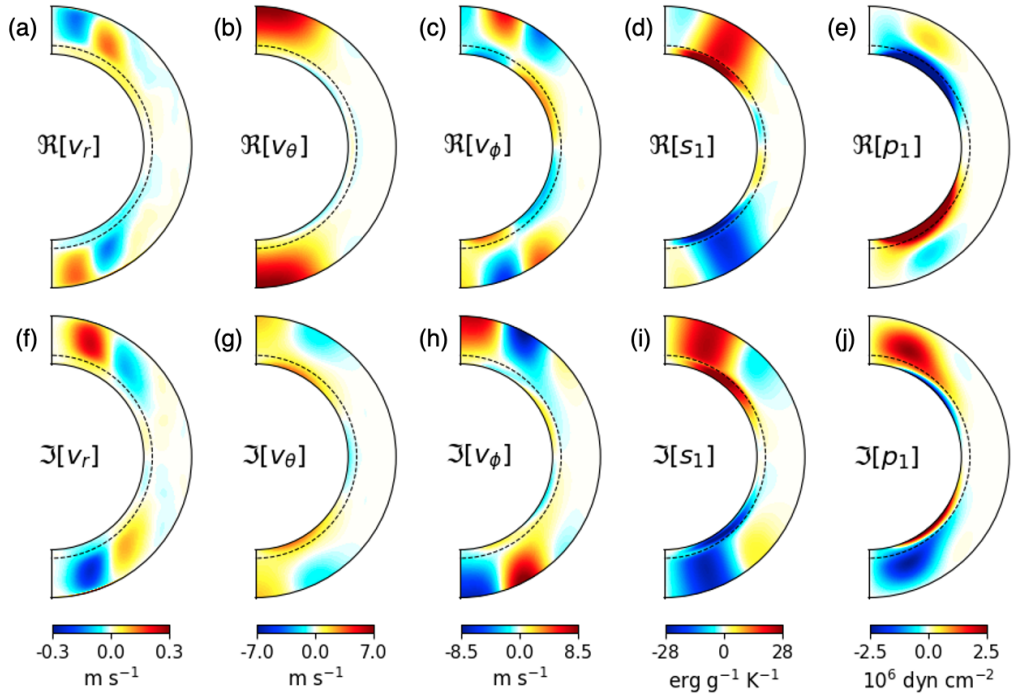

Figure 5.14: Meridional eigenfunctions of the $m = 1$ baroclinic mode extracted from the nonlinear simulation Case 2. Eigenfunctions of v_r, v_θ, v_ϕ, s_1, and p_1 are shown from left to right. Top and middle rows show the real and imaginary parts of the eigenfunctions, respectively, where we set the phase where v_θ is maximum at the surface as real. Note that the real phase is $\pi/2$ ahead in longitude with respect to the imaginary phase. The black dashed lines denote the location of the base of the convection zone, below which the stratification is weakly subadiabatic in our model.

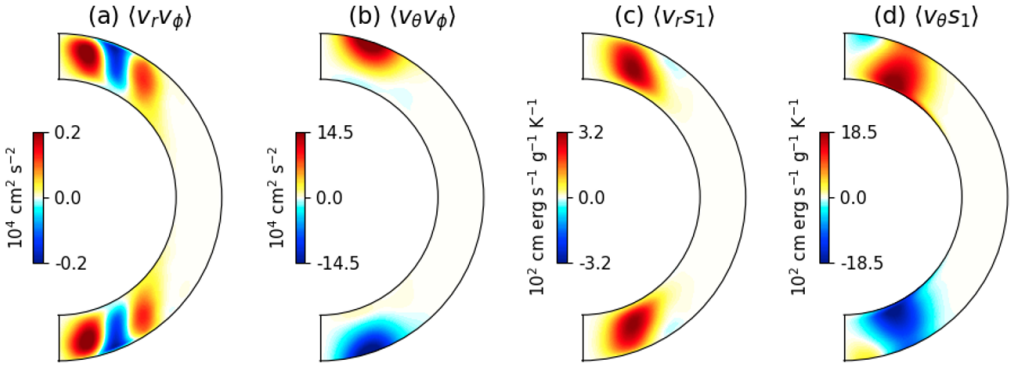

Figure 5.15: The velocity correlations (a) $\langle v_r v_\phi \rangle$ and (b) $\langle v_\theta v_\phi \rangle$, and the correlations between velocity and entropy (c) $\langle v_r s_1 \rangle$ and (d) $\langle v_\theta s_1 \rangle$ of the $m = 1$ baroclinic mode extracted from our nonlinear simulation Case 2.

the poles. It is also confirmed that the eigenfunctions of v_θ, v_ϕ, and p_1 have larger eastward inclination than that of s_1 as discussed in § 5.5.1. On the other hand, there are mainly two differences from the linear analysis: First, the extracted eigenfunction of v_ϕ at the surface peaks at 61° which is slightly lower in latitude than that obtained from linear analysis which peaks at 70°. Second, the strong entropy perturbation is generated in the weakly subadiabatic layer beneath the convection zone which is not included in our linear model.

Finally, let us estimate how much these baroclinic modes can contribute to the transport of thermal energy and angular momentum in the Sun. Figure 5.15 shows the Reynolds stress $\langle \boldsymbol{v}_m v_\phi \rangle$ and the velocity-entropy correlation $\langle \boldsymbol{v}_m s_1 \rangle$ associated with the $m = 1$ baroclinic mode extracted from Case 2. Here, $\boldsymbol{v}_m = (v_r, v_\theta)$ denotes the meridional velocity. It is shown from Figures 5.15a and b that the angular momentum is preferentially transported equatorward at high latitudes in both hemispheres, as suggested by observations (Hathaway and Upton 2021). The positive $\langle v_r s_1 \rangle$ in Fig. 5.15c means that the baroclinic mode transports the heat radially outward at high latitudes even though the bulk convection zone is adiabatic or weakly subadiabatic, as already pointed out in § 5.2.2. A substantial amount of the equatorward heat transport is represented by positive (negative) $\langle v_\theta s_1 \rangle$ in the northern (southern) hemisphere in Fig. 5.15d.

Table 5.2: Properties of the extracted $m = 1$ baroclinic mode from the nonlinear simulations.

Case	velocity [m s^{-1}]			entropy [erg g^{-1} K^{-1}]	Reynolds stress [m^{2} s^{-2}]		enthalpy flux $F_{\odot}^{-1}$[%]	
	v_r	v_θ	v_ϕ	s_1	$\langle v_r v_\phi \rangle$	$\langle v_\theta v_\phi \rangle$	$\rho_0 c_p \langle v_r T_1 \rangle$	$\rho_0 c_p \langle v_\theta T_1 \rangle$
2.....	0.25	7.60	9.14	26.16	0.49	17.89	0.09	0.68
3.....	0.90	52.20	58.28	158.08	16.62	450.11	1.80	48.63

Note: Maximum velocity amplitudes are taken from the middle convection zone for v_r and from the surface for v_θ and v_ϕ. The maximum entropy variation s_1 at the surface is also given. The radial and latitudinal components of the maximum associated Reynolds stress and the enthalpy flux are taken from the middle convection zone and from the surface, respectively. The enthalpy fluxes are normalized by the solar energy flux $F_\odot = L_\odot / 4\pi r^2$, where $L_\odot = 3.84 \times 10^{33}$ erg s^{-1}.

In both Cases 2 and 3, we have computed the maximum amplitudes of the velocity and entropy perturbation of the $m = 1$ baroclinic mode and shown in Table. 5.2. We also report in Table. 5.2 the amplitudes of the associated Reynolds stress $\langle \boldsymbol{v}_m v_\phi \rangle$ and the corresponding enthalpy flux $\boldsymbol{F}_e = \rho_0 c_p \langle \boldsymbol{v}_m T_1 \rangle$, where T_1 denotes the temperature fluctuation. Note that the enthalpy fluxes are normalized by the solar energy flux $F_\odot = L_\odot / 4\pi r^2$ where $L_\odot$ is the luminosity of the Sun. Since observations infer that the root-mean-square (RMS) velocity amplitude of the high-latitude flow feature is about $10 - 12$ m s^{-1} (Hathaway and Upton 2021, Gizon et al. 2021), we consider the baroclinicity in the Sun is slightly larger than our Case 2 but not as large as Case 3.

5.4 Summary and discussion

In this paper, we provide a concrete theoretical explanation for the high-latitude large-scale flow pattern observed on the solar surface (Hathaway et al. 2013, Bogart et al. 2015, Hathaway and Upton 2021, Gizon et al. 2021). We propose that they are baroclinically-induced Rossby modes in the solar convection zone, rather than the giant cell convection cells advected by differential rotation as previously argued. To support our argument, we present two series of numerical experiments.

First, in §5.2, we carry out the linear stability analysis of the rotating compressible fluid in the solar convection zone with the latitudinal entropy gradient and the corresponding thermal wind imposed. The similar linear analysis has been conducted to study the properties of Rossby modes (r modes) in the Sun but the latitudinal entropy gradient has never been considered in the previous studies (Bekki et al. 2022b). We find that the baroclinically-unstable modes involve strong velocity amplitudes only at high latitudes and exhibit spiralling patterns around the poles similar to the observations. Furthermore, they generally have negative frequencies, corresponding to a retrograde propagation. The computed dispersion relationships of the baroclinically-unstable modes agree quite well with the observed frequencies of the high-latitude flow features for $1 \leq m \leq 3$. It is interesting to note that these unstable modes can transport the thermal energy not only equatorward (as predicted in order to relax the strong latitudinal entropy variation) but also radially outward near the poles. Although the amount of enthalpy fluxes due to the baroclinic instability are expected to be small, this mechanism of thermal energy transport is regarded significant because it does not require the superadiabatic background.

Next, in §5.3, we carry out a set of three-dimensional simulations of rotating compressible fluid in a spherical shell to study the nonlinear evolution of baroclinic instability. It is found that, as the latitudinal entropy variation between the poles and the equator becomes strong enough (with the corresponding temperature variation of $7 - 8$ K), the baroclinic instability occurs at high latitudes (Case 3). The instability predominantly involves the $m = 1$ perturbation mode with north-south anti-symmetric v_ϕ, which transports the entropy and angular momentum latitudinally so as to reduce the baroclinicity of the mean state. These baroclinic modes exhibit many properties similar to those of the linear modes discussed in §5.2, including the spiralling flow structure around the poles, the dispersion relation of the retrograde-propagating modes at $1 \leq m \leq 3$, and the associated thermal energy transport both in latitudinal and radial direction.

When the latitudinal entropy variation is intermediate, i.e., large but not substantial

enough to cause the instability (in our Case 2), we still find that the non-axisymmetric perturbation is largely dominated by the $m = 1$ baroclinic mode with north-south anti-symmetric v_ϕ. In this circumstance, the $m = 1$ mode has a typical velocity amplitude of about 9 m s^{-1}, which is comparable to the solar observations. Therefore, we successfully demonstrate that our numerical model can reproduce most of the observed properties of the high-latitude flow features with the reasonable choice of model parameters.

In this study, in order to exclude the convective instability and to focus on the baroclinic instability, the background is assumed to be adiabatic (or weakly subadiabatic in the nonlinear calculations). Previous studies have shown that, when the background is superadiabatic, the columnar conevctive modes (thermal Rossby waves) become the fast-growing modes at low latitudes (Bekki et al. 2022b). However, it is still unclear how superadiabatic background influences the onset and development of the baroclinic instability at high latitudes. Therefore, it will be our primary future work to carry out a systematic parameter survey with varying background superadiabaticity δ. Furthermore, Gilman (1975) reported that the fastest-growing convective modes at high latitudes show spiralling patterns around the poles, which is another plausible explanation for the observed high-latitude inertial modes. Future work will also focus on distinguishing the physical origins of the high-latitude modes, i.e., whether they are convectively- or baroclinically-driven.

In three-dimensional realistic simulations of the rotating turbulent convection in the Sun, the baroclinic modes at high latitudes have never been investigated in detail. We have reported to detect the topographic Rossby modes at high latitudes in their rotating convection simulation in § 3.3.3 but the baroclinic modes as discussed in this paper were not observed. This might be because the thermal wind in their simulation is too weak for the baroclinic instability to occur. It will be a interesting future work to carry out mode-analyses for some of the recent simulations that successfully reproduced the non-Taylor-Proudman differential rotation with huge baroclinicity (Miesch et al. 2008, Karak et al. 2018, Hotta 2018) to examine if the baroclinic modes exist in their simulations.

Finally, possible effects of magnetic fields on the baroclinic modes in the Sun are discussed. Observations suggest that the high-latitude flow features are more prominent during the activity minima (2010, 2018-2020) and become fainter during the activity maxima (2012-2016) (Gizon et al. 2021). Thus, the dynamo-generated magnetic fields in the Sun can have a strong impact on the excitation of the baroclinic modes. Gilman (2015, 2017) have studied the stability of the tachocline in the presence of the strong toroidal fields and shown that the magnetic fields have a stabilizing effect for the baroclinic instability. We can easily expect the same mechanism works in the convection zone. Our linear analysis model will be extended into MHD regime to account for magnetic effects in the near future.

Acknowledgements

We thank A. Birch and B. Proxauf for helpful discussions. Figure 5.1 is produced using the data provided at http://solarcyclescience.com/giantcells.html. Y. B. is enrolled in the International Max-Planck Research School for Solar System Science at the University of Göttingen. Y .B. also acknowledges a support from long-term scholarship program for

degree-seeking graduate students abroad from the Japan Student Services Organization (JASSO). We acknowledge a support from ERC Synergy Grant WHOLE SUN 810218. All the numerical computations were performed at GWDG and the Max-Planck supercomputer RZG in Garching.

5.5 Appendix

5.5.1 Physical picture of baroclinic instability

In this Appendix, we briefly overview the physical picture of baroclinic instability. When the isobaric surfaces (constant pressure) are not parallel to the isosteric surfaces (constant density), the fluid is called "baroclinic" (e.g., Vallis 2006). By definition, baroclinic fluid accompanies the horizontal temperature (entropy) gradient and the vertical shear of the horizontal flow. The fluid parcel is unstable for a displacement in a narrow angle between the isobaric and isosteric surfaces. This angle amounts to the degree of baroclinicity, and is a measure of the available potential energy that is eventually converted to the kinetic energy of the growing modes after the instability. In this sense, the baroclinic instability is also called "slopping convection" in some literature.

To better illustrate how the baroclinic instability occurs in the Sun, let us consider an idealized cartesian box located near the north pole in the convection zone (Fig. 5.16). The background is assumed to be in a thermal wind balance, i.e., the Coriolis force acting on the vertical shear of the differential rotation $\partial U_\phi/\partial z$ (< 0) is geostrophically balanced by the latitudinal entropy gradient $\partial s_0/\partial\theta$ (< 0). Now, let us consider horizontal velocity perturbations represented by sinusoidal waves in longitude at $z = z_0$. Note that the positive (negative) pressure perturbation $p_1 > 0$ (< 0) is required where the circulation is clockwise (counterclockwise) $\zeta_z < 0$ (> 0) under the constraint of geostrophical balance. Here, ζ_z denotes the z-vorticity. At the interface of the circulation cells, the equatorward flow ($v_\theta > 0$) advects high entropy fluids ($s_1 > 0$) and thus are warmer than the surroundings. Owing to the gravitational stratification in a vertical direction, clockwise (counterclockwise) circulation with $p_1 > 0$ (< 0) is induced in the upper (lower) layer of the convection

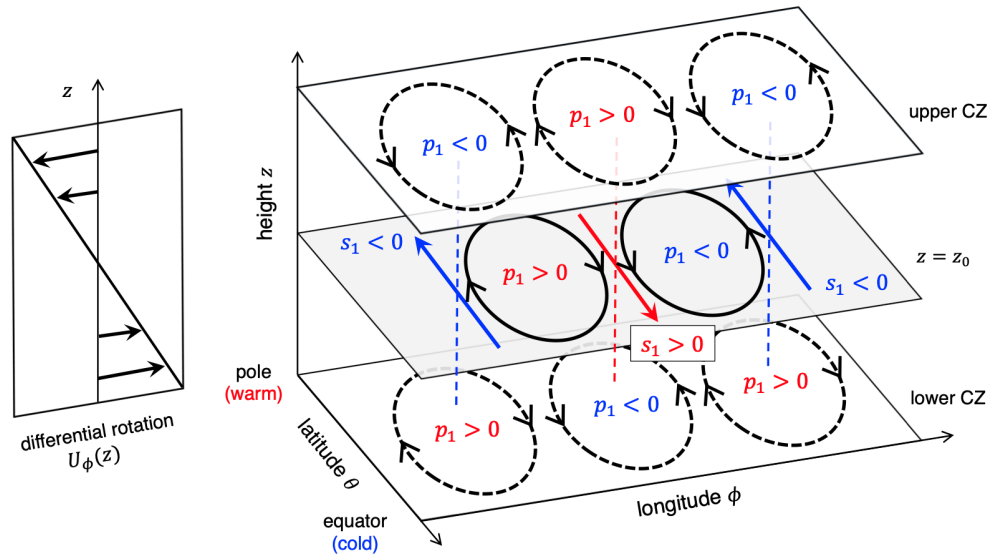

Figure 5.16: Schematic illustration explaining the baroclinic instability in the northern polar region of the solar convection zone. Left: Vertical shear of the azimuthal mean flow (differntial rotation). Right: Structure of velocity perturbation, and associated pressure and entropy perturbations that are unstable for baroclinic instability.

zone of the warm area ($s_1 > 0$). The opposite happens in the cooler area ($s_1 < 0$) where the latitudinal velocity perturbation is poleward ($v_\theta < 0$). This structure is essentially unstable because the velocity perturbations induced at the upper and lower layers lead to a further enhancement of the initial perturbations at $z = z_0$. The instability caused by this positive feedback is called baroclinic instability. The baroclinically-unstable structure illustrated in Fig. 5.16 clearly manifests that the velocity and pressure patterns are inclined eastward whereas the entropy or temperature has much less or the opposite inclination in longitudes (denoted by red and blue dashed lines) (e.g., Charney 1947, Eady 1949, Phillips 1954).

5.5.2 Stability analysis with increasing baroclinicity

In §5.2, we report the general properties of the baroclinic modes under the constraints of solar differential rotation and the latitudinal entropy gradient. In this Appendix, we report a linear stability analysis in which the latitudinally entropy variation is changed as a free parameter rather than imposed as a constraint. This numerical experiment will illustrate the inherent mechanism of regulating the latitudinal entropy difference in the Sun's convection zone. Furthermore, we will explain why the $m = 1$ north-south anti-symmetric mode always stands out in our nonlinear simulations in §5.3.2.

Now, instead of using the formula described in the Eq.(5.6), we consider the latitudinal background entropy variation simply expressed as

$$\frac{\partial s_0}{\partial \theta} = -\Delta_\theta s \sin(2\theta), \tag{5.14}$$

where $\Delta_\theta s = s_0(\theta = 0) - s_0(\theta = \pi/2)$ denotes the entropy difference between the poles and the equator, and is varied from $200 - 1800$ erg g^{-1} K^{-1}. Note that, for differential rotation, we keep using the same observational profile as used in §5.2. The viscous and thermal diffusivities are assumed to be spatially uniform and set as $\nu = \kappa = 10^{12}$ cm^2 s^{-1}.

Figure 5.17a shows the linear growth rates $\Im[\omega]$ of the $k_y = 0$ (the most unstable) baroclinic modes with north-south anti-symmetric v_ϕ in a range of azimuthal orders $1 \leq m \leq 5$. It is shown that, when the latitudinal entropy variation is sufficiently small ($\Delta_\theta s = 200$ erg g^{-1} K^{-1}), all the m-modes are stable for the baroclinic instability. However, as $\Delta_\theta s$ is increased and the baroclinicity of the system is enhanced, the low-m modes become unstable. This may explain why the $m = 1$ mode always become the most dominant baroclinic mode in our nonlinear simulations (see Fig. 5.10b and c). When $\Delta_\theta s$ is further increased, the modes become unstable for all m.

Figure 5.17b shows the maximum latitudinal enthalpy fluxes $F_{e,\theta} = \rho_0 c_p \langle v_\theta T_1 \rangle$ in the northern hemisphere associated with the $k_y = 0$ modes. Note that all the eigenfunctions are normalized such that all the eigenmodes have the same total kinetic energy. In general, as $\Delta_\theta s$ increases, the thermal energy is more and more efficiently transported equatorward by the baroclinic modes. This means that, when $\Delta_\theta s$ is sufficiently enhanced in the Sun, the baroclinic modes will grow very fast in time and will transport a substantial amount of the thermal energy from the poles to the equator, leading to a decrease in $\Delta_\theta s$. Owing to this so-called "baroclinic adjustment" (e.g., Stone 1978, Vallis 2006), the latitudinal entropy variation in the Sun is considered to be regulated within a certain range, which is estimated to be $\Delta_\theta s \approx 600 - 800$ erg g^{-1} K^{-1} according to our nonlinear simulations.

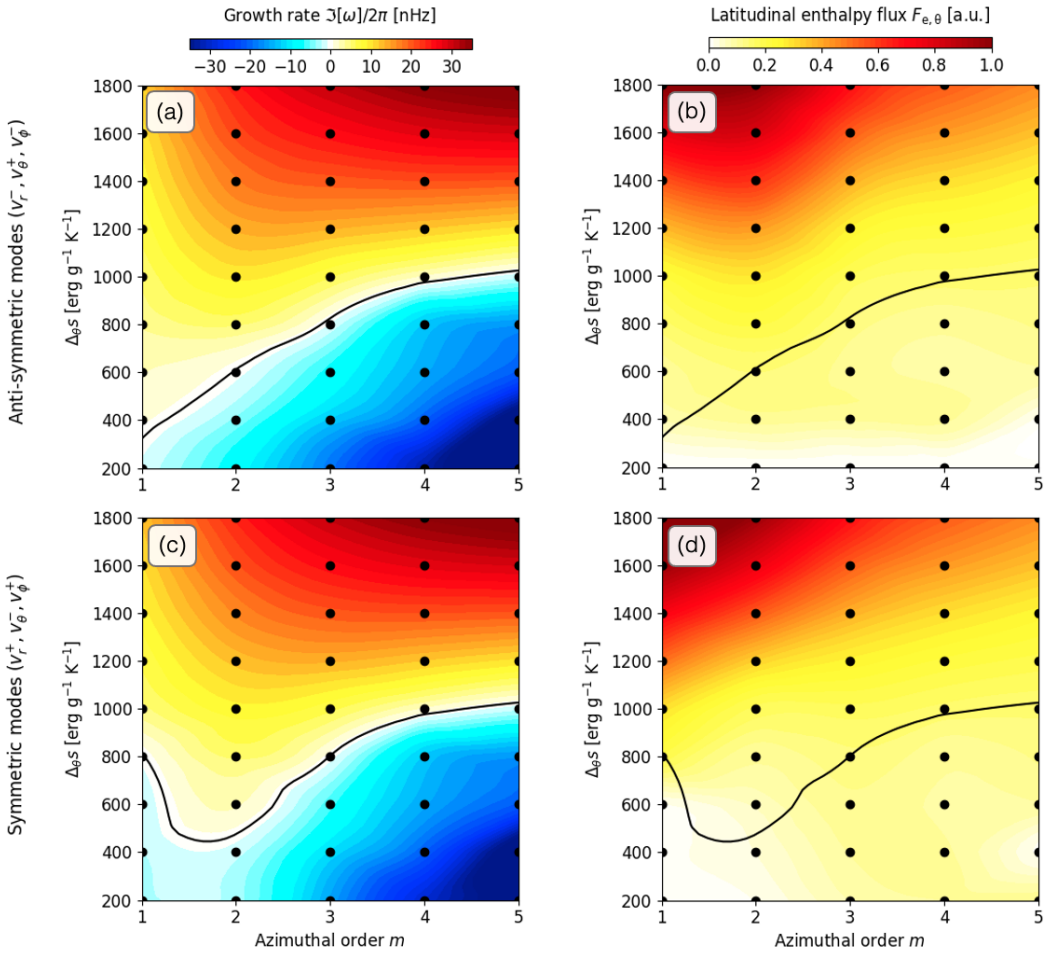

Figure 5.17: (Left) Growth rates of the $k_y = 0$ baroclinic modes for $1 \leq m \leq 5$ with varying latitudinal entropy difference between the poles and the equator $\Delta_\theta s = s_0(\theta = 0) - s_0(\theta = \pi/2)$. Top and bottom rows denote the modes with north-south anti-symmetric and north-south symmetric v_ϕ, respectively. Black solid lines represent the location where the growth rates are zero $\Im[\omega] = 0$. (Right) Latitudinal enthalpy fluxes $F_{e,\theta} = \rho_0 c_p \langle v_\theta T_1 \rangle$ of the $k_y = 0$ baroclinic modes for $1 \leq m \leq 5$ with varying $\Delta_\theta s$. Eigenfunctions are normalized such that each mode has the same kinetic energy. The black points denote the location where the linear stability analyses are carried out. The color contours are obtained by interpolating the data with bicubic method.

Figures 5.17c and d are the counterparts of the Fig. 5.17a and b for the north-south symmetric baroclinic modes. They share the general properties of the baroclinic modes, i.e., both the growth rates $\Im[\omega]$ and the latitudinal enthalpy fluxes $F_{e,\theta}$ tend to increase when $\Delta_\theta s$ becomes larger. However, the behavior at low m with small $\Delta_\theta s$ is found strikingly different. At $\Delta_\theta s \approx 400 - 800$ erg g^{-1} K^{-1}, the most unstable north-south symmetric mode is that of $m = 2$, which is in contrast to the north-south anti-symmetric case where the most unstable mode is $m = 1$. This probably explains why our nonlinear simulation (Case 3) produces the $m = 2$ baroclinic perturbation which is predominantly north-south symmetric in v_ϕ.

6 Three-dimensional magnetohydrodynamic simulation of Babcock-Leighton solar dynamo

Abstract

It still remains largely uncertain how the cyclic magnetic activity is maintained inside the Sun's convection zone (dynamo theory). Traditionally, numerical simulations of the solar dynamo have been carried out in a kinematic mean-field framework. More realistic models of rotating magneto-convection in the Sun have difficulty in reproducing the observed large-scale mean flows and solar-like magnetic cycles. In this study, we present a new numerical framework to simulate the solar dynamo in the three-dimensional (3D) magnetohydrodynamic (MHD) regime. We extend the conventional two-dimensional (2D) mean-field model of the Babcock-Leighton flux-transport dynamo into 3D MHD regime. The large-scale mean flows such as differential rotation and meridional circulation are driven by the parameterized Λ-effect. For the dynamo part, we use a new implementation of the Babcock-Leighton α-effect by which the surface bipolar-magnetic regions (BMRs) are produced in response to the dynamo-generated toroidal field inside the convection zone. Our simulation reproduces many observational features of the large-scale flows and magnetic fields such as solar-like differential rotation, single-cell meridional circulation, solar-like magnetic cycles, emergence of BMRs at low latitudes, equatorward migration of the BMRs. The flows and magnetic fields become substantially non-axisymmetric due to the BMRs at the surface. The simulation shows the torsional oscillation pattern similar to the solar observations but the equatorward branches are likely due to the thermal forcing associated with the diffusive heating of the superequipartition BMRs. Nonetheless, this study is significant because it is the only MHD dynamo simulation that is driven by observationally-friendly differential rotation and meridional circulation in our model. Our model will serve as a promising tool to study torsional oscillations, active region inflows, and Rossby modes in the context of the solar dynamo.

This chapter reproduces an initial draft of the article *Three-dimensional non-kinematic simulation of post-emergence evolution of bipolar magnetic regions and Babcock-Leighton dynamo of the Sun* by Y. Bekki and R. Cameron, submitted to Astronomy and Astrophysics. Contributions: Y. Bekki did most of the work.

6.1 Introduction

The Sun exhibits a 11-year cyclic magnetic activity which is sustained by the internal dynamo processes in the convection zone (e.g., Charbonneau 2020). Babcock-Leighton flux-transport model is one of the most promising solar dynamo models at present that can explain many observational features (e.g., Dikpati and Charbonneau 1999). In this model, the equator migration of the sunspots group is attributed to an equatorward transport of the dynamo-generated toroidal flux by the meridional flow near the base of the convection zone (Wang et al. 1991, Choudhuri et al. 1995). This is supported by the recent helioseismic observations in which meridional flow is found to be poleward at the surface and equatorward at the base (Rajaguru and Antia 2015, Gizon et al. 2020b). Another characteristic feature of this dynamo model is that the main conversion process from toroidal to poloidal fields is done by the so-called Babcock-Leighton mechanism, in which the surface poloidal fields are generated by the poleward advection and equatorial cancellation of the bipolar sunspots that are tilted with respect to east-west direction (Babcock 1961, Leighton 1964). Numerical investigations of this dynamo model have been mostly carried out in a two-dimensional (2D) mean-field framework both in a kinematic regime (Chatterjee et al. 2004, Hazra et al. 2014, Karak and Cameron 2016) and in a non-kinematic regime (Rempel 2006, Ichimura and Yokoyama 2017, Inceoglu et al. 2017).

There are several recent studies that aim to realize the Babcock-Leighton process in a more realistic three-dimensional (3D) domain. Yeates and Muñoz-Jaramillo (2013) presented a kinematic model in which the upward velocity perturbation associated with the magnetic buoyant flux tubes is explicitly prescribed to produce the tilted bipolar magnetic regions (BMRs) at the surface. This method has also been used in Kumar et al. (2019) and Whitbread et al. (2019). On the other hand, Miesch and Dikpati (2014) have developed a different model of the Babcock-Leighton dynamo, in which the BMRs are artificially placed at the surface in response to the toroidal field at the base under the constraint of Joy's law. This model has been used to study the long-term cycle variability (Karak and Miesch 2017). However, all of these models are kinematic. Therefore, it still remains unclear how the Lorentz-force of the surface BMRs affects the dynamo solution in the magnetohydrodynamic (MHD) regime.

The most realistic models of the solar dynamo are provided by MHD convective dynamo simulations in a spherical shell (e.g., Brun et al. 2004, Ghizaru et al. 2010, Brown et al. 2010, Fan and Fang 2014, Hotta et al. 2016, Strugarek et al. 2017). However, they have difficulty in reproducing the large-scale mean flows as we observe when the solar parameters are used (known as convective conundrum, e.g., Nelson et al. 2018). Moreover, they still cannot capture the full dynamics of the flux-emergence and the resulting formation of BMRs at the surface comprehensively (Nelson et al. 2011, Fan and Fang 2014, Chen et al. 2017). Therefore, it is still helpful to use mean-field models in which the large-scale mean-flows are largely controllable with proper parameterizations of the small-scale convective angular momentum transport (Λ-effect; see Kitchatinov and Ruediger (1995)).

In this study, we present a new numerical framework to study the solar dynamo in 3D MHD regime, which takes advantage of both the mean-field approach for the solar differential rotation / meridional circulation system and the 3D realization of the Babcock-Leighton process. Therefore, our model is more realistic than both 2D mean-field MHD models (e.g., Rempel 2006) and 3D kinematic Babcock-Leighton models (e.g., Miesch

and Teweldebirhan 2016). Although our model is less realistic than 3D MHD convective dynamo models (e.g., Hotta et al. 2016), this instead enables us to solve the MHD dynamo equations under the constraints of the observed differential rotation and meridional circulation. We believe that our model can potentially provide many future applications such as data assimilation, prediction of the next cycle, studies on non-axisymmetric MHD instabilities and modes in the Sun.

The organization of this chapter is as follows. The numerical model is explained in detail in §6.2. An implementation of the BL process is described in §6.2.3. Our initial results of our simulation are presented in §6.3. We close by summarizing our results and discussing the future prospects in §6.4.

6.2 Model

6.2.1 Governing equations

We numerically solve a set of MHD equations in a spherical coordinate (r, θ, ϕ):

$$\frac{\partial \rho_1}{\partial t} = -\nabla \cdot (\rho_0 \boldsymbol{v}), \tag{6.1}$$

$$\frac{\partial \boldsymbol{v}}{\partial t} = -\boldsymbol{v} \cdot \nabla \boldsymbol{v} - \frac{\nabla p_1}{\rho_0} - \frac{\rho_1}{\rho_0} g \boldsymbol{e}_r + 2\boldsymbol{v} \times \boldsymbol{\Omega_0} + \frac{1}{4\pi\rho_0}(\nabla \times \boldsymbol{B}) \times \boldsymbol{B} + \frac{1}{\rho_0}\nabla \cdot \boldsymbol{\mathcal{D}}, \tag{6.2}$$

$$\frac{\partial \boldsymbol{B}}{\partial t} = \nabla \times (\boldsymbol{v} \times \boldsymbol{B} + \boldsymbol{\mathcal{E}} - \eta \nabla \times \boldsymbol{B}), \tag{6.3}$$

$$\frac{\partial s_1}{\partial t} = \boldsymbol{v} \cdot \nabla \boldsymbol{s_1} + c_{\rm p}\delta \frac{v_r}{H_p} + \frac{1}{\rho_0 T_0}\nabla \cdot (\rho_0 T_0 \kappa \nabla s_1) \tag{6.4}$$

$$+ \frac{1}{\rho_0 T_0}\left[(\boldsymbol{\mathcal{D}} \cdot \nabla) \cdot \boldsymbol{v} + \frac{\eta}{4\pi}|\nabla \times \boldsymbol{B}|^2\right], \tag{6.5}$$

where g, ρ_0, p_0, and H_p denote the gravitational acceleration, density, pressure, and pressure scale height of the background state which is in an adiabatically-stratified hydrostatic equilibrium. We use the same background model as described in § 4.3, which mimics the standard model S (Christensen-Dalsgaard et al. 1996a). ρ_1 and p_1 are density and pressure perturbations with respect to the background that are assumed to be sufficiently small, i.e., $|p_1/p_0| \approx |\rho_1/\rho_0| \ll 1$, so that the equation of state is linearized.

$$p_1 = p_0\left(\gamma\frac{\rho_1}{\rho_0} + \frac{s_1}{c_v}\right), \tag{6.6}$$

where γ is the specific heat ratio and s_1 is entropy perturbation from the adiabatic background. Ω_0 denotes the rotation rate of the radiative core, for which we set the value as $\Omega_0/2\pi = 431.3$ nHz.

$\boldsymbol{\mathcal{D}}$ denotes the turbulent Reynolds stress associated with small-scale convective motions that are not explicitly resolved in our model. This in principle contains the effects

of turbulent diffusion and turbulent momentum transport (Λ-effect, see Kitchatinov and Ruediger (1995)). Therefore, the Reynolds stresses are expressed as

$$\mathcal{D}_{ik} = \rho_0 \left[\nu_{\rm vis} \left(S_{ik} - \frac{2}{3}\delta_{ik} \nabla \cdot \boldsymbol{v} \right) + \nu_{\rm lam} \Lambda_{ik} \Omega_0 \right], \tag{6.7}$$

where S_{ik} and δ_{ik} denote the velocity deformation tensor and Kronecker-delta unit tensor. Detail tensor expressions of $\mathcal{S}_{ij}$ in a spherical coordinate are given in the Eqs. (3.10)-(3.15).

In our model, turbulent viscous, thermal, and magnetic diffusivities are all assumed to be isotropic. We use the same radial profiles for the viscous ($\nu_{\rm vis}$), thermal (κ), and magnetic (η) diffusivities as of Rempel (2006). It will be instructive to give readers the diffusivity values at the top boundary; $\nu_{\rm vis} = \kappa = 5 \times 10^{12}$ cm^{2}s^{-1}, and $\eta = 10^{12}$ cm^2 s^{-1}.

In order to break the Taylor-Proudman's constraint of the differential rotation via the thermal wind balance, a latitudinal entropy gradient needs to be negative (positive) in the northern (southern) hemisphere. Rempel (2005) proposed that this can be achieved when the base of the convection zone is weakly subadiabatic and the meridional circulation is counter-clockwise (clockwise) in the northern (southern) hemisphere. We adopt the same physical model of Rempel (2005) to generate the latitudinal entropy gradient by giving the superadiabaticity $\delta = \nabla - \nabla_{\rm ad}$ as follows,

$$\delta(r, \theta) = \mathcal{T}_{-}(r; r_{\rm sub}, d_{\rm sub})\, \delta_{\rm sub}(\theta), \tag{6.8}$$

$$\delta_{\rm sub}(\theta) = \delta_{\rm pl} + (\delta_{\rm eq} - \delta_{\rm pl}) \sin^2 \theta, \tag{6.9}$$

$$r_{\rm sub}(\theta) = r_{\rm pl} + (r_{\rm eq} - r_{\rm pl}) \sin^2 \theta, \tag{6.10}$$

where $\mathcal{T}$ denotes a transition function defined by

$$\mathcal{T}_{\pm}(x; x_0, d) = \frac{1}{2} \left[1 \pm \tanh \left(\frac{x - x_0}{d} \right) \right]. \tag{6.11}$$

We set the base superadiabaticity at the poles and at the equator as $\delta_{\rm pl} = -1.5 \times 10^{-5}$ and $\delta_{\rm eq} = -2 \times 10^{-5}$, respectively. The depths where the stratification changes from subadiabatic to adiabatic are given as $r_{\rm pl} = 0.725 R_\odot$ and $r_{\rm eq} = 0.735 R_\odot$. The weakly subadiabatic layer near the base is thought to be an outcome of a nonlocal energy transport of strongly magnetized convection in the Sun (Skaley and Stix 1991, Brandenburg 2016) and is reported in the numerical experiments (Käpylä et al. 2017, Hotta 2017, Bekki et al. 2017). The subadiabaticity is slightly enhanced in the equatorial area owing to the latitudinal variation of the Coriolis force acting on low-entropy downdrafts (Karak et al. 2018).

6.2.2 Λ-effect

Λ_{ik} is a dimensionless tensor that specifies the amplitude and direction of the turbulent momentum transport. In this model, we only consider the turbulent angular momentum transport. Therefore, Λ_{ik} becomes nonzero only when k takes ϕ. We parameterize $\Lambda_{r\phi}$ and $\Lambda_{\theta\phi}$ similarly to the model presented in Rempel (2005),

$$\Lambda_{r\phi} = +\Lambda_0 \tilde{f}_l(r, \theta) \cos(\theta + \lambda) \left[1 + \zeta_r(r, \theta, \phi) \right], \tag{6.12}$$

$$\Lambda_{\theta\phi} = -\Lambda_0 \tilde{f}_l(r, \theta) \sin(\theta + \lambda) \left[1 + \zeta_\theta(r, \theta, \phi) \right]. \tag{6.13}$$

The overall amplitude of the Λ-effect is given as $\Lambda_0 = 0.85$. The inclination is set to $\lambda = +(-)15^\circ$ in the northern (southern) hemisphere. Thus, the associated angular momentum flux becomes largely equatorward and slightly cylindrically outward. The spatial distribution of the Λ-effect is specified as

$$\tilde{f}_l(r,\theta) = \frac{f_l(r,\theta)}{\max|f_l(r,\theta)|}, \tag{6.14}$$

$$f_l(r,\theta) = \sin^2\theta\cos\theta\tanh\left(\frac{r_{\rm max}-r}{d_l}\right). \tag{6.15}$$

where $d_l = 0.025R_\odot$. With this parameterization, the profiles of differential rotation and meridional circulation become similar to observations (Howe 2009, Gizon et al. 2020b)

ζ_r and ζ_θ denote random fluctuations due to the unresolved turbulent convection. In order to randomly vary the amplitude and direction of the Λ-effect in space, we construct ζ_r and ζ_θ separately. In our model, we construct the random field by simply superposing multiple gaussians for the sake of numerical feasibility,

$$\zeta(r,\theta,\phi) = \sum_{i=1}^{N} c_i \exp\left[-\left(\frac{r-r_i}{\delta r}\right)^2 - \left(\frac{\theta-\theta_i}{\delta\theta}\right)^2 - \left(\frac{\phi-\phi_i}{\delta\phi}\right)^2\right], \tag{6.16}$$

where the locations of gaussian peaks (r_i, θ_i, ϕ_i) are randomly chosen and their amplitudes c_i are also randomly determined within the range $-2 < c_i < 2$. The spatial scale of each gaussian is set as $(\delta r, \delta\theta, \delta\phi) = (0.03R_\odot, 5^\circ, 5^\circ)$. In our reference calculation, we set the number of gaussians $N = 30$. We generate the random field ζ at every time step and therefore it is uncorrelated in time. Note that the non-axisymmetric flows can be partially driven by the random fluctuation of the Λ-effect which has an azimuthal dependence.

6.2.3 Babcock-Leighton α-Effect

The electro-motive-force $\mathcal{E}$ in the Eq.(6.3) represents the Babcock-Leighton α-effect, by which the surface poloidal field is produced as a result of north-south tilt of the BMRs (Babcock 1961, Leighton 1964). In our model, the emergence of BMRs at the surface is assumed to occur in response to the dynamo-generated toroidal field near the base of the convection zone, i.e., toroidal flux that is sufficiently amplified by Ω-effect becomes unstable and rise up to the surface. During the rise and the subsequent emergence, the toroidal flux is twisted by Coriolis forces and acquires a north-south tilt in its apex (Fan 2009). In order to incorporate this physics into our model, we take the following steps to construct $\mathcal{E}$. Our approach differs from the method presented in Yeates and Muñoz-Jaramillo (2013) and Kumar et al. (2019) where the velocity associated with magnetic buoyancy is prescribed nor the method used in Miesch and Dikpati (2014) and Miesch and Teweldebirhan (2016) where the BMRs are explicitly spotted at the surface.

First, the mean toroidal field near the base of the convection zone is computed at every time step,

$$\bar{B}_{\rm tor}(\theta,\phi) = \frac{1}{r_b - r_a}\int_{r_a}^{r_b} B_\phi(r,\theta,\phi)dr, \tag{6.17}$$

where $r_a = 0.71R_\odot$ and $r_b = 0.735R_\odot$. Then, we determine the location of the flux emergence in a spherical surface (θ^*, ϕ^*). In order to suppress the emergence at high latitudes as suggested by the observations, we apply a latitudinal mask to $\bar{B}_{\rm tor}(\theta, \phi)$ such that

$$\bar{B}^*_{\rm tor}(\theta, \phi) = \mathcal{T}_+(\theta; \pi/2 - \theta_{\rm em}, \Delta\theta_{\rm tran}) \times \mathcal{T}_-(\theta; \pi/2 + \theta_{\rm em}, \Delta\theta_{\rm tran}) \bar{B}_{\rm tor}(\theta, \phi), \tag{6.18}$$

where $\theta_{\rm em} = 17.5^\circ$ and $\Delta\theta_{\rm tran} = 8.5^\circ$. A necessary condition for the flux emergence to occur is that $|\bar{B}^*_{\rm tor}(\theta, \phi)|$ exceeds a threshold field strength $B_{\rm crit} = 500$ G. The location of emergence (θ^*, ϕ^*) is randomly chosen when the above condition is satisfied on multiple points.

Eventually, $\boldsymbol{\mathcal{E}}$ is expressed as follows being proportional to $\bar{B}^*_{\rm tor}(\theta^*, \phi^*)$,

$$\begin{pmatrix} \mathcal{E}_r \\ \mathcal{E}_\theta \\ \mathcal{E}_\phi \end{pmatrix} = \alpha_0 \tilde{f}^*_\alpha(r, \theta, \phi) \begin{pmatrix} 0 \\ -\cos\psi^* \\ \sin\psi^* \end{pmatrix} \bar{B}^*_{\rm tor}(\theta^*, \phi^*), \tag{6.19}$$

where $\tilde{f}_\alpha$ represents the spatial distribution of BMRs,

$$\tilde{f}^*_\alpha(r, \theta, \phi) = \exp\left[-\left(\frac{r - r_{\rm max}}{d_{\rm sf}} \right)^2 - \left(\frac{\theta - \theta^*}{\Delta\theta_{\rm bmr}} \right)^2 - \left(\frac{\phi - \phi^*}{\Delta\phi_{\rm bmr}} \right)^2 \right]. \tag{6.20}$$

The Babcock-Leighton α-effect is confined near the surface with the thickness $d_{\rm sf} = 0.04R_\odot$. $\Delta\theta_{\rm bmr}$ and $\Delta\phi_{\rm bmr}$ determine the size of BMRs. In our model, we set $\Delta\theta_{\rm bmr} = \Delta\phi_{\rm bmr} = 6$ deg, which is consistent with observations suggesting the typical size of BMRs of $r_{\rm bmr} \approx 5-100$ Mm (e.g., Solanki 2003) that leads to $\Delta\theta_{\rm bmr} = \Delta\phi_{\rm bmr} \approx 2r_{\rm bmr}/R_\odot \approx 0.4-8$ deg. The overall amplitude of the Babcock-Leighton α-effect is set to $\alpha_0 = 50$ km s^{-1}. This value, in combination with the typical toroidal field strength near the base $\bar{B}^*_{\rm tor} \approx 5 - 20$ kG (Dikpati and Charbonneau 1999), leads to the total magnetic flux of BMRs of $10^{22} - 10^{23}$ Mx, which is consistent with observations (Schrijver and Harvey 1994).

The north-south tilt of BMRs (ψ^*) obeys Joy's law such that,

$$\psi^* = 35^\circ \cos\theta^* + \psi'_{\rm f}, \tag{6.21}$$

where $\psi'_{\rm f}$ denotes the random fluctuation of the tilt angle around Joy's law (Hale et al. 1919, Howard 1991, Stenflo and Kosovichev 2012, Wang et al. 2015). For simplicity, we assume that the probability distribution of $\psi'_{\rm f}$ is roughly given by the following Gaussian distribution,

$$P_{\rm f}(\psi'_{\rm f}) = \frac{1}{\sigma_{\rm f}\sqrt{2\pi}} \exp\left[-\psi'^2_{\rm f}/(2\sigma^2_{\rm f}) \right], \tag{6.22}$$

with $\sigma_{\rm f} = 15^\circ$. Unlike the kinematic model of Karak and Miesch (2017), a quenching term is not necessary in our model because the saturation of the dynamo occurs owing to the Lorentz-force feedback self-consistently (Rempel 2006, Ichimura and Yokoyama 2017).

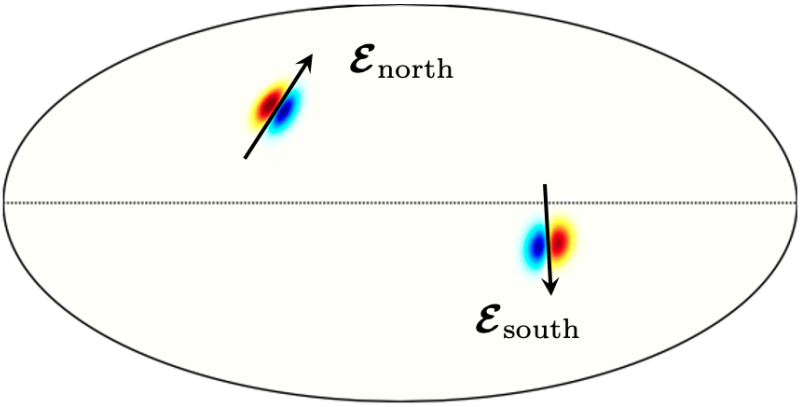

Figure 6.1: Example structure of BMRs per each hemisphere produced from our Babcock-Leighton α-effect modeling. Radial field at the solar surface is shown where red (blue) points represent positive (negative) B_r. Solid black arrows denote the direction of the electro-motive-force $\mathcal{E}$ defined by the Eq.(6.19). Positive (negative) toroidal field in the northern (southern) hemisphere is implicitly assumed at the base of the convection zone.

In order to prevent overlapping emergence events on the same location in a very short time span, we introduce a following time delay algorithm as presented in Miesch and Dikpati (2014), Miesch and Teweldebirhan (2016), Karak and Miesch (2017): The log-normal distribution of the emergence events is defined by

$$P_{\rm em}(\Delta_t) = \frac{1}{\sigma_t \Delta_t \sqrt{2\pi}} \exp\left[-\frac{(\Delta_t - \mu_t)^2}{2\sigma_t^2}\right], \tag{6.23}$$

where $\Delta_t = t - t_s$ is the time lag since the last emergence event at t_s. The flux emergence is allowed only when the cumulative of $P_{\rm em}$ exceeds a number $z \in [0, 1]$ randomly chosen at every time step. σ_t and μ_t are specified by the mean and mode of the distribution τ_s and τ_p, respectively, as

$$\tau_p = \frac{2.2 \text{ days}}{1 + (B_{\rm t,bc}/B_\tau)^2}, \quad \tau_s = \frac{20 \text{ days}}{1 + (B_{\rm t,bc}/B_\tau)^2} \tag{6.24}$$

where $B_{\rm t,bc}$ is the horizontally-averaged $\bar{B}^*_{\rm tor}$ defined in the Eq.() and B_τ denotes the threshold toroidal field strength near the base of the convection zone. The flux emergence becomes frequent when $B_{\rm t,bc}$ exceeds B_τ (solar maxima) and less frequent as the cycle ends. An example of the resulting BMR is illustrated in Fig. 6.1.

6.2.4 Numerical scheme

We numerically solve the Eqs (6.1)-(6.5) using the 4th-order centered-differencing method for space and 4-step Runge-Kutta scheme for time integration (Vögler et al. 2005). To avoid the severe CFL constraint for time step, the background sound speed is artificially reduced by a factor of $\xi = 200$, which still ensures that flows remain sufficiently subsonic (e.g., Hotta et al. 2014a). Moreover, we use the hyperbolic divergence cleaning method

(9-wave method) for minimizing the numerical error resulting from the divergence of magnetic field (Dedner et al. 2002). See the Appendix 6.5.2. In addition to the explicit diffusivities, the same artificial viscosity reported in Rempel (2014) is used to stabilize numerical computation.

The numerical domain is a full-spherical shell extending from $r_{\rm min} = 0.65R_\odot$ up to $r_{\rm max} = 0.985R_\odot$. The base of the convection zone is located at $r_{\rm bc} = 0.71R_\odot$. In order to avoid the numerical problems resulting from the singular points in a spherical coordinate, we use the Yin-Yang grid (Kageyama and Sato 2004). For more details about the implementation of the Yin-Yang grid, refer to §4.8.3. The grid resolution used in our reference case is $72(N_r) \times 72(N_\theta) \times 216(N_\phi) \times 2$(Yin and Yang grids). The code is parallelized using message passing interface (MPI). At both radial boundaries, impenetrable and stress-free boundary condition is assumed for velocity. The magnetic field is assumed to be radial at the top and horizontal at the bottom. The simulation is initiated in a hydrodynamic regime and then an axisymmetric dipolar field is added when the large-scale mean flows become stationary. We analyze the data after the dynamo saturates and shows a clear cyclic pattern.

6.3 Results

6.3.1 Cyclic dynamo

Figures 6.2a and b show the temporal evolution of the azimuthally-averaged radial field $\bar{B}_r$ at the surface and the toroidal field $\bar{B}_\phi$ near the base of the convection zone, represented in terms of the well-known magnetic butterfly diagram. We can clearly see the cyclic polarity reversals that occur roughly at every 9 yr, which is slightly shorter than the solar cycle yet comparable. In each cycle, there is an equatorward migration of sunspot groups (BMRs) and the build-up of the polar field by poleward advection of the magnetic fluxes associated with the trailing sunspots. These are owing to the single-cell meridional circulation achieved in our model, which has an amplitude of about 15 m s^{-1} at the surface and 2 m s^{-1} near the base of the convection zone. The black solid lines in Fig. 6.2b denote the range of the emergence latitudes of BMRs at each time. The phase of the equatorward advection of the toroidal field at the base corresponds to that of the emergence of the BMRs at the surface.

In our MHD model, the dynamo-generated fields are expected to have strong impacts on flows via the Lorentz force feedback. Figure 6.2c shows the temporal evolution of the differential rotation, which is commonly known as torsional oscillations. We clearly find both poleward and equatorward propagating oscillation patterns with the typical amplitude of about 5 nHz at the surface. Figures 6.3a and b show the time-latitude profiles of the latitudinal velocity at the top and bottom of the convection zone, respectively. Although poleward flow at the surface and equatorward flow near the base tend to be suppressed during the activity maxima, the feedback is not large enough to switch off the advection of the magnetic fields. Figure 6.3c shows the temporal evolution of the entropy perturbation at the surface with typical variation amplitude of about 250 erg g^{-1} K^{-1} which corresponds to the temperature fluctuation of about 1.4 K. The surface is heated when BMRs emerge due to the strong magnetic diffusion in our model.

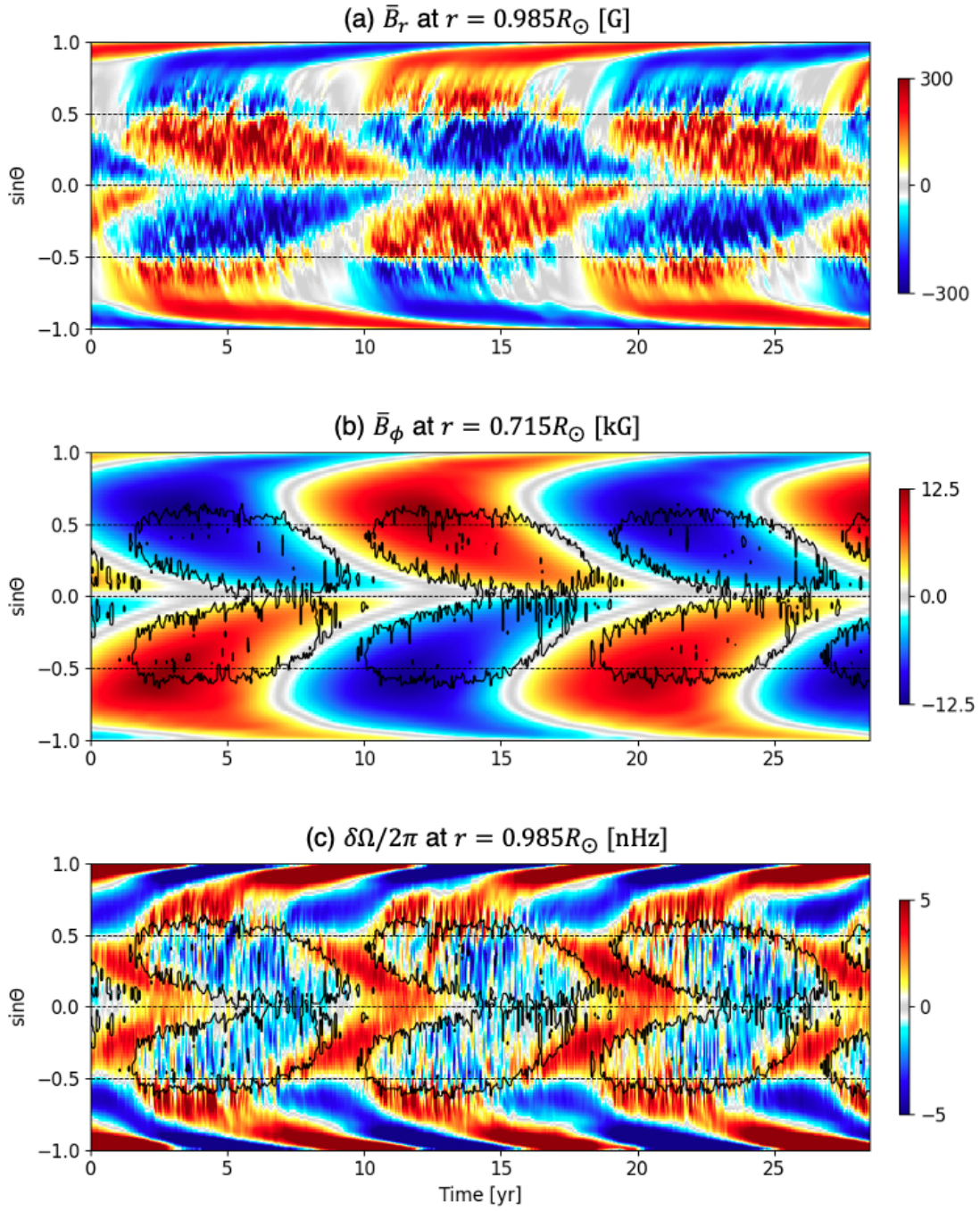

Figure 6.2: Temporal evolution of the azimuthally-averaged magnetic fields and torsional oscillation. (a) Azimuthal mean of the radial field $\bar{B}_r$ [G] at the surface $r = 0.985R_\odot$ where the bar denotes the azimuthal mean. (b) Azimuthal mean of the longitudinal field $\bar{B}_\phi$ [kG] near the base of the convection zone $r = 0.715R_\odot$. Black solid lines are the contours of the emerged BMRs at each time. (c) Torsional oscillation pattern $\delta\Omega = \Omega_1 - \langle\Omega_1\rangle_t$ [nHz] at the surface where $\langle\rangle_t$ denotes the temporal average.

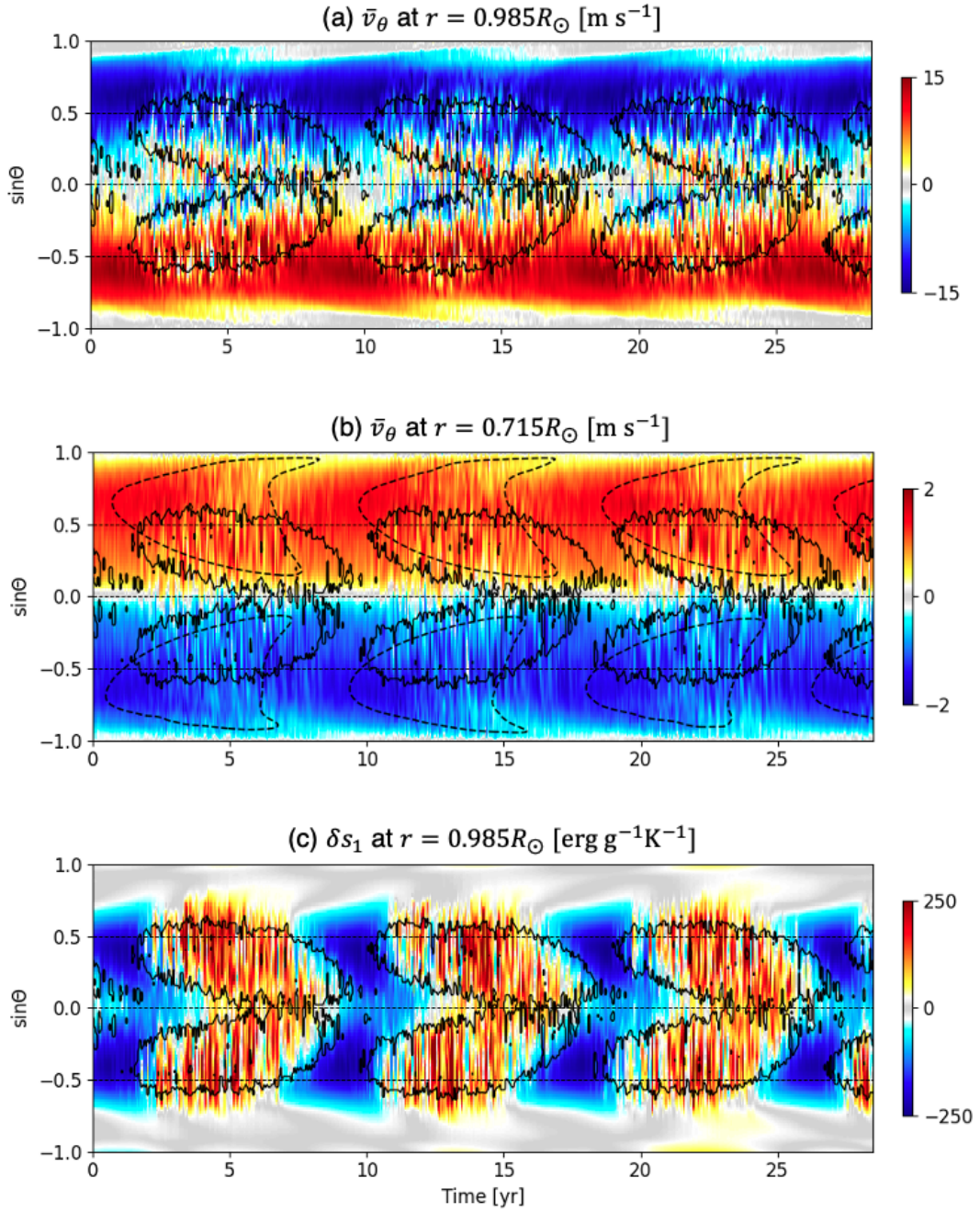

Figure 6.3: Temporal evolution of the latitudinal velocity and entropy perturbation. (a) Azimuthal mean of the latitudinal velocity $\bar{v}_\theta$ [m s^{-1}] at the surface. Red (blue) in the northern hemisphere represents the equatorward (poleward) flow. (b) The same as (a) but near the base of the convection zone. Black dashed lines denote the contours of the toroidal field at the base (8.5 kG). (c) Entropy perturbation $\delta s_1 = s_1 - \langle s_1 \rangle_t$ at the surface in units of erg g^{-1} K^{-1}.

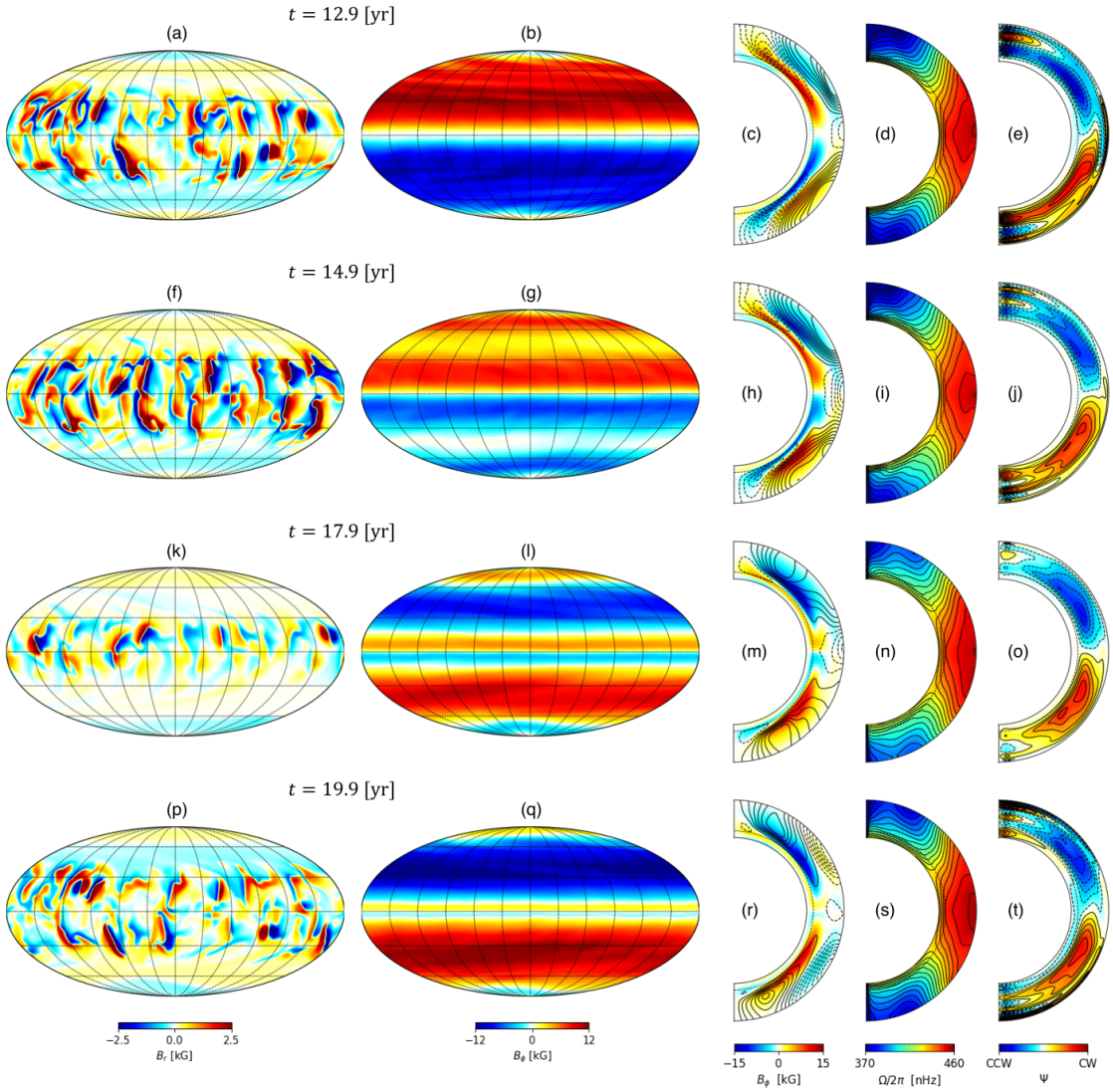

Figure 6.4: Time evolution of magnetic field and velocity. Shown are the snapshots at $t = 12.9$ yr (from (a) to (e)), $t = 14.9$ yr (from (f) to (j)), $t = 17.9$ yr (from (k) to (o)), $t = 19.9$ yr (from (p) to (t)) in Fig. 6.2. The mollweide projections on the 1st and 2nd columns show the radial field B_r at the surface $r = 0.985R_\odot$ and longitudinal field B_ϕ near the base of the convection zone $r = 0.715R_\odot$, respectively. The meridional plot in the 3rd column represents the azimuthally-mean toroidal field (color scales) and poloidal field (contours). The meridional plots in the 4th and 5th columns represent the azimuthally-mean differential rotation and streamfunction of the meridional circulation, respectively.

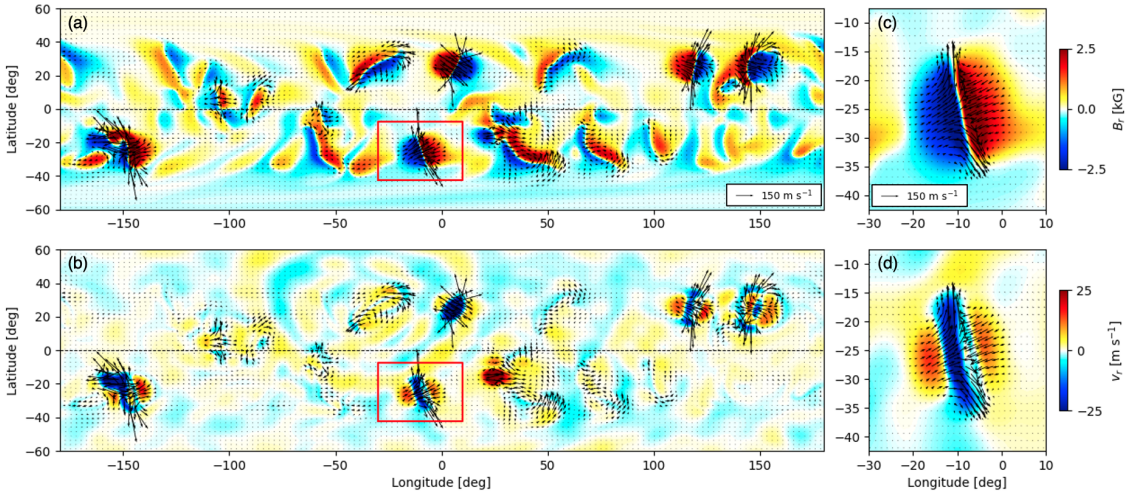

Figure 6.5: Snapshots of the radial field B_r [kG] at the surface (top rows) and the radial velocity v_r [m s^{-1}] near the surface (bottom rows) at $t = 10.3$ yr in Fig. 6.2. The black arrows represent the horizontal flow (v_θ, v_ϕ) at the surface. Panels (c) and (d) are the zoom-in of the panels (a) and (b), focusing on the single BMRs denoted by red thick solid lines.

Figure 6.4 shows the evolution of the magnetic fields and mean flows (differential rotation and meridional circulation) over the course of a magnetic cycle. The leftmost panels show mollweide projections of the surface radial field. As prescribed in our BL-source term, BMRs emerge at low latitudes obeying the Hale's and Joy's laws. Therefore, the magnetic fields near the surface are substantially non-axisymmetric. On the other hand, toroidal fields near the bottom convection zone are found to be almost axisymmetric. Meridional plots on the 3rd, 4th, and 5th columns of Fig. 6.4 show the azimuthally-mean profiles of the poloidal and toroidal magnetic fields, differential rotation, and meridional circulation, respectively. When azimuthally averaged, the solution show a similar pattern of time evolution as previous 2D mean-field models (e.g., Rempel 2006).

6.3.2 Flows associated with BMRs

In our model, non-axisymmetric flows are driven both by random fluctuations in the Λ-effect and by non-axisymmetric Lorentz forces. In the simulation reported here, the latter effect is found to be dominant. Figure 6.5 shows a snapshot of the radial field at the surface (top rows) and the radial velocity near the surface (bottom rows). Black arrows represent the horizontal flow motions at the surface. Strong flows are always magnetically-driven in the vicinity of the BMRs: When a BMRs emerge at the surface which happens instantaneously in our model, a horizontal converging flow is driven towards the polarity inversion line (between the two spots) with the typical amplitudes of about 100 m s^{-1}. This is owing to a strong magnetic tension force of the bipolar sunspots (whose subsurface structure is half-torus) that acts as an attractive force for the two spots. This strong converging flow further drives both horizontal outflows and radial downflows along the polarity inversion line, as shown in Fig. 6.5c and d. Due to these strong horizontal flows at the surface, a newly-emerged BMR that initially consists of two round-shaped sunspots

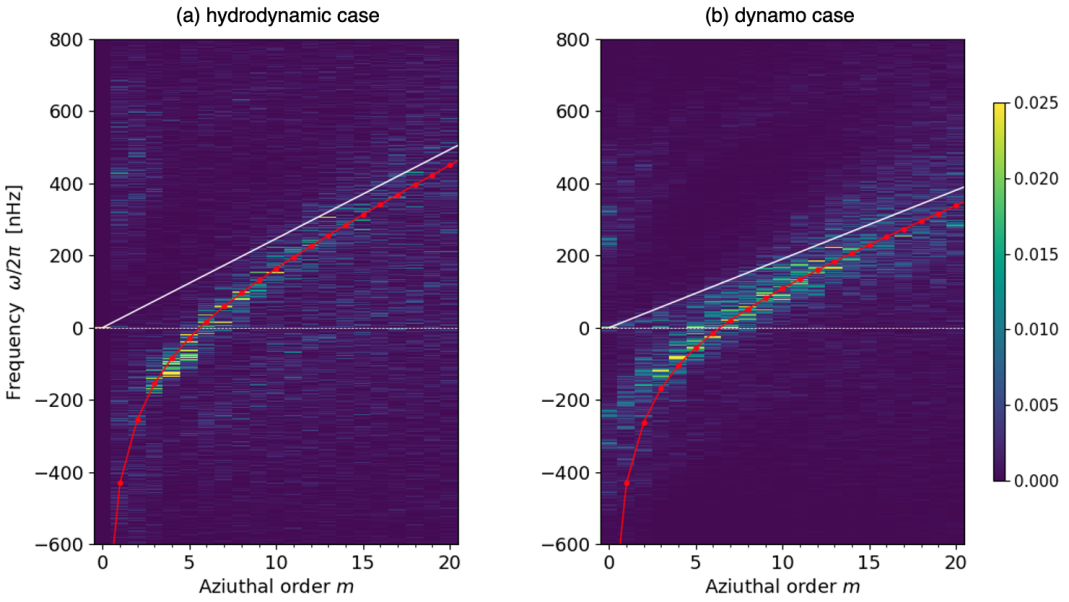

Figure 6.6: Equatorial power spectra of latitudinal velocity v_θ near the surface $r = 0.95R_\odot$ computed for (a) the hydrodynamic (non-magnetic) simulation and (b) the dynamo simulation. The spectra are computed in a frame rotating at $\Omega_0/2\pi = 431.3$ nHz. The power is normalized at each azimuthal order m. The white solid lines represent the advective effect by the differential rotation at the surface $\omega = m\,[\Omega(0.95R_\odot, \pi/2) - \Omega_0]$. The red lines denote the theoretical dispersion relation of the sectoral mode Rossby wave, $\omega = -2\Omega(0.95R_\odot, \pi/2)/(m+1) + m\,[\Omega(0.95R_\odot, \pi/2) - \Omega_0]$.

is quickly deformed into an elongated shape along the polarity inversion line, as seen in Fig. 6.5a.

6.3.3 Equatorial Rossby (r modes)

Other interesting non-axisymmetric flow features are the equatorial Rossby modes, which have recently been found to contribute a significant fraction of the vertical vorticity power at low latitudes (e.g., Löptien et al. 2018). In order to characterize the Rossby modes, we compute the equatorial power spectra of latitudinal velocity near the surface. The same analysis method as § 3.2 is used for the Fourier transform in time and longitude. Note, however, that unlike the rotating convection simulation of Bekki et al. (2022a), Rossby modes are excited by the non-axisymmetric random fluctuations in the Λ-effect and by the non-axisymmetric Lorentz-force in our non-convecting model. For comparison, we also compute the same power spectrum for the hydrodynamic (non-magnetic) simulation data, in which the non-axisymmetric flows are purely driven by the random fluctuations in the Λ-effect. The results are shown in Fig. 6.6. Note that all the spectra are computed in a frame rotating at $\Omega_{\rm ref}/2\pi = 431.3$ nHz. In both cases, we confirm the existence of Rossby modes as represented by clear power ridges along the expected dispersion relations (red lines) in the spectra. Compared to the hydrodynamic case where the Rossby modes exist for azimuthal orders $3 \le m \le 8$, the Rossby modes can be confirmed for $3 \le m \le 15$, and

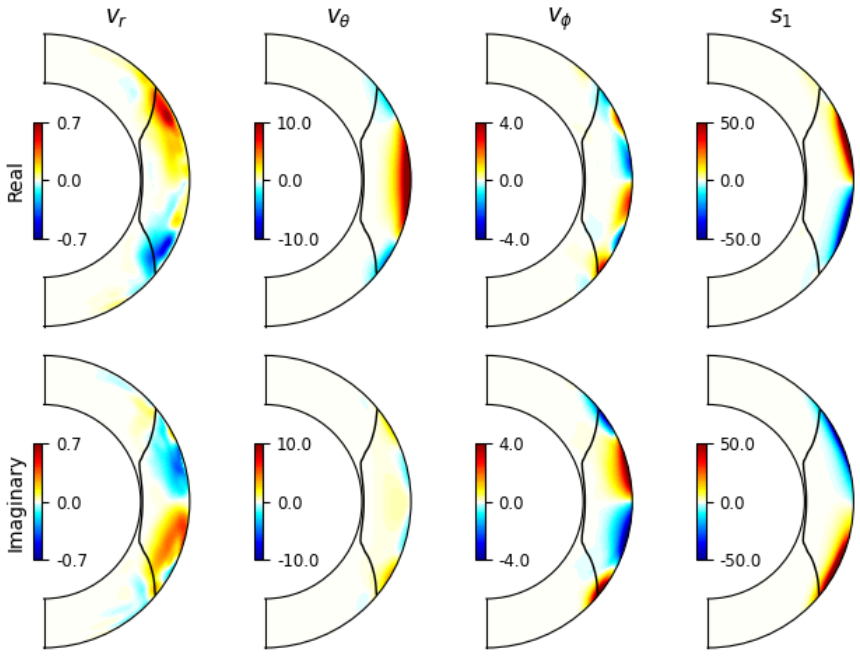

Figure 6.7: Eigenfunctions of the equatorial Rossby mode at $m = 10$ extracted from the dynamo simulation. Shown are the eigenfunctions of v_r, v_θ, v_ϕ (in units of m s^{-1}), and s_1 (in units of erg g^{-1} K^{-1}), from left to right. Top and bottom rows show the real and imaginary phases of the eigenfunctions, where we set the phase where v_θ becomes maximum at the equator as real, respectively. Overplotted in black solid line denotes the location of the viscous critical layer.

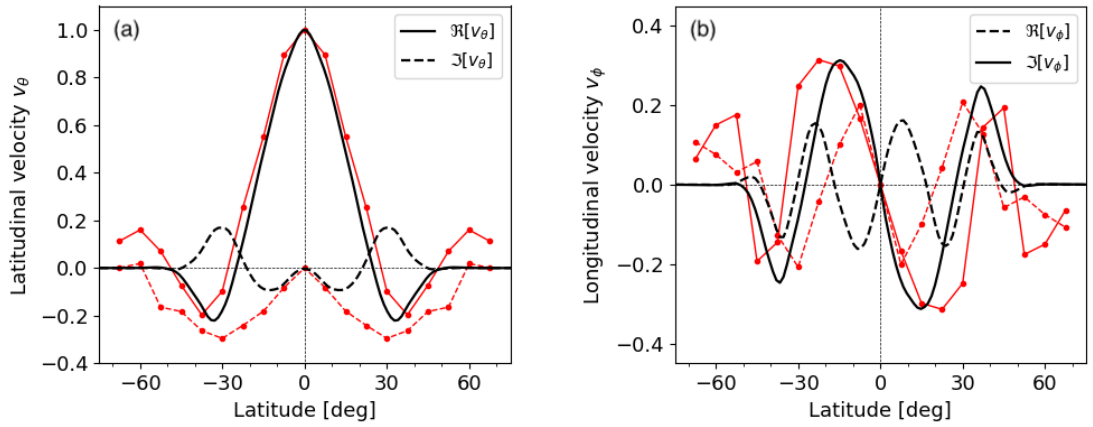

Figure 6.8: Normalized eigenfunctions of (a) v_θ and (b) v_ϕ at the surface. Solid and dashed lines represent the real and imaginary parts, respectively. Black and solid lines denote the simulation and observation, respectively.

their linewidths become broader in the frequency domain.

Figure 6.7 shows the extracted eigenfunctions of the equatorial Rossby modes at $m = 10$. For detail methods of the mode extraction from the simulation data, see §4.3.2.

Top and bottom rows show the real and imaginary phases, respectively. The latitudinal velocity peaks at the equator, switches sign at middle latitudes, and then decays at higher latitudes, which is similar to the observations (Löptien et al. 2018, Proxauf et al. 2020). This latitudinal variation is likely caused by the viscous critical layer under the influence of differential rotation as discussed in Gizon et al. (2020b) and in §3.6.1. It is also noteworthy that the equatorial Rossby mode involves substantial radial motions near the viscous critical layer. Figure 6.8 compares the latitudinal eigenfunctions of v_θ and v_ϕ at the surface between the simulation and the observations at $m = 10$. Solid and dashed lines denote the real and imaginary parts, respectively. It is striking that the real eigenfunctions of both velocity components agree quite well with the observations (Proxauf et al. 2020). However, the sign of the imaginary eigenfunctions turns out to be opposite: $\Im[v_\theta]$ becomes positive at middle latitudes unlike the observations. This issue has already been pointed out by Gizon et al. (2020b).

6.4 Summary and discussions

In this chapter, we have described numerical methods of the novel 3D MHD Babcock-Leighton flux-transport dynamo model and reported some initial results of our reference simulation. This model can be regarded as an extension of the 3D kinematic Babcock-Leighton dynamo models (Yeates and Muñoz-Jaramillo 2013, Miesch and Dikpati 2014, Karak and Miesch 2017, Kumar et al. 2019) to MHD regime where the dynamo-generated magnetism can give a feedback on the flows. In this model, we do not solve the small-scale convection and focus on the large-scale flow and magnetic structures in 3D spherical shell. The large-scale mean flows are driven not by rotationally-influenced convection but by parametrized Reynolds stresses (Λ-effect). The three-dimensional induction equation is solved with the Babcock-Leighton source. It should be noted that, in this study, we have presented a new method of implementing the Babcock-Leighton α-effect, by which the surface poloidal field is produced in response to the dynamo-generated toroidal field near the base of the convection zone. Although there are several artificial terms in the governing equations in our model, this treatment allows us to simulate for the first time the MHD dynamo under the observationally-constrained profiles of differential rotation and meridional circulation, which is hard to obtain in the spherical convective dynamo simulations (e.g., Hotta et al. 2016, Strugarek et al. 2017, Viviani et al. 2018).

We have successfully demonstrated that many of the observational dynamo features are reproduced in our model such as activity cycles with decadal period, equatorward migration of the sunspot groups (BMRs), poleward transport of the surface radial field, torsional oscillations with both poleward and equatorward branches. However, since our model is highly sensitive to various model parameters, there are still several disagreements with the solar observations such as a slightly shorter cycle period of 9 yr, stronger radial field strengths at the surface of typical amplitudes of about $200 - 300$ G, and slightly larger torsional oscillations. The most important model parameters would be Λ_0 that determines the amplitudes of the differential rotation and meridional circulation, and α_0 that determines the strengths of BMRs emerged at the surface. In principle, a larger Λ_0 will lead to faster meridional flows and shorten the cycle period, and a larger α_0 will increase the field amplitudes and lead to a larger torsional oscillations. Yet, the outcome

is not trivial in the MHD regime where the flows and magnetic fields interact nonlinearly with each other. A detailed parameter study is required in the future.

One of the most striking results is the emergence of low-latitude branches of the torsional oscillations, which was not obtained in the 2D non-kinematic mean-field models (Rempel 2006). It is often argued that, unlike the high-latitude branches of the torsional oscillations that originate from the mean-field Lorentz force feedback (mechanical forcing), the low-latitude branches are generally attributed to the enhanced surface cooling of the BMRs (thermal forcing) (Spruit 2003, Rempel 2006, 2007). In our model, there is no such an effect of the enhanced radiative cooling at the surface. It is found that the surface is rather heated due to the strong magnetic diffusion of the superequipartition BMRs as shown in Fig. 6.3 (c). As a consequence, the thermal forcing works in the opposite sense in our model. This can be confirmed by the fact that the equatorial region is more accelerated (decelerated) than average in the activity minima (maxima), which disagrees with the observations (Howard and Labonte 1980, Howe et al. 2000, Vorontsov et al. 2002). In the future model, we plan to include the effects of the enhanced radiative cooling associated with BMRs at the surface to study how the low-latitude branches of the torsional oscillations are affected.

It should also be pointed out that an inclusion of the enhanced radiative cooling at the surface will substantially affect the horizontal motions at the surface by geostrophycally inducing inflows towards active regions (e.g., Gizon et al. 2001, Gizon and Rempel 2008). These active regions inflows are expected to have significant impact on the properties of the solar dynamo by regulating the poleward transport of the poloidal fluxes at the surface (Cameron and Schüssler 2012, Martin-Belda and Cameron 2017). While this issue has been conventionally studied in a kinematic regime, our model will provide a promising tool to study the effects of active region inflows in a self-consistent MHD dynamo simulation.

Finally, we note that our code is also applicable to examine the impact of magnetic fields on Rossby modes which we found to exist in the simulation. In fact, these observations suggest that the amplitudes and frequencies of the solar Rossby modes exhibit a cycle dependence (Liang et al. 2019). If we properly understand the effects of deep-seated magnetic fields on the mode frequencies and eigenfunctions of the Rossby modes, observations could potentially be used to infer the location and strength of the magnetic fields hidden in the Sun (Goddard et al. 2020).

Acknowledgements

We thank B. Karak for helpful comments. Y. B. is enrolled in the International Max-Planck Research School for Solar System Science at the University of Göttingen. Y .B. also acknowledges a support from a long-term scholarship program for degree-seeking graduate students abroad from the Japan Student Services Organization (JASSO). We acknowledge a support from ERC Synergy Grant WHOLE SUN 810218. All the numerical computations were performed at the Max-Planck supercomputer RZG in Garching.

6.5 Appendix

6.5.1 Extention to MHD code

The code used in this study has been developed by adding magnetic terms to the hydrodynamic equations,

$$\frac{\partial \boldsymbol{v}}{\partial t} = [\ldots] + \frac{1}{4\pi\rho_0}(\nabla \times \boldsymbol{B}) \times \boldsymbol{B}, \tag{6.25}$$

$$\frac{\partial s_1}{\partial t} = [\ldots] + \frac{1}{\rho_0 T_0}\left(\frac{\eta}{4\pi}|\nabla \times \boldsymbol{B}|^2\right), \tag{6.26}$$

$$\frac{\partial \boldsymbol{B}}{\partial t} = \nabla \times (\boldsymbol{v} \times \boldsymbol{B}) - \nabla \times (\eta \nabla \times \boldsymbol{B}), \tag{6.27}$$

For the sake of numerical convenience, the right-hand-side of the equation of motion is expressed in a flux form,

$$\begin{aligned} & -\frac{\nabla p_1}{\rho_0} - \frac{\rho_1}{\rho_0} g \boldsymbol{e}_r + \frac{1}{\rho_0}\nabla \cdot \boldsymbol{\mathcal{D}} + \frac{1}{4\pi\rho_0}(\nabla \times \boldsymbol{B}) \times \boldsymbol{B} \\ = \; & -\nabla\left(\frac{p_1 + B^2/8\pi}{\rho_0}\right) + \left(\frac{B^2/8\pi}{p_0} + \frac{s_1}{c_v}\right)\frac{g}{\gamma}\boldsymbol{e}_r + \frac{1}{\rho_0}\nabla \cdot \left(\boldsymbol{\mathcal{D}} + \frac{\boldsymbol{BB}}{4\pi}\right). \end{aligned} \tag{6.28}$$

Here, the relation of the background hydrostatic balance is used,

$$\frac{1}{\rho_0}\frac{\partial \rho_0}{\partial r} + \frac{\rho_0}{p_0}\frac{g}{\gamma} = 0. \tag{6.29}$$

Note that the Lorentz force is decomposed into the magnetic pressure gradient and tension force,

$$(\nabla \times \boldsymbol{B}) \times \boldsymbol{B} = -\nabla\left(\frac{B^2}{2}\right) - \nabla \cdot (\boldsymbol{BB}) - (\nabla \cdot \boldsymbol{B})\boldsymbol{B}. \tag{6.30}$$

Here, the last term represents the artificial Lorentz force resulting from the numerical error of $\nabla \cdot \boldsymbol{B}$ in direction parallel to the magnetic field.

6.5.2 Divergence B cleaning

In order to minimize the numerical error related to the divergence of the magnetic field, the hyperbolic divergence cleaning method (9-wave method) suggested by Dedner et al. (2002) is adopted. In addition to the common set of the basic equations, we also solve the following equation coupled with the modified induction equation as

$$\frac{\partial \boldsymbol{B}}{\partial t} = -\nabla \cdot (\boldsymbol{vB} - \boldsymbol{Bv} + \psi \boldsymbol{I}) + (\text{diffusion}) \tag{6.31}$$

$$\frac{\partial \psi}{\partial t} = -c_{\rm d}^2(\nabla \cdot \boldsymbol{B}) - \frac{\psi}{\tau}. \tag{6.32}$$

Here, a scalar potential ψ is introduced to remove the divergence error and is initially set to zero. Due to the numerical error of ($\nabla \cdot \boldsymbol{B} \neq 0$), a potential ψ immediately emerges

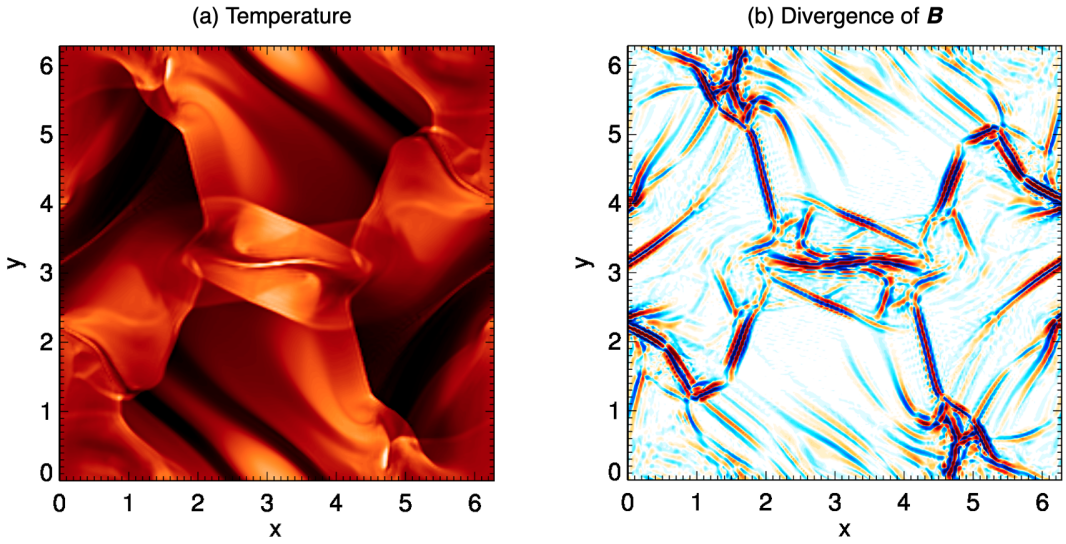

Figure 6.9: Results of the Orszag-Tang vortex problem. Shown are (a) the temperature and (b) the numerical error of the magnetic field's divergence $\nabla \cdot \boldsymbol{B}$.

which will soon disappear with a typical damping time-scale τ. Let us neglect magnetic diffusion for simplicity. We can eliminate $\boldsymbol{v}$ and $\boldsymbol{B}$ to get the so-called telegraph equations for ψ and $\nabla \cdot \boldsymbol{B}$,

$$\frac{\partial^2}{\partial t^2}\psi = c_\mathrm{d}^2 \nabla^2 \psi - \frac{1}{\tau}\frac{\partial \psi}{\partial t}, \tag{6.33}$$

$$\frac{\partial^2}{\partial t^2}(\nabla \cdot \boldsymbol{B}) = c_\mathrm{d}^2 \nabla^2 (\nabla \cdot \boldsymbol{B}) - \frac{1}{\tau}(\nabla \cdot \boldsymbol{B}). \tag{6.34}$$

Therefore, it is implied that both ψ and $\nabla \cdot \boldsymbol{B}$ evolve based on the same telegraph equation. c_d sets the propagation speed of the divergence error and given by the maximum propagation speed of information allowed, i.e., $c_d = c_\mathrm{max} = \max[C_s, C_A]$. The damping time scale is given by

$$\tau = \frac{\Delta t}{\ln(1/0.9)}, \tag{6.35}$$

so that the error is suppressed by 10% every time step. We solve the Orszag-Tang Vortex Problem (Orszag and Tang 1979) to check whether or not the cleaning properly works as shown in Fig. 6.9.

7 Summary and outlook

7.1 Summary of results

In this thesis, we have developed numerical models of the solar convection zone in several different regimes and demonstrated that these codes can be used to study the properties of low-frequency vorticity modes in the Sun. Our major findings are summarized as follows:

Linear / hydrodynamic regime:

- The dispersion relations and eigenfunctions of the equatorial Rossby modes, columnar convective modes, and high-latitude modes are obtained for the first time with the realistic background model of the Sun.
- The *mixed* modes between the equatorial Rossby modes with one radial node ($n = 1$) and the north-south anti-symmetric columnar convective modes are newly discovered. This mode mixing between the two oppositely-propagating vorticity modes can be understood in analogous to the Yanai waves (mixed Rossby-gravity waves) (Matsuno 1966).
- With moderate diffusivities included, $n = 0$ equatorial Rossby modes tend to be confined near the base of the convection zone and the surface eigenfunctions deviate from the sectoral form. This implies that the observed Rossby modes on the Sun are likely $n = 1$ modes (a part of the mixed modes) rather than $n = 0$ modes as normally assumed.
- When the latitudinal entropy gradient is taken into account, we find that the topographic Rossby waves become baroclinically unstable. The eigenfunctions and dispersion relations of the baroclinically-unstable modes agree nicely with observations of the high-latitude modes on the Sun (Gizon et al. 2021).

Nonlinear (convecting) / hydrodynamic:

- The mode-by-mode analysis of equatorial modes in the solar-like rotating convection simulation has been reported. Columnar convective modes are unambiguously identified in the surface longitudinal velocity power spectrum. They are responsible for about 80% of the required luminosity and angular momentum transport.
- Although weak in amplitudes compared to the columnar convective modes, we also successfully identify the equatorial Rossby modes with no radial node ($n = 0$). They are confined near the base of the convection zone. Near the surface, we robustly

confirm the existence of the mixed modes, as predicted by the linear analysis. Our analysis has shown that, owing to the mode mixing, the equatorial Rossby modes can be partially convective and contribute to the net angular momentum transport (a few percent of what is required).

Nonlinear (non-convecting) / hydrodynamic regime:

- When the convection zone is sufficiently baroclinic (.i.e. the latitudinal entropy gradient is large enough) a baroclinic instability occurs. This leads to a reduction of the latitudinal entropy gradient which will decrease the amount of differential rotation. In this way, the baroclinic instability might regulate the amplitude of differential rotation of the Sun. The latitudinal temperature difference required for the instability to occur is $7 - 8$ K. This is in the range required to produce the Sun's differential rotation.
- The spatial structure and the propagation frequencies of the baroclinic modes agree very well with the observations. The heat and angular momentum transport of the baroclinically-unstable modes are significant ingredients in the solar convection zone dynamics.

Nonlinear (non-conevcting) / magnetohydrodyanmic regime:

- The simulation reproduces many large-scale observational flow and magnetic features such as solar-like differential rotation, single-cell meridional circulation, 11-yr magnetic cycles, equatorward migration of the activity belts, and torsional oscillations at low and high-latitude branches.
- The BMRs emerged at the surface drive strong non-axisymmetric flows via the Lorentz force. The entropy perturbations associated to the BMRs become positive due to the turbulent diffusive heating, which geostrophically induces the low-latitude branch of the torsional oscillation.
- The equatorial Rossby modes are confirmed in the simulated power spectra at the surface. The extracted eigenfunction (real part) shows a similar latitudinal variation to the observations, i.e., sign changes at middle latitudes, which is caused by the viscous critical layer.

7.2 Discussions and outlook

Here we discuss the current status of the convective conundrum as well as some insights obtained from our studies. We also give our outlook for the future.

7.2.1 Missing columnar convective modes

As repeatedly emphasized throughout the thesis, the columnar convective modes play crucial roles in the solar convection zone dynamics in the numerical models. Various numerical simulations have them as the dominant convective pattern at low latitudes (where

they are commonly known as 'banana' cells) where they significantly contribute to the net angular momentum and enthalpy flux transport (e.g., Miesch et al. 2008, Matilsky et al. 2020, see also Chapter 4). However, the observations still have difficulties in detecting them, e.g. in the velocity spectra at the solar surface. In fact, it is reported in Chapter 2 that there is no excess power near the theoretical dispersion relation of $n = 0$ columnar convective modes in the observational spectrum of the north-south symmetric longitudinal flows (Gizon et al. 2021). Although some velocity power can be seen with the associated velocity amplitude of about $0.4 - 0.7$ m s^{-1} at frequencies lower than those of $n = 0$ columnar convective modes (slightly prograde with respect to the Carrington frame), it still remains uncertain whether these observed signals are from the columnar convective modes or from the flows around the active regions (denoted by purple shades in Fig. 2.6). However, even if we assume they are columnar convective modes in nature, the associated kinetic energy might be insufficient to explain the required Reynolds stress to maintain the solar differential rotation.

We find that the columnar convective modes with north-south antisymmetric longitudinal velocity are essentially mixed with the equatorial Rossby modes (§ 3.3.1.2) and these mixed modes can transport a significant fraction of enthalpy flux. These "mixed" modes also exist in our nonlinear convection simulations (§ 4.5.3). This is a promising result in terms of convective conundrum because the conventional (north-south v_ϕ-symmetric) columnar convective modes might not be crucial for the Sun's convection zone dynamics if the newly-discovered "mixed" modes have sufficient amplitudes. To determine what amplitudes are sufficient requires a better understanding of the modes: for example, how are they modified by a radial dependent superadiabaticity and/or turbulent viscosity inside the Sun's convection zone.

7.2.2 Constraining unknowns in the Sun

Superadiabaticity

There are many crucial yet unknown parameters in the solar convection zone that make the understanding the Sun's large-scale convection and dynamo difficult. The superadiabaticity δ is the most famous example among them. One of the most striking manifestations of the convective conundrum is that large-scale convective amplitudes are overestimated in numerical simulations and mixing-length models. This is likely due to the overestimated superadiabaticity δ in the numerical models. In fact, the convective amplitudes can be substantially suppressed if the superadiabaticity is substantially small than currently believed in the upper half and/or the mean stratification is weakly subadiabatic in the lower half of the convection zone (e.g., Brandenburg 2016, Bekki et al. 2017, Käpylä et al. 2017).

In this thesis (Chapter 2), we have carefully examined the δ-dependence of the eigenfunction of the high-latitude inertial modes, and derived an observational constraint of $\delta \leq 2 \times 10^{-7}$ in the convection zone. Although this is a first attempt to constrain δ using the observations of the inertial modes in the Sun, it is still a relevant constraint: typical values used in convection models are of the order of $\delta \approx 10^{-6}$. We also find that the frequencies and eigenfunctions of the other inertial modes (such as mixed modes and critical-latitude modes) as well are sensitive to a small change in δ, so this estimate should

be able to be improved in the future.

In the linear eigenmode model reported in Chapter 2, we have assumed a spatially uniform superadiabaticity values throughout the convection zone for simplicity. However, recent numerical studies suggest that δ can substantially vary in the convection zone; weakly subadiabatic in the lower half, weakly superadiabatic in the bulk, and strongly superadiabatic near the surface. The mode frequencies and eigenfunctions can be modified when the radial dependence is taken into account, which needs to be checked in the future work.

The superadiabaticity δ will directly impact the excitation process of the solar inertial modes, especially the columnar convective and mixed modes: As δ becomes large, the convective modes become more and more efficiently excited, and their amplitudes become large. On the other hand, the quasi-toroidal modes such as $(n = 0)$ equatorial Rossby modes are almost unaffected by the change in δ. Therefore, it is expected that the amplitudes of the inertial modes, as well as the mode frequencies and eigenfunctions, can potentially be used to infer the superadiabaticity. It will be a promising future work to conduct a systematic study of fully-nonlinear simulations of rotating convection with varying model parameters. Figure 7.1 shows the preliminary results (radial velocity and differential rotation) of this parameter survey where the luminosity and rotation rate are changed (therefore superadiabaticity δ and Rossby number Ro are varied, respectively).

Turbulent diffusivities

Turbulent diffusivities are important ingredients in the models of solar large-scale convection and dynamo (e.g., Charbonneau 2020). Generally, turbulent viscous (ν), thermal (κ), and magnetic (η) diffusivities are expected to be comparable assuming that the momentum, entropy, and magnetic fields should be mixed by the same turbulence eddies. In the mean-field theory (e.g., Moffatt 1978), they can be expressed as

$$\nu \approx \kappa \approx \eta \approx \frac{\tau_c}{3}\langle v_c^2 \rangle, \tag{7.1}$$

where τ_c is the convective turnover time and v_c is the convective speed. Thus, the observational constraint on the diffusivity provides an estimate of the large-scale convective flows inside the Sun.

In this thesis, we find that the turbulent diffusivities significantly affect the mode properties of some inertial modes, particularly critical-latitude modes. The critical-latitude modes owe their existence to the differential rotation and are localized near the viscous critical latitudes. By carefully comparing their eigenfunctions (spatial extent and tilt of the spiral) with the observations, we derived a constraint of $\nu \approx \kappa \leq 10^{12}$ cm^2 s^{-1}. The constraint on ν provided by this thesis (an upper limit of about 10^{12} cm^2 s^{-1}) is relevant because it is about one order of magnitude smaller than the conventional mixing-length estimate, $1 - 2 \times 10^{13}$ cm^2 s^{-1} in the bulk of the convection zone (e.g., Muñoz-Jaramillo et al. 2011). Because of Eq. (7.1), our measurement of the turbulent viscosity implies that mixing-length models overestimate the turbulent kinetic energy inside the convection zone by at least a factor of 10. This implies that the convective velocity power in numerical simulations (blue curve in Fig. 1.9) is overstimated about a factor of 10 if we assume that the results of numerical simulations are consistent with the mixing-length

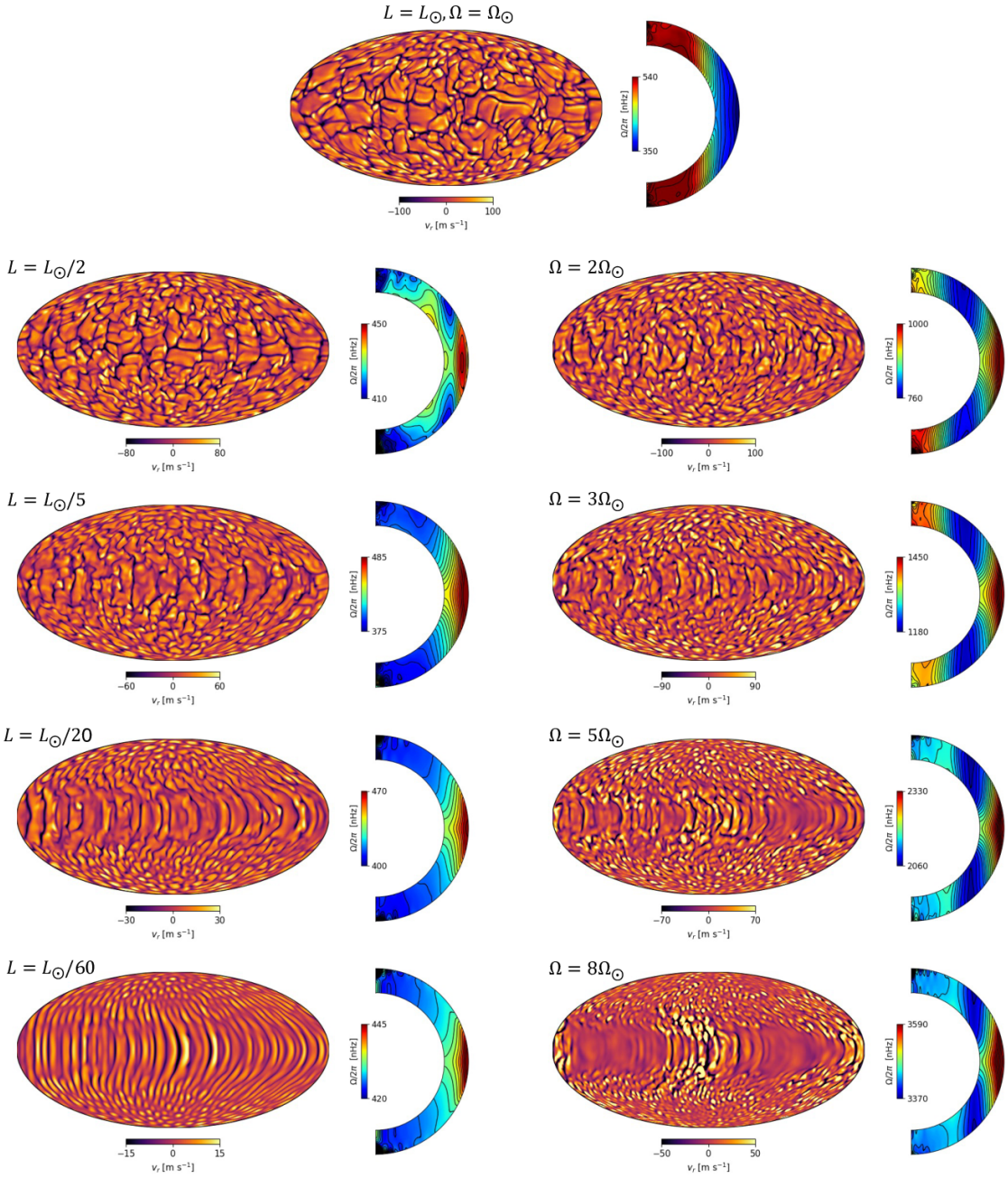

Figure 7.1: Snapshots of the radial velocity at the surface and the time-averaged differential rotation profiles for different values of luminosity L and rotation rate Ω. (Left) The simulations where the luminosity is reduced by a factor of 2, 5, 20, and 60 while the rotation rate is fixed to the solar value ($\Omega_\odot$). (Right) The simulations where the rotation rate is increased by a factor of 2, 3, 5, and 8 while the luminosity is fixed to the solar value ($L_\odot$). The same solar-like background is used for all calculations.

model. The inferred convetive velocity power based on our turbulent diffusivity estimate lies in between the numerical simulation of Miesch et al. (2008) and the time-distance helioseismic analysis of Hanasoge et al. (2012).

Baroclinicity

Global-helioseismology has revealed that the solar differential rotation deviates from the Taylor-Proudman's state, i.e., it should be in thermal wind balance (Schou et al. 1998). The baroclinicity in the Sun's convection zone, measured by latitudinal entropy (or temperature) variation, is conventionally estimated from the observed differential rotation based on the thermal wind balance as (Rempel 2005, Miesch et al. 2006, Brun et al. 2011)

$$\frac{g}{c_p}\frac{\partial s_0}{\partial \theta} \approx r^2 \sin\theta \frac{\partial \Omega^2}{\partial z}. \tag{7.2}$$

This gives the associated latitudinal temperature variation of about $5-10$ K in the convection zone, which is too small to be directly measured. The physical origin of this latitudinal entropy (or temperature) variation remains elusive; whether it comes due to the weakly subadiabatic tachocline (Rempel 2005), anisotropic turbulent heat transport (Kitchatinov and Ruediger 1995), small-scale magnetic effects (Hotta 2018), or magnetorotational instability near the tachocline (Masada 2011).

Note that the Eq. (7.2) is derived under the assumptions that the Reynolds stress, Lorentz forces, and viscous forces are all small relative to the Coriolis forces. However, some of these assumptions are non-trivial: Therefore, it is worth obtaining an independent observational constraint on the baroclinicity in the convection zone. In this thesis, we have demonstrated that the high-latitude inertial modes are essentially excited by baroclinic instability, and thus, these modes can be used to estimate the latitudinal entropy variation in the Sun in the near future.

Furthermore, we have suggested that the latitudinal entropy variation (whatever its physical origin is) can have a substantial impact on the solar convection zone dynamics. Baroclinic instability likely occurs in the convection zone, as inferred from the observations of the high-latitude inertial modes, which regulates the baroclinicity and controls the amplitude of differential rotation. This effect can only be captured in three-dimensional models as presented in Chapter 5. Therefore, results obtained by the conventional two-dimensional mean-field models of the solar differential rotation and meridional circulation can be substantially affected, which needs to be carefully examined in the future.

Bibliography

Aerts, C., 2021, Probing the interior physics of stars through asteroseismology, Rev. Mod. Phys., 93, 015001

Aerts, C., Christensen-Dalsgaard, J., Kurtz, D. W., 2010, Asteroseismology, Springer Berlin Heidelberg

Alvan, L., Strugarek, A., Brun, A. S., Mathis, S., Garcia, R. A., 2015, Characterizing the propagation of gravity waves in 3D nonlinear simulations of solar-like stars, A&A, 581, A112

Anders, E. H., Lecoanet, D., Brown, B. P., 2019, Entropy Rain: Dilution and Compression of Thermals in Stratified Domains, ApJ, 884, 65

Anderson, E., Bai, Z., Bischof, C., Blackford, S., Demmel, J., Dongarra, J., Du Croz, J., Greenbaum, A., Hammarling, S., McKenney, A., Sorensen, D., 1999, LAPACK Users' Guide, Society for Industrial and Applied Mathematics, Philadelphia, PA

Appourchaux, T., Belkacem, K., Broomhall, A. M., Chaplin, W. J., Gough, D. O., Houdek, G., Provost, J., Baudin, F., Boumier, P., Elsworth, Y., García, R. A., Andersen, B. N., Finsterle, W., Fröhlich, C., Gabriel, A., Grec, G., Jiménez, A., Kosovichev, A., Sekii, T., Toutain, T., Turck-Chièze, S., 2010, The quest for the solar g modes, A&A Rev., 18, 197–277

Appourchaux, T., Boumier, P., Leibacher, J. W., Corbard, T., 2018, Searching for g modes. I. A new calibration of the GOLF instrument, A&A, 617, A108

Augustson, K., Brun, A. S., Miesch, M., Toomre, J., 2015, Grand Minima and Equatorward Propagation in a Cycling Stellar Convective Dynamo, ApJ, 809, 149

Babcock, H. W., 1961, The Topology of the Sun's Magnetic Field and the 22-YEAR Cycle., ApJ, 133, 572

Balbus, S. A., Bonart, J., Latter, H. N., Weiss, N. O., 2009, Differential rotation and convection in the Sun, MNRAS, 400, 176–182

Baruteau, C., Rieutord, M., 2013, Inertial waves in a differentially rotating spherical shell, Journal of Fluid Mechanics, 719, 47–81

Basu, S., 2016, Global seismology of the Sun, Living Reviews in Solar Physics, 13, 2

Basu, S., Antia, H. M., 2010, Characteristics of Solar Meridional Flows during Solar Cycle 23, ApJ, 717, 488–495

Basu, S., Antia, H. M., Tripathy, S. C., 1999, Ring Diagram Analysis of Near-Surface Flows in the Sun, ApJ, 512, 458–470

Bekki, Y., Yokoyama, T., 2017, Double-cell-type Solar Meridional Circulation Based on a Mean-field Hydrodynamic Model, ApJ, 835, 9

Bekki, Y., Hotta, H., Yokoyama, T., 2017, Convective Velocity Suppression via the Enhancement of the Subadiabatic Layer: Role of the Effective Prandtl Number, ApJ, 851, 74

Bekki, Y., Cameron, R. H., Gizon, L., 2022a, Theory of solar oscillations in the inertial frequency range: Amplitudes of equatorial modes from a nonlinear rotating convection simulation, A&A, 666, A135

Bekki, Y., Cameron, R. H., Gizon, L., 2022b, Theory of solar oscillations in the inertial frequency range: Linear modes of the convection zone, A&A, 662, A16

Bessolaz, N., Brun, A. S., 2011, Hunting for Giant Cells in Deep Stellar Convective Zones Using Wavelet Analysis, ApJ, 728, 115

Bogart, R. S., Baldner, C., Basu, S., Haber, D. A., Rabello-Soares, M. C., 2011a, HMI ring diagram analysis I. The processing pipeline, in GONG-SoHO 24: A New Era of Seismology of the Sun and Solar-Like Stars, vol. 271 of Journal of Physics Conference Series, p. 012008

Bogart, R. S., Baldner, C., Basu, S., Haber, D. A., Rabello-Soares, M. C., 2011b, HMI ring diagram analysis II. Data products, in GONG-SoHO 24: A New Era of Seismology of the Sun and Solar-Like Stars, vol. 271 of Journal of Physics Conference Series, p. 012009

Bogart, R. S., Baldner, C. S., Basu, S., 2015, Evolution of Near-surface Flows Inferred from High-resolution Ring-diagram Analysis, ApJ, 807, 125

Böhm-Vitense, E., 1958, Über die Wasserstoffkonvektionszone in Sternen verschiedener Effektivtemperaturen und Leuchtkräfte. Mit 5 Textabbildungen, ZA, 46, 108

Bondi, H., Lyttleton, R. A., 1953, On the dynamical theory of the rotation of the earth. ii. the effect of precession on the motion of the liquid core, Mathematical Proceedings of the Cambridge Philosophical Society, 49, 498–515

Böning, V. G. A., Roth, M., Jackiewicz, J., Kholikov, S., 2017, Inversions for Deep Solar Meridional Flow Using Spherical Born Kernels, ApJ, 845, 2

Brandenburg, A., 2016, Stellar Mixing Length Theory with Entropy Rain, ApJ, 832, 6

Braun, D. C., Fan, Y., 1998, Helioseismic Measurements of the Subsurface Meridional Flow, ApJL, 508, L105–L108

Brown, B. P., Browning, M. K., Brun, A. S., Miesch, M. S., Toomre, J., 2008, Rapidly Rotating Suns and Active Nests of Convection, ApJ, 689, 1354–1372

Brown, B. P., Browning, M. K., Brun, A. S., Miesch, M. S., Toomre, J., 2010, Persistent Magnetic Wreaths in a Rapidly Rotating Sun, ApJ, 711, 424–438

Brun, A. S., Toomre, J., 2002, Turbulent Convection under the Influence of Rotation: Sustaining a Strong Differential Rotation, ApJ, 570, 865–885

Brun, A. S., Miesch, M. S., Toomre, J., 2004, Global-Scale Turbulent Convection and Magnetic Dynamo Action in the Solar Envelope, ApJ, 614, 1073–1098

Brun, A. S., Miesch, M. S., Toomre, J., 2011, Modeling the Dynamical Coupling of Solar Convection with the Radiative Interior, ApJ, 742, 79

Bryan, G. H., 1889, The Waves on a Rotating Liquid Spheroid of Finite Ellipticity, Philosophical Transactions of the Royal Society of London Series A, 180, 187–219

Busse, F. H., 1970, Thermal instabilities in rapidly rotating systems., Journal of Fluid Mechanics, 44, 441–460

Busse, F. H., 2002, Convective flows in rapidly rotating spheres and their dynamo action, Physics of Fluids, 14, 1301–1314

Busse, F. H., Or, A. C., 1986, Convection in a rotating cylindrical annulus - Thermal Rossby waves, Journal of Fluid Mechanics, 166, 173–187

Caligari, P., Moreno-Insertis, F., Schussler, M., 1995, Emerging Flux Tubes in the Solar Convection Zone. I. Asymmetry, Tilt, and Emergence Latitude, ApJ, 441, 886

Callies, J., Ferrari, R., 2018, Baroclinic instability in the presence of convection, Journal of Physical Oceanography, 48, 45 – 60

Cameron, R., Schüssler, M., 2015, The crucial role of surface magnetic fields for the solar dynamo, Science, 347, 1333–1335

Cameron, R. H., Schüssler, M., 2012, Are the strengths of solar cycles determined by converging flows towards the activity belts?, A&A, 548, A57

Cameron, R. H., Schüssler, M., 2016, The turbulent diffusion of toroidal magnetic flux as inferred from properties of the sunspot butterfly diagram, A&A, 591, A46

Cameron, R. H., Schüssler, M., 2017, An update of Leighton's solar dynamo model, A&A, 599, A52

Cartan, M., 1922, Sur les petites oscillations d'une masse de fluide, Bull. Sci. Math., 46, 317–369

Charbonneau, P., 2020, Dynamo models of the solar cycle, Living Reviews in Solar Physics, 17, 4

Charbonneau, P., Dikpati, M., Gilman, P. A., 1999, Stability of the Solar Latitudinal Differential Rotation Inferred from Helioseismic Data, ApJ, 526, 523–537

Charney, J. G., 1947, The Dynamics of Long Waves in a Baroclinic Westerly Current., Journal of Atmospheric Sciences, 4, 136–162

Chatterjee, P., Nandy, D., Choudhuri, A. R., 2004, Full-sphere simulations of a circulation-dominated solar dynamo: Exploring the parity issue, A&A, 427, 1019–1030

Chen, F., Rempel, M., Fan, Y., 2017, Emergence of Magnetic Flux Generated in a Solar Convective Dynamo. I. The Formation of Sunspots and Active Regions, and The Origin of Their Asymmetries, ApJ, 846, 149

Chou, D.-Y., Sun, M.-T., Huang, T.-Y., Lai, S.-P., Chi, P.-J., Ou, K.-T., Wang, C.-C., Lu, J.-Y., Chu, A.-L., Niu, C.-S., Mu, T.-M., Chen, K.-R., Chou, Y.-P., Jimenez, A., Rabello-Soares, M. C., Chao, H., Ai, G., Wang, G.-P., Zirin, H., Marquette, W., Nenow, J., 1995, Taiwan Oscillation Network, Sol. Phys., 160, 237–243

Choudhuri, A. R., 2021, The meridional circulation of the Sun: Observations, theory and connections with the solar dynamo, Science China Physics, Mechanics, and Astronomy, 64, 239601

Choudhuri, A. R., Schussler, M., Dikpati, M., 1995, The solar dynamo with meridional circulation., A&A, 303, L29

Christensen-Dalsgaard, J., 2002, Helioseismology, Reviews of Modern Physics, 74, 1073–1129

Christensen-Dalsgaard, J., Dappen, W., Ajukov, S. V., Anderson, E. R., Antia, H. M., Basu, S., Baturin, V. A., Berthomieu, G., Chaboyer, B., Chitre, S. M., Cox, A. N., Demarque, P., Donatowicz, J., Dziembowski, W. A., Gabriel, M., Gough, D. O., Guenther, D. B., Guzik, J. A., Harvey, J. W., Hill, F., Houdek, G., Iglesias, C. A., Kosovichev, A. G., Leibacher, J. W., Morel, P., Proffitt, C. R., Provost, J., Reiter, J., Rhodes, Jr., E. J., Rogers, F. J., Roxburgh, I. W., Thompson, M. J., Ulrich, R. K., 1996a, The Current State of Solar Modeling, Science, 272, 1286–1292

Christensen-Dalsgaard, J., Dappen, W., Ajukov, S. V., Anderson, E. R., Antia, H. M., Basu, S., Baturin, V. A., Berthomieu, G., Chaboyer, B., Chitre, S. M., Cox, A. N., Demarque, P., Donatowicz, J., Dziembowski, W. A., Gabriel, M., Gough, D. O., Guenther, D. B., Guzik, J. A., Harvey, J. W., Hill, F., Houdek, G., Iglesias, C. A., Kosovichev, A. G., Leibacher, J. W., Morel, P., Proffitt, C. R., Provost, J., Reiter, J., Rhodes, E. J., J., Rogers, F. J., Roxburgh, I. W., Thompson, M. J., Ulrich, R. K., 1996b, The Current State of Solar Modeling, Science, 272, 1286–1292

Claverie, A., Isaak, G. R., McLeod, C. P., van der Raay, H. B., Roca Cortes, T., 1979, Solar structure from global studies of the 5-minute oscillation, Nature, 282, 591–594

Cossette, J.-F., Rast, M. P., 2016, Supergranulation as the Largest Buoyantly Driven Convective Scale of the Sun, ApJL, 829, L17

Cowling, T. G., 1933, The magnetic field of sunspots, MNRAS, 94, 39–48

Cowling, T. G., 1941, The non-radial oscillations of polytropic stars, MNRAS, 101, 367

Damiani, C., Cameron, R. H., Birch, A. C., Gizon, L., 2020, Rossby modes in slowly rotating stars: depth dependence in distorted polytropes with uniform rotation, A&A, 637, A65

Deardorff, J. W., 1972, Theoretical expression for the countergradient vertical heat flux, J. Geophys. Res., 77, 5900–5904

Dedner, A., Kemm, F., Kröner, D., Munz, C. D., Schnitzer, T., Wesenberg, M., 2002, Hyperbolic Divergence Cleaning for the MHD Equations, Journal of Computational Physics, 175, 645–673

Deubner, F. L., 1975, Observations of low wavenumber nonradial eigenmodes of the sun., A&A, 44, 371–375

Dikpati, M., Charbonneau, P., 1999, A Babcock-Leighton Flux Transport Dynamo with Solar-like Differential Rotation, ApJ, 518, 508–520

Dintrans, B., Ouyed, R., 2001, On Jupiter's inertial mode oscillations, A&A, 375, L47–L50

D'Silva, S., Choudhuri, A. R., 1993, A theoretical model for tilts of bipolar magnetic regions, A&A, 272, 621

Durney, B. R., 1999, The Taylor-Proudman Balance and the Solar Rotational Data, ApJ, 511, 945–957

Duvall, T. L., J., 1979, Large-scale solar velocity fields., Sol. Phys., 63, 3–15

Duvall, T. L., J., Harvey, J. W., 1983, Observations of solar oscillations of low and intermediate degree, Nature, 302, 24–27

Duvall, T. L., J., Dziembowski, W. A., Goode, P. R., Gough, D. O., Harvey, J. W., Leibacher, J. W., 1984, Internal rotation of the Sun, Nature, 310, 22–25

Duvall, T. L., J., Kosovichev, A. G., Scherrer, P. H., Bogart, R. S., Bush, R. I., de Forest, C., Hoeksema, J. T., Schou, J., Saba, J. L. R., Tarbell, T. D., Title, A. M., Wolfson, C. J., Milford, P. N., 1997, Time-Distance Helioseismology with the MDI Instrument: Initial Results, Sol. Phys., 170, 63–73

Duvall, Jr., T. L., Jefferies, S. M., Harvey, J. W., Pomerantz, M. A., 1993, Time-distance helioseismology, Nature, 362, 430–432

Eady, E. T., 1949, Long waves and cyclone waves, Tellus, 1, 33–52

Elliott, J. R., Miesch, M. S., Toomre, J., 2000, Turbulent Solar Convection and Its Coupling with Rotation: The Effect of Prandtl Number and Thermal Boundary Conditions on the Resulting Differential Rotation, ApJ, 533, 546–556

Elsworth, Y., Howe, R., Isaak, G. R., McLeod, C. P., Miller, B. A., New, R., Wheeler, S. J., Gough, D. O., 1995, Slow rotation of the Sun's interior, Nature, 376, 669–672

Ertel, H., 1942, Ein neuer hydrodynamischer wirbelsatz, Met. Z., 59, 277–281

Evonuk, M., 2008, The Role of Density Stratification in Generating Zonal Flow Structures in a Rotating Fluid, ApJ, 673, 1154–1159

Evonuk, M., Samuel, H., 2012, Simulating rotating fluid bodies: When is vorticity generation via density-stratification important?, Earth and Planetary Science Letters, 317, 1–7

Fan, Y., 2009, Magnetic Fields in the Solar Convection Zone, Living Reviews in Solar Physics, 6, 4

Fan, Y., Fang, F., 2014, A Simulation of Convective Dynamo in the Solar Convective Envelope: Maintenance of the Solar-like Differential Rotation and Emerging Flux, ApJ, 789, 35

Fan, Y., Fisher, G. H., Deluca, E. E., 1993, The Origin of Morphological Asymmetries in Bipolar Active Regions, ApJ, 405, 390

Featherstone, N. A., Hindman, B. W., 2016a, The Spectral Amplitude of Stellar Convection and Its Scaling in the High-Rayleigh-number Regime, ApJ, 818, 32

Featherstone, N. A., Hindman, B. W., 2016b, The Emergence of Solar Supergranulation as a Natural Consequence of Rotationally Constrained Interior Convection, ApJ, 830, L15

Featherstone, N. A., Miesch, M. S., 2015, Meridional Circulation in Solar and Stellar Convection Zones, ApJ, 804, 67

Fournier, D., Gizon, L., Hyest, L., 2022, Viscous inertial modes on a differentially rotating sphere: Comparison with solar observations, A&A, 664, A6

García, R. A., Turck-Chièze, S., Jiménez-Reyes, S. J., Ballot, J., Pallé, P. L., Eff-Darwich, A., Mathur, S., Provost, J., 2007, Tracking Solar Gravity Modes: The Dynamics of the Solar Core, Science, 316, 1591

Gastine, T., Wicht, J., Aurnou, J. M., 2013, Zonal flow regimes in rotating anelastic spherical shells: An application to giant planets, Icarus, 225, 156–172

Gastine, T., Yadav, R. K., Morin, J., Reiners, A., Wicht, J., 2014, From solar-like to antisolar differential rotation in cool stars, MNRAS, 438, L76–L80

Ghizaru, M., Charbonneau, P., Smolarkiewicz, P. K., 2010, Magnetic Cycles in Global Large-eddy Simulations of Solar Convection, ApJL, 715, L133–L137

Giles, P. M., Duvall, T. L., Scherrer, P. H., Bogart, R. S., 1997, A subsurface flow of material from the Sun's equator to its poles, Nature, 390, 52–54

Gilman, P., Dikpati, M., 2014, Baroclinic Instability in the Solar Tachocline, ApJ, 787, 60

Gilman, P. A., 1975, Linear Simulations of Boussinesq Convection in a Deep Rotating Spherical Shell., Journal of Atmospheric Sciences, 32, 1331–1352

Gilman, P. A., 1986, The solar dynamo: observations and theories of solar convection, global circulation, and magnetic fields., in Physics of the Sun. Volume 1, (Eds.) P. A. Sturrock, T. E. Holzer, D. M. Mihalas, R. K. Ulrich, vol. 1, pp. 95–160

Gilman, P. A., 2015, Effect of Toroidal Fields On Baroclinic Instability in the Solar Tachocline, ApJ, 801, 22

Gilman, P. A., 2016, Baroclinic Instability in the Solar Tachocline. II. The Eady Problem, ApJ, 818, 170

Gilman, P. A., 2017, Baroclinic Instability in the Solar Tachocline for Continuous Vertical Profiles of Rotation, Effective Gravity, and Toroidal Field, ApJ, 842, 130

Gilman, P. A., Glatzmaier, G. A., 1981, Compressible convection in a rotating spherical shell. I - Anelastic equations. II - A linear anelastic model. III - Analytic model for compressible vorticity waves, ApJS, 45, 335–388

Gizon, L., Birch, A. C., 2002, Time-Distance Helioseismology: The Forward Problem for Random Distributed Sources, ApJ, 571, 966–986

Gizon, L., Birch, A. C., 2005, Local Helioseismology, Living Reviews in Solar Physics, 2, 6

Gizon, L., Birch, A. C., 2012, Helioseismology challenges models of solar convection, Proceedings of the National Academy of Science, 109, 11 896–11 897

Gizon, L., Rempel, M., 2008, Observation and Modeling of the Solar-Cycle Variation of the Meridional Flow, Sol. Phys., 251, 241–250

Gizon, L., Duvall, T. L., J., Larsen, R. M., 2001, Probing Surface Flows and Magnetic Activity with Time-Distance Helioseismology, in Recent Insights into the Physics of the Sun and Heliosphere: Highlights from SOHO and Other Space Missions, (Eds.) P. Brekke, B. Fleck, J. B. Gurman, vol. 203, p. 189

Gizon, L., Duvall, T. L., Schou, J., 2003, Wave-like properties of solar supergranulation, Nature, 421, 43–44

Gizon, L., Birch, A. C., Spruit, H. C., 2010, Local Helioseismology: Three-Dimensional Imaging of the Solar Interior, ARA&A, 48, 289–338

Gizon, L., Cameron, R. H., Pourabdian, M., Liang, Z.-C., Fournier, D., Birch, A. C., Hanson, C. S., 2020a, Meridional flow in the Sun's convection zone is a single cell in each hemisphere, Science, 368, 1469–1472

Gizon, L., Fournier, D., Albekioni, M., 2020b, Effect of latitudinal differential rotation on solar Rossby waves: Critical layers, eigenfunctions, and momentum fluxes in the equatorial β plane, A&A, 642, A178

Gizon, L., Cameron, R. H., Bekki, Y., Birch, A. C., Bogart, R. S., Brun, A. S., Damiani, C., Fournier, D., Hyest, L., Jain, K., Lekshmi, B., Liang, Z.-C., Proxauf, B., 2021, Solar inertial modes: Observations, identification, and diagnostic promise, A&A, 652, L6

Glatzmaier, G., Evonuk, M., Rogers, T., 2009, Differential rotation in giant planets maintained by density-stratified turbulent convection, Geophysical and Astrophysical Fluid Dynamics, 103, 31–51

Glatzmaier, G. A., 1984, Numerical simulations of stellar convective dynamos. I - The model and method, Journal of Computational Physics, 55, 461–484

Glatzmaier, G. A., Gilman, P. A., 1981, Compressible Convection in a Rotating Spherical Shell - Part Three - Analytic Model for Compressible Vorticity Waves, ApJS, 45, 381

Goddard, C. R., Birch, A. C., Fournier, D., Gizon, L., 2020, Predicting frequency changes of global-scale solar Rossby modes due to solar cycle changes in internal rotation, A&A, 640, L10

Goldreich, P., Keeley, D. A., 1977, Solar seismology. II. The stochastic excitation of the solar p-modes by turbulent convection., ApJ, 212, 243–251

Gough, D. O., 1984, Towards a solar model, Mem. Soc. Astron. Italiana, 55, 13

Grec, G., Fossat, E., Pomerantz, M., 1980, Solar oscillations: full disk observations from the geographic South Pole, Nature, 288, 541–544

Grec, G., Fossat, E., Pomerantz, M. A., 1983, Full-Disk Observations of Solar Oscillations from the Geographic South-Pole - Latest Results, Sol. Phys., 82, 55–66

Green, J. S. A., 1970, Transfer properties of the large-scale eddies and the general circulation of the atmosphere, Quarterly Journal of the Royal Meteorological Society, 96, 157–185

Greenspan, H., Batchelor, C., Ablowitz, M., Davis, S., Iserles, U., Hinch, E., Ockendon, J., Olver, P., 1968, The Theory of Rotating Fluids, Cambridge Monographs on Mechanics, Cambridge University Press

Greer, B. J., Hindman, B. W., Featherstone, N. A., Toomre, J., 2015, Helioseismic Imaging of Fast Convective Flows throughout the Near-surface Shear Layer, ApJL, 803, L17

Grisouard, N., Staquet, C., Pairaud, I., 2008, Numerical simulation of a two-dimensional internal wave attractor, Journal of Fluid Mechanics, 614, 1

Guenel, M., Baruteau, C., Mathis, S., Rieutord, M., 2016, Tidal inertial waves in differentially rotating convective envelopes of low-mass stars. I. Free oscillation modes, A&A, 589, A22

Guenther, D. B., Gilman, P. A., 1985, Inertial oscillations in the solar convection zone. I - Spherical shell model, ApJ, 295, 195–212

Guerrero, G., Smolarkiewicz, P. K., Kosovichev, A. G., Mansour, N. N., 2013, Differential Rotation in Solar-like Stars from Global Simulations, ApJ, 779, 176

Haber, D. A., Hindman, B. W., Toomre, J., Bogart, R. S., Thompson, M. J., Hill, F., 2000, Solar shear flows deduced from helioseismic dense-pack samplings of ring diagrams, Sol. Phys., 192, 335–350

Hale, G. E., Ellerman, F., Nicholson, S. B., Joy, A. H., 1919, The Magnetic Polarity of Sun-Spots, ApJ, 49, 153

Hanasoge, S., Mandal, K., 2019, Detection of Rossby Waves in the Sun using Normal-mode Coupling, ApJ, 871, L32

Hanasoge, S., Gizon, L., Sreenivasan, K. R., 2016, Seismic Sounding of Convection in the Sun, Annual Review of Fluid Mechanics, 48, 191–217

Hanasoge, S. M., Duvall, T. L., Sreenivasan, K. R., 2012, Anomalously weak solar convection, Proceedings of the National Academy of Science, 109, 11 928–11 932

Hanasoge, S. M., Hotta, H., Sreenivasan, K. R., 2020, Turbulence in the Sun is suppressed on large scales and confined to equatorial regions, Science Advances, 6, 9639

Hanson, C. S., Gizon, L., Liang, Z.-C., 2020, Solar Rossby waves observed in GONG++ ring-diagram flow maps, A&A, 635, A109

Hanson, C. S., Hanasoge, S., Sreenivasan, K. R., 2022, Discovery of high-frequency retrograde vorticity waves in the Sun, Nature Astronomy, 6, 708–714

Hathaway, D. H., 1996, Doppler Measurements of the Sun's Meridional Flow, ApJ, 460, 1027

Hathaway, D. H., Rightmire, L., 2010, Variations in the Sun's Meridional Flow over a Solar Cycle, Science, 327, 1350

Hathaway, D. H., Upton, L., 2014, The solar meridional circulation and sunspot cycle variability, Journal of Geophysical Research (Space Physics), 119, 3316–3324

Hathaway, D. H., Upton, L. A., 2021, Hydrodynamic Properties of the Sun's Giant Cellular Flows, ApJ, 908, 160

Hathaway, D. H., Upton, L., Colegrove, O., 2013, Giant Convection Cells Found on the Sun, Science, 342, 1217–1219

Hazra, G., Karak, B. B., Choudhuri, A. R., 2014, Is a Deep One-cell Meridional Circulation Essential for the Flux Transport Solar Dynamo?, ApJ, 782, 93

Hill, F., 1988, Rings and Trumpets—Three-dimensional Power Spectra of Solar Oscillations, ApJ, 333, 996

Hindman, B. W., Jain, R., 2022, Radial Trapping of Thermal Rossby Waves within the Convection Zones of Low-mass Stars, ApJ, 932, 68

Hindman, B. W., Featherstone, N. A., Julien, K., 2020, Morphological Classification of the Convective Regimes in Rotating Stars, ApJ, 898, 120

Holton, J. R., Hakim, G. J., 2013, Chapter 7 - baroclinic development, in An Introduction to Dynamic Meteorology (Fifth Edition), (Eds.) J. R. Holton, G. J. Hakim, pp. 213 – 254, Academic Press, Boston, fifth edition edn.

Hotta, H., 2017, Solar Overshoot Region and Small-scale Dynamo with Realistic Energy Flux, ApJ, 843, 52

Hotta, H., 2018, Breaking Taylor-Proudman Balance by Magnetic Fields in Stellar Convection Zones, ApJ, 860, L24

Hotta, H., Kusano, K., 2021, Solar differential rotation reproduced with high-resolution simulation, Nature Astronomy, 5, 1100–1102

Hotta, H., Rempel, M., Yokoyama, T., Iida, Y., Fan, Y., 2012, Numerical calculation of convection with reduced speed of sound technique, A&A, 539, A30

Hotta, H., Rempel, M., Yokoyama, T., 2014a, High-resolution Calculations of the Solar Global Convection with the Reduced Speed of Sound Technique. I. The Structure of the Convection and the Magnetic Field without the Rotation, ApJ, 786, 24

Hotta, H., Rempel, M., Yokoyama, T., 2014b, High-resolution Calculations of the Solar Global Convection with the Reduced Speed of Sound Technique. I. The Structure of the Convection and the Magnetic Field without the Rotation, ApJ, 786, 24

Hotta, H., Rempel, M., Yokoyama, T., 2015a, High-resolution Calculation of the Solar Global Convection with the Reduced Speed of Sound Technique. II. Near Surface Shear Layer with the Rotation, ApJ, 798, 51

Hotta, H., Rempel, M., Yokoyama, T., 2015b, Efficient Small-scale Dynamo in the Solar Convection Zone, ApJ, 803, 42

Hotta, H., Rempel, M., Yokoyama, T., 2015c, High-resolution Calculation of the Solar Global Convection with the Reduced Speed of Sound Technique. II. Near Surface Shear Layer with the Rotation, ApJ, 798, 51

Hotta, H., Rempel, M., Yokoyama, T., 2016, Large-scale magnetic fields at high Reynolds numbers in magnetohydrodynamic simulations, Science, 351, 1427–1430

Howard, R., Labonte, B. J., 1980, The sun is observed to be a torsional oscillator with a period of 11 years, ApJ, 239, L33–L36

Howard, R. F., 1991, Axial Tilt Angles of Sunspot Groups, Sol. Phys., 136, 251–262

Howe, R., 2009, Solar Interior Rotation and its Variation, Living Reviews in Solar Physics, 6, 1

Howe, R., Komm, R., Hill, F., 2000, Variations in solar sub-surface rotation from GONG data 1995-1998, Sol. Phys., 192, 427–435

Howe, R., Komm, R. W., Baker, D., Harra, L., van Driel-Gesztelyi, L., Bogart, R. S., 2015, Persistent Near-Surface Flow Structures from Local Helioseismology, Sol. Phys., 290, 3137–3149

Ichimura, C., Yokoyama, T., 2017, Non-kinematic Flux-transport Dynamos Including the Effects of Diffusivity Quenching, ApJ, 839, 18

Inceoglu, F., Arlt, R., Rempel, M., 2017, The Nature of Grand Minima and Maxima from Fully Nonlinear Flux Transport Dynamos, ApJ, 848, 93

Ingersoll, A. P., Pollard, D., 1982, Motion in the interiors and atmospheres of Jupiter and Saturn: scale analysis, anelastic equations, barotropic stability criterion, Icarus, 52, 62–80

Jackiewicz, J., Serebryanskiy, A., Kholikov, S., 2015, Meridional Flow in the Solar Convection Zone. II. Helioseismic Inversions of GONG Data, ApJ, 805, 133

Kageyama, A., Sato, T., 2004, "yin-yang grid": An overset grid in spherical geometry, Geochemistry, Geophysics, Geosystems, 5, Q09 005

Käpylä, P. J., Mantere, M. J., Brandenburg, A., 2011, Effects of stratification in spherical shell convection, Astronomische Nachrichten, 332, 883

Käpylä, P. J., Käpylä, M. J., Brandenburg, A., 2014, Confirmation of bistable stellar differential rotation profiles, A&A, 570, A43

Käpylä, P. J., Rheinhardt, M., Brand enburg, A., Arlt, R., Käpylä, M. J., Lagg, A., Olspert, N., Warnecke, J., 2017, Extended Subadiabatic Layer in Simulations of Overshooting Convection, ApJ, 845, L23

Käpylä, P. J., Viviani, M., Käpylä, M. J., Brandenburg, A., Spada, F., 2019, Effects of a subadiabatic layer on convection and dynamos in spherical wedge simulations, Geophysical and Astrophysical Fluid Dynamics, 113, 149–183

Karak, B. B., Cameron, R., 2016, Babcock-Leighton Solar Dynamo: The Role of Downward Pumping and the Equatorward Propagation of Activity, ApJ, 832, 94

Karak, B. B., Miesch, M., 2017, Solar Cycle Variability Induced by Tilt Angle Scatter in a Babcock-Leighton Solar Dynamo Model, ApJ, 847, 69

Karak, B. B., Käpylä, P. J., Käpylä, M. J., Brandenburg, A., Olspert, N., Pelt, J., 2015, Magnetically controlled stellar differential rotation near the transition from solar to anti-solar profiles, A&A, 576, A26

Karak, B. B., Miesch, M., Bekki, Y., 2018, Consequences of high effective Prandtl number on solar differential rotation and convective velocity, Physics of Fluids, 30, 046602

Kashimura, H., Sugimoto, N., Takagi, M., Matsuda, Y., Ohfuchi, W., Enomoto, T., Nakajima, K., Ishiwatari, M., Sato, T. M., Hashimoto, G. L., Satoh, T., Takahashi, Y. O., Hayashi, Y.-Y., 2019, Planetary-scale streak structure reproduced in high-resolution simulations of the Venus atmosphere with a low-stability layer, Nature Communications, 10, 23

Kholikov, S., Hill, F., 2014, Meridional-Flow Measurements from Global Oscillation Network Group Data, Solar Physics, 289, 1077–1084

Kitchatinov, L. L., 2013, Baroclinic instability in differentially rotating stars, Astronomy Letters, 39, 561–569

Kitchatinov, L. L., 2014, Baroclinic Instability in Stellar Radiation Zones, ApJ, 784, 81

Kitchatinov, L. L., Rüdiger, G., 1993, A-effect and differential rotation in stellar convection zones, A&A, 276, 96

Kitchatinov, L. L., Ruediger, G., 1995, Differential rotation in solar-type stars: revisiting the Taylor-number puzzle., A&A, 299, 446

Knobloch, E., Spruit, H. C., 1982, Stability of differential rotation in stars, A&A, 113, 261–268

Kosovichev, A. G., 2012, Local Helioseismology of Sunspots: Current Status and Perspectives, Sol. Phys., 279, 323–348

Küker, M., Stix, M., 2001, Differential rotation of the present and the pre-main-sequence Sun, A&A, 366, 668–675

Kumar, R., Jouve, L., Nandy, D., 2019, A 3D kinematic Babcock Leighton solar dynamo model sustained by dynamic magnetic buoyancy and flux transport processes, A&A, 623, A54

Kutsenko, A. S., 2021, The rotation rate of solar active and ephemeral regions - I. Dependence on morphology and peak magnetic flux, MNRAS, 500, 5159–5166

Larson, T. P., Schou, J., 2018, Global-Mode Analysis of Full-Disk Data from the Michelson Doppler Imager and the Helioseismic and Magnetic Imager, Sol. Phys., 293, 29

Lee, U., Saio, H., 1987, Low-frequency oscillations of uniformly rotating stars., MNRAS, 224, 513–526

Leibacher, J. W., Stein, R. F., 1971, A New Description of the Solar Five-Minute Oscillation, Astrophys. Lett., 7, 191–192

Leighton, R. B., 1964, Transport of Magnetic Fields on the Sun., ApJ, 140, 1547

Leighton, R. B., 1969, A Magneto-Kinematic Model of the Solar Cycle, ApJ, 156, 1

Leighton, R. B., Noyes, R. W., Simon, G. W., 1962, Velocity Fields in the Solar Atmosphere. I. Preliminary Report., ApJ, 135, 474

Liang, Z.-C., Gizon, L., Birch, A. C., Duvall, T. L., 2019, Time-distance helioseismology of solar Rossby waves, A&A, 626, A3

Liu, J., Schneider, T., 01 Nov. 2011, Convective generation of equatorial superrotation in planetary atmospheres, Journal of the Atmospheric Sciences, 68, 2742 – 2756

Liu, J., Schneider, T., 2010, Mechanisms of Jet Formation on the Giant Planets, Journal of Atmospheric Sciences, 67, 3652–3672

Löptien, B., Birch, A. C., Duvall, T. L., Gizon, L., Proxauf, B., Schou, J., 2017, Measuring solar active region inflows with local correlation tracking of granulation, A&A, 606, A28

Löptien, B., Gizon, L., Birch, A. C., Schou, J., Proxauf, B., Duvall, T. L., Bogart, R. S., Christensen, U. R., 2018, Global-scale equatorial Rossby waves as an essential component of solar internal dynamics, Nature Astronomy, 2, 568–573

Lord, J. W., 2014, Deep Convection, Magnetism and Solar Supergranulation, Ph.D. thesis, University of Colorado at Boulder

Lord, J. W., Cameron, R. H., Rast, M. P., Rempel, M., Roudier, T., 2014, The Role of Subsurface Flows in Solar Surface Convection: Modeling the Spectrum of Supergranular and Larger Scale Flows, ApJ, 793, 24

Lorenzani, S., Tilgner, A., 2001, Fluid instabilities in precessing spheroidal cavities, Journal of Fluid Mechanics, 447, 111–128

Maas, L. R. M., Lam, F.-P. A., 1995, Geometric focusing of internal waves, Journal of Fluid Mechanics, 300, 1–41

Mandal, K., Hanasoge, S., 2020, Properties of Solar Rossby Waves from Normal Mode Coupling and Characterizing Its Systematics, ApJ, 891, 125

Mandal, K., Hanasoge, S. M., Rajaguru, S. P., Antia, H. M., 2018, Helioseismic Inversion to Infer the Depth Profile of Solar Meridional Flow Using Spherical Born Kernels, ApJ, 863, 39

Mandal, K., Hanasoge, S. M., Gizon, L., 2021, Detection of Rossby modes with even azimuthal orders using helioseismic normal-mode coupling, A&A, 652, A96

Manders, A. M. M., Maas, L. R. M., 2003, Observations of inertial waves in a rectangular basin with one sloping boundary, Journal of Fluid Mechanics, 493, 59–88

Martin-Belda, D., Cameron, R. H., 2017, Inflows towards active regions and the modulation of the solar cycle: A parameter study, A&A, 597, A21

Masada, Y., 2011, Impact of magnetohydrodynamic turbulence on thermal wind balance in the Sun, MNRAS, 411, L26–L30

Matilsky, L. I., Hindman, B. W., Toomre, J., 2019, The Role of Downflows in Establishing Solar Near-surface Shear, ApJ, 871, 217

Matilsky, L. I., Hindman, B. W., Toomre, J., 2020, Revisiting the Sun's Strong Differential Rotation along Radial Lines, ApJ, 898, 111

Matloch, Ł., Cameron, R., Shelyag, S., Schmitt, D., Schüssler, M., 2010, Mesogranular structure in a hydrodynamical simulation, A&A, 519, A52

Matsuno, T., 1966, Quasi-geostrophic motions in the equatorial area, Journal of the Meteorological Society of Japan. Ser. II, 44, 25–43

Miesch, M. S., 2005, Large-Scale Dynamics of the Convection Zone and Tachocline, Living Reviews in Solar Physics, 2, 1

Miesch, M. S., Dikpati, M., 2014, A Three-dimensional Babcock-Leighton Solar Dynamo Model, ApJ, 785, L8

Miesch, M. S., Hindman, B. W., 2011, Gyroscopic Pumping in the Solar Near-surface Shear Layer, ApJ, 743, 79

Miesch, M. S., Teweldebirhan, K., 2016, A three-dimensional Babcock-Leighton solar dynamo model: Initial results with axisymmetric flows, Advances in Space Research, 58, 1571–1588

Miesch, M. S., Elliott, J. R., Toomre, J., Clune, T. L., Glatzmaier, G. A., Gilman, P. A., 2000, Three-dimensional Spherical Simulations of Solar Convection. I. Differential Rotation and Pattern Evolution Achieved with Laminar and Turbulent States, ApJ, 532, 593–615

Miesch, M. S., Brun, A. S., Toomre, J., 2006, Solar Differential Rotation Influenced by Latitudinal Entropy Variations in the Tachocline, ApJ, 641, 618–625

Miesch, M. S., Brun, A. S., DeRosa, M. L., Toomre, J., 2008, Structure and Evolution of Giant Cells in Global Models of Solar Convection, ApJ, 673, 557-575

Miesch, M. S., Featherstone, N. A., Rempel, M., Trampedach, R., 2012, On the Amplitude of Convective Velocities in the Deep Solar Interior, ApJ, 757, 128

Moffatt, K., 1978, The Generation of Magnetic Fields in Electrically Conducting Fluids, Cambridge University Press

Muñoz-Jaramillo, A., Nandy, D., Martens, P. C. H., 2011, Magnetic Quenching of Turbulent Diffusivity: Reconciling Mixing-length Theory Estimates with Kinematic Dynamo Models of the Solar Cycle, ApJ, 727, L23

Müller, P., 1995, Ertel's potential vorticity theorem in physical oceanography, Reviews of Geophysics, 33, 67–97

Nagashima, K., Birch, A. C., Schou, J., Hindman, B. W., Gizon, L., 2020, An improved multi-ridge fitting method for ring-diagram helioseismic analysis, A&A, 633, A109

Nelson, N. J., Brown, B. P., Brun, A. S., Miesch, M. S., Toomre, J., 2011, Buoyant Magnetic Loops in a Global Dynamo Simulation of a Young Sun, ApJ, 739, L38

Nelson, N. J., Brown, B. P., Brun, A. S., Miesch, M. S., Toomre, J., 2013, Magnetic Wreaths and Cycles in Convective Dynamos, ApJ, 762, 73

Nelson, N. J., Payne, C., Sorensen, C. M., 2016, Stellar midlife crises: Challenges and advances in simulating convection and differential rotation in sun-like stars, Proceedings of the International Astronomical Union, 12, 264

Nelson, N. J., Featherstone, N. A., Miesch, M. S., Toomre, J., 2018, Driving Solar Giant Cells through the Self-organization of Near-surface Plumes, ApJ, 859, 117

Nordlund, Å., Stein, R. F., Asplund, M., 2009, Solar Surface Convection, Living Reviews in Solar Physics, 6, 2

November, L. J., Simon, G. W., 1988, Precise Proper-Motion Measurement of Solar Granulation, ApJ, 333, 427

Ogilvie, G. I., 2014, Tidal Dissipation in Stars and Giant Planets, ARA&A, 52, 171–210

Ogilvie, G. I., Lin, D. N. C., 2004, Tidal Dissipation in Rotating Giant Planets, ApJ, 610, 477–509

O'Mara, B., Miesch, M. S., Featherstone, N. A., Augustson, K. C., 2016, Velocity amplitudes in global convection simulations: The role of the Prandtl number and near-surface driving, Advances in Space Research, 58, 1475–1489

Ong, H., Roundy, P. E., 2020, The Compressional Beta Effect: Analytical Solution, Numerical Benchmark, and Data Analysis, Journal of Atmospheric Sciences, 77, 3721–3732

Orszag, S. A., Tang, C. M., 1979, Small-scale structure of two-dimensional magnetohydrodynamic turbulence, Journal of Fluid Mechanics, 90, 129–143

Ossendrijver, M., 2003, The solar dynamo, A&A Rev., 11, 287–367

Ouazzani, R. M., Lignières, F., Dupret, M. A., Salmon, S. J. A. J., Ballot, J., Christophe, S., Takata, M., 2020, First evidence of inertial modes in γ Doradus stars: The core rotation revealed, A&A, 640, A49

Papaloizou, J., Pringle, J. E., 1978, Non-radial oscillations of rotating stars and their relevance to the short-period oscillations of cataclysmic variables., MNRAS, 182, 423–442

Parker, E. N., 1955, Hydromagnetic Dynamo Models., ApJ, 122, 293

Parker, E. N., 1975, The generation of magnetic fields in astrophysical bodies. X. Magnetic buoyancy and the solar dynamo., ApJ, 198, 205–209

Phillips, N. A., 1954, Energy Transformations and Meridional Circulations associated with simple Baroclinic Waves in a two-level, Quasi-geostrophic Model, Tellus, 6, 274–286

Platzman, G. W., 1968, The Rossby wave, Quarterly Journal of the Royal Meteorological Society, 94, 225–248

Provost, J., Berthomieu, G., Rocca, A., 1981, Low Frequency Oscillations of a Slowly Rotating Star - Quasi Toroidal Modes, A&A, 94, 126

Proxauf, B., Gizon, L., Löptien, B., Schou, J., Birch, A. C., Bogart, R. S., 2020, Exploring the latitude and depth dependence of solar Rossby waves using ring-diagram analysis, A&A, 634, A44

Rajaguru, S. P., Antia, H. M., 2015, Meridional Circulation in the Solar Convection Zone: Time-Distance Helioseismic Inferences from Four Years of HMI/SDO Observations, ApJ, 813, 114

Read, P. L., Lebonnois, S., 2018, Superrotation on venus, on titan, and elsewhere, Annual Review of Earth and Planetary Sciences, 46, 175–202

Rekier, J., 2022, Free Core Nutation and Its Relation to the Spin-over Mode, PSJ, 3, 133

Rempel, M., 2005, Solar Differential Rotation and Meridional Flow: The Role of a Sub-adiabatic Tachocline for the Taylor-Proudman Balance, ApJ, 622, 1320–1332

Rempel, M., 2006, Flux-Transport Dynamos with Lorentz Force Feedback on Differential Rotation and Meridional Flow: Saturation Mechanism and Torsional Oscillations, ApJ, 647, 662–675

Rempel, M., 2007, Origin of Solar Torsional Oscillations, ApJ, 655, 651–659

Rempel, M., 2014, Numerical Simulations of Quiet Sun Magnetism: On the Contribution from a Small-scale Dynamo, ApJ, 789, 132

Rhines, P. B., 1975, Waves and turbulence on a beta-plane, Journal of Fluid Mechanics, 69, 417–443

Rhodes, E. J., J., Ulrich, R. K., Simon, G. W., 1977, Observations of nonradial p-mode oscillations on the sun., ApJ, 218, 901–919

Rhodes, E. J., J., Kosovichev, A. G., Schou, J., Scherrer, P. H., Reiter, J., 1997, Measurements of Frequencies of Solar Oscillations from the MDI Medium-l Program, Sol. Phys., 175, 287–310

Rieutord, M., Rincon, F., 2010, The Sun's Supergranulation, Living Reviews in Solar Physics, 7, 2

Rieutord, M., Valdettaro, L., 1997, Inertial waves in a rotating spherical shell, Journal of Fluid Mechanics, 341, 77–99

Rieutord, M., Valdettaro, L., 2018, Axisymmetric inertial modes in a spherical shell at low Ekman numbers, Journal of Fluid Mechanics, 844, 597–634

Rieutord, M., Zahn, J. P., 1995, Turbulent plumes in stellar convective envelopes., A&A, 296, 127

Rieutord, M., Georgeot, B., Valdettaro, L., 2001, Inertial waves in a rotating spherical shell: attractors and asymptotic spectrum, Journal of Fluid Mechanics, 435, 103–144

Rossby, C. G., 1939, Relation between variations in the intensity of the zonal circulation of the atmosphere and the displacement of the semi-permanent centers of action, J. Marine Res, 2, 38–66

Rossby, C. G., 1940, Planetary flow patterns in the atmosphere, Q. J. R. Meteorol. Soc, 66, 68–87

Roudier, T., Rieutord, M., Malherbe, J. M., Renon, N., Berger, T., Frank, Z., Prat, V., Gizon, L., Švanda, M., 2012, Quasi full-disk maps of solar horizontal velocities using SDO/HMI data, A&A, 540, A88

Rüdiger, G., 1989, Differential Rotation and Stellar Convection: Sun and Solar-type Stars, Fluid mechanics of astrophysics and geophysics, Gordon and Breach Science Publishers

Saio, H., 1982, R-mode oscillations in uniformly rotating stars, ApJ, 256, 717–735

Saio, H., Lee, U., 1991, Excitation Mechanism for Nonradial Pulsations in Variable OB Stars, in European Southern Observatory Conference and Workshop Proceedings, vol. 36 of European Southern Observatory Conference and Workshop Proceedings, p. 293

Schou, J., Antia, H. M., Basu, S., Bogart, R. S., Bush, R. I., Chitre, S. M., Christensen-Dalsgaard, J., Di Mauro, M. P., Dziembowski, W. A., Eff-Darwich, A., Gough, D. O., Haber, D. A., Hoeksema, J. T., Howe, R., Korzennik, S. G., Kosovichev, A. G., Larsen, R. M., Pijpers, F. P., Scherrer, P. H., Sekii, T., Tarbell, T. D., Title, A. M., Thompson, M. J., Toomre, J., 1998, Helioseismic Studies of Differential Rotation in the Solar Envelope by the Solar Oscillations Investigation Using the Michelson Doppler Imager, ApJ, 505, 390–417

Schrijver, C. J., Harvey, K. L., 1994, The Photospheric Magnetic Flux Budget, Sol. Phys., 150, 1

Showman, A. P., Polvani, L. M., 2011, Equatorial Superrotation on Tidally Locked Exoplanets, ApJ, 738, 71

Sibgatullin, I. N., Ermanyuk, E. V., 2019, Internal and Inertial Wave Attractors: A Review, Journal of Applied Mechanics and Technical Physics, 60, 284–302

Skaley, D., Stix, M., 1991, The overshoot layer at the base of the solar convection zone, A&A, 241, 227–232

Smeyers, P., Craeynest, D., Martens, L., 1981, Rotational Modes in a Slowly and Uniformly Rotating Star, Ap&SS, 78, 483–501

Solanki, S. K., 2003, Sunspots: An overview, A&A Rev., 11, 153–286

Spruit, H., 1997, Convection in stellar envelopes: a changing paradigm, Mem. Soc. Astron. Italiana, 68, 397

Spruit, H. C., 2003, Origin of the torsional oscillation pattern of solar rotation, Sol. Phys., 213, 1–21

Spruit, H. C., 2011, Theories of the Solar Cycle: A Critical View, in The Sun, the Solar Wind, and the Heliosphere, vol. 4, p. 39

Spruit, H. C., Knobloch, E., 1984, Baroclinic instability in stars, A&A, 132, 89–96

Spruit, H. C., Nordlund, A., Title, A. M., 1990, Solar convection., ARA&A, 28, 263–301

Stein, R. F., Nordlund, A., 1989, Topology of convection beneath the solar surface, ApJL, 342, L95–L98

Stein, R. F., Nordlund, Å., 2006, Solar Small-Scale Magnetoconvection, ApJ, 642, 1246–1255

Stejko, A. M., Kosovichev, A. G., Pipin, V. V., 2021, Forward Modeling Helioseismic Signatures of One- and Two-cell Meridional Circulation, ApJ, 911, 90

Stenflo, J. O., Kosovichev, A. G., 2012, Bipolar Magnetic Regions on the Sun: Global Analysis of the SOHO/MDI Data Set, ApJ, 745, 129

Stewartson, K., Rickard, J. A., 1969, Pathological oscillations of a rotating fluid, Journal of Fluid Mechanics, 35, 759–773

Stix, M., 1976, Differential rotation and the solar dynamo., A&A, 47, 243–254

Stix, M., 2002, The sun: an introduction, Springer Berlin Heidelberg

Stone, P. H., 1978, Baroclinic Adjustment., Journal of Atmospheric Sciences, 35, 561–571

Strugarek, A., Beaudoin, P., Charbonneau, P., Brun, A. S., do Nascimento, J. D., 2017, Reconciling solar and stellar magnetic cycles with nonlinear dynamo simulations, Science, 357, 185–187

Thompson, M. J., Toomre, J., Anderson, E. R., Antia, H. M., Berthomieu, G., Burtonclay, D., Chitre, S. M., Christensen-Dalsgaard, J., Corbard, T., De Rosa, M., Genovese, C. R., Gough, D. O., Haber, D. A., Harvey, J. W., Hill, F., Howe, R., Korzennik, S. G., Kosovichev, A. G., Leibacher, J. W., Pijpers, F. P., Provost, J., Rhodes, E. J., J., Schou, J., Sekii, T., Stark, P. B., Wilson, P. R., 1996, Differential Rotation and Dynamics of the Solar Interior, Science, 272, 1300–1305

Thompson, M. J., Christensen-Dalsgaard, J., Miesch, M. S., Toomre, J., 2003, The Internal Rotation of the Sun, ARA&A, 41, 599–643

Thomson, S. W., 1880, Xxiv. vibrations of a columnar vortex, The London, Edinburgh, and Dublin Philosophical Magazine and Journal of Science, 10, 155–168

Tilgner, A., 1999, Non-axisymmetric shear layers in precessing fluid ellipsoidal shells, Geophysical Journal International, 136, 629–636

Tilgner, A., 2007, in Treatise on Geophysics, vol. 8.07, chap. 8.07 - Rotational Dynamics of the Core, pp. 207–243, Elsevier, Amsterdam

Triana, S. A., Zimmerman, D. S., Lathrop, D. P., 2012, Precessional states in a laboratory model of the earth's core, J. Geophys. Res., 117, 103

Triana, S. A., Guerrero, G., Barik, A., Rekier, J., 2022, Identification of Inertial Modes in the Solar Convection Zone, ApJ, 934, L4

Ulrich, R. K., 1970, The Five-Minute Oscillations on the Solar Surface, ApJ, 162, 993

Ulrich, R. K., 2010, Solar Meridional Circulation from Doppler Shifts of the Fe I Line at 5250 Å as Measured by the 150-foot Solar Tower Telescope at the Mt. Wilson Observatory, ApJ, 725, 658–669

Unno, W., Osaki, Y., Ando, H., Saio, H., Shibahashi, H., 1989, Nonradial oscillations of stars, University of Tokyo Press

Vallis, G. K., 2006, Atmospheric and Oceanic Fluid Dynamics, Cambridge University Press, Cambridge, U.K.

Vasil, G. M., Julien, K., Featherstone, N. A., 2021, Rotation suppresses giant-scale solar convection, Proceedings of the National Academy of Science, 118, 2022518118

Verhoeven, J., Stellmach, S., 2014, The compressional beta effect: A source of zonal winds in planets?, Icarus, 237, 143–158

Vitense, E., 1953, Die Wasserstoffkonvektionszone der Sonne. Mit 11 Textabbildungen, ZA, 32, 135

Viviani, M., Warnecke, J., Käpylä, M. J., Käpylä, P. J., Olspert, N., Cole-Kodikara, E. M., Lehtinen, J. J., Brandenburg, A., 2018, Transition from axi- to nonaxisymmetric dynamo modes in spherical convection models of solar-like stars, A&A, 616, A160

Vögler, A., Shelyag, S., Schüssler, M., Cattaneo, F., Emonet, T., Linde, T., 2005, Simulations of magneto-convection in the solar photosphere. Equations, methods, and results of the MURaM code, A&A, 429, 335–351

Vorontsov, S. V., Christensen-Dalsgaard, J., Schou, J., Strakhov, V. N., Thompson, M. J., 2002, Helioseismic Measurement of Solar Torsional Oscillations, Science, 296, 101–103

Švanda, M., 2012, Inversions for Average Supergranular Flows Using Finite-frequency Kernels, ApJ, 759, L29

Wang, Y. M., Sheeley, N. R., J., Nash, A. G., 1991, A New Solar Cycle Model Including Meridional Circulation, ApJ, 383, 431

Wang, Y. M., Colaninno, R. C., Baranyi, T., Li, J., 2015, Active-region Tilt Angles: Magnetic versus White-light Determinations of Joy's Law, ApJ, 798, 50

Watson, M., 1981, Shear instability of differential rotation in stars., Geophys. Astrophys. Fluid Dyn., 16, 285–298

Whitbread, T., Yeates, A. R., Muñoz-Jaramillo, A., 2019, The need for active region disconnection in 3D kinematic dynamo simulations, A&A, 627, A168

Wolff, C. L., Blizard, J. B., 1986, Properties of R-Modes in the Sun, Sol. Phys., 105, 1–15

Wu, Y., 2005, Origin of Tidal Dissipation in Jupiter. I. Properties of Inertial Modes, ApJ, 635, 674–687

Yeates, A. R., Muñoz-Jaramillo, A., 2013, Kinematic active region formation in a three-dimensional solar dynamo model, MNRAS, 436, 3366–3379

Yoshimura, H., 1975, Solar-cycle dynamo wave propagation., ApJ, 201, 740–748

Zaqarashvili, T. V., Albekioni, M., Ballester, J. L., Bekki, Y., Biancofiore, L., Birch, A. C., Dikpati, M., Gizon, L., Gurgenashvili, E., Heifetz, E., Lanza, A. F., McIntosh, S. W., Ofman, L., Oliver, R., Proxauf, B., Umurhan, O. M., Yellin-Bergovoy, R., 2021, Rossby waves in astrophysics, Space Science Reviews, 217, 15

Zhao, J., Bogart, R. S., Kosovichev, A. G., Duvall, Jr., T. L., Hartlep, T., 2013, Detection of Equatorward Meridional Flow and Evidence of Double-cell Meridional Circulation inside the Sun, ApJL, 774, L29

Publications

Refereed publications

- T.V. Zaqarashvili, M. Albekioni, J.L. Ballester, **Y. Bekki**, L. Biancofiore, A.C. Birch, M. Dikpati, L. Gizon, E. Gurgenashvili, E. Heifets, A.F. Lanza, S.W. McIntosh, L. Ofman, R. Oliver, B. Proxauf, O.M. Umurhan, and R. Yellin-Bergovoy, *Rossby waves in astrophysics*, Space Science Reviews **217**, 15 (2021).
DOI: https://doi.org/10.1007/s11214-021-00790-2

- L. Gizon, R.H. Cameron, **Y. Bekki**, A.C. Birch, R.S. Bogart, A.S. Brun, C. Damiani, D. Fournier, L. Hyest, K. Jain, B. Lekshmi, Z-C. Liang, and B. Proxauf, *Solar inertial modes: Observations, identification, and diagnostic promise*, Astronomy and Astrophysics **652**, L6 (2021).
DOI: https://doi.org/10.1051/0004-6361/202141462

- **Y. Bekki**, R.H. Cameron, and L. Gizon, *Theory of solar oscillations in the inertial frequency range: Linear modes of the convection zone*, Astronomy and Astrophysics **662**, A16 (2022).
DOI: https://doi.org/10.1051/0004-6361/202243164

- **Y. Bekki**, R.H. Cameron, and L. Gizon, *Theory of solar oscillations in the inertial frequency range: Amplitudes of equatorial modes from a nonlinear rotating convection simulation*, Astronomy and Astrophysics **666**, A135 (2022).
DOI: https://doi.org/10.1051/0004-6361/202244150

Paper submitted

- **Y. Bekki** and R.H. Cameron, *Three-dimensional non-kinematic simulation of post-emergence evolution of bipolar magnetic regions and Babcock-Leighton dynamo of the Sun*, submitted to Astronomy and Astrophysics on 16.09.2022.

Conference contributions

- Flux Emergence Workshop 2019, Tokyo, Japan, 18-22 March 2019.
  Oral presentation: *Examining the Subsurface Upper Boundary Conditions in Startified Magneto- Convection Simulations*
- WHOLE SUN Kick-off Meeting, Paris-Saclay, France, 27-29 May 2019.
  Oral presentation: *Effects of Rotation on Convection*
- Physics at the equator: from the lab to the stars, Lyon, France, 16-18 October 2019.
  Poster: *Rossby Waves and Rotationally-Influenced Convective Modes in the Solar Convection Simulations*
- WHOLE SUN Virtual Spring Meeting 2021, online (Paris-Saclay, France), 9-11 March 2021.
  Oral presentation: *Detecting Rossby waves in Simulations*
  Oral presentation: *A 3D non-kinematic mean-field dynamo model*
- WHOLE SUN Virtual Fall Meeting 2021, online (Paris-Saclay, France), 21-22 September 2021.
  Oral presentation: *Baroclinic instability in the Sun: Origin of the high-latitude inertial modes*
- ISSI Workshop "Solar and Stellar Dynamos: A New Era", Bern, Switzerland, 13-17 June 2022.
  Oral presentation (invited): *Numerical studies of Rossby and inertial modes in the Sun*

Acknowledgements

First and foremost, I owe much gratitude and appreciation to my supervisor Robert Cameron for his great and continuous support and patience during my PhD journey. My way of thinking has improved through daily discussions with him. I wish to express my gratitude to Laurent Gizon who provided me with the opportunity to complete this PhD work at MPS and also provided me with insightful guidance for my research projects. I also want to thank Andreas Tilgner for being a part of my thesis advisory committee.

I am very grateful to all the people in the Solar and Stellar Interiors Department at MPS. Particularly, I am thankful to Aaron Birch for many helpful discussions about Rossby waves. I am also grateful to Bastian Proxauf for kindly sharing the observational data. I also want to thank Jesper Schou, Zhi-Chao Liang, Vincent Böning, Chris Goddard, Krishnendu Mandal, Cilia Damiani, and Damien Fournier for always being supportive. I am especially grateful to Sonja Schuh for all her support as the IMPRS program coordinator. Great thanks to all the IMPRS fellows for making the off-hours very fruitful. My special thanks goes as well to Kaori Nagashima for helping me a lot to feel comfortable in Göttingen.

I wish to acknowledge the IMPRS for Solar System Science at the University of Göttingen for providing me with the opportunity to pursue my doctoral studies abroad. For additional funding, I am very thankful to the Japan Student Services Organization (JASSO). I would like to also acknowledge financial support from the WHOLE SUN ERC Synergy Grant project 810218.

Last but not least, I would like to express my deepest thanks to my family, my grandma Wakako, my parents Naoaki and Yoshiko, and my great brother Hohto, for their infinite love and support ever since my birth. My sincerest gratitude is finally dedicated to my beloved wife, Ayaka, for her endless support and encouragement in all my ups and downs.